FUNDAMENTAL LIMITS TO COLLECTIVE SENSING IN CELL POPULATIONS

A Dissertation

Submitted to the Faculty

of

Purdue University

by

Sean Fancher

In Partial Fulfillment of the

Requirements for the Degree

of

Doctor of Philosophy

May 2019

Purdue University

West Lafayette, Indiana

THE PURDUE UNIVERSITY GRADUATE SCHOOL
STATEMENT OF DISSERTATION APPROVAL

Dr. Andrew Mugler, Chair

Department of Physics and Astronomy

Dr. Erica Carlson

Department of Physics and Astronomy

Dr. Kenneth Ritchie

Department of Physics and Astronomy

Dr. Srividya Iyer-Biswas

Department of Physics and Astronomy

Approved by:

Dr. John Finley

Head of Department of Physics and Astronomy

TABLE OF CONTENTS

Page

ABSTRACT

Fancher, Sean PhD, Purdue University, May 2019. Fundamental Limits to Collective Sensing in Cell Populations. Major Professor: Andrew Mugler.

Cells live in inherently noisy environments. The machinery that cells use to sense their environment is also noisy. Yet, cells are exquisite environmental sensors, often approaching the limits of what is physically possible. This thesis investigates how the precision of environmental sensing is improved when cells behave collectively. We derive physical limits to cells' ability to collectively sense and respond to chemical concentrations and gradients. For concentration sensing, we find that when cell populations become sufficiently large, long-range communication can provide higher sensory precision than short-range communication, and that the optimal cell-cell separation in such a system can be large, due to a tradeoff between maintaining communication strength and reducing signal cross-correlations. We also show that concentration profiles formed diffusively are more precise for large profile lengths while those formed via directed transport are more precise for short profile lengths. These effects are due to increased molecule refresh rate and mean concentration respectively. For gradient sensing, we derive the sensory precision of the well-known the local excitation-global inhibition (LEGI) model and the more recently proposed regional excitation-global inhibition (REGI) model for two and three dimensional cell cluster geometries. We find that REGI systems achieve higher levels of precision than LEGI systems and give rise to optimally sensing geometries that are consistent with the shapes of naturally occurring gradient-sensing cell populations. Lastly, we analyze the precision with which migrating cell clusters can track a chemical gradient via an individual-based and emergent method. We show that one and two dimensional clusters utilizing the emergent chemotactic method have improved scaling

with population size due to differences in the scaling properties of the variance in the total polarization. By completing these studies we aim to understand the limits and precise roles of collective behavior in environmental sensing.

1. INTRODUCTION

Cells exist in a wide array of chemical environments subject to stochastic fluctuations. In order to properly react to these environments, cells must be able to sense their surroundings with sufficient precision to overcome both this external noise as well as fluctuations inherent in their own stochastic machinery. In some cases this precision approaches the physical limits set by molecular diffusion [1, 2]. Yet cells rarely perform these sensory tasks in isolation. Cells can exist in communities such as colonies, biofilms, and tissues. Within these communities, cells can influence each other through means such as chemical communication and mechanical interactions. Can cells utilize these effects to further improve their ability to sense and respond to various aspects of their environments?

Experiments have shown that cells are more sensitive in groups than they are alone. In some cases, such as with epithelial cells [3], cell-cell communication has been shown to be directly responsible for the enhanced sensitivity. Yet, from a theoretical perspective, the fundamental limits to concentration sensing [1, 2, 4–8] or gradient sensing [9–11] have been largely limited to single receptors or single cells. Here we focus on expanding the understanding of these limits by determining how groups of cells can utilize different methods of chemical communication to improve their ability to sense. Specifically, we look at whether these limits depend on the exact communication mechanism and how they scale with collective properties such as communication strength and population size.

In addition to simple environmental sensing, groups of cells can also influence each other through self-created chemical cues. This is prominently seen in developing systems utilizing morphogen profiles to induce morphological changes such as the concentration of Bicoid dictating the expression of the Hunchback gene [12]. Exactly how the method by which these profiles are formed affects the cells' ability to precisely

decipher such a cue remains poorly understood though. Morphogens such as Fgf8 in Zebrafish appear to have molecular dynamics consistent with Brownian diffusion [13], but others such as Hedgehog in *Drosophila* appear to track membrane protrusions [14]. Here we investigate how these methods differ in their limits to the cells' sensory precision of the resultant profiles.

In some instances though, a method which allows groups of cells to sense one aspect of their environment more precisely might hinder their ability to sense another. In the case of stripe formation in *Drosophila*, spatial averaging of concentration measurements made by cells has been shown to improve the precision of concentration sensing [15]. However, the effects such a mechanism might have on gradient sensing has only been studied for one dimensional chains of cells [3, 16] despite biological systems frequently existing in two and three dimensional geometries. Here we expand upon this by ascertaining the role that dimensions transverse to a gradient play in determining the precision of gradient sensing.

Lastly, groups of cells typically perform these sensory tasks so as to act upon the results, such as in the phenomenon of collective migration in response to chemical cues in the environment. This process, known as chemotaxis, can be performed by each cell acting individually in a manner identical to that of a single, isolated cell [17] or by cells changing their behavior when they enter a group so as to facilitate a more emergent strategy [18–21]. Here we study how these methods allow groups of cells to improve their chemotactic precision in responding to a chemical gradient and the effects of the geometry of the cell cluster.

In these works we use stochastic modeling to make theoretical predictions about the physical limits to how precisely groups of cells can perform and act on a variety of sensory tasks. We compare our results to several experimental systems which suggest that whichever of these tasks a group of cells is performing, it does so in a manner that maximizes this precision. The culmination of these works represents a step forward in our understanding of the underlying physics behind collective behavior in noisy environments.

2. THESIS PLAN

Here we briefly describe the basic components of the thesis. Further details on each component will follow in Chapters 4-7.

2.1 Collective Concentration Sensing

We first develop the mathematical framework used throughout the rest of the works presented by examining a collection of cells sensing a uniform ligand concentration. We model the system with a series of stochastic equations that describe i) the diffusion of the ligand through three dimensional (3-D) space, ii) the binding and unbinding of the ligand to receptors on the cell surface, and iii) the production, degredation, and movement of messenger molecules between cells. We show that when these equations are expressed as Langevin equations in which the noise terms have well known properties, relavent results such as the mean and variance of time averaged measurements of the system variables can be exactly solved for. With these solutions, we compare the precision in concentration sensing of the juxtacrine and autocrine communication methods to establish which produces lesser noise for a given set of parameters.

2.2 Morphogen Profile Sensing

We next investigate a system in which cells perform concentration sensing of a nonuniform concentration field. In particular, we focus on the problem of morphogen profile sensing in developing systems. We consider profiles formed via diffusion in a similar manner to our previous work as well as via direct transport of morphogen through cytonemes. These distinct methods of profile formation create different mean

distributions and have fluctuations that scale differently with the various parameters of the system. We compare these fluctuations to determine which method creates the profile with less inherent noise given certain system properties and contrast this with experimental measurements of systems observed to use one method or the other.

2.3 Juxtacrine Gradient Sensing

In conjunction with concentration sensing, we also develop a simplified model of gradient sensing. Utilizing the same mathematical methods and the assumption that the ligand diffusion and receptor binding occur at rates significantly faster than the relevant time scales of the messenger molecules, we solve for the precision with which a collection of cells arranged in a square or cubic lattice and communicating via juxtacrine signalling can detect a constant gradient in the ligand profile. We look at both the local excitation-global inhibition (LEGI) and regional excitation-global inhibition (REGI) models to discern which method provides higher precision under a variety of cluster configurations. For the REGI mechanism, we then find the optimal configuration for a fixed number of cells in both 2-D and 3-D.

2.4 Multicellular Chemotaxis

Lastly, we continue to investigate gradient sensing but through collectives of cells utilizing mechanical coupling rather than chemical communication. We consider 1-D, 2-D, and 3-D configurations of cells in which each cell adheres to its neighbors and makes its own individual measurement of its local environment. Cells either directly measure the local gradient attempt to move the cluster in that direction, or they measure the local concentration and attempt to move outwardly away from the cluster. We show that while both these methods produce similar mean chemotactic velocities, they can have different noise properties depending on the dimensionality of the cluster configuration.

3. BACKGROUND INFORMATION ON MATHEMATICAL TECHNIQUES

3.1 Brief Analysis of Single Cell Sensing

Cells live and operate in enviroments that are inherently stochastic in nature. As such, models of cellular mechanics must incorporate an inherent amount of noise in their systems which in turn causes said systems to have a finite level of precision. Among the first to study the limits to this precision were Berg and Purcell, who calculated the noise-to-signal ratio of a cell acting as a perfect counting instrument [1]. In their model, the cell is taken to be a perfect sphere of radius a and volume V into and out of which molecules can freely diffuse. Assuming the molecular concentration is spatially uniform on average, when the cell counts the number of molecules inside itself, it will measure a mean value of $\bar{n} = \bar{c}V \sim \bar{c}a^3$, where $\bar{c}$ is the mean concentration. Since diffusion is a Poissonian process, the variance in this count will be inherently equal to its mean. Thus, the noise-to-signal ratio, the ratio of the variance to the square of the mean, takes the form

$$\frac{\sigma_n^2}{\bar{n}^2} = \frac{1}{\bar{n}} \sim \frac{1}{\bar{c}a^3}. \tag{3.1}$$

The cell can decrease this error by taking multiple independent measurements. However, in order for measurements to be independent, the molecules must be given enough time to diffuse into or out of the cell and refresh themselves. This time scale is given by the characteristic diffusion time $\tau \sim a^2/D$, where D is the diffusion constant. Assuming the cell integrates its measurements over a time T, it is effectively making $N = T/\tau$ independent measurements, which in turn reduces the variance by a factor of $1/N$. Thus, the noise-to-signal ratio now takes the form

$$\frac{\sigma_n^2}{\bar{n}^2} \sim \frac{1}{\bar{c}a^3N} = \frac{a^2/D}{\bar{c}a^3T} = \frac{1}{a\bar{c}DT}. \tag{3.2}$$

The noise-to-signal ratio is seen to decrease with increased cell size, molecular concentration, molecular diffusion rate, and integration time. The first two factors stem from the fact that increasing cell size and molecular concentration increases the mean. Increasing the diffusion rate decreases the noise as it allows more independent measurements to be taken in a time T. Similarly, increasing the integration also decreases the noise as it creates more independent measurements. This limit has been rigorously derived by Berg and Purcell to produce the result [1]

$$\frac{\sigma_n^2}{\bar{n}^2} = \frac{3}{5}\frac{1}{\pi a\bar{c}DT}. \tag{3.3}$$

3.2 Mathematical Definitions: Correlation Function and Power Spectrum

We proceed to study cellular precision in the same vein as Berg and Purcell, by examining the noise-to-signal ratio of our modelled systems, but choose to utilize different techniques to solve the stochastic equations that describe such systems. There are several techniques avaliable for mathematically modelling stochastic systems, such as master equations and Fokker-Planck equations. Here we will make use of Langevin equations as our primary tool. Unlike master equations and Fokker-Planck equations, which perform time evolutions on probability distributions of the system, Langevin equations incorporate random noise into the time evolution of the state variables themselves to account for fluctuations. For a given state variable $x\,(t)$, this is typically written in the form

$$\frac{dx}{dt} = \mathcal{O}\,(x) + \eta, \tag{3.4}$$

where $\mathcal{O}$ is some operator being applied to the system state and η is the Langevin noise term that accounts for fluctuations away from the mean equation.

Equations of the form seen in Eq. 3.4 have a number of solution methods, but here we will focus on derivations of the correlation function, cross spectrum, and power spectrum. First, let $\delta x\left(t\right)$ be defined as $x\left(t\right)-\left\langle x\left(t\right)\right\rangle$, where $\left\langle x\left(t\right)\right\rangle$ is the ensemble average of the state varable $x\left(t\right)$ at time t. Thus, $\delta x\left(t\right)$ gives the fluctuations from the mean at any given time. The correlation function can then be defined as

$$C\left(t,t'\right)=\left\langle \delta x\left(t'\right)\delta x\left(t\right)\right\rangle . \tag{3.5}$$

If the system is in steady state, then absolute time becomes irrelevant and the correlation function depends only on the difference in time, $C\left(t,t'\right)=C\left(t-t'\right)$. This steady state assumption will be how we view the correlation function throughout this work. Now, let the cross spectrum, $\left\langle \tilde{\delta x}^{*}\left(\omega'\right)\tilde{\delta x}\left(\omega\right)\right\rangle$, be defined as the correlation function Fourier transformed in the unprimed coordinates and conjugate Fourier transformed in the primed coordinates. This allows us to define the power spectrum, $S\left(\omega\right)$, as the integral of the cross spectrum over the primed coordinates, which leads to the relation

$$\begin{aligned} S_{x}\left(\omega\right) &= \int\frac{d\omega'}{2\pi}\left\langle \tilde{\delta x}^{*}\left(\omega'\right)\tilde{\delta x}\left(\omega\right)\right\rangle =\frac{1}{2\pi}\int d\omega' dt dt'\left\langle \delta x\left(t'\right)\delta x\left(t\right)\right\rangle e^{i\omega t}e^{-i\omega' t'} \\ &= \int dt dt' C\left(t-t'\right)e^{i\omega t}\delta\left(t'\right)=\int dt C\left(t\right)e^{i\omega t}. \end{aligned} \tag{3.6}$$

Thus, the power spectrum is the Fourier transform of the steady state correlation function. Inverting this relationship will allow us to obtain the correlation function once the power spectrum is solved for.

With these definitions, we can now calculate the correlation function of a measurement of $\delta x\left(t\right)$ averaged over a time period T.

$$C_T\left(t-t'\right) = \left\langle \left(\frac{1}{T}\int_{t'}^{t'+T} d\tau' \delta x\left(\tau'\right)\right)\left(\frac{1}{T}\int_{t}^{t+T} d\tau \delta x\left(\tau\right)\right)\right\rangle$$
$$= \frac{1}{T^2}\int_{t}^{t+T} d\tau \int_{t'}^{t'+T} d\tau' \left\langle \delta x\left(\tau'\right)\delta x\left(\tau\right)\right\rangle$$
$$= \frac{1}{T^2}\int_{t}^{t+T} d\tau \int_{t'}^{t'+T} d\tau' C\left(\tau-\tau'\right) \tag{3.7}$$

Let $y \equiv (\tau-\tau') - (t-t')$ and $z \equiv (\tau+\tau') - (t+t')$. This transforms Eq. 3.7 into

$$C_T\left(t-t'\right) = \frac{1}{T^2}\int_{-T}^{T} dy \int_{|y|}^{2T-|y|} dz \frac{1}{2} C\left(y+t-t'\right)$$
$$= \frac{1}{T^2}\int_{-T}^{T} dy \left(T-|y|\right) C\left(y+t-t'\right). \tag{3.8}$$

By inverting the relationship found in Eq. 3.6, $C\left(y+t-t'\right)$ can be replaced with an inverse Fourier transform of $S\left(\omega\right)$ to produce

$$C_T\left(t-t'\right) = \frac{1}{T^2}\int_{-T}^{T} dy \int \frac{d\omega}{2\pi}\left(T-|y|\right) S_x\left(\omega\right) e^{-i\omega\left(y+t-t'\right)}$$
$$= \int \frac{d\omega}{2\pi}\left(\frac{2}{\omega T}\sin\left(\frac{\omega T}{2}\right)\right)^2 S_x\left(\omega\right) e^{-i\omega\left(t-t'\right)}. \tag{3.9}$$

The factor of $(\omega T)^{-2}$ in the integrand of Eq. 3.9 forces only small values of ω to contribute when T is large. Thus, the approximation $S_x\left(\omega\right) \approx S_x\left(0\right)$ can be made since only values of ω near 0 are contributing. This causes $C_T\left(0\right)$ to be exactly calculable to

$$C_T\left(0\right) \approx S_x\left(0\right)\int \frac{d\omega}{2\pi}\left(\frac{2}{\omega T}\sin\left(\frac{\omega T}{2}\right)\right)^2 = \frac{S_x\left(0\right)}{T}, \tag{3.10}$$

where the integration can be easily performed by noting that $\sin\left(x\right)/x$ is the 0th spherical bessel function and using a table of integral properties of bessel functions.

When $t = t'$, the correlation function as defined in Eq. 3.5 becomes simply the variance of $x\left(t\right)$. Thus, Eq. 3.10 relates the variance in the time averaged measurement of $x\left(t\right)$ to the zero-frequency power spectrum of a non-time averaged measurement of $x\left(t\right)$, assuming that $S_x\left(\omega\right)$ does not change in value significantly

when ω is changed by $\sim T^{-1}$. The technique presented here is for a state variable $x(t)$ that is a function of only a single coordinate, but it is easily generalizable to state variables that are functions of an arbitrary number of coordinates by simply adding the appropriate Fourier integrals to any Fourier transformations.

3.3 Historical Example: Berg and Purcell's Perfect Instrument

With the relations between the time averaged correlation function and power spectrum defined, we can apply them to a well known system. In particular, we can analytically solve for the perfect instrument as defined by Berg and Purcell. This is a system consisting of a ligand field, $c(\vec{x},t)$, that is on average uniform in space, $\bar{c}(\vec{x}) = \bar{c}$ and diffuses throughout space with diffusion constant D_c. Additionally, there is a spherical cell of radius a whose membrane is perfectly permeable to the ligand. The cell then makes a measurement of $n(t)$, the number of ligand molecules within its volume, averaged over a time T. As given by Eq. 3.3, Berg and Purcell calculated the noise to signal ratio $\sigma_{nT}^2/\langle n\rangle^2$, the ratio of the variance of such a measurement to the square of its mean, to be

$$\frac{\sigma_{nT}^2}{\langle n\rangle^2} = \frac{3}{5}\frac{1}{\pi a\bar{c}D_cT}. \tag{3.11}$$

We will show that we can derive this result via a Langevin formalism. To begin, we must define how $c(\vec{x},t)$ evolves with time. Since the ligand's only interaction is diffusion, this can be simply written as

$$\frac{dc}{dt} = D_c\nabla^2 c + \eta_c, \tag{3.12}$$

where η_c is the Langevin noise term that accounts for fluctuations in the ligand field. As shown in [22] and derived in Appendix A, η_c has a correlation function of the form

$$\left\langle \eta_c\left(\vec{x}',t'\right)\eta_c\left(\vec{x},t\right)\right\rangle = 2D_c\delta\left(t-t'\right)\vec{\nabla}_x\cdot\vec{\nabla}_{x'}\left(\bar{c}\left(\vec{x}\right)\delta^3\left(\vec{x}-\vec{x}'\right)\right). \tag{3.13}$$

Since $\bar{c}(\vec{x})$ is a constant, Fourier transforming Eq. 3.13 is relatively straightforward and yields

$$\left\langle \tilde{\eta}_c^* \left(\vec{k}', \omega'\right) \tilde{\eta}_c \left(\vec{k}, \omega\right) \right\rangle = 2D_c \bar{c} k^2 \left(2\pi\delta\left(\omega - \omega'\right)\right) \left(\left(2\pi\right)^3 \delta^3 \left(\vec{k} - \vec{k}'\right)\right). \tag{3.14}$$

A detailed derivation of Eq. 3.14 can be seen in Appendix A.

Now, Eq. 3.12 must be linearized by defining $\delta c(\vec{x}, t)$ such that $c(\vec{x}, t) = \bar{c} + \delta c(\vec{x}, t)$. This allows Eq. 3.12 to be rewritten as

$$\frac{d\delta c}{dt} = D_c \nabla^2 (\delta c) + \eta_c. \tag{3.15}$$

Fourier transforming Eq. 3.15 transforms the derivatives into factors of $-i\omega$ and $-k^2$ respectively and allows for $\tilde{\delta c}$ to be solved for as

$$\tilde{\delta c} = \frac{\tilde{\eta}_c}{D_c k^2 - i\omega}. \tag{3.16}$$

Returning to $n(t)$, the number of ligand molecules within the cell volume V at time t, this can be easily defined as

$$n(t) = \int_V d^3 x c(\vec{x}, t). \tag{3.17}$$

Since the cell is considered spherical and the ligand field constant on the level of the mean, the mean of $n(t)$ is easily calcualted to be

$$\langle n(t) \rangle = \int_V d^3 x \bar{c} = \frac{4}{3}\pi a^3 \bar{c}. \tag{3.18}$$

To calculate the noise however, we must first linearize and Fourier transform Eq. 3.17 into

$$\delta n(t) = \int_V d^3 x \delta c(\vec{x}, t) \tag{3.19}$$

$$\implies \tilde{\delta n}\left(\omega\right) = \int_V d^3x \int \frac{d^3k}{\left(2\pi\right)^3} \tilde{\delta c}\left(\vec{k},\omega\right) e^{-i\vec{k}\cdot\vec{x}}$$
$$= \int_V d^3x \int \frac{d^3k}{\left(2\pi\right)^3} \frac{\tilde{\eta}_c\left(\vec{k},\omega\right)}{D_c k^2 - i\omega} e^{-i\vec{k}\cdot\vec{x}}. \tag{3.20}$$

Since the cross spectrum of η_c is known, this makes the cross spectrum of n also solvable as

$$\left\langle \tilde{\delta n}^*\left(\omega'\right) \tilde{\delta n}\left(\omega\right)\right\rangle = \left(2\pi\delta\left(\omega-\omega'\right)\right) \frac{16\pi\bar{c}a^5}{15D_c} f\left(a\sqrt{\frac{2|\omega|}{D_c}}\right), \tag{3.21}$$

where

$$f(x) \equiv \frac{15}{x^5}\left(e^{-x}\cos\left(x\right)\left(\frac{x^2}{2}+2x+1\right) + \left(1+e^{-x}\sin\left(x\right)\right)\left(\frac{x^2}{2}-1\right)\right). \tag{3.22}$$

A detailed derivation of Eq. 3.21 can be seen in Appendix A. From here, the power spectrum takes the form

$$S_n\left(\omega\right) = \int \frac{d\omega'}{2\pi} \left\langle \tilde{\delta n}^*\left(\omega'\right) \tilde{\delta n}\left(\omega\right)\right\rangle = \frac{16\pi\bar{c}a^5}{15D_c} f\left(a\sqrt{\frac{2|\omega|}{D_c}}\right). \tag{3.23}$$

Combining this with Eq. 3.18 yields and noise to signal ratio of

$$\frac{\sigma_{nT}^2}{\langle n\rangle^2} = \frac{C_{n,T}\left(0\right)}{\langle n\rangle^2} \approx \frac{S_n\left(0\right)}{\langle n\rangle^2 T} = \frac{1}{T}\left(\frac{4}{3}\pi a^3\bar{c}\right)^{-2} \lim_{\omega\to 0} \frac{16\pi\bar{c}a^5}{15D_c} f\left(a\sqrt{\frac{2|\omega|}{D_c}}\right)$$
$$= \frac{3}{5}\frac{1}{\pi a\bar{c}D_c T} \tag{3.24}$$

Thus, we see that our method of utilizing Langevin noise terms reproduces the same result as that obtained by Berg and Purcell [1]. Of important note is that in order to justify the approximation used in Eq. 3.10, $S_n\left(\omega\right)$ must not change drastically when ω changes by T^{-1}. Since the ω dependence of $S_n\left(\omega\right)$ is contained

entirely in $f\left(a\sqrt{2|\omega|/D_c}\right)$ and $f(x)$ as defined in Eq. 3.22 has a finite value and first derivative, the factor $a\sqrt{2|\omega|/D_c}$ should be approximately equal for $\omega = 0$ or T^{-1}. This is equivalent to requiring $a/\sqrt{D_c T} \ll 1$, or $T \gg a^2/D_c$. Thus, Eq. 3.24 is valid only for $T \gg a^2/D_c$, which is the characteristic diffusive timescale for a ligand molecule to diffuse around the cell.

As an additional check, we can exactly calculate the variance in an instantaneous measurement of n by inverting the relationship found in Eq. 3.6. This yields

$$\sigma_n^2 = C_n(0) = \int \frac{d\omega}{2\pi} S_n(\omega) = \frac{8\bar{c}a^5}{15D_c} \int d\omega f\left(a\sqrt{\frac{2|\omega|}{D_c}}\right) = \frac{4}{3}\pi a^3 \bar{c} = \langle n \rangle. \qquad (3.25)$$

Thus, we see that our method of utilizing Langevin noise terms also recovers the Poissonian nature of diffusion by equating the variance to the mean.

4. FUNDAMENTAL LIMITS TO COLLECTIVE CONCENTRATION SENSING IN CELL POPULATIONS

This work has been published in Physical Review Letters [23]

Single cells sense chemical concentrations with extraordinary precision. In some cases this precision approaches the physical limits set by molecular diffusion [1, 2]. Yet, no cell performs this sensory task in isolation. Cells exist in communities, such as colonies, biofilms, and tissues. Within these communities, cells communicate in diverse ways. Communication mechanisms include the exchange of molecules between cells in contact (juxtacrine signaling), and secretion and detection of diffusible molecules over distances comparable to the cell size or longer (autocrine signaling) [24–27]. This raises the question of whether cell-cell communication improves a cell's sensory precision, beyond what the cell achieves alone.

Experiments have shown that cells are more sensitive in groups than they are alone. Groups of neurons [28], lymphocytes [19], and epithelial cells [3] exhibit biased morphological or motile responses to chemical gradients that are too shallow for cells to detect individually. Groups of cell nuclei in fruit fly embryos detect morphogen concentrations with a higher precision than is expected for a single nucleus [12, 15, 29]. In some cases, such as with epithelial cells [3], cell-cell communication has been shown to be directly responsible for the enhanced sensitivity. Yet, from a theoretical perspective, the fundamental limits to concentration sensing [1, 2, 4–8, 30, 31] or gradient sensing [9–11] have been largely limited to single receptors or single cells. Analogous limits for groups of communicating cells have been derived only for specific geometries [16], and are otherwise poorly understood. In particular, it remains unknown whether the limits depend on the communication mechanism (juxtacrine vs.

autocrine), and how they scale with collective properties like communication strength and population size.

Here we derive the fundamental limits to the precision of collective sensing by one, two, and three dimensional (3D) populations of cells. We focus on the basic task of sensing a uniform chemical concentration. We compare two ubiquitous communication mechanisms depicted in Fig. 4.1, juxtacrine signaling and autocrine signaling. Intuitively one expects that sensory precision is enhanced by communication, that communication is strongest when cells are close together, and therefore that juxtacrine signaling should result in the higher sensory precision. Instead, we find that under a broad range of conditions, autocrine signaling results in the higher sensory precision. In fact, we find that for autocrine signaling, it is not optimal for cells to be as close as possible. Rather, an optimal cell-to-cell distance emerges due to a tradeoff between maintaining sufficient communication strength and minimizing signal cross-correlations. For sufficiently large populations, this distance can be many times the cell diameter, meaning that these populations are porous, not tightly packed. Surprisingly, the sensory precision in these porous populations is then higher than that in the case of juxtacrine signaling, where cells are adjacent and communicate directly. We discuss the implications of these findings for cell populations, compare our results to data from a wide variety of communicating cell types, and make predictions for future experiments.

4.1 Recptor Binding and Unbinding

Consider N cells with radii a in the presence of a ligand that diffuses in three dimensions with coefficient D_c (Fig. 4.1). The ligand concentration $c\left(\vec{x},t\right)$ fluctuates due to the particulate nature of the ligand molecules, but on average the steady-state concentration $\bar{c}(\vec{x}) = \bar{c}$ is uniform. Ligand molecules bind and unbind to receptors on

the surface of cell i with rates α and μ, respectively, leading to $r_i(t)$ bound receptors. The dynamics of c and r are

$$\frac{dc}{dt} = D_c \nabla^2 c - \sum_{j=1}^{N} \delta^3 \left(\vec{x} - \vec{x}_j\right) \frac{dr_j}{dt} + \eta_c, \tag{4.1}$$

$$\frac{dr_j}{dt} = \alpha c \left(\vec{x}_j, t\right) - \mu r_j + \eta_{rj}. \tag{4.2}$$

The first term on the righthand side of Eq. 4.1 describes the ligand diffusion, while the second term describes the binding and unbinding of ligand at cell positions $\vec{x}_i$, with the binding dynamics given by Eq. 4.2. The noise terms obey

$$\left\langle \eta_c \left(\vec{x}, t\right) \eta_c \left(\vec{x}', t'\right) \right\rangle = 2 D_c \bar{c} \delta \left(t - t'\right) \vec{\nabla}_x \cdot \vec{\nabla}_{x'} \delta^3 \left(\vec{x} - \vec{x}'\right), \tag{4.3}$$

$$\left\langle \eta_{rj} \left(t\right) \eta_{rl} \left(t'\right) \right\rangle = 2 \mu \bar{r} \delta_{jl} \delta \left(t - t'\right), \tag{4.4}$$

and account for the spatiotemporally correlated diffusive fluctuations [22] and the stochastic nature of the binding reactions [32], respectively. Here $\bar{r} = \alpha \bar{c}/\mu$ is the mean bound receptor number of each cell in steady state. In Eq. 4.2 we have assumed that the receptors are numerous enough such that the binding of ligand does not significantly affect the available number of unbound receptors, which is to say we have neglected the effects of receptor saturation.

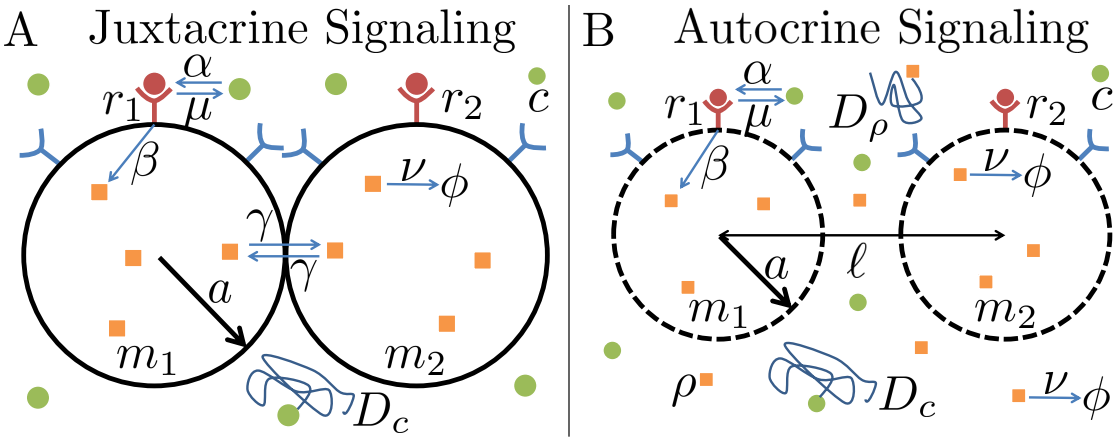

Figure 4.1. Cells with (A) short-range (juxtacrine) or (B) long-range (autocrine) communication, sensing a uniform ligand concentration.

We must first consider the properties of c and r_j. Following the same method as was used for the perfect instrument, Eq. 4.1 can be linearized, Fourier transformed, and solved for $\tilde{\delta c}$ to yield

$$\tilde{\delta c}\left(\vec{k},\omega\right)=\frac{i\omega\sum_j\tilde{\delta r}_j e^{i\vec{k}\cdot\vec{x}_j}+\tilde{\eta}_c}{D_c k^2-i\omega}. \tag{4.5}$$

The summation term in Eq. 4.5 induces a relation between all the $\tilde{\delta r}_j$'s when Eq. 4.2 is similarly linearized, Fourier transformed, and Eq. 4.5 is used to substitute for $\tilde{\delta c}$. This summation can be solved by writing the $\tilde{\delta r}_j$ relations in matrix form, yielding the solution

$$\tilde{\delta r}_j\left(\omega\right)=\sum_l R_{jl}^{-1}\left(\omega\right)\left(\alpha\int\frac{d^3k}{\left(2\pi\right)^3}\frac{\tilde{\eta}_c}{D_c k^2-i\omega}e^{-i\vec{k}\cdot\vec{x}_l}+\tilde{\eta}_{rl}\right), \tag{4.6}$$

where the matrix

$$R_{jl}\left(\omega\right)=\left(\mu-i\omega\right)\delta_{jl}-i\omega\Sigma\left(\vec{x}_j-\vec{x}_l,\omega\right) \tag{4.7}$$

along with the function

$$\Sigma\left(\vec{x},\omega\right)=\alpha\int\frac{d^3k}{\left(2\pi\right)^3}\frac{1}{D_c k^2-i\omega}e^{i\vec{k}\cdot\vec{x}}=\frac{\alpha}{4\pi D_c|\vec{x}|}e^{(i-1)|\vec{x}|\sqrt{\frac{\omega}{2D_c}}} \tag{4.8}$$

accounts for the cross-correlations between the cells.

The $\Sigma\left(x,\omega\right)$ function introduces an important issue with how we have modelled the ligand diffusion in Eq. 4.1. When $j=l$ in Eq. 4.7, $\Sigma\left(0,\omega\right)$ as defined in Eq. 4.8 diverges. This is due to the treatment of cells as point particles, which is seen in the use of the Dirac δ-functions in Eq. 4.1. Realistically, wavevectors large enough such that the corresponding wavelengths are less than the cell radius will be averaged out to negligible contributions. Thus, for sufficiently small values of $\left|\vec{x}_j-\vec{x}_l\right|$, we cut off the integral in Eq. 4.8 to a maximal magnitude of $\frac{2\pi}{ga}$, where g is a geometric factor. This allows for the calculation

$$\Sigma\left(0,\omega\right)\approx\frac{\alpha}{\pi D_c g a}\left(1+\mathrm{sgn}\left(\omega\right)\frac{iga}{4}\sqrt{\frac{|\omega|}{2D_c}}\right), \tag{4.9}$$

where we have assumed $\omega^{-1}\gg a^2/D_c$. This assumption is validated when Eq. 3.10 is used to calculate the variance and forces $\omega^{-1}\sim T\gg a^2/D_c$.

With the explicit forms of $R_{jl}(\omega)$ and $\Sigma(\vec{x},\omega)$ defined, Eq. 4.6 can be used to calculate the cross spectrum in r_j, which takes the simplified form

$$\left\langle \tilde{\delta r}_l^{\,*}(\omega')\,\tilde{\delta r}_j(\omega)\right\rangle = \left(2\pi\delta\left(\omega-\omega'\right)\right)\frac{2\alpha\bar{c}}{\omega}\mathrm{Im}\left(R_{jl}^{-1}(\omega)\right). \tag{4.10}$$

A detailed derivation of Eq. 4.10 can be seen in Appendix B. Eq. 4.10 is particularly reassuring in its form as it can be seen to be of the exact form the fluctuation-dissipation theorem would predict, namely proportional to the imaginary component of the matrix element used to connect $\tilde{\delta r}_j$ to the noise terms in Eq. 4.6 [22].

Of important note is that for the time averaged noise of r_j to be calculated as was done for the perfect instrument, there must be restrictions put on T. In particular, the power spectrum of r_j cannot change significantly when ω changes by $\sim T^{-1}$. Since $\Sigma(\vec{x},\omega)$ is a function that monotonically decreases with $|\vec{x}|$, we only need consider the $j=l$ case. Utilizing Eq. 4.9 and the fact that g is merely a geometric factor of order unity, it follows that the factor $a\sqrt{|\omega|/2D_c}$ should be small for $\omega = T^{-1}$. This is equivalent to requiring

$$T \gg \tau_1 = a^2/D_c, \tag{4.11}$$

where τ_1 is the time scale over which the ligand can diffuse around the cell, just as for the perfect instrument.

Additionally, $R_{jl}(\omega)$ cannot change significantly when ω changes by $\sim T^{-1}$. Continuing to focus on the $j=l$ case, it follows that $\omega\left(1+\Sigma(0,0)\right) \ll \mu$ should be true for $\omega = T^{-1}$. Utilizing the explicit form of $\Sigma(0,0)$ given in Eq. 4.9, this is equivalent to requiring

$$T \gg \tau_2 = \frac{1}{\mu} + \frac{1}{k_D K_D}, \tag{4.12}$$

where τ_2 is the receptor equilibration timescale including rebinding, with diffusion-limited rate $k_D = \pi g a D_c$ and dissociation constant $K_D = \mu/\alpha$ [4]. Since $g = 4$ corresponds to the diffusion-limited rate $k_D = 4\pi a D_c$ for a sphere of radius a, we take $g = 4$ from here on.

4.2 Juxtacrine Signalling

With the properties of c and r_j thoroughly understood, we now consider juxtracrine signaling, in which a messenger molecule is exchanged between adjacent cells at a rate γ (Fig. 4.1A). Messenger molecules are produced in each cell by the bound receptors at a rate β and degraded at a rate ν, such that the messenger acts as both the mediator of communication and the sensory readout. The dynamics of $m_j(t)$, the number of messenger molecules in cell i, are

$$\frac{dm_j}{dt} = \beta r_j - \nu m_j + \gamma \sum_{l \in \mathcal{N}_i} \left(m_l - m_j \right) + \eta_{mj}, \tag{4.13}$$

where $\mathcal{N}_i$ denotes the set of cells that are neighbors of cell i. The noise term obeys

$$\left\langle \eta_{mj}\left(t\right) \eta_{ml}\left(t'\right) \right\rangle = 2\bar{m} M_{jl}\left(0\right) \delta\left(t - t'\right), \tag{4.14}$$

where the matrix

$$M_{jl}\left(\omega\right) = \left(\nu + \left|\mathcal{N}_j\right| \gamma - i\omega \right) \delta_{jl} - \gamma \delta_{l \in \mathcal{N}_j} \tag{4.15}$$

accounts for the stochasticity of the reactions (first term) and the anti-correlations induced by the exchange (second term) [32]. Here $\bar{m} = \beta \bar{r}/\nu$ is the mean messenger molecule number of each cell in steady state, and $\left|\mathcal{N}_j\right|$ is the number of neighbors of cell i.

The precision of concentration sensing is given by the signal-to-noise ratio of the readout in a particular cell, $\bar{m}^2/(\delta m_j)^2$. We assume that each cell integrates its messenger molecule count over a time T, such that $(\delta m_j)^2$ is the variance in the time average $T^{-1}\int_0^T dt\ m_j(t)$ [1]. As seen in Section 3.3, this can be done by first calculating the instantaneous power spectrum of m_j. To do this, we proceed to linearize and Fourier transform Eq. 4.13, then solve for $\delta\tilde{m}_j$. Utilizing the definintion of $M_{jl}\left(\omega\right)$ in Eq. 4.15, this solution takes the form

$$\delta\tilde{m}_j\left(\omega\right) = \sum_l M_{jl}^{-1}\left(\omega\right) \left(\beta \delta\tilde{r}_l + \tilde{\eta}_{ml} \right). \tag{4.16}$$

Since the form of $M_{jl}(\omega)$ and the cross spectrums of r_j and η_{mj} are already known, Eq. 4.16 allows for the cross spectrum of m_j to be calculated to be

$$\left\langle \delta\tilde{m}_l^*(\omega')\,\delta\tilde{m}_j(\omega)\right\rangle = 2\left(2\pi\delta(\omega-\omega')\right)\left(\bar{m}\mathrm{Re}\left(M_{jl}^{-1}(\omega)\right)\right.$$
$$\left.+\frac{\alpha\beta^2\bar{c}}{\omega}\sum_{s,u}M_{js}^{-1}(\omega)\left(M_{lu}^{-1}(\omega)\right)^*\mathrm{Im}\left(R_{su}^{-1}(\omega)\right)\right). \quad (4.17)$$

The factor of $R_{su}^{-1}(\omega)$ comes from the dependence of m_j on r_j and thus represents the noise m_j inherits from r_j. This also implies that when the time averaged variance of m_j is calculated, it will also inherit the restrictions $T \gg [\tau_1, \tau_2]$. Additionally, the dependence of $M_{jl}(\omega)$ on ω means that it too will provide another restriction on T. Utilizing the explicit form of $M_{jl}(\omega)$ as given in Eq. 4.15, it follows that $\omega \ll \nu + \gamma$ should be true for $\omega = T^{-1}$. This is equivalent to requiring

$$T \gg \tau_3 = \frac{1}{\nu+\gamma}, \quad (4.18)$$

where τ_3 is the turnover timescale of the messenger molecule. Thus, for the juxtacrine model, $[\tau_1, \tau_2, \tau_3]$ represents the timescales the cell must integrate its measurements over to obtain the precisions our results predict. Special cases illuminate the key physics, below.

First, for either $N = 1$ or $\gamma = 0$, we can use Eq. 4.17 to obtain the result for a single, isolated cell,

$$\frac{\sigma_{mT}^2}{\bar{m}^2} = \frac{1}{2}\frac{1}{\pi a\bar{c}D_cT} + \frac{2}{\mu T\bar{r}} + \frac{2}{\nu T\bar{m}}. \quad (4.19)$$

Eq. 4.19 is the inverse of the precision, which we call the error, and its detailed derivation can be seen in Appendix C. The first term is the well-known Berg-Purcell limit for the extrinsic noise propagated from ligand diffusion [1]. The second and third terms are the intrinsic noise arising from the finite numbers of bound receptors $\bar{r}$ and messenger molecules $\bar{m}$. In the limit of large molecule numbers $\{\bar{r}, \bar{m}\} \to \infty$, these terms vanish. From here on we consider only the extrinsic noise, since extrinsic factors such as $\bar{c}$ and D_c are not under direct control of the cell (see Appendix C for the general case).

Second, for $N = 2$ (as in Fig. 4.1A) the extrinsic part of the error for either cell is (as calculated in Appendix C)

$$\frac{\sigma_{mT}^2}{\bar{m}^2} = \frac{1}{2}\left[1 - \frac{\hat{\lambda}^2(1+\hat{\lambda}^2)}{(1+2\hat{\lambda}^2)^2}\right]\frac{1}{\pi a \bar{c} D_c T} \tag{4.20}$$

$$\to \frac{3}{8}\frac{1}{\pi a \bar{c} D_c T} \qquad \lambda \gg a. \tag{4.21}$$

Here $\hat{\lambda} \equiv \lambda/(2a)$, where $\lambda \equiv 2a\sqrt{\gamma/\nu}$ is the communication length: it is the lengthscale of the exponential kernel that governs the exchange of messenger molecules [3, 16]. The prefactor in Eq. 4.20 is a monotonically decreasing function of $\hat{\lambda}$, which demonstrates that noise decreases with increasing communication. In the limit of weak communication $\lambda \ll a$, the prefactor becomes 1/2 as in the one-cell case (Eq. 4.19). In the limit of strong communication $\lambda \gg a$, it becomes 3/8 (Eq. 4.21). The fact that 3/8 is larger than half of 1/2 means that two cells are less than twice as good as one cell in terms of sensory precision, even with perfect communication. The reason is that, with juxtacrine signaling, the cells are sampling adjacent regions of extracellular space, and correlations mediated by the diffusing ligand molecules prevent their measurements from being independent [16]. Can autocrine signaling avoid this drawback?

4.3 Autocrine Signalling

To answer this question, we consider autocrine signaling (Fig. 4.1B). As before, a messenger molecule is produced by each cell at rate β and degraded at rate ν, but now it diffuses within the extracellular space with coefficient D_ρ. Thus, the autocrine model retains Eqs. 4.1 and 4.2 but replaces Eq. 4.13 with

$$\frac{d\rho}{dt} = D_\rho \nabla^2 \rho - \nu\rho + \sum_{i=1}^{N} \delta^3\left(\vec{x} - \vec{x}_i\right)\left(\beta r_i + \eta_{pi}\right) + \eta_d, \tag{4.22}$$

where $\rho\left(\vec{x}, t\right)$ is the concentration of the messenger molecule. The production noise obeys [32]

$$\left\langle \eta_{pj}\left(t\right)\eta_{pl}\left(t'\right)\right\rangle = \beta\bar{r}\delta_{jl}\delta\left(t - t'\right), \tag{4.23}$$

while the degradation and diffusion noise obeys [22]

$$\left\langle \eta_d\left(\vec{x},t\right)\eta_d\left(\vec{x}',t'\right)\right\rangle = \nu\bar{\rho}\left(\vec{x}\right)\delta\left(t-t'\right)\delta^3\left(\vec{x}-\vec{x}'\right) + 2D_\rho\delta\left(t-t'\right)\vec{\nabla}_x\cdot\vec{\nabla}_{x'}\left[\bar{\rho}\left(\vec{x}\right)\delta^3\left(\vec{x}-\vec{x}'\right)\right]. \tag{4.24}$$

Here

$$\bar{\rho}\left(\vec{x}\right) = \frac{\beta\bar{r}}{4\pi D_\rho}\sum_{j=1}^{N}\frac{e^{-\left|\vec{x}-\vec{x}_j\right|/\lambda(0)}}{\left|\vec{x}-\vec{x}_j\right|} \tag{4.25}$$

with

$$\lambda\left(\omega\right) = \sqrt{\frac{D_\rho}{\nu-i\omega}} \tag{4.26}$$

is the steady-state concentration profile of the messenger molecule, which is non-uniform due to the multiple cell sources. $\lambda\left(0\right)$ sets the communication length in the autocrine case.

We then imagine that each cell counts the number $m_j(t) = \int_{V_j} d^3x\rho\left(\vec{x},t\right)$ of messenger molecules within its volume V_j (such a prescription yields similar concentration-sensing results to one in which receptor binding is explicitly accounted for [1]). As in the juxtacrine case, the model remains linear with well understood noise terms. Therefore, we use the same procedure as above to exactly solve for the error for arbitrary parameters and cell configuration. A detailed derivation of the general case can be seen in Appendix D.

In calculating the cross spectrum of m_j, the factor of $R_{su}\left(\omega\right)$ can be seen to be inheritted once again, and with it the restrictions $T \gg [\tau_1,\tau_2]$. The only other dependencies on ω to be found within the cross spectrum of m_j come in the form of functions of $a/\lambda\left(\omega\right)$. Utilizing the explicit form of $\lambda\left(\omega\right)$ as given in Eq. 4.26, it then follows that $\omega \ll \nu + a^2/D_\rho$ should be true for $\omega = T^{-1}$. This is equivalent to requiring

$$T \gg \tau_4 = \frac{1}{\nu + \frac{a^2}{D_\rho}}, \tag{4.27}$$

where τ_4 is the messenger turnover timescale. Thus, for the autocrine model, $[\tau_1,\tau_2,\tau_4]$ represents the timescales the cell must integrate its measurements over to obtain the precisions our results predict.

For the special case of $N = 2$ cells separated by a distance ℓ (as in Fig. 4.1B), in the limit of strong communication $\lambda \gg a$, the result for the extrinsic noise is

$$\frac{\sigma^2_{mT}}{\bar{m}^2} = \frac{1 + \Lambda^2(\hat{\ell}) + 2\Lambda(\hat{\ell})/\hat{\ell}}{2[1 + \Lambda(\hat{\ell})]^2} \frac{1}{\pi a \bar{c} D_c T} \tag{4.28}$$

$$\rightarrow \frac{2}{5} \frac{1}{\pi a \bar{c} D_c T} \qquad \ell = \ell^* = \frac{8}{3} a. \tag{4.29}$$

where

$$\Lambda(\hat{\ell}) = \begin{cases} 1 - \frac{\hat{\ell}^2}{3} & \hat{\ell} < 1 \\ \frac{2}{3\hat{\ell}} & \hat{\ell} \geq 1 \end{cases} \tag{4.30}$$

and $\hat{\ell} \equiv \ell/a$. In the limit of large separation $\ell \gg a$, the prefactor in Eq. 4.28 becomes $1/2$ as in the one-cell case (Eq. 4.19), since here each cell only detects messenger molecules produced by itself (proper autocrine signaling). In general, since $\Lambda(\hat{\ell})$ is a continuous, monotonically decreasing function of $\hat{\ell}$, the denominator in Eq. 4.28 decreases with ℓ; this is because the mean decreases with cell separation due to the decay of the messenger molecule concentration profile (Eq. 4.25). The numerator in Eq. 4.28 also decreases with ℓ; this is once again because the cells are sampling nearby regions of extracellular space, and the variance decreases with their separation as their measurements become more independent. The tradeoff between these effects results in a minimum value of the prefactor equal to $2/5$, when $\ell = \ell^* = 8a/3$ (Eq. 4.29).

4.4 Comparision of Juxtacrine and Autocrine Precision

Evidently, for $N = 2$ cells autocrine signaling has improved the precision of concentration sensing less than juxtacrine signaling has ($2/5 > 3/8$). Do the results change for larger N? Because we have exact results for arbitrary N and arbitrary cell positions (as seen in Appendix D), we can answer this question immediately. Fig. 4.2A, B, and C compare as a function of N the error of the two communication mechanisms in the limit of strong communication for 1D, 2D, and 3D configurations of cells, respectively. For juxtacrine signaling, cells are arranged within a line (1D), circle

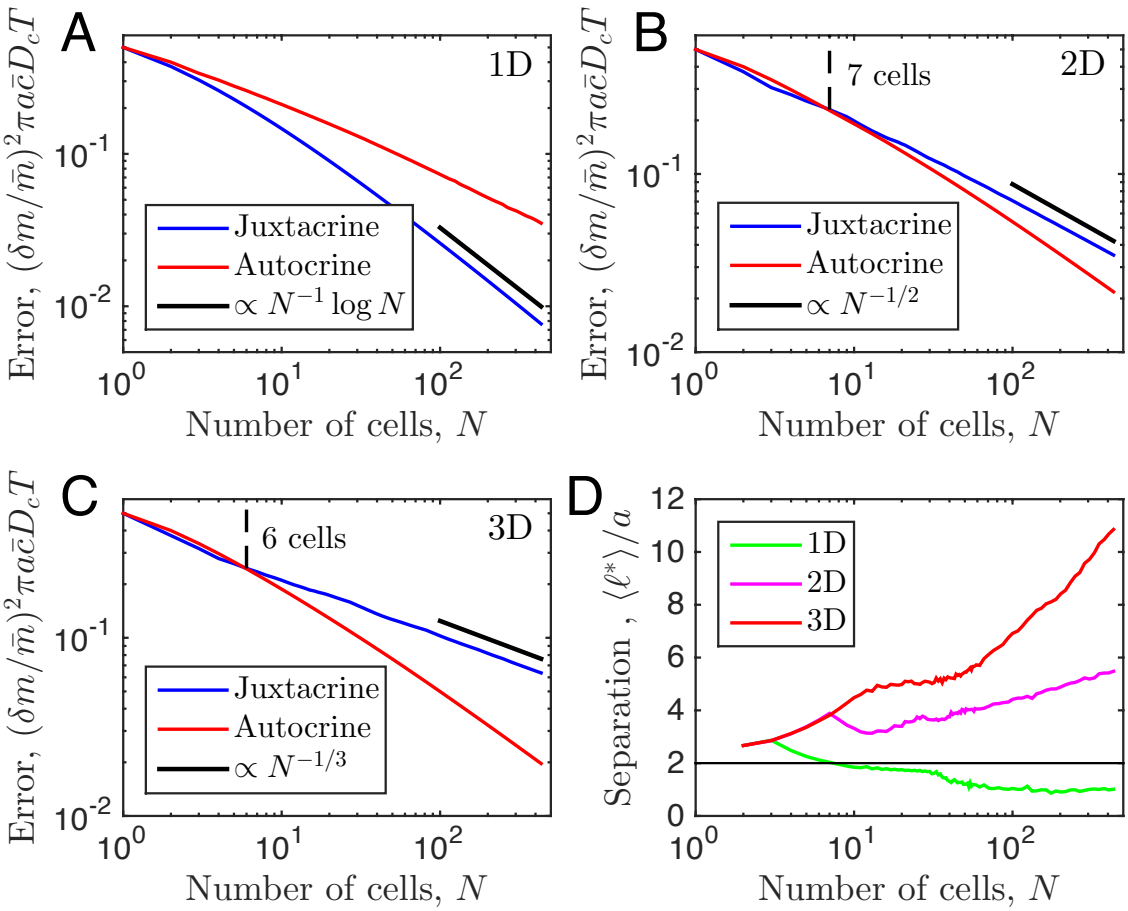

Figure 4.2. (A-C) Error in concentration sensing for the two communication strategies vs. the size of 1D, 2D and 3D populations. Error is calculated for the center cell. (D) Average optimal nearest-neighbor separation in the autocrine case. $\langle \ell^* \rangle < 2a$ corresponds to overlapping cells.

(2D), or sphere (3D) on a rectangular lattice with spacing $2a$. For autocrine signaling, cells are confined to the respective dimensionality, but are otherwise allowed to adjust their positions via a Monte Carlo scheme until the minimum error is reached. The average nearest-neighbor separation $\langle \ell^* \rangle$ in this case is shown in Fig. 4.2D. We see in Fig. 4.2A-C that the error always decreases with N, meaning that communication among an increasing number of cells monotonically improves sensory precision. In 1D, we see that juxtacrine signaling results in a smaller error than autocrine signaling for all N (Fig. 4.2A). In fact, in the case of autocrine signaling in 1D, the optimal separation decreases with N, and beyond $N = 7$, cells overlap, $\langle \ell^* \rangle < 2a$ (Fig. 4.2D). However, in 2D and 3D, autocrine signaling results in the smaller error beyond $N = 7$ and $N = 6$ cells, respectively (Fig. 4.2B and C), and the optimal separation increases with N (Fig. 4.2D). By $N = 400$ cells, the optimal separation in 3D becomes more than 10 cell radii, meaning that the optimal arrangement of cells is highly "porous".

It is clear from Fig. 4.2A-C that the errors of the two communication strategies scale differently with population size. The scaling in the juxtacrine case can be understood quantitatively. In the limit of strong communication, the entire population of contiguous cells acts as one large detector. The error of a long ellipsoidal (1D), disk-shaped (2D), or spherical detector (3D) scales inversely with its longest lengthscale (with a log correction in 1D) [33]. This lengthscale in turn scales with N, $N^{1/2}$, or $N^{1/3}$, respectively, leading to the predicted scalings in Fig. 4.2A-C, which are seen to agree excellently at large N. On the other hand, the scaling for autocrine signaling is different from that for juxtacrine signaling in each dimension. Evidently diffusive communication and non-contiguous arrangement lead to fundamentally different physics of sensing. In particular, in 2D and 3D the autocrine scaling is clearly steeper at large N (Fig. 4.2B and C), meaning that not only is the autocrine strategy more precise for a sufficiently large population, but more importantly, the improvement in precision will continue to grow with population size.

How do our results compare to actual biological systems? Arguably the most biologically unrealistic assumption that we make in Fig. 4.2 is that of strong communication,

$\lambda \gg a$. Since our calculations are exact for any λ (as seen in Appendix D), we relax this assumption in Fig. 4.3, allowing us to identify phases in the space of λ and N in which either communication strategy leads to the larger sensory precision. We now ask where particular biological systems fall in this phase space. Bacteria communicate via autocrine signaling, and it has been suggested that this communication enables collective sensing during swarming [34,35]. Data are available from studies of bacterial quorum sensing [36], which itself has been argued to also play a role in sensing environmental features [37]. The quorum-sensing messenger molecule AHL has $D_\rho \sim 490\ \mu\text{m}^2/\text{s}$ [38] and $\nu \sim 0.1{-}1\ \text{day}^{-1}$ [39, 40], yielding $\lambda \sim 5{-}20$ mm. Quorum or swarm sizes N are typically large but can be as small as tens or hundreds of cells [41]. Gap junctions are a ubiquitous mediator of juxtacrine signaling [42]. Gap junctions extracted from mouse tissues with a range of sizes N were found to propagate small molecules over approximately $1{-}2$ cell lengths, or $\lambda \sim 10{-}20$ μm [43]. Mammary epithelial cells also communicate via gap junctions across $3{-}4$ cell lengths, or $\lambda \sim 30{-}40$ μm [3], and typical sensory units at the ends of mammary ducts contain $N \sim 10^1{-}10^3$ cells [3, 44]. We see in Fig. 4.3 that these systems fall within the phases where we would predict that the observed communication strategy of each leads to the larger sensory precision.

Of course, bacteria are single-cellular, whereas mammalian cells are multicellular, so one might argue that these strategies are predisposed for other functional reasons. However, many multicellular components adopt porous cell arrangements and exhibit autocrine signaling. In particular, recent experiments have shown that glioblastoma tumor cells in groups of $N \sim 10^3{-}10^4$ secrete the autocrine factors IL-6 and VEGF [45], for which $D_\rho \sim 30\ \mu\text{m}^2/\text{s}$ [46] and $100\ \mu\text{m}^2/\text{s}$ [47], and $\nu \sim 0.2\ \text{hr}^{-1}$ [48] and $0.7\ \text{hr}^{-1}$ [49], respectively, yielding $\lambda \sim 700$ μm. Indeed, in this regime, we would predict that autocrine signaling provides the higher sensory precision (Fig. 4.3). In fact, in these experiments, cells autonomously adopted a typical spacing of several cell diameters, which is consistent with the predicted optimal spacing $\langle \ell^* \rangle$ shown in

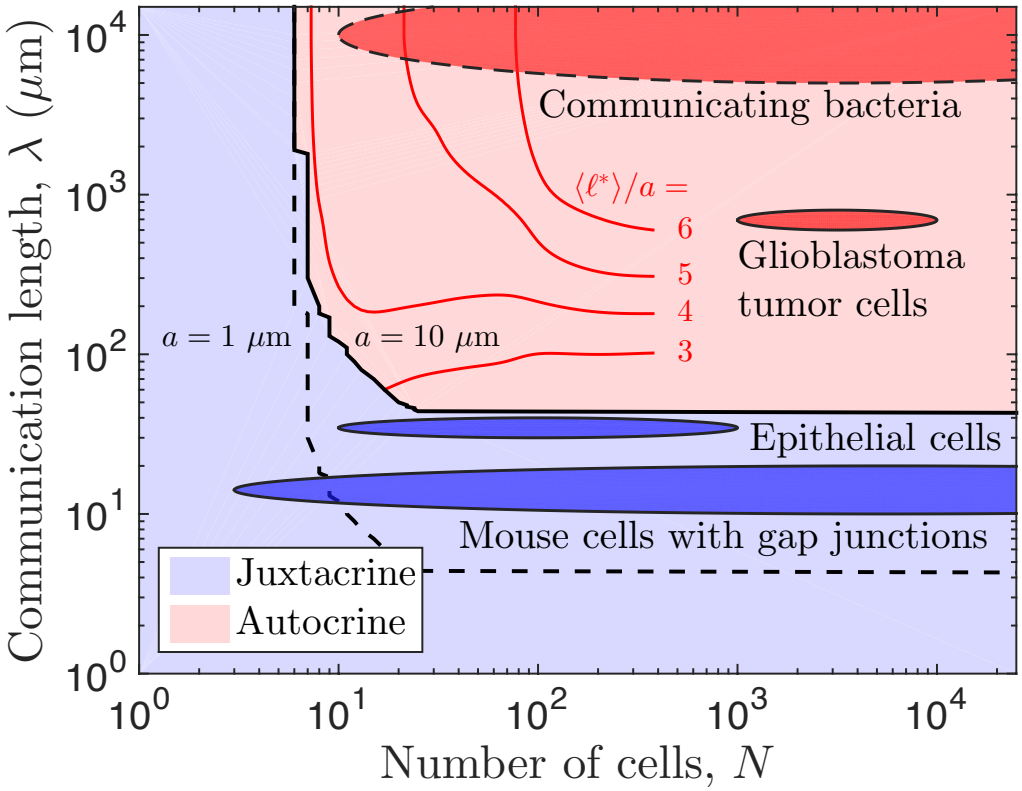

Figure 4.3. Phase plot showing the communication strategy that results in the lower error in 3D (results are similar for 2D). Ellipses are estimates from biological systems described in the text. Solid (dashed) black phase boundary is for $a = 10$ μm ($a = 1$ μm), to be compared with mammalian (bacterial) cell ellipses. Red contour lines show $\langle \ell^* \rangle$ for $a = 10$ μm in the autocrine phase up to largest numerically tractable $N = 400$. Phase boundaries are extrapolated from largest numerically tractable $N = 10^3$.

the red contours in Fig. 4.3. The authors argued that this spacing minimized the signaling noise [45], suggesting a mechanism similar to the one we uncover here.

We have shown that communicating cells maximize the precision of concentration sensing by adopting an optimal separation that can be many cell diameters. This is surprising, since separation weakens the impact of the communication. However, we have demonstrated that cells weigh this drawback against the benefit of obtaining independent measurements of their environment. We predict that the concentration

detection threshold for communicating cells should decrease with the cell number, which could be tested using an intracellular fluorescent reporter. Moreover, if cell positions are controllable [45], we predict that a small concentration would be detected by modestly separated cells, but not adjacent or far-apart cells.

5. DIFFUSION VS. DIRECT TRANSPORT IN THE PRECISION OF MORPHOGEN READOUT

This work has been submitted to Physical Review Letters [50]

Within developing organisms, morphogen profiles provide cells with information about their position relative to other cells. Cells use this information to determine their position with extremely high precision [12,15,51–53]. However, not all morphogen profiles are formed via the same mechanism, and for some profiles the mechanism is still not well understood. One well-known mechanism is the synthesis-diffusion-clearance (SDC) model in which morphogen molecules are produced by localized source cells and diffuse through extracellular space before degrading or being internalized by target cells [54–59]. Alternatively, a direct transport (DT) model has been proposed where morphogen molecules travel through protrusions called cytonemes directly from the source cells to the target cells [54,57,59–61]. The presence of these two alternative theories raises the question of whether there exists a difference in the performance capabilities between cells utilizing one or the other.

Experiments have shown that morphogen profiles display many characteristics consistent with the SDC model. The concentration of morphogen as a function of distance from the source cells has been observed to follow an exponential distribution for a variety of different morphogens [52, 62]. The accumulation times for several morphogens in *Drosophila* have been measured and found to match the predictions made by the SDC model [63]. In zebrafish, the molecular dynamics of the morphogen Fgf8 have been measured and found to be consistent with Brownian diffusion through extracellular space [13]. Despite these consistencies, recent experiments have lent support to the theory that morphogen molecules are transported through cytonemes rather than extracellular space. The establishment of the Hedgehog morphogen

gradient in *Drosophila* is highly correlated in both space and time with the formation of cytonemes [14], while Wnt morphogens have been found to be highly localized around cell protrusions such as cytonemes [64, 65]. Theoretical studies of both the SDC and DT models have examined these measurable effects [60, 63, 66–68], but direct comparisons between the two models have thus far been poorly explored. In particular, it remains unknown whether one model allows for a cell to sense its local morphogen concentration more precisely than the other given biological parameters such as the number of cells or the characteristic lengthscale of the profile.

Here we derive fundamental limits to the precision of morphogen concentration sensing for both the Synthesis-Diffusion-Clearance (SDC) and Direct Transport (DT) models. We investigate the hypothesis that sensory precision plays a major role in the selection of a gradient formation mechanism during evolution, and we test this hypothesis by quantitatively comparing our theory to morphogen data. Precision depends not only on stochastic fluctuations in the morphogen concentration, but also on the shape of the morphogen profile, as the shape determines concentration differences between adjacent cells that may adopt different fates [12, 69]. However, because the morphogens to which we will later compare our results generally have exponential profiles, we restrict ourselves to the exponential regimes of both the SDC and DT models and focus only on the stochastic noise caused by production, transport, and degradation of the morphogen molecules. Several past studies have focused on the dynamics of morphogen profiles and their accumulation times [60, 63, 66–68]. Here, we model morphogen profiles in the steady state regime as many of the experimental measurements to which we will later compare our results were taken during stages when the steady state approximation is valid [13, 70–73].

Intuitively one might expect the DT model to have less noise due to the fact that molecules are directly deposited at their target. Indeed, we find below that the noise arises only from molecular production and degradation, with no additional noise from molecular transport. Surprisingly, however, we also find below that for sufficiently large morphogen profile lengthscales, the SDC model produces less noise than the

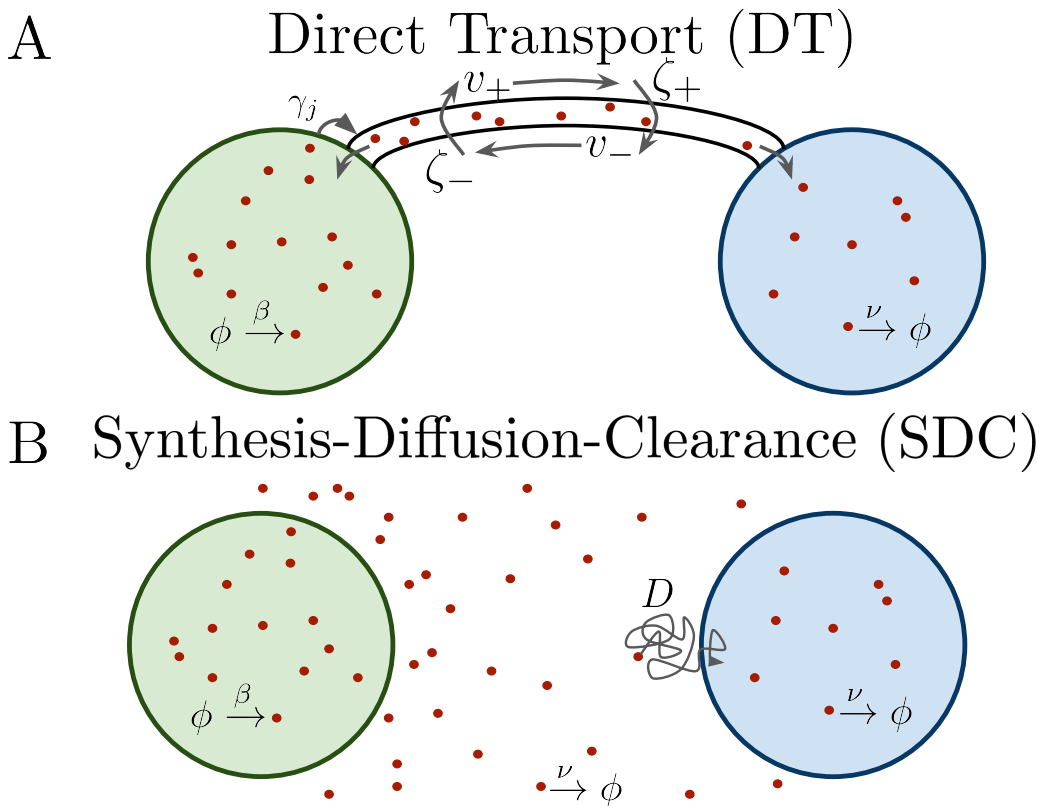

Figure 5.1. Source cell (green) produces morphogen which is delivered to target cells (blue) via (A) direct transport (DT) or (B) synthesis-diffusion-clearance (SDC).

DT model due to it being able achieve a higher effective unique molecule count. This result holds for one-, two-, and three-dimensional geometries. We compare our results with measurements of the above morphogens and find quantitative agreement with our predictions, suggesting that readout precision plays an important role in determining the mechanisms of morphogen profile establishment.

5.1 Direct Transport

We first consider the DT case, where morphogen molecules are transported via cytonemes that connect a single source cell to multiple target cells (Fig. 5.1A).

Cytonemes are tubular protrusions that are hundreds of nanometers thick and between several and hundreds of microns long [61, 74]. They are supported by actin filaments, and it is thought that morphogen molecules are actively transported along the filaments via molecular motors [61, 64, 74, 75]. It was recently shown that a DT model that includes forward and backward transport of molecules within cytonemes reproduces experimentally measured accumulation times [60, 67], although the noise properties of this model were not considered. Here, we review the steady state properties of this model and then derive its noise properties.

Consider a single source cell that produces morphogen at rate β. Morphogen molecules enter each cytoneme at rate γ. The cytoneme that leads to the jth target cell has length L_j. Once inside a cytoneme, morphogen molecules move forward towards the target cell with velocity v_+ or backwards toward the source cell with velocity v_-, and can switch between these states with rates ζ_+ (forward-to-backward) or ζ_- (backward-to-forward). Once a molecule reaches the forward (backward) end of the cytoneme it is immediately absorbed into the target (source) cell. Molecules within a target cell spontaneously degrade with rate ν. Calling N the total number of target cells, the dynamics of the mean number of morphogen molecules in the source cell $\bar{m}_0(t)$ and jth target cell $\bar{m}_j(t)$, and the mean density of forward-moving molecules $\bar{u}_j^+(x,t)$ and backward-moving molecules $\bar{u}_j^-(x,t)$ in the jth cytoneme are [60]

$$\begin{aligned}
\frac{\partial \bar{m}_0}{\partial t} &= \beta - \sum_{j=1}^{N} \left[\gamma \bar{m}_0 - v_- \bar{u}_j^-(0,t)\right], \\
\frac{\partial \bar{u}_j^+}{\partial t} &= -v_+ \frac{\partial \bar{u}_j^+}{\partial x} + \zeta_- \bar{u}_j^- - \zeta_+ \bar{u}_j^+ + \gamma \bar{m}_0 \delta(x) - v_+ \bar{u}_j^+ \delta(x - L_j), \\
\frac{\partial \bar{u}_j^-}{\partial t} &= v_- \frac{\partial \bar{u}_j^-}{\partial x} - \zeta_- \bar{u}_j^- + \zeta_+ \bar{u}_j^+ - v_- \bar{u}_j^- \delta(x), \\
\frac{\partial \bar{m}_j}{\partial t} &= v_+ \bar{u}_j^+(L_j,t) - \nu \bar{m}_j.
\end{aligned} \tag{5.1}$$

The steady-state solution for this model is calculated in [60], but for completeness and notational clarity we rederive it in Appendix E. The solution for $\bar{m}_j$ specifically is given by

$$\bar{m}_j = \frac{\beta\Gamma\left(L_j\right)}{\nu\sum_{k=1}^{N}\Gamma\left(L_k\right)}, \tag{5.2}$$

where

$$\Gamma(L) = \gamma e^{\kappa L}\frac{1-e^{\phi}}{1-e^{\phi+\kappa L}} \tag{5.3}$$

is the effective transport rate of morphogen molecules to the jth target cell. Here $\phi = \log(d_+/d_-)$ and $\kappa = d_-^{-1} - d_+^{-1}$ are defined in terms of the average distance a molecule would move forward $d_+ = v_+/\zeta_+$ or backward $d_- = v_-/\zeta_-$ within a cytoneme before switching direction. When $d_+ \gg d_-$ the transport rate $\Gamma(L) = \gamma$ is constant, whereas when $d_+ \ll d_-$ the transport rate $\Gamma(L) = \gamma e^{-L/d_+}$ decays exponentially with cytoneme length.

Despite the complexity of the transport process in Eq. 5.1, we find that it adds no noise to $\bar{m}_j$. This can be seen by considering the probability that a molecule born at some time t enters the jth target cell at time $t+\tau$. This probability can be split into the product $P(\tau|j)P(j)$, where $P(\tau|j)$ is the probability per unit time that the molecule enters the jth target cell a time τ after it is born given that it will eventually enter the jth target cell and $P(j)$ is the probability that it will eventually enter the jth target cell. Since $\Gamma(L_j)$ is known to be the effective transport rate of molecules from the source cell into the jth target cell, we can take $P(j) = \Gamma(L_j)/\sum_{k=1}^{N}\Gamma(L_k)$.

We now consider $P_j(t)$, the probability per unit time of a molecule entering the jth target cell at time t. This can be broken up into a summation over all of past time, t', of $P(t-t'|j)P(j)\beta dt'$, where $\beta dt'$ represents the probability the molecule is born in the infinitesimal time window dt'. Turning this summation into integration allows $P(t)$ to be written as

$$P_j\left(t\right) = \int_{-\infty}^{t} dt'\beta P\left(t-t'|j\right)P\left(j\right) = \beta P\left(j\right)\int_{0}^{\infty} d\tau P\left(\tau|j\right) = \beta P\left(j\right). \tag{5.4}$$

Thus, the probability per unit time of a molecule entering the jth target cell is $\beta P(j)$ which is constant in time and independent of the exact form of $P(\tau|j)$. This

is significant because it implies that the specific transport mechanism can only alter the statistical properties of m_j through $P(j)$ and cannot impart any noise inherent in such a process to m_j. Given this, we can define an effective arrival rate $\beta_j = \beta P(j)$ and write the dynamics of m_j as

$$\frac{\partial m_j}{\partial t} = \beta_j - \nu m_j + \eta_j. \tag{5.5}$$

Eq. 5.5 reproduces the mean value given in Eq. 5.2, and when it is linearized and Fourier transformed as was done in our previous work we obtain

$$\left\langle \delta\tilde{m}_j^* \left(\omega'\right) \delta\tilde{m}_j \left(\omega\right) \right\rangle = \frac{\left\langle \tilde{\eta}_j^* \left(\omega'\right) \tilde{\eta}_j \left(\omega\right) \right\rangle}{\left(\nu - i\omega\right)\left(\nu + i\omega'\right)}, \tag{5.6}$$

where

$$\left\langle \tilde{\eta}_j^* \left(\omega'\right) \tilde{\eta}_j \left(\omega\right) \right\rangle = 2\beta_j \left(2\pi\delta\left(\omega - \omega'\right)\right) \tag{5.7}$$

is known from summing the mean propensities seen on the right-hand side of Eq. 5.5 [32]. With these, we calculate the relative of a time averaged measurement of m_j to be

$$\frac{\delta m_{jT}^2}{\bar{m}_j^2} = \frac{2}{\nu T \bar{m}_j}, \tag{5.8}$$

so long as $T \gg \nu^{-1}$.

We see that, as expected for a time-averaged Poisson process [23], the relative error $(\sigma_{mjT}/\bar{m}_j)^2$ decreases with both the mean number of molecules $\bar{m}_j$ and the number νT of independent measurements that can be made in the time T, where independence requires separation by a correlation time ν^{-1}. The transport process influences the noise only via the functional form of $\bar{m}_j$.

5.2 Synthesis-Diffusion-Clearance

We next consider the SDC case (Fig. 5.1B). We begin in one-dimensional space, as is typical [63, 66, 68], although we also consider other geometries later on. Consider a single source cell at the origin which produces morphogen molecules at rate β. These molecules diffuse freely with coefficient D and degrade spontaneously at any point in space with rate ν. The dynamics of the morphogen concentration $c(x,t)$ are

$$\frac{\partial c}{\partial t} = D\nabla^2 c + \eta_D - \nu c - \eta_\nu + \left(\beta + \eta_\beta\right)\delta(x), \tag{5.9}$$

where the noise terms associated with diffusion, degradation, and production obey

$$\begin{aligned} \left\langle \eta_D(x',t')\eta_D(x,t)\right\rangle &= 2D\delta(t-t')\vec{\nabla}_x \cdot \vec{\nabla}_{x'}\bar{c}(x)\delta(x-x') \\ \left\langle \eta_\nu(x',t')\eta_\nu(x,t)\right\rangle &= \nu\bar{c}(x)\delta(t-t')\delta(x-x'), \\ \left\langle \eta_\beta(t')\eta_\beta(t)\right\rangle &= \beta\delta(t-t'), \end{aligned} \tag{5.10}$$

respectively [22, 23, 32, 76]. Here $\bar{c}(x)$ is the steady state mean concentration of morphogen molecules, which for a one-dimensional system with a single source takes the form

$$\bar{c}(x) = \frac{\beta\lambda}{2D}e^{-|x|/\lambda} \tag{5.11}$$

with characteristic lengthscale $\lambda = \sqrt{D/\nu}$.

We then imagine a target cell located at x that is perfectly permeable to the morphogen and counts the number

$$m\left(x,t\right) = \int_V dy\, c\left(x+y,t\right) \tag{5.12}$$

of morphogen molecules within its volume V. We use this simpler, perfect instrument style prescription over explicitly accounting for more realistic mechanisms such as surface receptor binding because it ultimately yields similar concentration sensing results up to a factor of order unity [1]. Assuming $|x| \geq 2a$ for cell radius a enforces the condition that there is no overlap between the source and target cell and produces a steady state mean value of

$$\bar{m}\left(x\right) = \frac{\beta}{\nu}\sinh\left(\frac{a}{\lambda}\right)e^{-|x|/\lambda}. \tag{5.13}$$

We once again use our method of Fourier transforming Eq. 5.9 in space and time, calculating the power spectrum of $m(x,t)$, and taking its low-frequency limit to obtain

$$\frac{\delta m_T^2(x)}{\bar{m}^2(x)} = \frac{2}{\nu T \bar{m}(x)} \left[1 - \frac{(2/\hat{\lambda}) + \sinh(2/\hat{\lambda})}{4\sinh(1/\hat{\lambda}) e^{1/\hat{\lambda}}} \right], \tag{5.14}$$

where $\hat{\lambda} \equiv \lambda/a$, and again $T \gg \nu^{-1}$. A detailed derivation of Eqs. 5.11, 5.13, and 5.14 as well as there respective forms in different geometries and number of spatial dimensions can be seen in Appendix F.

As in Eq. 5.8, we see that the relative error decreases with both the mean number of molecules $\bar{m}(x)$ and the quantity νT. However, we also see an additional factor in brackets, which is always less than one and decreases with $\hat{\lambda}$. This factor accounts for the fact that, unlike in the DT model, molecules can leave a target cell not only by degradation, but also by diffusion. Therefore, the rate at which molecules are refreshed is larger than that from degradation alone. As a result, more independent measurements can made in the time T, and the noise is reduced.

To understand this effect quantitatively, consider a simplified SDC model in which diffusion is modeled as discrete hopping between adjacent target cells at rate h. The number of molecules in the jth target cell is Poisson distributed, such that the instantaneous variance is equal to the mean $\bar{m}_j$. The autocorrelation function in this model is

$$C_j(t) = \bar{m}_j I_0(2h|t|) e^{-(2h+\nu)|t|}, \tag{5.15}$$

where I_0 is the zeroth modified Bessel function of the first kind. Thus the correlation time is

$$\tau = \int_0^\infty dt \, \frac{C_j(t)}{C_j(0)} = \frac{1}{\sqrt{\nu(4h+\nu)}}. \tag{5.16}$$

We see that the correlation time depends on both degradation (ν) and diffusion (h). More precisely, we see that for fast diffusion ($h \gg \nu$), the number of independent measurements scales like $T/\tau \sim T\sqrt{\nu h}$ and therefore increases with both ν and h. Correspondingly, in the fast-diffusion limit of Eq. 5.14 ($\hat{\lambda} \gg 1$), the term in brackets reduces to $\hat{\lambda}^{-1}$, and therefore the number of independent measurements scales like

$\nu T\hat{\lambda} = T\sqrt{\nu(D/a^2)}$. These are identical scalings, with D/a^2 playing the role of the hopping rate h, as expected. A detailed derivation of Eqs. 5.15 and 5.16 can be seen in Appendix G.

5.3 Comparison of DT and SDC

By comparing Eqs. 5.8 and 5.14, it is possible to determine which model achieves the lower relative error. We take an example system in which there are N target cells in a line extending from the source cell, such that the position of the jth target cell in the SDC model and the length of the jth cytoneme in the DT model is $x_j = L_j = 2aj$. The production rate β, the integration time T, and the cell radius a are common to both models and are taken to be equivalent. The degradation rate ν is not taken to be equivalent because in the SDC model the molecules can degrade anywhere but in the DT model they can only degrade in the target cells. Instead, we equate the effective lengthscale of $\bar{m}$, which we define as $\lambda = \int_0^\infty dx\,[\bar{m}(x) - \bar{m}(\infty)]/[\bar{m}(0) - \bar{m}(\infty)]$. In the SDC model this is simply the characteristic lengthscale $\lambda = \sqrt{D/\nu}$. In the DT model, because $\bar{m}_j$ is proportional to Γ_j, it is $\lambda \approx \int_0^\infty dL\,[\Gamma(L) - \Gamma(\infty)]/[\Gamma(0) - \Gamma(\infty)] = (e^{|\phi|} - 1)[\,|\phi| - \log(e^{|\phi|} - 1)]/|\kappa|$, where the approximation applies in the limit of many cells $N \gg 1$.

With these equivalencies set, the ratio of Eq. 5.14 to Eq. 5.8 for the jth target cell is

$$\rho_j = \frac{e^{2j/\hat{\lambda}}\Gamma\,(2aj)}{\sinh(1/\hat{\lambda})\sum_{k=1}^{N}\Gamma\,(2ak)}\left[1 - \frac{(2/\hat{\lambda}) + \sinh(2/\hat{\lambda})}{4\sinh(1/\hat{\lambda})e^{1/\hat{\lambda}}}\right]. \tag{5.17}$$

When ρ_j is less (greater) than 1, the SDC (DT) model achieves lesser error in the jth target cell. Here Γ depends on ϕ and κ, but κ depends on ϕ and λ via the expression for λ in the DT model above. Therefore, Eq. 5.17 depends only on N, $\hat{\lambda}$, and ϕ. Whereas N and $\hat{\lambda}$ can be estimated for particular experimental systems (as we later discuss), we know of no experimental estimates for ϕ. Large ϕ reduces noise in the DT model for most values of j, but it also causes $\bar{m}_j$ to deviate from an exponential profile, which is the functional form generally observed for the morphogens considered

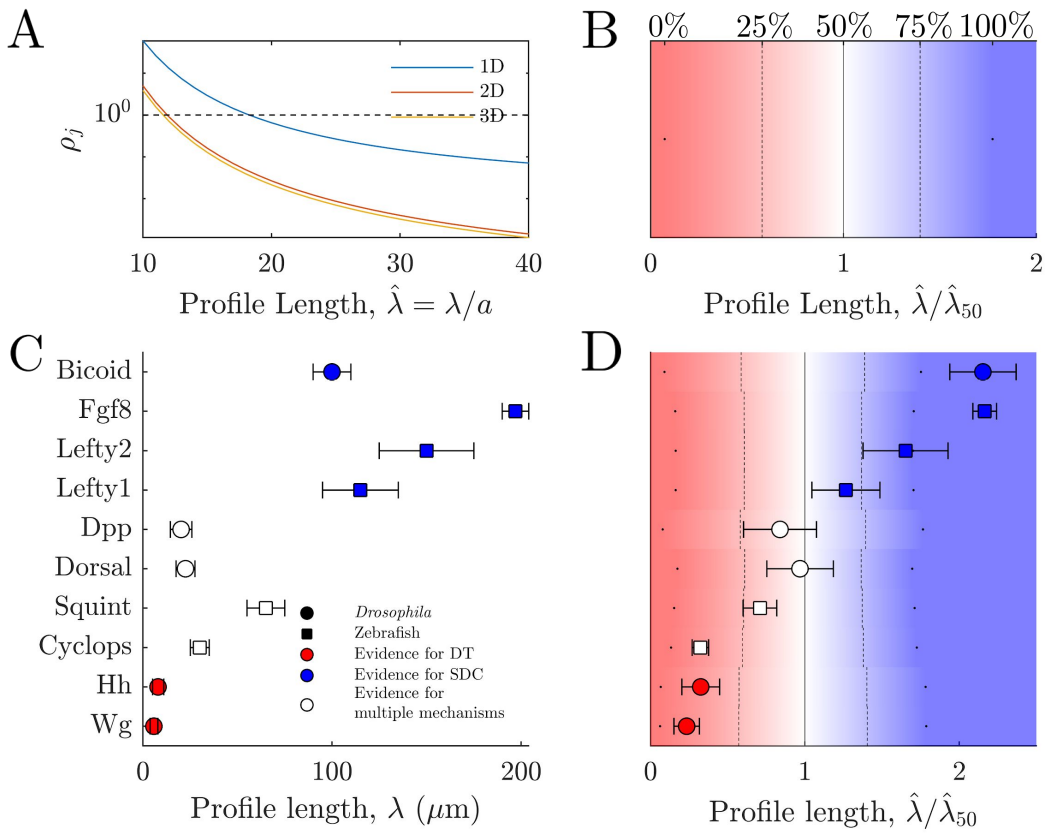

Figure 5.2. Comparing theory and experiment. (A) Ratio ρ_j of SDC to DT relative error in central cell vs. profile lengthscale for $N = 100$ target cells in 1D, 2D, or 3D geometry. (B) Percentage of cells for which $\rho_j < 1$ (1D). (C) λ values for various morphogens estimated from experiments, colored by whether experiments support a DT (red), SDC (blue), or multiple mechanisms (white). (D) Data from C overlaid with theory from B using values of a and N estimated from experiments.

here. Therefore, we set ϕ to the largest value for which a linear regression of $\log(\bar{m}_j)$ vs. j maintains an R^2 value of at least 0.95, which we find to be $\phi \sim -0.05$.

Fig. 5.2A shows ρ_j as a function of profile length $\hat{\lambda}$ for a cell in the center ($j = N/2$) of a line of $N = 100$ target cells. We see that for short profiles the DT model is more precise ($\rho_j > 1$) whereas for long profiles the SDC model is more precise ($\rho_j < 1$). The reason that the SDC model is more precise for long profiles is that long profiles

correspond to fast diffusion, which increases the refresh rate and reduces the noise as discussed above. Conversely, the reason that the DT model is more precise for short profiles is that the mean molecule number is larger. For ϕ near 0 such as the $\phi \sim -0.05$ values obtained to generate Fig. 5.2, $\Gamma(L) \approx \gamma/(1 + L(\lfloor\phi| - \ln(\lfloor\phi|))/\lambda)$. Since this is a power law of L as opposed to the SDC model's decaying exponential given in the form of $\bar{m}(x)$, the DT model's $\bar{m}_j$ will obtain a larger mean for all cells sufficiently far away from the source. This sufficient distance must scale with λ, thus allowing the DT model to obtain a higher mean for all cells when λ is small. We also see in Fig. 5.2A that the behavior of ρ_j is the same when we consider a 2D target cell geometry with a line of source cells, or a 3D target-cell geometry with a plane of source cells.

Fig. 5.2B shows similar information as Fig. 5.2A, but for all target cells j in the line. Specifically, at each $\hat{\lambda}$ value, the color shows the percentage of cells for which the SDC model is more precise ($\rho_j < 1$). We normalize the $\hat{\lambda}$ axis by $\hat{\lambda}_{50}$, the value at which this percentage is 50% (equivalent to the value of $\hat{\lambda}$ at which $\rho_j = 1$ in Fig. 5.2A). As expected, we see that for short profile lengths the DT model is more precise in the majority of cells, whereas for long profiles the SDC model is more precise in the majority of cells.

5.4 Comparison to Experimental Systems

We now test our predictions against data for ten of the morphogens presented in Table 1 of [77] and obtain data from the references therein. In *Drosophila*, the morphogen Wingless (Wg) is localized near cell protrusions such as cytonemes [64,65], and the Hedgehog (Hh) gradient correlates highly in both space and time with the formation of cytonemes [14], suggesting that these two morphogen profiles are formed via a DT mechanism. Conversely, Bicoid has been understood as a model example of SDC for decades [12, 52, 62]. Similarly, Dorsal is spread by diffusion, however its absorption is localized to a specific region of target cells via a nonuniform degradation

mechanism, making it more complex than the simple SDC model [78]. Finally, for Dpp there is evidence for a variety of different gradient formation mechanisms [54, 57, 59].

For each of these morphogens, we then obtain estimates of λ, a, and N. For Bicoid, we obtain a value of λ of $\sim$100μm from the text of [71] with and error of $\pm$10μm from the finding in [12] that cells have a $\sim$10% error in measuring the Bicoid gradient. We then take the a value of the *Drosophila* embryo cells that are subjected to the Bicoid gradient to be $\sim$2.8μm based on Fig. 3A of [12]. We use the same figure to estimate the size of the whole embryo to be $\sim$500μm or $\sim$90 cells. This value of a is also used for Dorsal as measurements of both Bicoid and Dorsal occur in the *Drosophila* embryo at nuclear cycle 14. For the value of λ for Dorsal, we use Fig. 3D from [79] to obtain a full width at 60% max of 45$\pm$10μm. Since this represents the width of Gaussian fit on both sides of the source whereas our model uses an exponential profile, we assume the appropriate λ value for such an exponential fit would be half this value, 22.5$\pm$5μm. Fig. 3A from the same source also shows that the distance from the ventral midline to the dorsal midline is $\sim$200μm or $\sim$35 cells.

For Dpp and Wg, [72] provides explicit measurements of λ for each. These values are 20.2$\pm$5.7μm and 5.8$\pm$2.04μm respectively. For Hh, we use Fig. S2C in the supplementary material of [80] to determine λ to be 8$\pm$3μm. Dpp, Wg, and Hh all occur in the wing disc during the third instar of the *Drosophila* development. As such, we use a common value of a for all three. This value is taken to be 1.3μm based on the area of the cells being reported as 5.5$\pm$0.8μm^2 in the supplementary material of [72] and the assumption that the cells are circular. Additionally, the scale bar for Fig. 1A in [80] shows the maximal distance from the morphogen producing midline of the wing disc to its edge to be $\sim$250μm or $\sim$100 cells.

In zebrafish, the morphogen Fgf8 has been studied at the single molecule level and found to have molecular dynamics closely matching the Brownian movement expected in an SDC mechanism [13]. Similarly, Cyclops, Squint, Lefty1, and Lefty2, all of which are involved in the Nodal/Lefty system, have been shown to spread diffusively and affect cells distant from their source [57,81]. This would support the SDC mechanism,

although Cyclops and Squint have been argued to be tightly regulated via a Gierer-Meinhardt type system, thus diminishing their gradient sizes to values much lower than what they would be without this regulation [55, 81].

The λ value of Fgf8 is reported as being $197\pm7\mu$m in [13]. Additionally, based off the scale bars seen in Fig. 2C-E of [13], we estimate the value of a for the cells to be $\sim10\mu$m. For the morphogens involved in the Nodal/Lefty system (cyclops, squint, lefty1, and lefty2), measurements of λ for each are taken from Fig. 2C-F of [82] by observing where the average of the three curves crosses the 37% of max threshold with error bars given by the width of the region in which the vertical error bars of each plot intersect this threshold line. We assume the a value of each morphogen in the Nodal/Lefty system to be equivalent to the a value of cells in the Fgf8 measurements performed in [13]. This is because the measurements made in [82] were taken during the blastula stage of the zebrafish development while measurements taken in [13] we taken in the sphere germ ring stage. These stages occur at $\sim$2.25 and $\sim$5.67 hpf respectively, but the blastula stage can last until $\sim$6 hpf based on the timeline of zebrafish development presented in [83]. As such, since there is potential overlap in the time frame of these two stages, we assume the cells maintain a relatively fixed size and thus that the value of a for the Nodal/Lefty system can be taken as the same value of a used for Fgf8. Additionally, as seen in Figs. 8F and 11B in [83], these two stages also share a rougly equal overall diameter of the embryo of $\sim500\mu$m at the largest point. This creates a circumference of $\sim1600\mu$m or $\sim$80 cells, which in turn means the morphogen must travel a maximum distance of $\sim$40 cells away from the source.

For all of these morphogens, we estimate the profile lengthscales λ from the experimental data described above [12, 13, 71, 72, 79, 80, 82]. Fig. 5.2C shows these λ values and indicates for each morphogen whether the evidence described above suggests a DT mechanism (red), an SDC mechanism (blue), or multiple mechanisms including DT and SDC (white). We see that in general, the three cases correspond

to short, long, and intermediate profile lengths, respectively, which is qualitatively consistent with our predictions.

To make the comparison quantitative, we estimate the values of cell radius a and cell number N from the experimental data also as described above [12,13,72,79,83], in order to calculate ρ_j from our theory in each case. Estimated values of each of these parameters along with derived values of ϕ are given in Table 5.1. Fig. 5.2D shows the percentage of cells for which we predict that the SDC model is more precise as a function of $\hat{\lambda}$, along with the values of $\hat{\lambda}$ from the experiments (both normalized by $\hat{\lambda}_{50}$ from the theory). We see that in almost all cases, morphogens for which the evidence suggests either a DT or an SDC mechanism (red or blue) fall into the regime in which we predict that mechanism to be more precise for most of the cells, and the morphogens with multiple mechanisms (white) fall in between. This result provides quantitative support for the idea that morphogen profiles form according to the mechanism that maximizes the sensory precision of the target cells.

We have shown that in the steady-state regime, the DT and SDC models of morphogen profile formation yield different scalings of readout precision with the length of the profile and population size. As a result, there exist regimes in this parameter space in which either mechanism is more precise. While the DT model experiences no additional noise or premature degradation from the transport process, the ability of molecules to diffuse into and away from a target cell in the SDC model allows the cell to measure a greater number of effectively unique molecules in the same time frame. By examining how these phenomena affect the cells' sensory precision, we predicted that morphogen profiles with shorter lengths should utilize cytonemes or some other form of direct transport mechanism, whereas morphogens with longer profiles should rely on extracellular diffusion, a prediction that is in quantitative agreement with measurements on known morphogens.

Of important note is the fact that this work has not taken into account the effects of profile steepness, which is known to influence the accuracy of positional information obtained via a morphogen gradient [12]. It remains to be seen how the

Table 5.1.
Experimentally determined values of λ, a, and N for a variety of morphogens from *Drosophila* and Zebrafish. Values of ϕ are determined from maintaining a roughly exponential profile in the DT model.

Morphogen	Organism	λ (μm)	a (μm)	N	ϕ
Bicoid	*Drosophila*	100±10	2.8	90	-0.0906
Fgf8	Zebrafish	197±7	10	40	-0.0761
Lefty2	Zebrafish	150±25	10	40	-0.0814
Lefty1	Zebrafish	115±20	10	40	-0.0794
Dpp	*Drosophila*	20.2±5.7	1.3	100	-0.0671
Dorsal	*Drosophila*	22.5±5	2.8	35	-0.0708
Squint	Zebrafish	65±10	10	40	-0.0597
Cyclops	Zebrafish	30±5	10	40	-0.0295
Hh	*Drosophila*	8±3	1.3	100	-0.0290
Wg	*Drosophila*	5.8±2.04	1.3	100	-0.0205

results obtained here are affected by the consideration of profile steepness. We leave such an investigation to future studies. Nevertheless, it will be interesting to observe whether the trends seen here are further strengthened as more experimental evidence is obtained for different morphogens, as well as to expand the theory of morphogen gradient sensing to further biological contexts.

6. ROLE OF SPATIAL AVERAGING IN MULTICELLULAR GRADIENT SENSING

This work has been published in Physical Biology [84]

Determining the strength and direction of a chemical concentration gradient is an essential task for a diverse array of biological processes. Gradient sensing underlies the polarization of single cells, the orientation and migration of cells and cell collectives, and the changes in tissue morphology that occur during embryogenesis and the subsequent development of an organism [3, 19, 28, 85–93]. Experiments have shown that cells are remarkably precise gradient sensors [3, 28], and a large amount of effort has gone into understanding the mechanisms of, and the limits to, biological gradient sensing [1, 10, 11, 16, 85, 94–97].

At its core, gradient sensing requires the comparison of concentration measurements between the "front" and the "back" of a detector. Detectors that are longer in the gradient direction have a higher gradient sensing precision due to the front and back being more separated and causing the concentration measurements to be more different [10, 11, 94, 96]. However, this argument neglects the fact that information must be communicated between different parts of a detector, especially if the detector is multicellular. Limits to the precision of gradient sensing including communication have been studied and it has been found that for a one-dimensional (1-D) detector, the precision indeed increases with detector length, but then saturates due to the fact that communication introduces its own noise [3, 16]. Yet biological detectors are not 1-D in general. Two-dimensional (2-D) detectors include the quasi-cylindrical arrangement of cell nuclei during the early stages of *Drosophila* development [12] and the planar arrangement of epithelial cell layers [90]. Three-dimensional (3-D) detectors include single cells and the multicellular tips of growing epithelial ducts [98],

as well as border cells exhibiting collective guidance in *Drosophila* [88]. This raises the question of what effect the dimensions transverse to the gradient direction have on the precision of gradient sensing.

Intuition about this question can be drawn from the similar task of sensing the value of a concentration (as opposed to sensing its difference between two points in space, i. e., the gradient). If the concentration profile is uniform in space, then the precision of concentration sensing benefits from increasing the detector length in any direction. The reason is that communication with other parts of the detector, or *spatial averaging*, does not change the mean of a particular measurement within the detector, but it does reduce the noise [1, 10, 96]. Even if the concentration profile is graded, but the goal is still concentration (rather than gradient) sensing, as in stripe formation in early *Drosophila* development, the precision still benefits from spatial averaging [15]. These considerations, drawn from the problem of concentration sensing, suggest that the precision of gradient sensing should also increase with the length of a detector in a direction transverse to the gradient.

Here we investigate theoretically and computationally the precision of gradient sensing for 2-D and 3-D multicellular detectors. We start with one of the simplest models of gradient sensing, the local excitation–global inhibition (LEGI) model [95, 97]. This is an accepted basic model when gradient sensing is adaptive (that is, background concentration largely does not effect the gradient sensing). Surprisingly, in contrast to the case of concentration sensing, we find that the precision of gradient sensing decreases with the length of the detector in a direction transverse to the gradient direction. The reason is that gradient sensing fundamentally relies on a subtraction of concentration measurements, e.g. between the front and back of the detector. While spatial averaging reduces the intrinsic noise in these measurements, which increases precision, it also reduces the covariance between the measurements, which decreases precision. We demonstrate that the latter effect dominates, such that the net result is a decrease in precision with transverse detector size. Then we show that this decrease can actually be overcome by a gradient-sensing strategy that

was recently introduced, termed regional excitation–global inhibition (REGI) [16]. We demonstrate that REGI retains a high covariance between measurements and restores the benefit of transverse averaging. Using a REGI-based model, we compute the optimal 2-D and 3-D detector shapes, which arise from an interplay of the effects of transverse averaging on both the signal and the noise of gradient detection. We argue that these shapes are consistent with the shapes of the multicellular tips of epithelial ducts, suggesting that this and other similarly shaped gradient-sensing systems benefit from spatial averaging in all dimensions.

6.1 LEGI Concentration Sensing

We consider the local excitation–global inhibition (LEGI) model of multicellular gradient sensing, which is a minimal, adaptive, spatially extended model of gradient sensing [3, 16]. We consider a signal concentration profile c that varies linearly in a particular direction in 3-D space, with concentration gradient g (Fig. 6.1A, C). In the nth cell, both a local molecular species X and a global molecular species Y are produced at a rate β and degraded at a rate μ. The production rate is also proportional to the number of signal molecules in the cell's vicinity $c_n a^3$, where a is the cell diameter. As such, X and Y follow similar dynamics to those seen for m in Section 4.2.

Whereas the local species X is confined to each cell, the global species Y is exchanged between neighboring cells at a rate γ_y (Fig. 6.1C; note that although all cells are producing X and Y molecules, we show as examples in Fig. 6.1A and C only those molecules originating from the rightmost, middle cell). Conceptually, X measures the local concentration of signal molecules, while Y represents their

spatially-averaged concentration. As in [3,16] we consider the linear response regime, in which the dynamics of the local and global species satisfy the stochastic equations

$$\begin{aligned} \frac{dx_n}{dt} &= \beta(c_n a^3) - \mu x_n + \eta_n, & (6.1) \\ \frac{dy_n}{dt} &= \beta(c_n a^3) - \mu y_n + \gamma_y \sum_{n' \in \mathcal{N}_n} (y_{n'} - y_n) + \xi_n \\ &= \beta(c_n a^3) - \mu \sum_{n'} M^y_{nn'} y_{n'} + \xi_n. & (6.2) \end{aligned}$$

Here

$$M^y_{nn'} = (1 + |\mathcal{N}_n|\gamma_y/\mu)\delta_{nn'} - (\gamma_y/\mu)\delta_{n' \in \mathcal{N}_n} \quad (6.3)$$

is the connectivity matrix for the global species that accounts for degradation and molecule exchange. $\mathcal{N}_n$ and $|\mathcal{N}_n|$ denote the indices and the number of nearest neighbors of cell n, respectively. The intrinsic noise terms η_n and ξ_n correspond to the Poissonian production, degradation, and exchange reactions [3]. The signal c_n also fluctuates, which introduces extrinsic noise. As described below, in this work we assume that these fluctuations are slow compared to the downstream signal processing, which is equivalent to assuming either slow diffusion of signaling molecules or instantaneous downstream processing, and leads to Poisson-distributed signal molecule counts [3].

In the LEGI paradigm, X excites a downstream species while Y inhibits it. If the cell is at the higher edge of the gradient, then the local concentration (X) is higher than the spatial average (Y), and the excitation exceeds the inhibition. While such comparison of the excitation and the inhibition can be done by many different molecular mechanisms [97], we consider here the limit of shallow gradients, where the comparison is equivalent to subtracting Y from X [3]. This difference, $\Delta_n = x_n - y_n$, is the readout of the model. If Δ_n is positive, the nth cell is further up the gradient than average; if Δ_n is negative, the nth cell is further down the gradient than average. In this work, we always focus on the readout Δ_N of the cell highest up the gradient, which we denote as the Nth cell.

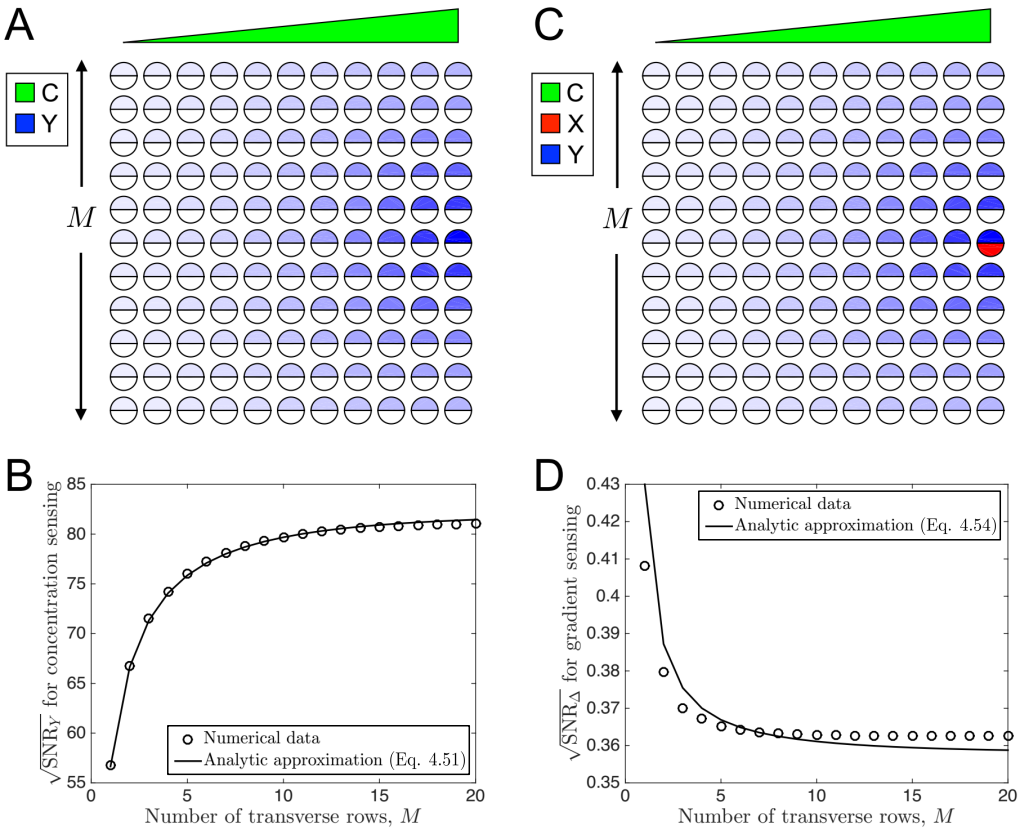

Figure 6.1. Spatial averaging transverse to a gradient improves concentration sensing, but worsens gradient sensing. (A) A 2-D array of cells is exposed to a concentration profile C that varies linearly in the horizontal direction (green wedge). In each cell, Y molecules are produced in proportion to the local C value. Y molecules are also exchanged between neighboring cells, providing the spatial averaging. Thus Y is the readout for the average concentration in the vicinity of a particular cell. Blue indicates the mean number of Y molecules $\bar{y}$ in each cell that have originated from the rightmost, middle cell. (B) The signal-to-noise ratio (SNR) for y increases with the number M of rows of cells added transverse to the gradient direction. (C) As in A, but with an additional internal species X. The molecules are also produced in proportion to the local C value, but they are not exchanged between cells. Red indicates the mean number of X molecules $\bar{x}$ in each cell that have originated from the rightmost, middle cell. The difference $\Delta = x - y$ provides the readout for the gradient (LEGI). (D) In contrast to B, the SNR for Δ decreases with the number of transverse rows M. In B and D, the numerical results are compared with the theoretical approximations (see Eqs. 6.21 and 6.24, respectively) and agree at small M as expected. Parameters are similar to the experiments in [3]: $\bar{c}_N = 1.25$ nM, $g = 0.5$ nM/mm, $a = 10$ μm, $n_y = \sqrt{\gamma_y/\mu} = 4$, $N = 50$ cells per row, and $G = \beta/\mu = 10$. In B and D the numerical value of $\bar{y}_N$ is used in the approximations.

Unlike in previous chapters, we assume that the cells do not average concentrations of the signal C and the messenger molecules X and Y over time (though generalizations with averaging are certainly possible [16]). Then the precision of gradient sensing is given by the square root of the instantaneous signal-to-noise ratio (SNR) for the readout, $\mathrm{SNR}_\Delta = (\bar{\Delta}_N/\delta\Delta_N)^2$, where the mean and variance are given by [3]

$$\begin{aligned} \bar{\Delta}_N &= \bar{x}_N - \bar{y}_N, && (6.4)\\ \bar{x}_N &= Ga^3\bar{c}_N, && (6.5)\\ \bar{y}_N &= Ga^3\sum_n K_n^y \bar{c}_{N-n}, && (6.6) \end{aligned}$$

and

$$\begin{aligned} \delta\Delta_N^2 &= (\sigma_{xN})^2 + (\sigma_{yN})^2 - 2\mathrm{cov}(x_N, y_N), && (6.7)\\ \delta x_N^2 &= \bar{x}_N + G^2a^3\bar{c}_N, && (6.8)\\ \delta y_N^2 &= \bar{y}_N + G^2a^3\sum_n (K_n^y)^2\bar{c}_{N-n}, && (6.9)\\ \mathrm{cov}(x_N, y_N) &= G^2a^3K_0^y\bar{c}_N, && (6.10) \end{aligned}$$

respectively. Here

$$K_n^y = (M^y)^{-1}_{N,N-n} \qquad (6.11)$$

is the communication kernel, and $G = \beta/\mu$ is the gain. The first terms in Eqs. 6.8 and 6.9 correspond to intrinsic noise, while the second terms correspond to extrinsic noise and assume that the diffusion of the signal is slow [3]. Computing the precision for a given configuration of cells only requires inverting the connectivity matrix M^y.

In the recently introduced regional excitation–global inhibition (REGI) model [16], the local species X is also exchanged among cells, but at a lower rate $\gamma_x < \gamma_y$. Then Eq. 6.1 becomes analogous to Eq. 6.2, and Eqs. 6.5, 6.8, and 6.10 are replaced by

$$\begin{aligned} \bar{x}_N &= Ga^3\sum_n K_n^x \bar{c}_{N-n}, && (6.12)\\ \delta x_N^2 &= \bar{x}_N + G^2a^3\sum_n (K_n^x)^2\bar{c}_{N-n}, && (6.13)\\ \mathrm{cov}(x_N, y_N) &= G^2a^3\sum_n K_n^xK_n^y\bar{c}_{N-n}, && (6.14) \end{aligned}$$

respectively, where

$$K_n^x \equiv (M^x)^{-1}_{N,N-n} \tag{6.15}$$

is the communication kernel for the local species, and

$$M^x_{nn'} \equiv (1 + |\mathcal{N}_n|\gamma_x/\mu)\delta_{nn'} - (\gamma_x/\mu)\delta_{n'\in\mathcal{N}_n}. \tag{6.16}$$

Once more, computing the precision for a given configuration of cells in the REGI model only requires inverting the connectivity matrices M^x and M^y. While diffusion of X decreases $\bar{x}_N$ at the Nth cell, and hence decreases the difference $\bar{\Delta}_N$, it also averages X over a larger volume, hence decreasing its noise. As shown in Ref. [16], under a broad range of conditions, the decrease in the noise dominates, and the overall precision of the REGI model is higher than that of LEGI.

Before investigating gradient sensing, we focus on the simpler problem of concentration sensing. In the local excitation–global inhibition (LEGI) model, both X and Y provide readouts of the local concentration, while their difference Δ provides a readout of the gradient. The concentration readout provided by Y is spatially averaged, whereas the concentration readout provided by X is not. Even if the signal profile is graded, X and Y are concentration readouts if viewed independently (with different spatial averaging), not gradient readouts. For example, during Drosophila development, the morphogen profiles are graded, but individual nuclei in the embryo measure (and threshold) the local concentration, possibly with some spatial averaging [12, 15, 99, 100].

How does the precision of concentration sensing depend on transverse detector size? To answer this question, we focus on the spatially averaged concentration readout Y. We consider a linear signal profile with gradient g and compute the SNR of Y in the Nth cell, as we vary the number M of rows of cells in a direction transverse to the gradient (Fig. 6.1A). We see in Fig. 6.1B (circles) that the precision of concentration sensing increases with M. The reason is that adding rows of cells transverse to the gradient allows for Y molecules to be exchanged between rows (in addition to along each row). This does not change the mean $\bar{y}_N$ due to the

translational symmetry in the transverse direction. However, it does reduce the variance, since the global species Y is now averaged over more cells. The net effect is an increase in the SNR beyond what is allowed by longitudinal averaging.

We can elucidate the effect of spatial averaging more quantitatively by appealing to the expression for the variance in Y (Eq. 6.9). In a single row of cells, and in the limit of many cells ($N \gg 1$) and fast communication ($\gamma_y \gg \mu$), the kernel reduces to

$$K_n^y \approx \frac{e^{-n/n_y}}{n_y}, \tag{6.17}$$

where $n_y = \sqrt{\gamma_y/\mu}$ sets the effective length scale of communication [3]. Approximating the sum in Eq. 6.9 as an integral that extends to infinity (since N is large) obtains

$$(\delta y_N^{(1)})^2 \approx \bar{y}_N + \frac{G^2 a^3 \bar{c}_{N-n_y/2}}{2n_y} \tag{6.18}$$

for a single row. In the case of M rows, Y is averaged with the communication kernel K^y over M cells transverse to the gradient. This will not affect the intrinsic component of the variance (since the mean is unchanged), but the extrinsic component will be reduced according to

$$(\delta y_N^{(M)})^2_{\text{ext}} = \sum_{m=-M/2}^{M/2} (K_m^y)^2 (\sigma_{yN}^{(1)})^2_{\text{ext}}. \tag{6.19}$$

We again make the exponential kernel approximation, this time normalizing over the finite domain of size M, giving

$$K_m^y \approx \frac{e^{-|m|/n_y}}{\sum_{m'=-M/2}^{M/2} e^{-|m'|/n_y}}. \tag{6.20}$$

Finally, again approximating the sums as integrals, we obtain

$$\delta y_N^2 \approx \bar{y}_N + \frac{G^2 a^3 \bar{c}_{N-n_y/2}}{2n_y} \frac{n_y(1-e^{-M/n_y})}{[2n_y(1-e^{-M/(2n_y)})]^2}. \tag{6.21}$$

In deriving this approximation, we have neglected effects that the transverse edges have on the exponential shape of the kernel, as well as correlations between exchange reactions parallel and perpendicular to the gradient. Nonetheless, the SNR calculated

using this approximation is compared with the numerical result in Fig. 6.1B, and we see that the agreement is excellent. In the limit $M \ll n_y$, Eq. 6.21 simplifies to

$$\delta y_N^2 \approx \bar{y}_N + \frac{G^2 a^3 \bar{c}_{N-n_y/2}}{2 n_y M}. \tag{6.22}$$

We see that for a small number of rows, the averaging over rows is nearly uniform, and the extrinsic component of the variance is reduced by a factor of M, as expected.

6.2 LEGI Gradient Sensing

We now turn our attention to gradient sensing. How does the precision of gradient sensing depend on transverse detector size? To answer this question for a linear signal profile, we compute the SNR of the gradient readout Δ_N as a function of the number M of rows of cells in a direction transverse to the gradient (Fig. 6.1C). We see in Fig. 6.1D that the precision of gradient sensing decreases with M (circles). This is in contrast to the precision of concentration sensing, which increases with M (Fig. 6.1B).

To understand why the precision of gradient sensing decreases with M, we once again consider the mean and the variance of the readout. The mean $\bar{\Delta}_N = \bar{x}_N - \bar{y}_N$ does not change with M because neither $\bar{x}_N$ nor $\bar{y}_N$ changes with M. However, the variance $\delta\Delta_N^2 = \delta x_N^2 + \delta y_N^2 - 2\mathrm{cov}(x_N, y_N)$ changes with M due to two effects. First, the variance in the global species δy_N^2 decreases with M due to spatial averaging, as discussed in the previous section. Second, the covariance $\mathrm{cov}(x_N, y_N)$ also decreases with M because Y is exchanged with a larger number of cells, whereas X is not exchanged, so the two covary more weakly. The effects have opposite signs. To understand which effect dominates, we again appeal to analytic approximation. For a single row of cells, under the exponential kernel approximation, the covariance in Eq. 6.10 reduces to $\mathrm{cov}^{(1)}(x_N, y_N) \approx G^2 a^3 \bar{c}_N / n_y$. For M rows of cells, since only Y is exchanged, the covariance is reduced according to

$$\mathrm{cov}^{(M)}(x_N, y_N) = K_{m=0}^{y} \mathrm{cov}^{(1)}(x_N, y_N). \tag{6.23}$$

Making the same approximation as above for K_m^y of an exponential in a finite domain, we obtain

$$\begin{aligned}\delta\Delta_N^2 &\approx \delta x_N^2 + \bar{y}_N + \frac{G^2a^3\bar{c}_{N-n_y/2}}{2n_y}\frac{n_y(1-e^{-M/n_y})}{[2n_y(1-e^{-M/(2n_y)})]^2} \\ &\quad -2G^2a^3\frac{\bar{c}_N}{n_y}\frac{1}{2n_y(1-e^{-M/(2n_y)})}. \end{aligned} \tag{6.24}$$

The SNR calculated using this approximation is compared with the numerical result in Fig. 6.1D, and we see good agreement. In the limit $M \ll n_y$, Eq. 6.24 simplifies to

$$\delta\Delta_M^2 \approx \delta x_N^2 + \bar{y}_N + \frac{G^2a^3\bar{c}_{N-n_y/2}}{2n_yM} - 2\frac{G^2a^3\bar{c}_N}{n_yM} \tag{6.25}$$

$$= \delta x_N^2 + \bar{y}_N - \frac{G^2a^3[4\bar{c}_N - \bar{c}_{N-n_y/2}]}{2n_yM}. \tag{6.26}$$

Eq. 6.25 shows that in this limit of near-uniform averaging, both (i) the extrinsic component of the variance in Y and (ii) the covariance are reduced by a factor of M, as expected. Furthermore, because the Nth cell is at the highest concentration, we have $\bar{c}_N > \bar{c}_{N-n_y/2}$, and we see that Eq. 6.26 is an increasing function of M. Thus, this limit elucidates the fact that the decrease of the covariance dominates over the decrease of the variance in Y, causing the variance of Δ_N to increase with M for all parameter values. Because the mean $\bar{\Delta}_N$ does not change with M, we conclude that the precision of gradient sensing decreases with transverse detector size.

6.3 REGI Gradient Sensing

In the previous section we saw that the precision of gradient sensing using the LEGI model (local messenger X is not exchanged among the cells) decreases with the size of a detector in a direction transverse to the gradient, due to the fact that the covariance between the subtracted variables decreases with the transverse size. For the REGI model, exchange of the X molecules has an additional effect beyond increasing the sensing precision for 1-D line of cells [16]: it increases the covariance of X and Y, compared to the LEGI mechanism. Indeed, now both X and Y are downstream signals from some of the same external ligand molecules. Since the

decrease of gradient sensing precision with transverse detector size is due to the loss of covariance (Fig. 6.1D), this raises the question of whether the REGI strategy can overcome this effect and allow gradient sensing precision to benefit from transverse averaging.

To answer this question, we once again consider a linear signal profile, and we compute the SNR of the gradient readout Δ_N under the REGI model as a function of the number M of rows of cells in a direction transverse to the gradient (Fig. 6.2A). We see in Fig. 6.2B that for a sufficiently large value of $n_x \equiv \sqrt{\gamma_x/\mu}$, which sets the lengthscale of spatial averaging for the local species, the precision of gradient sensing increases with M. This is in contrast to the case of LEGI, for which the precision decreases with M (Fig. 6.1D and black circles in Fig. 6.2B). Therefore, the recovery of covariance between X and Y in the REGI mechanism avoids the loss of gradient sensing precision and restores the benefit of transverse averaging.

To understand this effect quantitatively, we turn once more to analytic approximation. The variance in X (Eq. 6.13) and Y (Eq. 6.9) for M rows of cells will be approximated by expressions of the form of Eq. 6.21. The covariance (Eq. 6.14) for a single row of cells under the exponential kernel approximation for both X and Y is $\mathrm{cov}^{(1)}(x_N, y_N) \approx G^2 a^3 \bar{c}_{N-\bar{n}}/(n_x + n_y)$, where $\bar{n} \equiv n_x n_y/(n_x + n_y)$. For M rows of cells the covariance is therefore

$$\mathrm{cov}^{(M)}(x_N, y_N) = \sum_{m=-M/2}^{M/2} K_m^x K_m^y \mathrm{cov}^{(1)}(x_N, y_N). \tag{6.27}$$

Again approximating K_m^x and K_m^y as exponentials in a finite domain, we obtain

$$\begin{aligned}
\delta\Delta_N^2 \;\approx\; & \bar{x}_N + \frac{G^2 a^3 \bar{c}_{N-n_x/2}}{2n_x} \frac{n_x(1-e^{-M/n_x})}{[2n_x(1-e^{-M/(2n_x)})]^2} \\
& + \bar{y}_N + \frac{G^2 a^3 \bar{c}_{N-n_y/2}}{2n_y} \frac{n_y(1-e^{-M/n_y})}{[2n_y(1-e^{-M/(2n_y)})]^2} \\
& - 2\frac{G^2 a^3 \bar{c}_{N-\bar{n}}}{n_x+n_y} \frac{\bar{n}(1-e^{-M/(2\bar{n})})}{2n_x(1-e^{-M/(2n_x)})n_y(1-e^{-M/(2n_y)})}.
\end{aligned} \tag{6.28}$$

This approximation has assumed $\{n_x, n_y\} \gg 1$, and we find that for $n_y = 4$ the SNR calculated using this approximation agrees very well with the numerical result for $n_x \geq 1$; see Fig. 6.2B. In the limit $M \ll n_x$, Eq. 6.28 simplifies to

$$\delta\Delta_N^2 \approx \bar{x}_N + \frac{G^2 a^3 \bar{c}_{N-n_x/2}}{2n_x M} + \bar{y}_N + \frac{G^2 a^3 \bar{c}_{N-n_y/2}}{2n_y M} - 2\frac{G^2 a^3 \bar{c}_{N-\bar{n}}}{(n_x + n_y)M}, \tag{6.29}$$

in which the extrinsic components of the variances and the covariance are reduced by M, as expected. If we further assume that the gradient is shallow compared to the background concentration ($ag \ll \bar{c}_N$), we may approximate $\bar{c}_{N-n_x/2} \approx \bar{c}_{N-n_y/2} \approx \bar{c}_{N-\bar{n}} \approx \bar{c}_N$, yielding

$$\delta\Delta_N^2 \approx \bar{x}_N + \bar{y}_N + \frac{G^2 a^3 \bar{c}_N}{n_y M}\left[\frac{1}{2\rho} + \frac{1}{2} - \frac{2}{\rho + 1}\right], \tag{6.30}$$

where $\rho \equiv n_x/n_y$. The expression in brackets in Eq. 6.30 is positive for all $0 < \rho < 1$, which demonstrates analytically that in this limit the variance in the readout decreases with M, and therefore that the REGI strategy restores the benefit of transverse averaging.

We also see in Fig. 6.2B that a maximal precision emerges in the REGI model as a function of M at a particular number of rows M^*. This maximum is due to the fact that the exchange of X, which causes an increase in precision with M, and the exchange of Y, which causes a decrease in precision with M, occur on different length scales, $n_x < n_y$. Indeed, we see that as n_x increases, the location of the maximum M^* increases concomitantly. Additionally, we see that the maximal precision value first increases with n_x, then decreases with n_x, leading to an optimal value n_x^*. This is due to the previously understood tradeoff that is introduced when n_x increases: on the one hand the variance of X is reduced, which increases precision; on the other hand, the means of X and Y are more similar, which decreases the precision [16]. Here this tradeoff is modified by the additional benefit of increasing n_x, namely that it increases the covariance of X and Y in the transverse direction, and thus further reduces the noise in gradient sensing.

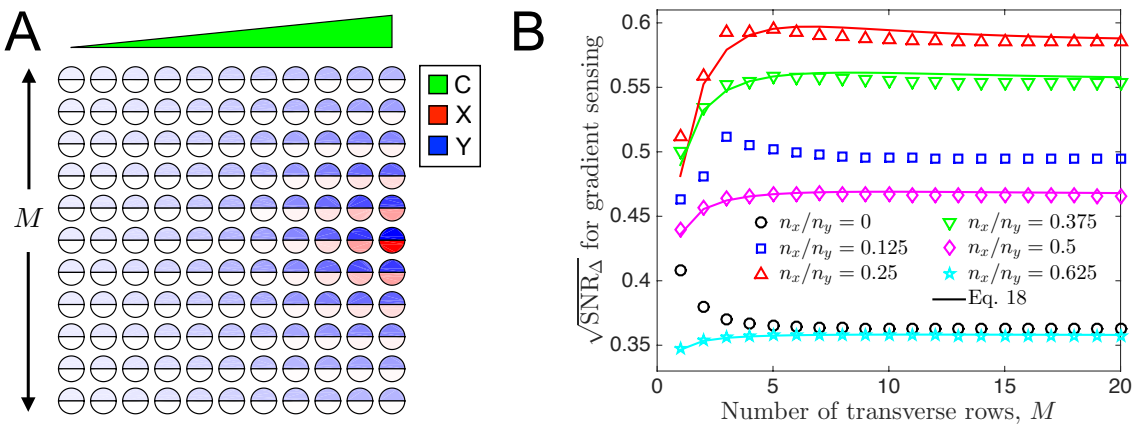

Figure 6.2. The regional excitation–global inhibition (REGI) strategy allows cells to exploit transverse spatial averaging for gradient sensing. (A) As in Fig. 6.1C, but for REGI. X molecules are exchanged between neighboring cells, at a lower rate than Y molecules. The difference $\Delta = x - y$ still provides the readout for the gradient. (B) In contrast to Fig. 6.1D, for sufficiently large communication length n_x the SNR *increases* with the number of transverse rows M, before ultimately decreasing, which leads to an optimum as a function of M. Since $n_x = 0$ (LEGI) and $n_x = n_y = 4$ (no sensing) are suboptimal, a global optimum emerges over both M and n_x. Parameters are as in Fig. 6.1, with $n_x = 1$ in A, which is near its optimal value as seen in B. In B the numerical value of $\bar{y}_N$ is used in the approximations.

6.4 Optimal Shape of Multicellular Gradient Sensor

The emergence of an optimal number of transverse rows of cells, seen in the previous section, raises the more general question of whether there is an optimal detector shape for spatially extended gradient sensing. This question has relevance for both 2-D and 3-D multicellular geometries involved in gradient sensing. Is the optimal detector shape more "hairlike", to maximize its extent in the gradient direction, or more "globular", to exploit potential benefits of extending along the transverse direction?

To address this question, we perform a controlled optimization for both 2-D and 3-D multicellular geometries. For a fixed number of cells $N = 50$, we confine cells to an elliptical (2-D) or ellipsoidal (3-D) envelope, and compute the precision of gradient sensing as a function of the ellipse axis parameters (LEGI), as well as the ratio of averaging length scales n_x/n_y (REGI), exhaustively exploring substantial ranges of both. In addition to the extra shape parameter, there is one more important difference between the 2-D and 3-D cases: in the 2-D case, we assume that every cell detects signal molecules, since we imagine that these molecules diffuse in the 3-D bulk, while the cells form a sensory sheet exposed to the bulk. In contrast, in the 3-D case, we assume that only the surface cells detect signal molecules, whereas cells that are blocked on all six sides by neighboring cells are "shielded" and thus do not detect signal molecules (although all cells still communicate via molecule exchange). The optimal detector shapes determined by such exhaustive search for the REGI model are shown in Fig. 6.3A, for 2-D (top) and 3-D (bottom).

To explain why these optimal shapes emerge, we present the precision of gradient sensing as a function of the control parameters. First we investigate the behavior of the LEGI model in 2-D (Fig. 6.3B). The control parameter is N_g, the (projected) number of cells in the gradient direction, which is set uniquely in 2-D by the ratio of the ellipse axis parameters. Small $N_g \to 1$ corresponds to a chain of cells transverse to the gradient, while large $N_g \to N$ corresponds to a chain of cells parallel to the

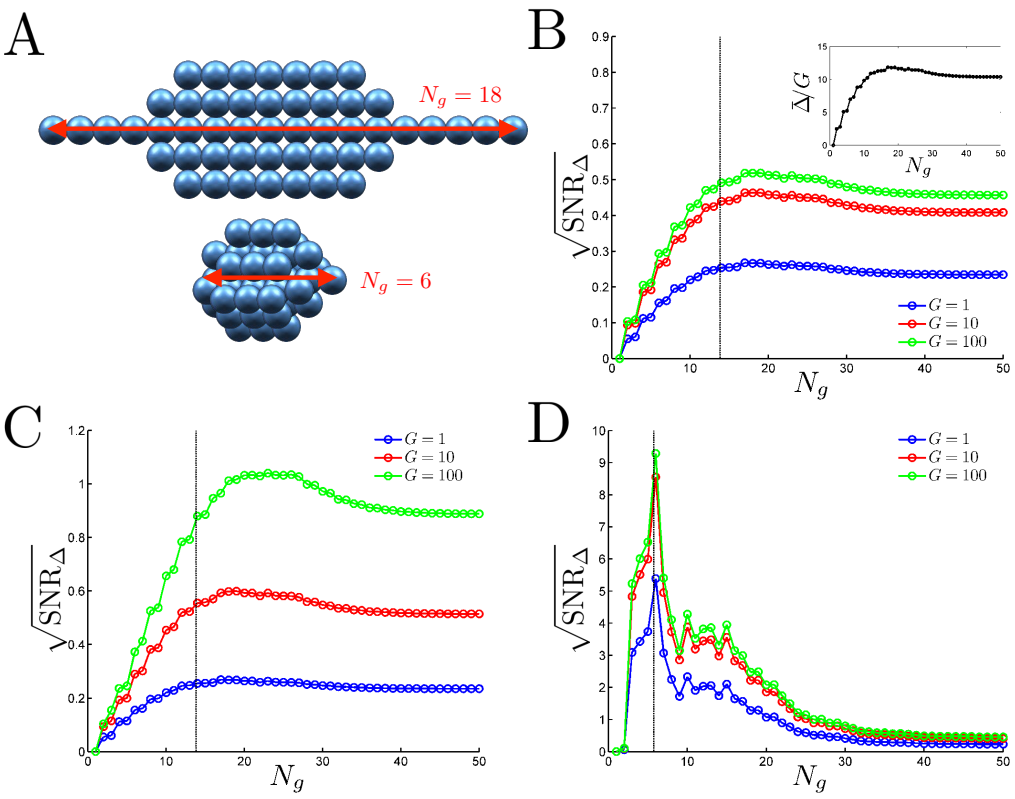

Figure 6.3. Optimal gradient sensing by 2-D and 3-D detectors. (A) Optimal elliptical (2-D, top) or ellipsoidal (3-D, bottom) configurations of $N = 50$ cells for the REGI model. The number of cells in the gradient direction for each shape is $N_g = 18$ (top) and $N_g = 6$ (bottom). Cells are depicted as spheres, even though in the 3-D configuration (bottom) only the outermost cells sense the signal; the rest are shielded. Gradient sensing precision is optimized at the rightmost cell, and the signal profile increases linearly to the right. We see that the optimal shapes are "globular", not "hairlike", especially in 3-D. (B) Precision vs. N_g (the projected number of cells in the gradient direction) for the LEGI model in 2-D, for various gains G. Inset: mean readout $\bar{\Delta}$ normalized by G (all three curves overlap and are colored black). (C) As in B, but for REGI. The additional REGI parameter n_x is optimized over at each N_g value, and the optimal precision is shown. At the observed optima in C, these values are $n_x^*/n_y = 0.09$ ($G = 1$), 0.30 ($G = 10$), and 0.53 ($G = 100$). (D) As in B but for 3-D. Internal cells are shielded and do not sense, but do communicate. Ellipsoid axes transverse to gradient are equal. Optimal $n_x^* = 0$ for all N_g. Curve jaggedness arises due to numerical effects of fitting a cubic lattice of cells in a smooth ellipsoidal envelope. Black vertical dashed lines correspond to a perfect circle (B, C) or sphere (D). Parameters are as in Fig. 6.1.

gradient. The small "stair steps" in the curves are due to the numerical task of fitting the discrete multicellular square lattice within the continuous elliptical envelope. We see that the precision vanishes at $N_g = 1$, as expected, since in our model a single cell cannot perform gradient detection. The precision is near maximal at $N_g = N$. This trend is analogous to that seen for LEGI in Fig. 6.1D, where here $N/N_g \sim M$ is the analog of the number of transverse rows. However, unlike in Fig. 6.1D, we see in Fig. 6.3B that there is a weak optimum at an intermediate value of N_g. This is due to a difference between the protocols of adding rows of cells (Fig. 6.1D) and reshaping a fixed number of cells (Fig. 6.3B). Adding rows does not change $\bar{\Delta}_N$. In contrast, as seen in the inset of Fig. 6.3B, reshaping changes $\bar{\Delta}_N$. The reason is that elliptical configurations (like Fig. 6.3A, top) are not translationally symmetric in the transverse direction. In particular, a large density of cells in the middle of the configuration is a sink for molecules of Y. This decreases the mean number of Y in the rightmost cell, $\bar{y}_N$, which weakly increases the signal $\bar{\Delta}_N = \bar{x}_N - \bar{y}_N$ at intermediate values of N_g (Fig. 6.3B inset), and therefore increases the precision (Fig. 6.3B). Finally, we see that the precision increases with the gain G, as expected, and that the increase saturates with G, since then the variance of X and Y is dominated entirely by extrinsic, and not intrinsic, noise.

Next we investigate the behavior of REGI in 2-D (Fig. 6.3C). Once again the control parameter is N_g. Additionally, at every N_g we optimize the local species' averaging length scale n_x (generally we find an optimal value between $\sim 0.1n_y$ and $\sim 0.5n_y$, see Fig. 6.3). We see in Fig. 6.3C that the trend of precision versus N_g is similar to that of the LEGI model (Fig. 6.3C), but with two key differences. First, the precision is higher for REGI than for LEGI. This is due to regional averaging reducing the variance of the local species, as was known previously for the 1-D model [16]. Second, the optimum in the precision as a function of N_g is more pronounced for REGI than for LEGI. This is because the region surrounding the optimum corresponds to near-circular ellipses, where considerable transverse averaging occurs. As shown in the previous section, transverse averaging increases precision in the REGI model. Overall,

the optimal structure (Fig. 6.3A, top) is closer to a "globular" circle than to "hairlike" chain (compare locations of the optima to the dashed vertical line in Fig. 6.3C, which corresponds to a perfect circle). Therefore, we see that optimal gradient sensing by a 2-D structure benefits from an elliptical shape in which transverse averaging occurs.

Finally, we investigate the behavior of REGI in 3-D (Fig. 6.3D). Here there are two control parameters: the number of cells in the gradient direction N_g, and the asymmetry of the ellipsoid in the two directions transverse to the gradient. Generally we find that the optimal shape at a fixed N_g displays symmetry in the two transverse directions, and therefore we impose this symmetry explicitly and focus on the control parameter N_g. As before, at every N_g we optimize the local species' averaging length scale n_x. Importantly, in the 3-D geometry, we find that the optimal value at every N_g is $n_x^* = 0$, corresponding to no averaging of the local species (an effective LEGI model). This is due to the shielding of internal cells: since internal cells do not detect signal molecules, averaging of the local species would dramatically reduce the mean local readout, making it far less than the actual local signal value at the edge cell. This would severely reduce the mean $\bar{\Delta}_N$, and thus the precision. The dependence of precision on N_g is shown in Fig. 6.3D. The additional jaggedness is again due to the incommensurate nature of the cubic cell lattice with the smooth ellipsoidal envelope, here amplified due to the additional dimension. We see in Fig. 6.3D that there is again an optimum. In fact, it is much more pronounced than in 2-D: the overall value of the precision is ten-fold higher than in 2-D. This is again due to the shielding of internal cells: the global species Y is averaged among internal cells that do not produce it, which sharply decreases $\bar{y}_N$, and thereby increases $\bar{\Delta}_N$ and thus the precision. Note that this particular effect of shielding will result in the value of $\bar{\Delta}_N$ being positive in every edge cell, instead of only the edge cells at the high end of the gradient. The sensory outcomes are still biased, but are less adaptive, similar to "tug-of-war" chemotaxis mechanisms that have been proposed [101]. Overall, the optimal structure is very "globular" (Fig. 6.3A, bottom). Indeed, it is almost a sphere (compare the optima to the dashed vertical line in Fig. 6.3D). We conclude that, due

to the combined effects of spatial averaging and shielding, the optimal 3-D detector of linear gradients extends significantly in all three spatial dimensions.

6.5 Discussion

We have investigated theoretically and computationally the ways in which the precision of spatially extended, multi-component gradient sensing is affected by detector geometry. Using a minimal model of adaptive gradient sensing (LEGI), we have found that, unlike for concentration sensing, the precision of gradient sensing decreases with the size of the detector in a direction transverse to the gradient. This is due to the competing effects of noise reduction and a reduction of the covariance between concentrations subtracted to estimate the gradient. We have demonstrated that a simple modification of LEGI (REGI) restores the covariance and recovers the benefit of transverse averaging for gradient sensing. The result is that the optimal detectors in 2-D and 3-D are more globular than hairlike.

Our study elucidates the important roles of spatial averaging in gradient sensing, which are several-fold. First, there is spatial averaging along the gradient. In both LEGI and REGI, the global species Y is averaged along the gradient. For a linear signal profile, this averaging both increases the signal $\bar{\Delta}^2$, and decreases the noise $\delta\Delta^2$. Therefore, it is optimal for Y to be averaged along the gradient to as large an extent as possible. Second, in the REGI model, the local species X is also averaged along the gradient. This decreases the signal but also decreases the noise [16]. Therefore, there is often an optimal ratio n_x/n_y of the spatial extents of the averaging. Third, there is spatial averaging transverse to the gradient. In the LEGI model, only Y is averaged transverse to the gradient. In a translationally symmetric geometry, this does not change the signal, but it changes the noise by both decreasing the variance of Y and decreasing the covariance between X and Y. These have opposite effects on the precision. For LEGI, the latter dominates, decreasing the precision. Therefore, transverse averaging is detrimental for gradient sensing. However, in the REGI

model, X is also averaged transverse to the gradient. Once again, in a translationally symmetric geometry, this does not change the signal with respect to REGI in 1-D, but it decreases the noise, both by further reducing the variance in X and by restoring a larger covariance between X and Y. Therefore, transverse averaging is beneficial for REGI-type gradient sensing. These roles of spatial averaging are modified in geometries without translational symmetry as we discussed above. However, the net result remains the same: the optimal 2-D and 3-D REGI-type gradient detectors are globular, benefitting from extensive spatial averaging in the transverse directions.

How do our results compare to experimental systems? A well-studied example of a natural gradient-sensing system is the growth factor-directed extension of mammary epithelial ducts [93, 98]. Gradient sensing in this system has been shown to be multicellular and adaptive [3]. *In vivo*, the extension is led by an "end bud" of cells at the duct tip. These tips can form either long hairlike structures or coalesce into nearly spherical globules, as was observed in organotypic studies with different chemical and genetic perturbations [3]. Long hairs could act as "feelers" for the duct, sampling a long swath of the environment in the gradient direction. However, our analysis predicts that such hairlike morphologies are suboptimal, and the globular bud shape, as in Fig. 6.3A, would produce a better precision. In agreement with the prediction, the end buds in wildtype mice are nearly spherical, and the globule is often wider than the duct itself [93]. Similarly, neither chemotaxing amoeba [102] and neutrophils [85], nor growing neurons [28] form very thin hairlike protrusions to facilitate sensing. Instead they keep the aspect ratio of the gradient sensing part of the protrusions closer to one, again supporting our findings. Further, in Drosophila border cell migration, another example of directional collective cell behavior, groups of cells travel as a sphere in a confined space, where it would have been easier to travel as a chain [88]. All of these examples provide indirect evidence that transverse averaging is used in multiple biological contexts.

7. EMERGENT VS. INDIVIDUAL-BASED MULTICELLULAR CHEMOTAXIS

This work has been published in Physical Review Letters [76]

Collective migration is ubiquitous in cell biology, occurring in organism development [88,103–105], tissue morphogenesis [3] and metastatic invasion [89,106–108]. Collective migration often occurs in response to chemical cues in the environment, a process known as chemotaxis. The simplest way for cells to collectively chemotax is by individual detection and response to the chemical attractant: each cell measures the spatial difference in chemoattractant across its body and moves in the perceived direction of the gradient, while short-range coupling keeps the group together. Groups performing this type of *individual-based chemotaxis* (IC) are found not only in cell biology [17] but also in ecological systems such as bird flocks [109]. However, recent experiments have uncovered an alternative type of chemotaxis, in which cells grouped together chemotax differently than if they were alone [18–21]. For example, outer cells may polarize while inner cells do not, a mechanism observed in neural crest cells [103] and considered in several recent modeling studies [19,101,110]. This type of *emergent chemotaxis* (EC) behavior seen in cell collectives presupposes a machinery within cells which allows for behavior to change once a cell is in a group. Since this machinery may come at a cost, this raises the question of whether EC offers any fundamental advantage over IC.

We address this question using simple physical models of EC and IC. Cell collectives respond to graded profiles of freely diffusing molecules, and we quantify the migratory behavior of one-dimensional (1D) cell chains, two-dimensional (2D) cell sheets, and three-dimensional (3D) cell clusters (Fig. 7.1A), configurations designed to mimic physiological multicellular structures such as filaments and ducts [89,111,112]. Collectives

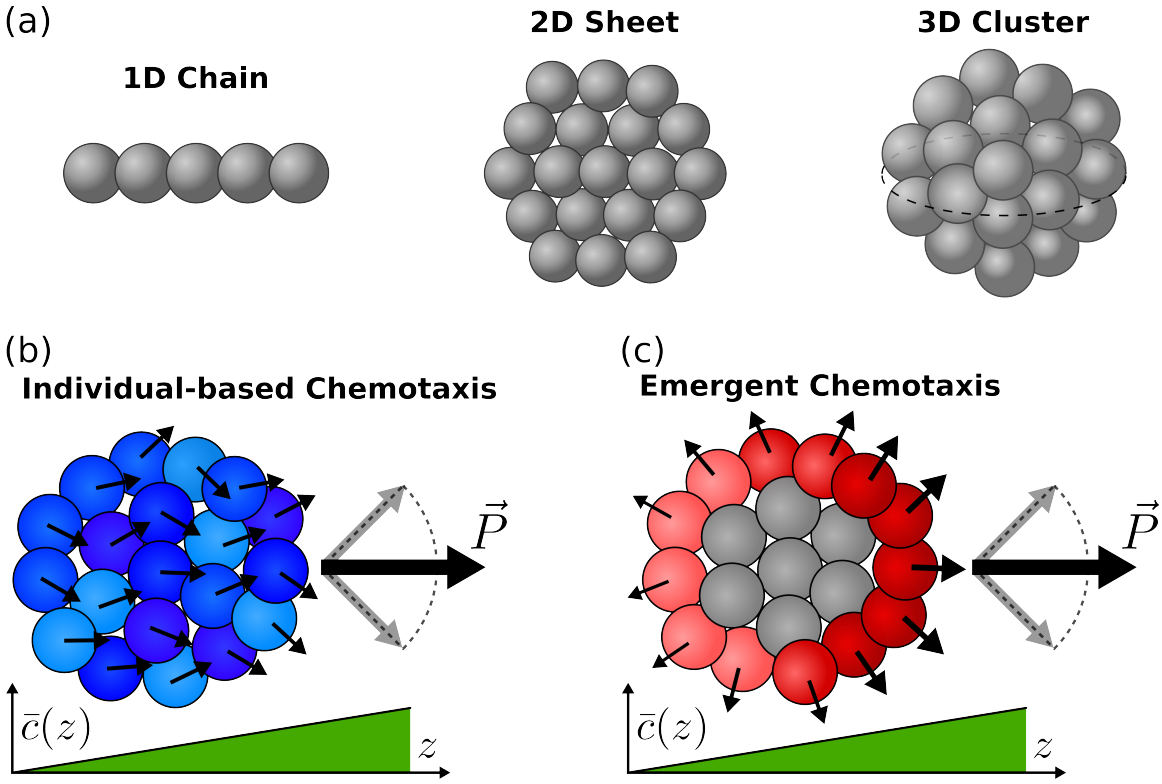

Figure 7.1. (a) We study the chemotactic performance of 1D chains, 2D sheets, and 3D clusters of cells. (b) In individual-based chemotaxis (IC), cells in the collective polarize based on their own gradient measurement. (c) In emergent chemotaxis (EC), cell polarization depends on intercellular interactions: cells on the edge polarize based on their measurement of the concentration, and cells in the bulk do not polarize. In both mechanisms the total polarization $\vec{P}$ will fluctuate in magnitude and direction due to noise in cell measurements.

performing EC and IC are found to have very similar mean speed, with polarization strength scaling linearly with the number of cells regardless of chemotactic mechanism or dimensionality. However, 1D and 2D EC collectives have higher chemotactic precision than IC collectives: we find that for N cells, the relative error in EC scales as $\{N^{-2}, N^{-3/2}, N^{-1}\}$ for 1D, 2D, and 3D, respectively, whereas in IC it scales as N^{-1} for any dimension. We explain the physical origin of this difference and discuss its implications.

7.1 Individual-based Chemotaxis

We first consider IC (Fig. 7.1B). Due to the chemoattractant molecules in the environment, the ith cell becomes polarized with vector $\vec{p}_i$ in its desired direction of motion [97]. The components of $\vec{p}_i$ reflect the difference in concentration $c(\vec{r},t)$ between the front and back of the cell in each respective direction. This concentration difference will fluctuate due to the particulate nature of diffusion. Focusing on this extrinsic source of noise, we treat each cell as a sphere of radius a through which molecules freely diffuse, akin to the "perfect instrument" described by Berg and Purcell [1]. The concentration difference is encoded internally as a weighted count of the molecules within the cell volume V_i. The weighting function will depend on the sensory network, but will generally be positive at the front and negative at the back; here we choose cosine for simplicity. Orienting our coordinate system such that $\hat{z}$ is parallel to the gradient, the components of $\vec{p}_i$ become

$$\vec{p}_i(t) = \int_{V_i} d^3r \ \vec{w}c(\vec{r},t), \tag{7.1}$$

where $\vec{w} = \{\sin\theta\cos\phi, \sin\theta\sin\phi, \cos\theta\}$ is the angular unit vector extending from the center of the cell. The concentration is a random variable which obeys regular diffusion

$$\frac{\partial c}{\partial t} = D\nabla^2 c + \eta_c \tag{7.2}$$

with D the diffusion coefficient and η_c the Langevin noise. The mean concentration is taken to be

$$\bar{c}(\vec{r}) = c_0 + \vec{r}\cdot\vec{g}, \tag{7.3}$$

and first we consider a constant gradient $\vec{g} = g\hat{z}$ that is shallow ($ag \ll c_0$). Cells are assumed to preferentially adhere to one another, hence the polarization of a collective of N cells is the sum of its constituent cells' polarization vectors $\vec{P}(t) = \sum_{i=1}^{N} \vec{p}_i(t)$.

The collectives exist at low Reynolds number, hence their velocity $\vec{v}$ is proportional to the motility force, and in turn the polarization $\vec{P}$. Therefore, understanding the behavior of $\vec{P}$ will inform us of the collective migratory performance. We focus

on two measures of performance: the mean and the relative error of time averaged measurements of the polarization in the gradient direction P_z, where measurements are averaged over a time T and the relative error is defined

$$\epsilon^2 = \frac{\delta P_{zT}^2}{\langle P_z \rangle^2} = \frac{\delta v_{zT}^2}{\langle v_z \rangle^2}. \tag{7.4}$$

Eq. 7.1 indicates that a single cell will have mean polarization proportional to the concentration difference across the cell,

$$\langle \vec{p}_i \rangle = \int_{V_i} d^3r \ \vec{w}\,(c_0 + \vec{r}\cdot g\hat{z}) = \frac{\pi}{3} a^4 g \hat{z}, \tag{7.5}$$

regardless of the cell's location. Therefore the mean collective polarization is geometry-independent, depending only on the number of cells present,

$$\langle \vec{P} \rangle_{\mathrm{IC}} = \frac{\pi}{3} a^4 g N \ \hat{z}, \tag{7.6}$$

as shown in Fig. 7.2A (blue lines) along with consistent results from simulations performed by a previous group member.

We next investigate the relative error for IC collectives. We linearize the concentration $c(\vec{r},t) = \bar{c}(\vec{r}) + \delta c(\vec{r},t)$ as well as the cell polarization $\vec{p}_i(t) = \langle \vec{p}_i \rangle + \delta\vec{p}(t)$, and through the same power spectrum analysis performed in previous works we derive analytic expressions for δP_{zT}^2 and thereby ϵ^2. Since $P_z = \sum_{i=1}^{N} p_{iz}$, the variance in the total polarization is a linear combination of all cell polarization variances and covariances present in the collective,

$$\delta P_{zT}^2 = \sum_i \delta p_{i,zT}^2 + \sum_{i \neq j} \mathrm{Cov}[p_{iz}, p_{jz}] \equiv V + C, \tag{7.7}$$

The covariances are derived from the power spectrum in polarization cross correlations in a similar manner to the variances, taking the general form [2, 16]

$$\mathrm{Cov}[p_{i\alpha}, p_{j\alpha}] = \frac{1}{T} \lim_{\omega \to 0} \int \frac{d\omega'}{2\pi} \langle \delta\tilde{p}_{i\alpha}^*(\omega') \delta\tilde{p}_{j\alpha}(\omega) \rangle, \tag{7.8}$$

Eq. 7.8 assumes that the integration time is larger than the timescale of molecule diffusion over the radius R of the collective, $T \gg \tau_D = R^2/D$, though we relax this

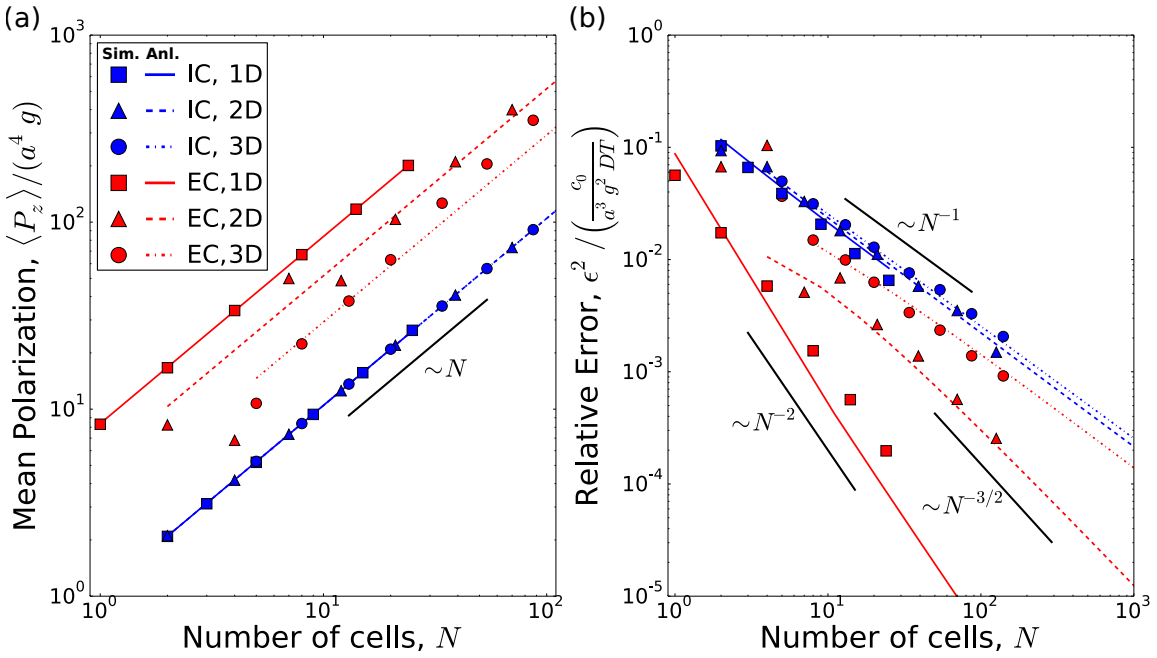

Figure 7.2. (a) Mean cluster polarization and (b) relative error for both mechanisms of collective chemotaxis in every configuration. Points are simulation data, colored lines are analytical predictions. 1D EC data plotted with respect to $N-1$.

assumption in later simulations. Following this procedure we find that V and C for IC are

$$V_{\mathrm{IC}} = \frac{4\pi a^5 c_0}{45DT} N, \tag{7.9}$$

$$C_{\mathrm{IC}} = -\frac{\pi a^5 c_0}{18DT} \sum_{i \neq j}^{N} \frac{3\cos^2\Theta_{ij} - 1}{n_{ij}^3}. \tag{7.10}$$

Here n_{ij} is the number of cell radii separating the centers of cells i and j, and Θ_{ij} is the angle between the gradient direction and a line connecting the two cells.

V_{IC} scales with N since each cell is involved in gradient sensing. However, Eq. 7.10 reveals an angular dependence on the correlations between two IC cells. A pair of cells can be correlated or anti-correlated depending on their locations relative to the gradient. For example, if a pair of cells is parallel to the gradient then $\cos^2\Theta_{ij} = 1$, resulting in a negative covariance, indicating that their gradient measurements

are anti-correlated. In contrast, if two cells are perpendicular to the gradient then $\cos^2\Theta_{ij} = 0$, resulting in a positive covariance and correlations between the two cells. The resulting contribution of C_{IC} to δP_{zT}^2 is dimensionality-dependent since the angles made between pairs of cells is determined by geometry, whereas V_{IC} is dimension-independent.

For a 1D chain of IC cells, every pair is parallel to the gradient resulting in anti-correlated measurements. This allows us to exactly evaluate Eq. 7.10 which when combined with Eq. 7.9 produces

$$\delta P_{zT}^2 = \frac{\pi a^5 c_0}{9DT}\left[\frac{4}{5}N - \frac{1}{8}\left(NH_{N-1}^{(3)} - H_{N-1}^{(2)}\right)\right], \tag{7.11}$$

where $H_n^{(m)} = \sum_{k=1}^{n} k^{-m}$ is the generalized harmonic number. Since $H_{N-1}^{(i)}$ approaches a constant for $i \geq 2$, we see that Eq. 7.11 scales as $\sim N$ to leading order, which in turn means ϵ^2 will scale as $\sim N^{-1}$.

As dimensionality increases, more and more pairs of cells will be perpendicular to the gradient resulting in reduced anti-correlations in the collective. This means C_{IC} will have diminishing impact on δP_{zT}^2, culminating in 3D clusters having zero cell-cell covariance contribution to the total cluster variance. This results in $\epsilon^2 \sim N^{-1}$ regardless of dimensionality. This is significant as it is exactly the scaling we would expect to see if each cell was treated as completely independent of each other cell, indicating that IC cells behave as effectively independent gradient sensors even with diffusion-mediated cross-correlations. These scalings for V and C are summarized in Table 7.1. The resulting ϵ^2 predictions are plotted in Fig. 7.2B (blue lines), and we see excellent agreement with the aforementioned simulation results. A detailed derivation of Eq. 7.11 as well as its analogous 2D and 3D results can be seen in Appendix H.

7.2 Emergent Chemotaxis

Next we turn our attention to EC, the mechanism in which grouped cells sense and migrate differently than individuals. Often cells in a cluster differentiate, with edge cells polarized and bulk cells unpolarized [19, 104]. In accordance with previous

Table 7.1.
Summary of scaling behavior. N dependence of the leading order term for the mean $\langle P_z \rangle$, and the variance (V) and covariance (C) contributions to the relative error $\epsilon^2 = (V + C)/\langle P_z \rangle^2$. C for EC in 2D has a log correction.

		$\langle P_z \rangle$	V	C	ϵ^2
IC	1D	N^1	N^1	$-N^1$	N^{-1}
	2D	N^1	N^1	$-N^1$	N^{-1}
	3D	N^1	N^1	0	N^{-1}
EC	1D	N^1	N^0	$-N^{-1}$	N^{-2}
	2D	N^1	$N^{1/2}$	$N^{1/2}$	$N^{-3/2}$
	3D	N^1	$N^{2/3}$	N^1	N^{-1}

studies [101,110], we assume that cell interactions are mediated by contact inhibition of locomotion [113]. The interactions result in edge cells polarized away from their neighbors, and interior cells that remain uninvolved in chemical sensing and do not polarize (Fig. 7.1C). The edge cells polarize with strength proportional to the local concentration which, again like Berg and Purcell's perfect instrument [1], is estimated by counting the molecules present within their cell volume. Hence we define the polarization of the ith cell in the collective as

$$\vec{p}_i(t) = \begin{cases} \hat{r}_i \int_{V_i} d^3r \; c(\vec{r}, t) & i \in \{N_{\text{edge}}\} \\ 0 & i \in \{N_{\text{bulk}}\} \; , \end{cases} \tag{7.12}$$

where $\hat{r}_i$ is a unit vector that points radially outwards from the collective. Eq. 7.12 dictates that $\vec{p}_i$ is dependent on a cell's location relative to the collective. As illustrated in Fig. 7.1C, only the cells on the edge sense the chemoattractant,

polarizing with a larger magnitude on the high concentration side of the collective, and the total polarization depends only on the cells along the edge: $\vec{P} = \sum_i \vec{p}_i \ , \ \forall i \in \{N_{\text{edge}}\}$.

For 1D EC, only the two opposing cells at either end of the chain are polarized so $\langle \vec{P} \rangle$ can be solved for exactly. Using the fact that these two cells must have their centers separated by a distance of $2a(N-1)$, the mean of the total polarization can be expressed as

$$\begin{aligned} \left\langle \vec{P} \right\rangle_{\text{EC}} &= \langle \vec{p}_N \rangle + \langle \vec{p}_1 \rangle = \hat{z} \int_{V_N} d^3r \ \ (c_0 + \vec{r} \cdot g\hat{z}) - \hat{z} \int_{V_1} d^3r \ \ (c_0 + \vec{r} \cdot g\hat{z}) \\ &= \frac{4\pi}{3} a^3 \hat{z} \left((\vec{r}_N - \vec{r}_1) \cdot g\hat{z} \right) = \frac{8\pi}{3} a^4 g \, (N-1) \, \hat{z}. \end{aligned} \tag{7.13}$$

In order to calculate the mean total polarization for two and three dimensional clusters we assume that the cluster size is relatively large ($a \ll R$) and approximate the sum as an integral. For a 2D disc of cells the sum $\vec{P} = \sum_i^{N_{\text{edge}}} \vec{p}_i$ becomes an integral over the circumference of the cluster. The circumference and the total number of cells along the edge are related by $2\pi R = 2aN_{\text{edge}}$, and so a segment along the perimeter of length $R\theta$ is equivalent in length to $2an$ with n the number of edge cells in that segment. Hence $n = \frac{R}{2a}\theta$ allowing us to write integrals for $\left\langle \vec{P} \right\rangle$ as

$$\begin{aligned} \langle \vec{P} \rangle &= \frac{R}{2a} \int_0^{2\pi} d\theta \ \langle \vec{p} \rangle = \frac{R}{2a} \int_0^{2\pi} d\theta \ \vec{w} \left(\frac{4\pi}{3} a^3 (c_0 + gR\cos\theta) \right) = \frac{2\pi^2}{3} a^2 g R^2 \hat{z} \\ &= \frac{2\pi^2}{3} a^4 g N \hat{z}, \end{aligned} \tag{7.14}$$

where the last equality utilizes the relation $N = (R/a)^2$.

Similarly, in 3D we approximate the sum as an integral of the spherical surface of the cluster. A patch on the surface of area ΩR^2 encompasses $n = \Omega R^2/(\pi a^2)$ edge cells. The total polarization can therefore be written as an integral over the surface of a spherical cluster:

$$\begin{aligned} \langle \vec{P} \rangle &= \frac{R^2}{\pi a^2} \int d\Omega \ \langle vecp \rangle = \frac{R^2}{\pi a^2} \int d\Omega \ \vec{w} \left(\frac{4\pi}{3} a^3 (c_0 + gR\cos\theta) \right) = \frac{16\pi}{9} a g R^3 \hat{z} \\ &= \frac{16\pi}{9} a^4 g N \hat{z}, \end{aligned} \tag{7.15}$$

where for such a spherical cluster, $N = (R/a)^3$. Eqs. 7.13-7.15 are shown in Fig. 7.2A (red lines), and we again see good agreement. We can understand why $\langle P_z \rangle$ scales with N by noting that it depends on the product of $N_{\text{edge}} \sim N^{(d-1)/d}$ and the distance spanned in the gradient direction $R \sim N^{1/d}$, resulting in a mean polarization which is geometry invariant [19].

Comparing EC and IC shows that $\langle P_z \rangle \sim N$ regardless of collective migration mechanism or geometry as seen in Fig. 7.2A. $\langle P_z \rangle$ has the same parameter dependency for both EC and IC, namely $a^4 g$, which is the average change in the number of chemoattractant molecules across a cell. Although $\langle P_z \rangle_{\text{EC}} \approx 6 \langle P_z \rangle_{\text{IC}}$ meaning that EC speed is faster than IC, this relatively small difference may be difficult to detect in biological systems. Moreover, both mechanisms have the same N scaling. Does the same equivalence between EC and IC also hold for the relative error?

Following the procedure outlined by Eqs. 7.7 and 7.8 we find analytic expressions for $\delta P_{zT}^2 = V + C$ for EC,

$$V_{\text{EC}} = \frac{16\pi a^5 c_0}{15DT} \sum_{i=1}^{N_{\text{edge}}} \cos^2 \Theta_i, \tag{7.16}$$

$$C_{\text{EC}} = \frac{8\pi a^5 c_0}{9DT} \sum_{i \neq j}^{N_{\text{edge}}} \frac{\cos \Theta_i \cos \Theta_j}{n_{ij}}, \tag{7.17}$$

with Θ_i being the angle $\hat{r}_i$ makes with the gradient. Both V_{EC} and C_{EC} depend on dimensionality simply because $N_{\text{edge}} \sim N^{(d-1)/d}$. From Eqs. 7.16 and 7.17 we see that $V \sim N_{\text{edge}}$, and that C depends on the angles edge cells make with the gradient. The angular dependence means that cells along the front and back sides of the cluster (relative to the gradient) are strongly anti-correlated since $\cos \Theta_i \cos \Theta_j \approx -1$, whereas pairs of edge cells near the middle are very weakly correlated ($\cos \Theta_i \cos \Theta_j \approx 0$).

For a 1D chain of EC cells the summations only go over the two edge cells with $\cos \Theta = \pm 1$. This allows us to exactly evaluate Eqs. 7.16 and 7.17 to produce

$$\delta P_{zT}^2 = \frac{8\pi a^5 c_0}{3DT} \left(\frac{4}{5} - \frac{1}{6\,(N-1)} \right). \tag{7.18}$$

To leading order, Eq. 7.18 scales as $\sim N^0$, which in turn means ϵ^2 will scale as $\sim N^{-2}$. Unlike in the case of IC, the scaling of C with N increases with dimensionality as summarized in Table 7.1, and the resulting ϵ^2 predictions show good agreement with the simulation results (Fig. 7.2B). A detailed derivation of Eq. 7.18 as well as its analogous 2D result and a discussion of the 3D geometry can be seen in Appendix I.

The dimension dependence of the EC relative error can be understood by thinking of the collective as one large detector whose sensory surface is comprised of two halves. If both halves were to take measurements of their local concentrations and then polarize in opposing directions with strengths proportional to their measurements, then ϵ^2 would depend on the size of each half a_{eff} and their separation distance A_{eff} according to $\epsilon^2 \sim a_{\text{eff}}^{-1} A_{\text{eff}}^{-2}$ [16]. The size of each half is independent of N for a 1D chain (each half is a single cell), but it scales as $a_{\text{eff}} \sim N^{1/d}$ for $d = 2$ or 3 dimensions. The separation distance scales with the radius of the collective for all d, $A_{\text{eff}} \sim N^{1/d}$. This results in $\epsilon^2 \sim \{N^{-2}, N^{-3/2}, N^{-1}\}$ for $d = \{1, 2, 3\}$ (Fig. 7.2B, black lines), which agree with the scalings seen in simulations and analytics.

7.3 Discussion

The physical origin of the advantage of EC over IC lies in how the errors scale with the collective size N. In IC, all N cells contribute to the sensing, and cross-correlations between them scale either linearly or sublinearly with N, leading to a scaling $\epsilon \sim 1/\sqrt{N}$ that is characteristic of independent sensors. But in EC, only $N_{\text{edge}} \sim N^{(d-1)/d}$ cells contribute to the sensing, leading to a sublinear scaling with N of the variance contributions of the individual cells. The total variance of the collective, then, depends on the cross-correlations, which are geometry-specific: in 1D they are dwarfed by the individual variances, in 2D they are commensurate, and in 3D they dominate (Table 7.1). As a result, 1D and 2D EC collectives benefit from a variance that scales subextensively, i.e., sublinearly with N.

In our model, IC polarization is adaptive to the background concentration as observed in the Ras signalling pathway for *Dictyostelium discoideum* chemotaxis [114]. On the other hand, our EC model is non-adaptive. Cell polarization increases with background concentration causing tension in the collective (Fig. 7.1C), as previously studied [101]. However, adaptive collective sensing has been observed in mammary epithelial cells [3]. Our EC model could be made adaptive by replacing the integrand in Eq. 7.12 with $c(\vec{r}+\vec{r}',t)-c_0$. This change does not affect the properties of $\vec{P}$ since the background concentration cancels out when summing over all edge cells, but it does remove the internal tension in the collective.

Besides the advantage revealed here in terms of chemotactic precision, another benefit of EC is in terms of cell differentiation. In EC only edge cells need to be involved in chemical sensing and polarization, freeing bulk cells from the obligation of receptor and protein production necessary for chemotaxis. Bulk cells are free to differentiate into other phenotypes, possibly serving different uses for the collective. This is in stark contrast with IC where every cell must be of the polarized phenotype, leaving no cells with the freedom to differentiate.

The two EC advantages of improved chemotactic precision and the possibility of cell differentiation may be why EC-style collective migration is more prevalent than IC. For example, EC has been observed in two dimensional collectives of malignant lymphocytes [19] and in border cell migration [104]. In cancer, metastatic invasion sometimes occurs in the form of chains of cells leaving the tumor with a leader cell at the front [89, 111], analogous to our 1D EC model. Two-dimensional EC migration may also be implicated in tumorigenesis and metastasis in pancreatic ductal cells given the cylindrical surface-like geometry of pancreas ducts [112].

How can our predictions be tested in experiments? The chemotactic index (CI), commonly defined as $\mathrm{CI} \equiv \langle \cos\theta \rangle$ where θ is the angle between the trajectory and the gradient [115], is actually a simple monotonic function of ϵ^2. For small deviations from perfect chemotaxis, we have $\mathrm{CI} \approx 1 - \langle \theta^2 \rangle/2 = 1 - \mathrm{Var}[\theta]/2$. If v_z and v_x are the components of the velocity of the collective parallel and perpendicular to

the gradient, respectively, then $\theta \approx v_x/v_z$ with $\langle v_z \rangle > 0$ and $\langle v_x \rangle = 0$, resulting in $\mathrm{Var}[\theta] = \mathrm{Var}[v_z]/\langle v_z \rangle^2 = \epsilon^2$. Therefore the relative error and chemotactic index are related as $\mathrm{CI} = 1 - \epsilon^2/2$ for small errors. With this relationship the predicted scalings of ϵ^2 for EC and IC may be tested with chemotaxis experiments. Additionally, the CI scaling behavior could be used to determine whether an EC- or IC-style migration is at play in an unknown system.

We have shown how the fluctuations in a diffusing attractant concentration set physical limits to collective chemotactic performance. By focusing on two fundamental classes of collective chemotaxis, we have found that the mean speed scales with the size of the collective irrespective of the mechanism or geometry, but that an emergent mechanism outperforms an individual-based one for 1D and 2D geometries in terms of chemotactic precision. This advantage arises due to the ways that errors accumulate in the two mechanisms: in an emergent strategy, fewer cells contribute their sensory noise to the collective, and in 1D and 2D the cross-correlations between cells remain low, ultimately leading to a subextensive scaling of polarization variance with collective size. As such, the performance advantage is an inherent property of the emergent mechanism, and we suspect that it not only helps explain the prevalence of emergent chemotaxis in cellular systems, but that it also is detectable using standard measures such as the chemotactic index.

8. CONCLUSIONS

Cells are exquisite sensors, and they also display diverse mechanisms of interacting within collective groups. By utilizing Langevin equation techniques, we have successfully calculated the physical limits to the precision with which these collectives and perform a variety of sensory tasks. We have shown that for autocrine signalling in a uniform concentration there exists a finite, nonzero optimal cell-cell separation to minimize the noise-to-signal ratio. This is caused by a tradeoff between communication strength and signal cross-correlations both decreasing with increasing separation, which in turn allows porous autocrine systems to achieve higher precision than tightly packed juxtacrine systems. In the case of cells making concentration measurements of a nonuniform morphogen profile we have uncovered the benefits of having diffusive transport at long ranges and direct transport at short ranges due to an increased rate of the morphogen being refreshed and an increased mean expression level respectively.

For gradient sensing, we proceeded to show that higher precision can be obtained when the cells communicate via the REGI mechanism as opposed to LEGI. This is caused by the reduced variance in the local species brought on by the transverse averaging, resulting in the optimal cluster configuration to be very spherical as opposed to a long, thin chain. Lastly, we determined how 1D and 2D geometries of cell clusters can improve their ability to chemotax in response to a gradient by changing their behavior in a group and utilizing an emergent form of chemotaxis. This allows for the total error to scale with population size more favorably by altering how many cells contribute to the overall polarization of the cluster. These results showcase the diverse ways in which collectives of cells can improve how precisely they can perform tasks well beyond the physical limits of what a single cell can do.

A. CALCULATIONS FOR BERG AND PURCELL'S PERFECT INSTRUMENT

For the perfect instrument, a ligand species diffuses in a solution via

$$\frac{dc}{dt} = D_c \nabla^2 c + \eta_c, \tag{A.1}$$

where $c(\vec{x}, t)$ is the ligand concentration, D_c is the ligand diffusion constant, and $\eta_c(\vec{x}, t)$ is the noise intrinsic to the diffusion process.

The cross spectrum of η_c can be obtained from its correlation function. To derive such a correlation function, we first consider a separate Markovian system comprised of a 1-dimensional lattice of discrete compartments that a diffusing species Y can exist in. The dimensionality is chosen purely for simplicity, as the method outlined below can be easily generalized to higher dimensions to produce the same result. Let $y_i(t)$ be the number of Y molecules in the ith compartment at time t and d be the rate at which these molecules move to the $i-1$ or $i+1$ compartment. Given a sufficiently small time step δt, the probability of a molecule moving from the ith compartment to the $i \pm 1$ compartment is

$$P\left(\{y_i(t+\delta t), y_{i\pm1}(t+\delta t)\} = \{y_i(t) - 1, y_{i\pm1}(t) + 1\}\right) = y_i(t)\, d\delta t. \tag{A.2}$$

Higher order interactions in which multiple molecules are transfered within the time step δt will have probabilites of order $(\delta t)^2$ or higher and can thus be ignored. This allows the mean of $\delta y_i(t) = y_i(t+\delta t) - y_i(t)$ to take the form

$$\left\langle \delta y_i(t) \right\rangle = \left(y_{i-1}(t) + y_{i+1}(t) - 2y_i(t)\right) d\delta t, \tag{A.3}$$

where the first two terms come from molecules moving into the ith compartment from the $i-1$ and $i+1$ compartments respectively and the third term comes from the

two different ways molecules can leave the ith compartment. As δt is small, each of these transfer processes can be treated as being Poissonianly distributed. This allows the variance of $\delta y_i(t)$ to simply be the right-hand side of Eq. A.3 but with each term taken to be its absolute value so there are no subtractions. Additionally, this approximation allows the covariance between δy_i and $\delta y_{i\pm1}$ to be taken as the negative of the sum of the expected number of molecules moving from the ith compartment to the $i \pm 1$ compartment and vice versa. With these, the correlation function between $\delta y_i(t)$ and $\delta y_j(t)$ can be written as

$$\begin{aligned}\left\langle \delta y_j(t)\, \delta y_i(t) \right\rangle = &\left(y_{i-1}(t) + y_{i+1}(t) + 2y_i(t)\right) d\delta t \delta_{i,j} - \left(y_i(t) + y_{i-1}(t)\right) d\delta t \delta_{i-1,j} \\ &- \left(y_i(t) + y_{i+1}(t)\right) d\delta t \delta_{i+1,j}. \end{aligned} \tag{A.4}$$

We now take the system to continuous space by letting $y_i(t) \to \ell c(x,t)$ and $\delta_{i,j} \to \ell\delta(x - x')$ with any intances of ±1 in the indices also being converted to $\pm\ell$. Putting these substitutions into Eq. A.4 and dividing by $(\ell\delta t)^2$ yields

$$\begin{aligned}\left\langle \frac{\delta c(x',t)}{\delta t} \frac{\delta c(x,t)}{\delta t} \right\rangle = &\frac{d}{\delta t}\Big(\left(c(x-\ell,t) + c(x+\ell,t) + 2c(x,t)\right)\delta\left(x - x'\right) \\ &- \left(c(x,t) + c(x-\ell,t)\right)\delta\left(x - \ell - x'\right) \\ &- \left(c(x,t) + c(x+\ell,t)\right)\delta\left(x + \ell - x'\right)\Big) \\ = \frac{d}{\delta t}\Big(&\Big(c(x+\ell,t)\,\delta\left(x - x'\right) - c(x+\ell,t)\,\delta\left(x + \ell - x'\right)\Big) \\ &- \Big(c(x,t)\,\delta\left(x - \ell - x'\right) - c(x,t)\,\delta\left(x - x'\right)\Big) \\ &+ \Big(c(x,t)\,\delta\left(x - x'\right) - c(x,t)\,\delta\left(x + \ell - x'\right)\Big) \\ &- \Big(c(x-\ell,t)\,\delta\left(x - \ell - x'\right) - c(x-\ell,t)\,\delta\left(x - x'\right)\Big)\Big). \end{aligned} \tag{A.5}$$

Eq. A.5 has been rearranged into this form so as to easily apply the operators $\partial_x^{\pm}$ defined as

$$\partial_x^+ f(x) = \frac{f(x+\ell) - f(x)}{\ell}, \tag{A.6a}$$

$$\partial_x^- f(x) = \frac{f(x) - f(x-\ell)}{\ell}. \tag{A.6b}$$

Using this notation, Eq. A.5 can be simplfied into

$$\begin{aligned}\left\langle \frac{\delta c(x',t)}{\delta t} \frac{\delta c(x,t)}{\delta t} \right\rangle &= \frac{\ell d}{\delta t} \Big(\partial_x^+ \Big(c(x,t)\,\delta\left(x-\ell-x'\right) - c(x,t)\,\delta\left(x-x'\right)\Big) \\ &\qquad + \partial_x^- \Big(c(x,t)\,\delta\left(x-x'\right) - c(x,t)\,\delta\left(x+\ell-x'\right)\Big)\Big) \\ &= \frac{\ell^2 d}{\delta t} \left(\partial_x^+ \partial_{x'}^+ + \partial_x^- \partial_{x'}^-\right) \Big(c(x,t)\,\delta\left(x-x'\right)\Big). \end{aligned} \tag{A.7}$$

Taking the $\ell \to 0$ limit while holding $D = \ell^2 d$ constant allows $\partial_x^{\pm}$ and $\partial_{x'}^{\pm}$ to converge to true derivatives, ∂_x and $\partial_{x'}$. Additionally, if the $\delta c(x',t)/\delta t$ term on the left-hand side of Eq. A.7 is replaced with $\delta c(x',t')/\delta t$ for $t' \neq t$, then the entire right-hand side must go to 0 as the system is Markovian. This can be accomplished by multiplying the right-hand side by a factor of $\delta_{t,t'}$. Taking the $\delta t \to 0$ limit then turns the two terms on the left-hand side into true derivatives in time, ∂_t and $\partial_{t'}$, acting on $c(x,t)$ and $c(x',t')$ respectively while the factor of $\delta_{t,t'}/\delta t$ on the right-hand side becomes $\delta(t-t')$. Altogether, this transforms Eq. A.7 into

$$\left\langle \partial_{t'} c\left(x',t'\right) \partial_t c(x,t) \right\rangle = 2D\delta\left(t-t'\right) \partial_x \partial_{x'} \Big(c(x,t)\,\delta\left(x-x'\right)\Big). \tag{A.8}$$

Finally, by approximating the system as being in steady state, $c(x,t)$ can be replaced with $\bar{c}(x)$ and $\partial_t c(x,t)$ becomes equivalent to $\eta_D(x,t)$. Making these substitutions and generalizing Eq. A.8 to three dimensions yields

$$\left\langle \eta_c\left(\vec{x}',t'\right) \eta_c(\vec{x},t) \right\rangle = 2D\delta\left(t-t'\right) \vec{\nabla} \cdot \vec{\nabla}' \Big(\bar{c}(\vec{x})\,\delta^3\left(\vec{x}-\vec{x}'\right)\Big). \tag{A.9}$$

Here $\bar{c}(\vec{x})$ is the mean value of $c(\vec{x},t)$ as a function of space, which in this system is taken to be a constant. Performing a Fourier transformation on Eq. A.9 then yields

$$\left\langle \tilde{\eta}_c^* \left(\vec{k}', \omega'\right) \tilde{\eta}_c \left(\vec{k}, \omega\right) \right\rangle = \int d^3x d^3x' dt dt' \left\langle \eta_c \left(\vec{x}', t'\right) \eta_c \left(\vec{x}, t\right) \right\rangle \left(e^{i\vec{k}\cdot\vec{x}} e^{i\omega t}\right) \left(e^{i\vec{k}'\cdot\vec{x}'} e^{i\omega' t'}\right)^*$$
$$= \int d^3x d^3x' dt dt' 2D_c \bar{c} e^{i\left(\vec{k}\cdot\vec{x} - \vec{k}'\cdot\vec{x}'\right)} e^{i\left(\omega t - \omega' t'\right)} \delta\left(t - t'\right) \vec{\nabla}_x \cdot \vec{\nabla}_{x'} \left(\delta^3\left(\vec{x} - \vec{x}'\right)\right). \tag{A.10}$$

Due to the factor of $\delta\left(t - t'\right)$, the integral in t' becomes trivial and leaves the only time dependent factor as $e^{it\left(\omega - \omega'\right)}$. This allows the integral in t to be solved via the Fourier definition of the d-dimensional δ function

$$\delta^d\left(\vec{z}\right) = \int \frac{d^d\kappa}{\left(2\pi\right)^d} e^{i\vec{\kappa}\cdot\vec{z}}. \tag{A.11}$$

By letting $d = 1$, $\vec{z} = \omega - \omega'$, and $\kappa = t$, utilizing Eq. A.11 in Eq. A.10 yields

$$\left\langle \tilde{\eta}_c^* \left(\vec{k}', \omega'\right) \tilde{\eta}_c \left(\vec{k}, \omega\right) \right\rangle$$
$$= 2D_c \bar{c} \left(2\pi\delta\left(\omega - \omega'\right)\right) \int d^3x d^3x' e^{i\left(\vec{k}\cdot\vec{x} - \vec{k}'\cdot\vec{x}'\right)} \vec{\nabla}_x \cdot \vec{\nabla}_{x'} \left(\delta^3\left(\vec{x} - \vec{x}'\right)\right). \tag{A.12}$$

Eq. A.11 can then be put back into Eq. A.12 by letting $d = 3$ and $\vec{z} = \vec{x}$ to change the form of $\delta^3\left(\vec{x} - \vec{x}'\right)$,

$$\left\langle \tilde{\eta}_c^* \left(\vec{k}', \omega'\right) \tilde{\eta}_c \left(\vec{k}, \omega\right) \right\rangle$$
$$= 2D_c \bar{c} \left(2\pi\delta\left(\omega - \omega'\right)\right) \int d^3x d^3x' e^{i\left(\vec{k}\cdot\vec{x} - \vec{k}'\cdot\vec{x}'\right)} \vec{\nabla}_x \cdot \vec{\nabla}_{x'} \int \frac{d^3\kappa}{\left(2\pi\right)^3} e^{i\vec{\kappa}\cdot\left(\vec{x} - \vec{x}'\right)}$$
$$= \frac{2D_c \bar{c}}{\left(2\pi\right)^3} \left(2\pi\delta\left(\omega - \omega'\right)\right) \int d^3x d^3x' d^3\kappa e^{i\vec{x}\cdot\left(\vec{k} + \vec{\kappa}\right)} e^{-i\vec{x}'\cdot\left(\vec{k}' + \vec{\kappa}\right)} \kappa^2. \tag{A.13}$$

Continuing to utilize Eq. A.11, all remaining integrals in Eq. A.13 either become δ functions or are over δ functions by integrating over x then κ then x'. This yields the power spectrum of $\eta_c\left(\vec{x}, t\right)$ to be

$$\left\langle \tilde{\eta}_c^* \left(\vec{k}', \omega'\right) \tilde{\eta}_c \left(\vec{k}, \omega\right) \right\rangle = 2D_c\bar{c} \left(2\pi\delta\left(\omega - \omega'\right)\right) \int d^3x' d^3\kappa \delta^3 \left(\vec{k} + \vec{\kappa}\right) \kappa e^{-i\vec{x}'\cdot\left(\vec{k}'+\vec{\kappa}\right)} \kappa^2$$
$$= 2D_c\bar{c}k^2 \left(2\pi\delta\left(\omega - \omega'\right)\right) \int d^3x' e^{-i\vec{x}'\cdot\left(\vec{k}'-\vec{k}\right)}$$
$$= 2D_c\bar{c}k^2 \left(2\pi\delta\left(\omega - \omega'\right)\right) \left(\left(2\pi\right)^3 \delta^3 \left(\vec{k} - \vec{k}'\right)\right). \tag{A.14}$$

Now, let $c\left(\vec{x}, t\right) = \bar{c} + \delta c\left(\vec{x}, t\right)$. This linearizes Eq. A.1 into

$$\frac{d\delta c}{dt} = D_c \nabla^2 \delta c + \eta_c. \tag{A.15}$$

Eq. A.15 can then be Fourier transformed into

$$-i\omega\tilde{\delta c} = -D_c k^2 \tilde{\delta c} + \tilde{\eta} \implies \tilde{\delta c} = \frac{\tilde{\eta}}{D_c k^2 - i\omega}. \tag{A.16}$$

Utilizing Eq. A.16 to solve for the power spectrum of $\delta c\left(\vec{x}, t\right)$ gives the solution

$$\left\langle \tilde{\delta c}^* \left(\vec{k}', \omega'\right) \tilde{\delta c} \left(\vec{k}, \omega\right) \right\rangle = \frac{\left\langle \eta^* \left(\vec{k}', \omega'\right) \eta \left(\vec{k}, \omega\right) \right\rangle}{\left(D_c k^2 - i\omega\right) \left(D_c k'^2 + i\omega'\right)}$$
$$= \frac{2D_c\bar{c}k^2 \left(2\pi\delta\left(\omega - \omega'\right)\right) \left(\left(2\pi\right)^3 \delta^3 \left(\vec{k} - \vec{k}'\right)\right)}{\left(D_c k^2 - i\omega\right) \left(D_c k'^2 + i\omega'\right)}$$
$$= \frac{2D_c\bar{c}k^2 \left(2\pi\delta\left(\omega - \omega'\right)\right) \left(\left(2\pi\right)^3 \delta^3 \left(\vec{k} - \vec{k}'\right)\right)}{\left(D_c k^2\right)^2 + \omega^2}, \tag{A.17}$$

where the last equality stems from letting $\omega = \omega'$ and $\vec{k} = \vec{k}'$, which is forced by the δ functions. Generalizing the definition of $S\left(\omega\right)$ found in Eq. 3.6 to a 4-dimensional system, Eq. A.17 gives the power spectrum of $\delta c\left(\vec{x}, t\right)$ to be exactly that derived by Bialek,

$$
\begin{aligned}
S_c\left(\vec{k},\omega\right) &= \int \frac{d^3k'}{\left(2\pi\right)^3}\frac{d\omega'}{2\pi}\left\langle \tilde{\delta c}^{\,*}\left(\vec{k}',\omega'\right)\tilde{\delta c}\left(\vec{k},\omega\right)\right\rangle \\
&= \int \frac{d^3k'}{\left(2\pi\right)^3}\frac{d\omega'}{2\pi}\frac{2D\bar{c}k^2\left(2\pi\delta\left(\omega-\omega'\right)\right)\left(\left(2\pi\right)^3\delta^3\left(\vec{k}-\vec{k}'\right)\right)}{\left(Dk^2\right)^2+\omega^2} \\
&= \frac{2D\bar{c}k^2}{\left(Dk^2\right)^2+\omega^2}.
\end{aligned} \tag{A.18}
$$

Now, let $n(t)$ be the number of molecules in a permeable spherical cell of volume V and radius a. $n(t)$ can be calculated from $c\left(\vec{x},t\right)$ via

$$
n(t) = \int_V d^3x c\left(\vec{x},t\right). \tag{A.19}
$$

Once again, let $n(t) = \bar{n} + \delta n(t)$, where $\bar{n}$ is the mean value of $n(t)$. Since $\bar{c}$ is the mean value of $c\left(\vec{x},t\right)$, this implies

$$
\bar{n} = \int_V d^3x\bar{c} = \frac{4}{3}\pi a^3\bar{c} \implies \delta n(t) = \int_V d^3x\delta c\left(\vec{x},t\right). \tag{A.20}
$$

Fourier transforming the second part of Eq. A.20 then yields

$$
\tilde{\delta n}\left(\omega\right) = \int_V d^3x \int \frac{d^3k}{\left(2\pi\right)^3}\tilde{\delta c}\left(\vec{k},\omega\right)e^{-i\vec{k}\cdot\vec{x}}. \tag{A.21}
$$

With this and Eq. A.17, the power spectrum of $n(t)$ can be calculated to be

$$
\begin{aligned}
&\left\langle \tilde{\delta n}^{\,*}\left(\omega'\right)\tilde{\delta n}\left(\omega\right)\right\rangle \\
&= \left\langle \left(\int_V d^3x' \int \frac{d^3k'}{\left(2\pi\right)^3}\tilde{\delta c}^{\,*}\left(\vec{k}',\omega'\right)e^{i\vec{k}'\cdot\vec{x}'}\right)\left(\int_V d^3x \int \frac{d^3k}{\left(2\pi\right)^3}\tilde{\delta c}\left(\vec{k},\omega\right)e^{-i\vec{k}\cdot\vec{x}}\right)\right\rangle \\
&= \frac{1}{\left(2\pi\right)^6}\int_V d^3xd^3x' \int d^3kd^3k' \left\langle \tilde{\delta c}^{\,*}\left(\vec{k}',\omega'\right)\tilde{\delta c}\left(\vec{k},\omega\right)\right\rangle e^{-i\left(\vec{k}\cdot\vec{x}-\vec{k}'\cdot\vec{x}'\right)} \\
&= \frac{2D_c\bar{c}}{\left(2\pi\right)^3}\left(2\pi\delta\left(\omega-\omega'\right)\right)\int_V d^3xd^3x' \int d^3kd^3k' \frac{k^2\delta^3\left(\vec{k}-\vec{k}'\right)}{\left(D_ck^2\right)^2+\omega^2}e^{-i\left(\vec{k}\cdot\vec{x}-\vec{k}'\cdot\vec{x}'\right)} \\
&= \frac{2D_c\bar{c}}{\left(2\pi\right)^3}\left(2\pi\delta\left(\omega-\omega'\right)\right)\int_V d^3xd^3x' \int d^3k \frac{k^2}{\left(D_ck^2\right)^2+\omega^2}e^{-i\vec{k}\cdot\vec{x}}e^{i\vec{k}\cdot\vec{x}'}.
\end{aligned} \tag{A.22}
$$

Since the integrations in Eq. A.22 are over three dimensional spaces, the expression

$$\int d\Omega_\kappa e^{i\vec{\kappa}\cdot\vec{z}} = 4\pi \frac{\sin\left(\kappa|\vec{z}|\right)}{\kappa|\vec{z}|}, \tag{A.23}$$

where Ω_κ is the solid angle at radius κ, can be used to solve the solid angle components of the x and x' integrals, yielding

$$\begin{aligned}
&\left\langle \tilde{\delta n}^{\,*}\left(\omega'\right)\tilde{\delta n}\left(\omega\right)\right\rangle \\
&\quad = \frac{4}{\pi}D_c\bar{c}\left(2\pi\delta\left(\omega-\omega'\right)\right)\int_0^a dxdx'\int d^3k\frac{k^2}{\left(D_ck^2\right)^2+\omega^2}\left(x^2\frac{\sin\left(kx\right)}{kx}\right)\left(x'^2\frac{\sin\left(kx'\right)}{kx'}\right) \\
&\quad = \frac{4}{\pi}D_c\bar{c}\left(2\pi\delta\left(\omega-\omega'\right)\right)\int d^3k\frac{k^2}{\left(D_ck^2\right)^2+\omega^2}\left(\frac{\sin\left(ka\right)-ka\cos\left(ka\right)}{k^3}\right)^2 \\
&\quad = 16D_c\bar{c}a^2\left(2\pi\delta\left(\omega-\omega'\right)\right)\int_0^\infty dk\frac{1}{\left(D_ck^2\right)^2+\omega^2}\left(\frac{\sin\left(ka\right)}{ka}-\cos\left(ka\right)\right)^2.
\end{aligned} \tag{A.24}$$

To solve this integral, it must first be noted that the integrand is even in k. Thus, the lower limit can be extended to $-\infty$ simply by introducing a factor of $\frac{1}{2}$. Additionally, the sin and cos terms can be broken into their exponential forms to produce

$$\begin{aligned}
\left\langle \tilde{\delta n}^{\,*}\left(\omega'\right)\tilde{\delta n}\left(\omega\right)\right\rangle &= 16D_c\bar{c}a^2\left(2\pi\delta\left(\omega-\omega'\right)\right)\frac{1}{2}\int_{-\infty}^\infty dk\frac{1}{\left(Dk^2\right)^2+\omega^2} \\
&\qquad\cdot\left(\frac{1}{2ika}\left(e^{ika}-e^{-ika}\right)-\frac{1}{2}\left(e^{ika}+e^{-ika}\right)\right)^2 \\
&= 2D_c\bar{c}a^2\left(2\pi\delta\left(\omega-\omega'\right)\right)\int_{-\infty}^\infty dk\frac{1}{\left(Dk^2\right)^2+\omega^2} \\
&\quad\cdot\left(e^{2ika}\left(1+\frac{i}{ka}\right)^2+e^{-2ika}\left(1-\frac{i}{ka}\right)^2+2\frac{1+k^2a^2}{k^2a^2}\right).
\end{aligned} \tag{A.25}$$

Note that the integrand in Eq. A.25 has four poles at $k=\sqrt{\frac{|\omega|}{D_c}}e^{i\theta}$ for $\theta\in\left[\frac{\pi}{4},\frac{3\pi}{4},\frac{5\pi}{4},\frac{7\pi}{4}\right]$. These poles can be used to solve the integral via contour integration. Let C_1 be a counter-clockwise path around the infinite half circle enclosing the upper half plane and C_2 be a clockwise path around the infinite half circle enclosing the

lower half plane. This split allows for terms of the form e^{ika} to be integrated around C_1 and terms of the form e^{-ika} to be integrated around C_2 without any divergences. Additionally, this split will cause poles to form at $k = 0$, but since the integrand in Eq. A.25 has no poles at $k = 0$ all subsequent $k = 0$ poles must cancel and thus need not be taken into account. With these contours, the residue theorem can be used to produce

$$\left\langle \tilde{\delta n}^{\,*}\left(\omega'\right)\tilde{\delta n}\left(\omega\right)\right\rangle = \frac{2\bar{c}a^2}{D_c}\left(2\pi\delta\left(\omega-\omega'\right)\right)$$
$$\cdot\left(\int_{C_1} dk \frac{e^{2ika}\left(1+\frac{i}{ka}\right)^2 + 2\frac{1+k^2a^2}{k^2a^2}}{\left(k-\sqrt{\frac{|\omega|}{D_c}}e^{i\frac{\pi}{4}}\right)\left(k-\sqrt{\frac{|\omega|}{D_c}}e^{i\frac{3\pi}{4}}\right)\left(k-\sqrt{\frac{|\omega|}{D_c}}e^{i\frac{5\pi}{4}}\right)\left(k-\sqrt{\frac{|\omega|}{D_c}}e^{i\frac{7\pi}{4}}\right)}\right.$$
$$\left.+\int_{C_2} dk \frac{e^{-2ika}\left(1-\frac{i}{ka}\right)^2}{\left(k-\sqrt{\frac{|\omega|}{D_c}}e^{i\frac{\pi}{4}}\right)\left(k-\sqrt{\frac{|\omega|}{D_c}}e^{i\frac{3\pi}{4}}\right)\left(k-\sqrt{\frac{|\omega|}{D_c}}e^{i\frac{5\pi}{4}}\right)\left(k-\sqrt{\frac{|\omega|}{D_c}}e^{i\frac{7\pi}{4}}\right)}\right)$$

$$= \frac{4\pi\bar{c}a^2 i}{D_c}\left(2\pi\delta\left(\omega-\omega'\right)\right)\left(\left.\frac{e^{2ika}\left(1+\frac{i}{ka}\right)^2+2\frac{1+k^2a^2}{k^2a^2}}{\left(k-\sqrt{\frac{|\omega|}{D_c}}e^{i\frac{3\pi}{4}}\right)\left(k-\sqrt{\frac{|\omega|}{D_c}}e^{i\frac{5\pi}{4}}\right)\left(k-\sqrt{\frac{|\omega|}{D_c}}e^{i\frac{7\pi}{4}}\right)}\right|_{k=\sqrt{\frac{|\omega|}{D_c}}e^{i\frac{\pi}{4}}}\right.$$

$$+\left.\frac{e^{2ika}\left(1+\frac{i}{ka}\right)^2+2\frac{1+k^2a^2}{k^2a^2}}{\left(k-\sqrt{\frac{|\omega|}{D_c}}e^{i\frac{\pi}{4}}\right)\left(k-\sqrt{\frac{|\omega|}{D_c}}e^{i\frac{5\pi}{4}}\right)\left(k-\sqrt{\frac{|\omega|}{D_c}}e^{i\frac{7\pi}{4}}\right)}\right|_{k=\sqrt{\frac{|\omega|}{D_c}}e^{i\frac{3\pi}{4}}}$$

$$-\left.\frac{e^{-2ika}\left(1-\frac{i}{ka}\right)^2}{\left(k-\sqrt{\frac{|\omega|}{D_c}}e^{i\frac{\pi}{4}}\right)\left(k-\sqrt{\frac{|\omega|}{D_c}}e^{i\frac{3\pi}{4}}\right)\left(k-\sqrt{\frac{|\omega|}{D_c}}e^{i\frac{7\pi}{4}}\right)}\right|_{k=\sqrt{\frac{|\omega|}{D_c}}e^{i\frac{5\pi}{4}}}$$

$$-\left.\frac{e^{-2ika}\left(1-\frac{i}{ka}\right)^2}{\left(k-\sqrt{\frac{|\omega|}{D_c}}e^{i\frac{\pi}{4}}\right)\left(k-\sqrt{\frac{|\omega|}{D_c}}e^{i\frac{3\pi}{4}}\right)\left(k-\sqrt{\frac{|\omega|}{D_c}}e^{i\frac{5\pi}{4}}\right)}\right|_{k=\sqrt{\frac{|\omega|}{D_c}}e^{i\frac{7\pi}{4}}}\right). \tag{A.26}$$

After some algebraic manipulation of Eq. A.26, the final form of the power spectrum of $n\left(t\right)$ is found to be

$$\left\langle \tilde{\delta n}^{*}\left(\omega'\right)\tilde{\delta n}\left(\omega\right)\right\rangle = \left(2\pi\delta\left(\omega-\omega'\right)\right)\frac{16\pi\bar{c}a^5}{15D_c}f\left(a\sqrt{\frac{2|\omega|}{D_c}}\right), \tag{A.27}$$

where

$$f(x) \equiv \frac{15}{x^5}\left(e^{-x}\cos\left(x\right)\left(\frac{x^2}{2}+2x+1\right)+\left(1+e^{-x}\sin\left(x\right)\right)\left(\frac{x^2}{2}-1\right)\right). \tag{A.28}$$

This allows the power spectrum of $n\left(t\right)$ to be written as

$$S_n\left(\omega\right) = \int\frac{d\omega'}{2\pi}\left\langle \tilde{\delta n}^{*}\left(\omega'\right)\tilde{\delta n}\left(\omega\right)\right\rangle = \frac{16\pi\bar{c}a^5}{15D_c}f\left(a\sqrt{\frac{2|\omega|}{D_c}}\right), \tag{A.29}$$

and the subsequent correlation function as

$$C_n(t) = \int \frac{d\omega}{2\pi} S_n(\omega) e^{-i\omega t} = \frac{8\bar{c}a^5}{15D_c} \int d\omega f\left(a\sqrt{\frac{2|w|}{D_c}}\right) e^{-i\omega t}$$
$$= \frac{8\bar{c}a^5}{15D_c} \int_0^\infty d\omega \left(f\left(a\sqrt{\frac{2\omega}{D_c}}\right) e^{-i\omega t} + f\left(a\sqrt{\frac{2\omega}{D_c}}\right) e^{i\omega t} \right)$$
$$= \frac{16\bar{c}a^5}{15D_c} \int_0^\infty d\omega f\left(a\sqrt{\frac{2\omega}{D_c}}\right) \cos(\omega t). \tag{A.30}$$

Let $x \equiv a\sqrt{\frac{2\omega}{D_c}}$. This transforms Eq. A.30 into

$$C_n(t) = \frac{16\bar{c}a^3}{15} \int_0^\infty dx x f(x) \cos\left(x^2 \frac{D_c t}{2a^2}\right). \tag{A.31}$$

While the integral in Eq. A.31 is not explicitly doable, several of its most important properties can be determined. For one, the instantaneous variance, $C_n(0)$, can be exactly calculated to be

$$\sigma_n^2 = C_n(0) = \frac{16\bar{c}a^3}{15} \int_0^\infty dx x f(x) = \frac{16\bar{c}a^3}{15} \frac{5\pi}{4} = \frac{4}{3}\pi a^3 \bar{c} = \bar{n}. \tag{A.32}$$

Thus, the instantaneous variance is seen to be equal to the mean, exactly as expected. Additionally, the time averaged correlation function can be obtained by utilizing Eq. 3.10. This exactly yields the result first derived by Berg and Purcell:

$$\frac{\delta^2 n_T}{\langle n \rangle^2} = \frac{C_{n,T}(0)}{\langle n \rangle^2} \approx \frac{S_n(0)}{\langle n \rangle^2 T} = \frac{1}{T} \left(\frac{4}{3}\pi a^3 \bar{c}\right)^{-2} \lim_{\omega \to 0} \frac{16\pi \bar{c} a^5}{15 D_c} f\left(a\sqrt{\frac{2|\omega|}{D_c}}\right)$$
$$= \frac{3}{5} \frac{1}{\pi a \bar{c} D_c T} \tag{A.33}$$

B. CALCULATIONS FOR RECEPTOR BINDING AND UNBINDING

We begin wth multiple cells all modelled as spheres of radius a in contact with each other. The cells exist within a ligand bath of density profile $c(\vec{x},t)$ assumed to fluctuate around a spatially constant mean profile ($\bar{c}(\vec{x})=\bar{c}$). The ligand molecules diffuse with diffusion constant D_c and can bind and unbind to receptors on the surface of each cell at rates α and μ respectively.

Assume that each cell can be treated as a point particle with respect to the ligand field and that the number of receptors on each cell is large enough to neglect the effects of increased bound receptor number on the overall binding propensity (i.e. receptor saturation). This system can thus be modeled via

$$\frac{dc}{dt}=D_c\nabla^2 c-\sum_j \delta^3\left(\vec{x}-\vec{x}_j\right)\frac{dr_j}{dt}+\eta_c \tag{B.1a}$$

$$\frac{dr_j}{dt}=\alpha c\left(\vec{x}_j,t\right)-\mu r_j+\eta_{rj} \tag{B.1b}$$

where η_c is the noise intrinsic to the diffusion of ligand molecules and η_{rj} is the noise intrinsic to the bound receptor number of the jth celll. The purpose of this section is to calculate the statistics of the ligand and bound receptor number of a particular cell based off of this model.

We begin by determining the noise properties of the ligand diffusion and receptor binding-unbinding process. Let $c(\vec{x},t)=\bar{c}+\delta c(\vec{x},t)$ and $r_j(t)=\bar{r}_j+\delta r_j(t)$, where $\bar{r}_j$ is the mean value of $r_j(t)$. Eq. B.1b then dictates

$$0=\alpha\bar{c}-\mu\bar{r}_j \implies \bar{r}_j=\frac{\alpha\bar{c}}{\mu}, \tag{B.2}$$

while Eqs. B.1a and B.1b can be written in the form

$$\frac{d\delta c}{dt}=D_c\nabla^2\delta c-\sum_j \delta^3\left(\vec{x}-\vec{x}_j\right)\frac{d\delta r_j}{dt}+\eta_c \tag{B.3a}$$

$$\frac{d\delta r_j}{dt} = \alpha\delta c\left(\vec{x}_j, t\right) - \mu\delta r_j + \eta_{rj}. \tag{B.3b}$$

Fourier transforming Eq. B.3a then yields

$$\begin{aligned} -i\omega\tilde{\delta c} &= -D_c k^2\tilde{\delta c} - \sum_j e^{i\vec{k}\cdot\vec{x}_j}\left(-i\omega\tilde{\delta r}_j\right) + \tilde{\eta}_c \\ \implies \tilde{\delta c} &= \frac{i\omega\sum_j \tilde{\delta r}_j e^{i\vec{k}\cdot\vec{x}_j} + \tilde{\eta}_c}{D_c k^2 - i\omega}. \end{aligned} \tag{B.4}$$

Similarly Fourier transforming Eq. B.3b then yields

$$\begin{aligned} -i\omega\tilde{\delta r}_j &= \alpha\int\frac{d^3k}{(2\pi)^3}\tilde{\delta c}\left(\vec{k},\omega\right)e^{-i\vec{k}\cdot\vec{x}_j} - \mu\tilde{\delta r}_j + \tilde{\eta}_{rj} \\ &= \alpha\int\frac{d^3k}{(2\pi)^3}\frac{i\omega\sum_l \tilde{\delta r}_l e^{i\vec{k}\cdot\vec{x}_l} + \tilde{\eta}_c}{D_c k^2 - i\omega}e^{-i\vec{k}\cdot\vec{x}_j} - \mu\tilde{\delta r}_j + \tilde{\eta}_{rj} \\ \implies (\mu - i\omega)\,\tilde{\delta r}_j - i\omega\sum_l \tilde{\delta r}_l\Sigma\left(\vec{x}_l - \vec{x}_j,\omega\right) &= \alpha\int\frac{d^3k}{(2\pi)^3}\frac{\tilde{\eta}_c}{D_c k^2 - i\omega}e^{-i\vec{k}\cdot\vec{x}_j} + \tilde{\eta}_{rj}, \end{aligned} \tag{B.5}$$

where

$$\Sigma\left(\vec{x},\omega\right) \equiv \alpha\int\frac{d^3k}{(2\pi)^3}\frac{1}{D_c k^2 - i\omega}e^{i\vec{k}\cdot\vec{x}} = \frac{\alpha}{4\pi D_c|\vec{x}|}e^{-|\vec{x}|\sqrt{\frac{\omega}{2D_c}}}e^{i|\vec{x}|\sqrt{\frac{\omega}{2D_c}}}. \tag{B.6}$$

Thus, it is seen that $\Sigma\left(\vec{x},\omega\right)$ is dependent only on the magnitude of $\vec{x}$, implying $\Sigma\left(-\vec{x},\omega\right) = \Sigma\left(\vec{x},\omega\right)$.

Unfortunately, $\Sigma\left(\vec{x},\omega\right)$ diverges as $\vec{x} \to 0$. This case can be rectified by truncating the range of integration in Eq. B.6 to be inside of a sphere, S, in k space with radius

$\frac{2\pi}{ga}$, where a is the cell radius and g is a geometric factor. This lets $\Sigma(0,\omega)$ to be evaluated as

$$\begin{aligned}\Sigma(0,\omega) &\approx \alpha \int_S \frac{d^3k}{(2\pi)^3}\frac{1}{D_c k^2 - i\omega} \\ &= \frac{\alpha}{\pi g a D_c}\left(1 + \frac{ga}{8\pi}\sqrt{\frac{\omega}{2D_c}}\left(\log\left(\frac{4D_c\pi^2 + \omega g^2 a^2 - 2\pi ga\sqrt{2\omega D_c}}{4D_c\pi^2 + \omega g^2 a^2 + 2\pi ga\sqrt{2\omega D_c}}\right)\right.\right. \\ &\quad \left.\left. -2\arctan\left(\frac{2\pi ga\sqrt{2\omega D_c}}{\omega g^2 a^2 - 4D_c\pi^2}\right)\right)\right) + \frac{i\alpha}{2\pi\omega}\left(\frac{|\omega|}{2D_c}\right)^{\frac{3}{2}} \\ &\approx \frac{\alpha}{\pi g a D_c} + \frac{i\alpha}{2\pi\omega}\left(\frac{|\omega|}{2D_c}\right)^{\frac{3}{2}}, \end{aligned} \tag{B.7}$$

where the final approximation was made assuming $\omega a^2 \ll D_c$. This is equivalent to the assumption $T \gg \tau_1 = a^2/D_c$, i.e. that over a time T the ligand can easily diffuse around the whole cell.

Now, let R be a matrix defined as:

$$R_{jl}(\omega) \equiv \begin{cases} \mu - i\omega\left(1 + \Sigma(0,\omega)\right) & j = l \\ -i\omega\Sigma\left(\vec{x}_j - \vec{x}_l, \omega\right) & j \neq l \end{cases}. \tag{B.8}$$

Since $\Sigma\left(\vec{x}_j - \vec{x}_l, \omega\right) = \Sigma\left(\vec{x}_l - \vec{x}_j, \omega\right)$, R is seen to be a symmetric matrix. With this, Eq. B.5 can be rewritten as

$$\begin{aligned}\sum_l R_{jl}(\omega)\,\tilde{\delta r}_l &= \alpha \int \frac{d^3k}{(2\pi)^3}\frac{\tilde{\eta}_c}{D_c k^2 - i\omega}e^{-i\vec{k}\cdot\vec{x}_j} + \tilde{\eta}_{rj} \\ \implies \tilde{\delta r}_j &= \sum_l R^{-1}_{jl}(\omega)\left(\alpha\int\frac{d^3k}{(2\pi)^3}\frac{\tilde{\eta}_c}{D_c k^2 - i\omega}e^{-i\vec{k}\cdot\vec{x}_l} + \tilde{\eta}_{rl}\right). \end{aligned} \tag{B.9}$$

Utilizing Eq. B.9 yields the cross spectrum of $r_j(t)$ and $r_l(r)$ to be

$$\begin{aligned}\left\langle \tilde{\delta r}^*_l\left(\omega'\right)\tilde{\delta r}_j(\omega)\right\rangle &= \left\langle\left(\sum_u R^{-1}_{lu}\left(\omega'\right)\left(\alpha\int\frac{d^3k'}{(2\pi)^3}\frac{\tilde{\eta}_c\left(\vec{k}',\omega'\right)}{D_c k'^2 - i\omega'}e^{-i\vec{k}'\cdot\vec{x}_n} + \tilde{\eta}_{ru}\left(\omega'\right)\right)\right)^*\right. \\ &\quad \left.\cdot\left(\sum_s R^{-1}_{js}(\omega)\left(\alpha\int\frac{d^3k}{(2\pi)^3}\frac{\tilde{\eta}_c\left(\vec{k},\omega\right)}{D_c k^2 - i\omega}e^{-i\vec{k}\cdot\vec{x}_m} + \tilde{\eta}_{rs}(\omega)\right)\right)\right\rangle. \end{aligned} \tag{B.10}$$

At this point it is necessary to determine the properties of η_{rj} since the power spectrum of η_c is already known from Appendix A. For η_{rj}, since the binding-unbinding process for a given cell is independent of the binding-unbinding process of any other cell and the ligand diffusion, it must be true that cross correlations between η_{rj} and η_{rl}, for $j \neq l$, or η_c vanish. Additionally, since Eq. B.3b is of the form of a birth-death process, the power spectrum of η_{rj} must be the sum of the mean propensities of its reactions. These all imply

$$\begin{aligned}\left\langle \tilde{\eta}_{rl}^{*}\left(\omega'\right), \tilde{\eta}_{rj}\left(\omega\right)\right\rangle &= \left(\alpha\bar{c} + \mu\bar{r}_j\right)\delta_{jl}\left(2\pi\delta\left(\omega-\omega'\right)\right) \\ &= 2\alpha\bar{c}\delta_{jl}\left(2\pi\delta\left(\omega-\omega'\right)\right), \end{aligned} \tag{B.11}$$

as in the main text. Ignoring the vanishing cross terms between $\tilde{\eta}_c$ and $\tilde{\eta}_{rj}$ allows Eq. B.10 to be written in the form

$$\begin{aligned}\left\langle \tilde{\delta r}_l^{*}\left(\omega'\right)\tilde{\delta r}_j\left(\omega\right)\right\rangle = \sum_{s,u} R_{js}^{-1}\left(\omega\right)\left(R_{lu}^{-1}\left(\omega'\right)\right)^{*}\Bigg(&\left\langle \tilde{\eta}_{ru}^{*}\left(\omega'\right), \tilde{\eta}_{rs}\left(\omega\right)\right\rangle \\ &+\alpha^2\int\frac{d^3k d^3k'}{\left(2\pi\right)^6}\frac{\left\langle \tilde{\eta}_c^{*}\left(\vec{k}',\omega'\right), \tilde{\eta}_c\left(\vec{k},\omega\right)\right\rangle}{\left(D_c k^2 - i\omega\right)\left(D_c k'^2 + i\omega'\right)}e^{i\left(\vec{k}'\cdot\vec{x}_u - \vec{k}\cdot\vec{x}_s\right)}\Bigg).\end{aligned} \tag{B.12}$$

Utilizing Eqs. A.14 and B.11 to evaluate the noise correlation terms then yields

$$\begin{aligned}\left\langle \tilde{\delta r}_l^{*}\left(\omega'\right)\tilde{\delta r}_j\left(\omega\right)\right\rangle &= \sum_{s,u} R_{js}^{-1}\left(\omega\right)\left(R_{lu}^{-1}\left(\omega'\right)\right)^{*}\Bigg(2\alpha\bar{c}\delta_{su}\left(2\pi\delta\left(\omega-\omega'\right)\right) \\ &\quad +\alpha^2\int\frac{d^3k d^3k'}{\left(2\pi\right)^6}\frac{2D_c\bar{c}k^2\left(2\pi\delta\left(\omega-\omega'\right)\right)\left(\left(2\pi\right)^3\delta^3\left(\vec{k}-\vec{k}'\right)\right)}{\left(D_c k^2 - i\omega\right)\left(D_c k'^2 + i\omega'\right)}e^{i\left(\vec{k}'\cdot\vec{x}_u - \vec{k}\cdot\vec{x}_s\right)}\Bigg) \\ &= 2\alpha\bar{c}\left(2\pi\delta\left(\omega-\omega'\right)\right)\sum_{s,u} R_{js}^{-1}\left(\omega\right)\left(R_{lu}^{-1}\left(\omega\right)\right)^{*} \\ &\quad\cdot\left(\delta_{su} + \alpha\int\frac{d^3k}{\left(2\pi\right)^3}\frac{D_c k^2}{\left(D_c k^2\right)^2 + \omega^2}e^{i\vec{k}\cdot\left(\vec{x}_u - \vec{x}_s\right)}\right),\end{aligned} \tag{B.13}$$

where all instances of ω' outside of the δ function were freely replaced with ω due to the δ function being a global factor.

Utilizing Eq. A.23 shows that the angular portion of the integral in Eq. B.13 will cause the imaginary component to vanish. Thus, the integral is completely real and may be expressed as the real part of $\Sigma\left(\vec{x}_u - \vec{x}_s, \omega\right)$

$$\begin{aligned}&\left\langle \tilde{\delta r}_l^{\,*}\left(\omega'\right)\tilde{\delta r}_j\left(\omega\right)\right\rangle \\ &\quad = 2\alpha\bar{c}\left(2\pi\delta\left(\omega-\omega'\right)\right)\sum_{s,u} R_{js}^{-1}\left(\omega\right)\left(R_{lu}^{-1}\left(\omega\right)\right)^{*}\left(\delta_{su}+\mathrm{Re}\left(\Sigma\left(\vec{x}_u-\vec{x}_s,\omega\right)\right)\right).\end{aligned} \tag{B.14}$$

Comparing the last term in Eq. B.14 with Eq. B.8 then allows Eq. B.14 to be written as

$$\left\langle \tilde{\delta r}_l^{\,*}\left(\omega'\right)\tilde{\delta r}_j\left(\omega\right)\right\rangle = 2\alpha\bar{c}\left(2\pi\delta\left(\omega-\omega'\right)\right)\sum_{s,u} R_{js}^{-1}\left(\omega\right)\left(R_{lu}^{-1}\left(\omega\right)\right)^{*}\left(\frac{1}{\omega}\mathrm{Im}\left(\left(R_{us}\left(\omega\right)\right)^{*}\right)\right). \tag{B.15}$$

In order to simplify Eq. B.15, first let a and b be two arbitrary complex numbers. The product $a\mathrm{Im}\left(b\right)$ can be reordered as

$$\begin{aligned}a\mathrm{Im}\left(b\right) &= \mathrm{Re}\left(a\right)\mathrm{Im}\left(b\right)+i\mathrm{Im}\left(a\right)\mathrm{Im}\left(b\right)\\ &= \left(\mathrm{Re}\left(a\right)\mathrm{Im}\left(b\right)+\mathrm{Im}\left(a\right)\mathrm{Re}\left(b\right)\right)-\mathrm{Im}\left(a\right)\left(\mathrm{Re}\left(b\right)-i\mathrm{Im}\left(b\right)\right)\\ &= \mathrm{Im}\left(ab\right)-b^{*}\mathrm{Im}\left(a\right)=\mathrm{Im}\left(ab\right)+b^{*}\mathrm{Im}\left(a^{*}\right).\end{aligned} \tag{B.16}$$

Applying Eq. B.16 to the $\left(R_{lu}^{-1}\left(\omega\right)\right)^{*}\mathrm{Im}\left(\left(R_{us}\left(\omega\right)\right)^{*}\right)$ term in Eq. B.15 yields

$$\begin{aligned}\left\langle \tilde{\delta r}_l^{\,*}\left(\omega'\right)\tilde{\delta r}_j\left(\omega\right)\right\rangle = \frac{2\alpha\bar{c}}{\omega}&\left(2\pi\delta\left(\omega-\omega'\right)\right)\sum_{s,u} R_{js}^{-1}\left(\omega\right)\\ &\cdot\left(\mathrm{Im}\left(\left(R_{lu}^{-1}\left(\omega\right)\right)^{*}\left(R_{us}\left(\omega\right)\right)^{*}\right)+R_{us}\left(\omega\right)\mathrm{Im}\left(R_{lu}^{-1}\left(\omega\right)\right)\right).\end{aligned} \tag{B.17}$$

Separating out the sums then yields

$$\left\langle \tilde{\delta r}_l^{\,*}\left(\omega'\right)\tilde{\delta r}_j\left(\omega\right)\right\rangle = \frac{2\alpha\bar{c}}{\omega}\left(2\pi\delta\left(\omega-\omega'\right)\right)\left(\sum_s R_{js}^{-1}\left(\omega\right)\sum_u \mathrm{Im}\left(\left(R_{lu}^{-1}\left(\omega\right)R_{us}\left(\omega\right)\right)^*\right)\right.$$
$$\left.+\sum_u \mathrm{Im}\left(R_{lu}^{-1}\left(\omega\right)\right)\sum_s R_{js}^{-1}\left(\omega\right)R_{us}\left(\omega\right)\right). \tag{B.18}$$

In the first term of Eq. B.18 the summation over u can be brought inside the Im and complex conjugation operators and causes the product $R_{lu}^{-1}\left(\omega\right)R_{us}\left(\omega\right)$ to collapse to δ_{ls}. However, since the Kronecker δ function is real, its imaginary component must be 0, and thus the whole first term vanishes. In the second term, the fact that R is symmetric can be used to make the substitutions $R_{lu}^{-1}\left(\omega\right)\rightarrow R_{ul}^{-1}\left(\omega\right)$ and $R_{us}\left(\omega\right)\rightarrow R_{su}\left(\omega\right)$, which causes Eq. B.18 to simplify to

$$\begin{aligned}\left\langle \tilde{\delta r}_l^{\,*}\left(\omega'\right)\tilde{\delta r}_j\left(\omega\right)\right\rangle &= \frac{2\alpha\bar{c}}{\omega}\left(2\pi\delta\left(\omega-\omega'\right)\right)\sum_u \mathrm{Im}\left(R_{ul}^{-1}\left(\omega\right)\right)\sum_s R_{js}^{-1}\left(\omega\right)R_{su}\left(\omega\right)\\ &= \frac{2\alpha\bar{c}}{\omega}\left(2\pi\delta\left(\omega-\omega'\right)\right)\sum_u \mathrm{Im}\left(R_{ul}^{-1}\left(\omega\right)\right)\delta_{ju}\\ &= \frac{2\alpha\bar{c}}{\omega}\left(2\pi\delta\left(\omega-\omega'\right)\right)\mathrm{Im}\left(R_{jl}^{-1}\left(\omega\right)\right).\end{aligned} \tag{B.19}$$

Thus, Eq. B.19 can be seen to be formed from the imaginary component of the matrix element used to connect $\tilde{\delta r}_j$ to the noise terms, exactly as would be predicted by the fluctuation-dissipation theorem.

Under the limit $\mu \gg \omega\left(1+\Sigma\left(0,\omega\right)\right)$, which is equivalent to $\omega \ll \left(\mu^{-1}+\left(k_D K_D\right)^{-1}\right)^{-1}$ for $k_D = \pi g a D_c$ and $K_D = \frac{\mu}{\alpha}$ as in the text, R_{jl}^{-1} can be easily approximated. Let A_{jl} be a matrix equivalent to R with the jth row and lth column removed such that $(-1)^{j+l}\det\left(A_{jl}\right) = C_{jl}$, where C is the cofactor matrix of R. Under this definition,

$$R_{jl}^{-1}\left(\omega\right) = (-1)^{j+l}\frac{\det\left(A_{lj}\right)}{\det\left(R\right)}. \tag{B.20}$$

By the rules of determinants, any term within the determinant of R that has off-diagonal elements must have at least 2 off-diagonal elements. Since all the off-diagonal terms of R are of the form $-i\omega\Sigma\left(\vec{x},\omega\right)$ and $\Sigma\left(\vec{x},\omega\right)$ does not diverge as $\omega\rightarrow 0$, each of these terms must have a factor of ω that is of order 2 or higher. Thus, in the small

ω limit, only the diagonal elements of R contribute to its determinant. For $j \neq l$, the creation of A_{jl} will cause two of the diagonal elements of R to be removed and $|j-l|-1$ more to be shifted to off-diagonal elements. This will in turn cause every term in the determinant of A_{jl} to have at least one factor of the form $-i\omega\Sigma\left(\vec{x},\omega\right)$. However, only the term with all $N-2$ remaining factors of $\mu - i\omega\left(1+\Sigma\left(0,\omega\right)\right)$, where N is the number of cells, will have an order of ω less than 2 and will thus be the only nonnegligible term. This term will also carry a prefactor of $(-1)^{|j-l|-1}$ by the rules of determinants. With this, R_{jl}^{-1} takes the form

$$\begin{aligned} R_{jl}^{-1}\left(\omega\right) &\approx (-1)^{j+l+|j-l|-1}\frac{-i\omega\Sigma\left(\vec{x}_j-\vec{x}_l,\omega\right)\left(\mu-i\omega\left(1+\Sigma\left(0,\omega\right)\right)\right)^{N-2}}{\left(\mu-i\omega\left(1+\Sigma\left(0,\omega\right)\right)\right)^{N}} \\ &= \frac{i\omega\Sigma\left(\vec{x}_j-\vec{x}_l,\omega\right)}{\left(\mu-i\omega\left(1+\Sigma\left(0,\omega\right)\right)\right)^{2}}. \end{aligned} \tag{B.21}$$

Thus, R_{jl}^{-1} is seen to carry a dependence on the separation between the two cells. For $j=l$, A_{jj} is a symmetric matrix, and just like R, all of its off-diagonal components are of the form $-i\omega\Sigma\left(\vec{x},\omega\right)$. By the same argument as that used for the determinant of R, only the diagonal terms contribute to the determinant of A_{jj}. This lets $R_{jj}^{-1}\left(\omega\right)$ to be approximated as

$$R_{jj}^{-1}\left(\omega\right) \approx (-1)^{2j}\frac{\left(\mu-i\omega\left(1+\Sigma\left(0,\omega\right)\right)\right)^{N-1}}{\left(\mu-i\omega\left(1+\Sigma\left(0,\omega\right)\right)\right)^{N}} = \frac{1}{\mu-i\omega\left(1+\Sigma\left(0,\omega\right)\right)}, \tag{B.22}$$

which is identical to R^{-1} for the $N=1$ cell case. Thus, for long time averaging the presence of other cells does not affect any individual cell's power spectrum at the level of bound receptors.

This single cell power spectrum can be computed as

$$\begin{aligned} \left\langle \tilde{\delta r}^{\,*}\left(\omega'\right)\tilde{\delta r}\left(\omega\right)\right\rangle &= \frac{2\alpha\bar{c}}{\omega}\left(2\pi\delta\left(\omega-\omega'\right)\right)\mathrm{Im}\left(\left(\mu-i\omega\left(1+\Sigma\left(0,\omega\right)\right)\right)^{-1}\right) \\ &= \frac{2\alpha\bar{c}}{\omega}\left(2\pi\delta\left(\omega-\omega'\right)\right)\frac{\omega\left(1+\mathrm{Re}\left(\Sigma\left(0,\omega\right)\right)\right)}{\left(\mu+\omega\mathrm{Im}\left(\Sigma\left(0,\omega\right)\right)\right)^{2}+\omega^{2}\left(1+\mathrm{Re}\left(\Sigma\left(0,\omega\right)\right)\right)^{2}} \end{aligned} \tag{B.23}$$

$$\implies S_r(\omega) = \int \frac{d\omega'}{2\pi} \left\langle \tilde{\delta r}^*(\omega') \, \tilde{\delta r}(\omega) \right\rangle$$
$$= \frac{2\alpha\bar{c}\left(1 + \mathrm{Re}\left(\Sigma(0,\omega)\right)\right)}{\left(\mu + \omega \mathrm{Im}\left(\Sigma(0,\omega)\right)\right)^2 + \omega^2\left(1 + \mathrm{Re}\left(\Sigma(0,\omega)\right)\right)^2}. \tag{B.24}$$

To obtain the time averaged noise-to-signal ratio, Eq. 3.10 can be utilized assuming $T \gg \tau_2 = \mu^{-1} + (k_D K_D)^{-1}$ as was done for ω eariler. With this, the time averaged noise-to-signal ratio in the single cell case can be approximated to be

$$\frac{C_{r_T}(0)}{\bar{r}^2} \approx \frac{S_r(0)}{\bar{r}^2 T} = \frac{1}{\bar{r}^2 T} \frac{2\alpha\bar{c}\left(1 + \mathrm{Re}\left(\Sigma(0,0)\right)\right)}{\mu^2}. \tag{B.25}$$

Utilizing Eqs. B.2 and B.7 as well as setting $g = 4$ as explained in the text, Eq. B.25 simplifies to

$$\frac{(\delta r)^2}{\bar{r}^2} = \frac{C_{r_T}(0)}{\bar{r}^2} \approx \frac{1}{\bar{r}^2 T} \frac{2\alpha\bar{c}\left(1 + \frac{\alpha}{4\pi a D_c}\right)}{\mu^2} = \frac{1}{\pi a D_c T} \frac{\alpha^2\bar{c}}{2\mu^2\bar{r}^2} + \frac{2}{T}\frac{\alpha\bar{c}}{\mu^2\bar{r}^2}$$
$$= \frac{1}{2}\frac{1}{\pi a \bar{c} D_c T} + \frac{2}{\mu\bar{r}T}. \tag{B.26}$$

Eq. B.26 can be seen to be the sum of the noise the receptors inherit from the ligand diffusion, the $\frac{1}{2}\frac{1}{\pi a\bar{c}D_cT}$ term, and the noise inherent in the ligand binding-unbinding process itself, the $\frac{2}{\mu\bar{r}T}$ term.

C. CALCULATIONS FOR JUXTACRINE SIGNALING MODEL

We now add to the model that each cell produces a messenger molecule species, m_j, at rate β proportional to that cell's number of bound receptors, r_j. This species degrades at rate ν and can also be exchanged between neighboring cells at rate γ. Let $\mathcal{N}_j$ be the set of cells neighboring the jth cell. The dynamics of m_j can be modeled via

$$\frac{dm_j}{dt} = \beta r_j - \nu m_j + \sum_{l \in \mathcal{N}_j} \gamma \left(m_l - m_j \right) + \eta_{mj}, \tag{C.1}$$

where η_{mj} is the noise intrinsic to the creation, degredation, and exchange of m molecules in the jth cell. As before, let $m_j(t) = \bar{m}_j + \delta m_j(t)$, where $\bar{m}_j$ is the mean value of $m_j(t)$. Eq. C.1 then dictates

$$0 = \beta \bar{r}_j - \nu \bar{m}_j + \sum_{l \in \mathcal{N}_j} \gamma \left(\bar{m}_l - \bar{m}_j \right). \tag{C.2}$$

Assuming the binding and unbinding as well as the production and degredation parameters are the same in each cell, Eq. B.2 forces $\bar{r}_j = \bar{r}_l$ for all j and l, which by Eq. C.2 then forces

$$\bar{m}_j = \bar{m}_l = \frac{\beta}{\nu} \bar{r}_j \tag{C.3}$$

for all j and l. Additionally, Eq. C.1 also dictates

$$\frac{d\delta m_j}{dt} = \beta \delta r_j - \nu \delta m_j + \sum_{l \in \mathcal{N}_j} \gamma \left(\delta m_l - \delta m_j \right) + \eta_{mj}, \tag{C.4}$$

which can be Fourier transformed into

$$-i\omega \tilde{\delta m}_j = \beta \tilde{\delta r}_j - \nu \tilde{\delta m}_j + \sum_{l \in \mathcal{N}_j} \gamma \left(\tilde{\delta m}_l - \tilde{\delta m}_j \right) + \tilde{\eta}_{mj}. \tag{C.5}$$

Let N_j be the number of cells neighboring the jth cell and the matrix M be defined as

$$M_{jl}(\omega) = \begin{cases} \nu + N_j\gamma - i\omega & j = l \\ -\gamma & l \in \mathcal{N}_j \\ 0 & \text{otherwise} \end{cases} . \tag{C.6}$$

Thus, M is seen to be a symmetric matrix. The form of M also dictates that when ω is taken to be a small parameter later, it must meet the requirement $\omega \ll \nu + \gamma$ as those are the variables ω is seen to be compared to in M. This notation allows Eq. C.5 to be written as

$$\sum_l M_{jl}(\omega)\,\delta\tilde{m}_l = \beta\delta\tilde{r}_j + \tilde{\eta}_{mj} \implies \delta\tilde{m}_j = \sum_l M^{-1}_{jl}(\omega)\left(\beta\delta\tilde{r}_l + \tilde{\eta}_{ml}\right) \tag{C.7}$$

Utilizing Eq. C.7 yields the cross spectrum of $m_j(t)$ and $m_l(t)$ to be

$$\left\langle \delta\tilde{m}^*_l(\omega')\,\delta\tilde{m}_j(\omega)\right\rangle = \left\langle \left(\sum_u M^{-1}_{lu}(\omega')\left(\beta\delta\tilde{r}_u(\omega') + \tilde{\eta}_{mu}(\omega')\right)\right)^* \cdot \left(\sum_s M^{-1}_{js}(\omega)\left(\beta\delta\tilde{r}_s(\omega) + \tilde{\eta}_{ms}(\omega)\right)\right)\right\rangle . \tag{C.8}$$

At this point it is necessary to determine the properties of η_{mj}. Just as for η_{rj}, Eq. C.1 is in the form of a birth-death process, which allows the power spectrum of η_{mj} to simply be written as the sum of the mean propensities. However, due to the exchange term, η_{mj} and η_{ml} cannot be independent if $l \in \mathcal{N}_j$. The cross spectrum, in this case, must be negative due to the fact that exchange means one cell is losing m molecules when the other is gaining them and must also be the sum of propensities of the exchange reaction. Thus, the power spectrum of η_{mj} takes the form

$$\left\langle \tilde{\eta}^*_{ml}(\omega')\,\tilde{\eta}_{mj}(\omega)\right\rangle = \left(\beta\bar{r}_j + \nu\bar{m}_j + \sum_{s\in\mathcal{N}_j}\gamma\left(\bar{m}_s + \bar{m}_j\right)\right)\delta_{jl}\left(2\pi\delta\left(\omega - \omega'\right)\right) - \gamma\left(\bar{m}_l + \bar{m}_j\right)\delta_{l\in\mathcal{N}_j}\left(2\pi\delta\left(\omega - \omega'\right)\right), \tag{C.9}$$

which is the Fourier transform of the η_{mj} correlator in the main text. Utilizing Eqs. C.3 and C.6 allows Eq. C.9 to be simplified to

$$\left\langle \tilde{\eta}^*_{ml}(\omega')\,\tilde{\eta}_{mj}(\omega)\right\rangle = 2\bar{m}\mathrm{Re}\left(M_{jl}(\omega)\right)\left(2\pi\delta\left(\omega - \omega'\right)\right) \tag{C.10}$$

Since the ligand binding-unbinding process is independent of the noise in the m molecule production, any cross terms between δr_j and η_{ml} must vanish. This allows Eq. C.8 to be written as

$$\begin{aligned}
&\left\langle \delta\tilde{m}_l^* \left(\omega'\right) \delta\tilde{m}_j \left(\omega\right) \right\rangle \\
&= \sum_{s,u} M_{js}^{-1} \left(\omega\right) \left(M_{lu}^{-1} \left(\omega'\right)\right)^* \left(\beta^2 \left\langle \delta\tilde{r}_u^* \left(\omega'\right) \delta\tilde{r}_s \left(\omega\right) \right\rangle + \left\langle \tilde{\eta}_{ms}^* \left(\omega'\right) \tilde{\eta}_{mu} \left(\omega\right) \right\rangle \right) \\
&= 2 \left(2\pi\delta \left(\omega - \omega'\right)\right) \sum_{s,u} M_{js}^{-1} \left(\omega\right) \left(M_{lu}^{-1} \left(\omega\right)\right)^* \\
&\quad \cdot \left(\beta^2 \frac{\alpha\bar{c}}{\omega} \mathrm{Im} \left(R_{su}^{-1} \left(\omega\right)\right) + \bar{m} \mathrm{Re} \left(\left(M_{su} \left(\omega\right)\right)^*\right)\right),
\end{aligned} \tag{C.11}$$

where Eq. B.18 has been used, $\mathrm{Re}\left(M_{su}\left(\omega\right)\right)$ from Eq. C.10 has been freely changed to $\mathrm{Re}\left(\left(M_{su}\left(\omega\right)\right)^*\right)$, and all instances of ω' outside the δ function were freely replaced with ω due to the δ function being a global factor.

In order to simplify Eq. C.11, first let a and b be two arbitrary complex numbers. The product $a\mathrm{Re}\left(b\right)$ can be reordered as

$$\begin{aligned}
a\mathrm{Re}\left(b\right) &= \mathrm{Re}\left(a\right)\mathrm{Re}\left(b\right) + i\mathrm{Im}\left(a\right)\mathrm{Re}\left(b\right) \\
&= \left(\mathrm{Re}\left(a\right)\mathrm{Re}\left(b\right) - \mathrm{Im}\left(a\right)\mathrm{Im}\left(b\right)\right) + \mathrm{Im}\left(a\right)\left(\mathrm{Im}\left(b\right) + i\mathrm{Re}\left(b\right)\right) \\
&= \mathrm{Re}\left(ab\right) + ib^*\mathrm{Im}\left(a\right) = \mathrm{Re}\left(ab\right) - ib^*\mathrm{Im}\left(a^*\right)
\end{aligned} \tag{C.12}$$

Temporarily ignorning the R_{su}^{-1} term and applying Eq. C.12 to the $\left(M_{lu}^{-1}\left(\omega\right)\right)^* \mathrm{Re}\left(\left(M_{su}\left(\omega\right)\right)^*\right)$ term in Eq. C.11 yields

$$\begin{aligned}
&\sum_{s,u} M_{js}^{-1} \left(\omega\right) \left(M_{lu}^{-1} \left(\omega\right)\right)^* \mathrm{Re}\left(\left(M_{su} \left(\omega\right)\right)^*\right) \\
&\quad = \sum_{s,u} M_{js}^{-1} \left(\omega\right) \left(\mathrm{Re}\left(\left(M_{lu}^{-1} \left(\omega\right) M_{su} \left(\omega\right)\right)^*\right) - iM_{su} \left(\omega\right) \mathrm{Im}\left(M_{lu}^{-1} \left(\omega\right)\right)\right).
\end{aligned} \tag{C.13}$$

Separating out the sums and freely changing $\mathrm{Re}\left(\left(M_{lu}^{-1}(\omega)\,M_{su}(\omega)\right)^*\right)$ to $\mathrm{Re}\left(M_{lu}^{-1}(\omega)\,M_{su}(\omega)\right)$ then yields

$$\sum_{s,u} M_{js}^{-1}(\omega)\left(M_{lu}^{-1}(\omega)\right)^* \mathrm{Re}\left(\left(M_{su}(\omega)\right)^*\right)$$
$$= \sum_{s} M_{js}^{-1}(\omega) \sum_{u} \mathrm{Re}\left(M_{lu}^{-1}(\omega)\,M_{su}(\omega)\right) - i\sum_{u} \mathrm{Im}\left(M_{lu}^{-1}(\omega)\right) \sum_{s} M_{js}^{-1}(\omega)\,M_{su}(\omega)\,. \tag{C.14}$$

Since M is symmetric, $M_{su}(\omega)$ in the first term can be freely changed to $M_{us}(\omega)$. This implies that when the summation over u is brought inside the Re operator, $M_{lu}^{-1}(\omega)\,M_{su}(\omega)$ will collapse to δ_{ls}, which has no imaginary part. Thus, the entire summation simplifies to δ_{ls}. Similarly, the summation over s in the second term will collapse into δ_{ju}. These along with once again using the symmetry of M to freely change $M_{lu}^{-1}(\omega)$ to $M_{ul}^{-1}(\omega)$ in the second term then yields

$$\sum_{s,u} M_{js}^{-1}(\omega)\left(M_{lu}^{-1}(\omega)\right)^* \mathrm{Re}\left(\left(M_{su}(\omega)\right)^*\right) = \sum_{s} M_{js}^{-1}(\omega)\,\delta_{ls} - i\sum_{u} \mathrm{Im}\left(M_{ul}^{-1}(\omega)\right)\delta_{ju}$$
$$= M_{jl}^{-1}(\omega) - i\mathrm{Im}\left(M_{jl}^{-1}(\omega)\right) = \mathrm{Re}\left(M_{jl}^{-1}(\omega)\right). \tag{C.15}$$

Applying Eq. C.15 to Eq. C.11 then yields

$$\left\langle \tilde{\delta m}_l^*(\omega')\,\tilde{\delta m}_j(\omega)\right\rangle$$
$$= 2\left(2\pi\delta\left(\omega-\omega'\right)\right)\left(\bar{m}\mathrm{Re}\left(M_{jl}^{-1}(\omega)\right) + \frac{\alpha\beta^2\bar{c}}{\omega}\sum_{s,u} M_{js}^{-1}(\omega)\left(M_{lu}^{-1}(\omega)\right)^* \mathrm{Im}\left(R_{su}^{-1}(\omega)\right)\right). \tag{C.16}$$

This allows the power spectrum of m_j to take the form

$$S_m(\omega) = \int \frac{d\omega'}{2\pi}\left\langle \tilde{\delta m}_j^*(\omega')\,\tilde{\delta m}_j(\omega)\right\rangle$$
$$= 2\bar{m}\mathrm{Re}\left(M_{jj}^{-1}(\omega)\right) + \frac{2\alpha\beta^2\bar{c}}{\omega}\sum_{s,u} M_{js}^{-1}(\omega)\left(M_{ju}^{-1}(\omega)\right)^* \mathrm{Im}\left(R_{su}^{-1}(\omega)\right), \tag{C.17}$$

which by Eq. 3.10 yields a noise-to-signal ratio of

$$\begin{aligned}\frac{(\delta m)^2}{\bar{m}^2} &= \frac{C_{m,T}(0)}{\bar{m}^2} \approx \frac{S_m(0)}{\bar{m}^2 T} \\ &= \frac{2}{\bar{m}T}\mathrm{Re}\left(M_{jj}^{-1}(0)\right) + \frac{2\alpha\nu^2\bar{c}}{\bar{r}^2 T}\lim_{\omega\to 0}\sum_{s,u} M_{js}^{-1}(\omega)\left(M_{ju}^{-1}(\omega)\right)^* \frac{1}{\omega}\mathrm{Im}\left(R_{su}^{-1}(\omega)\right) \\ &= \frac{2}{\bar{m}T}\mathrm{Re}\left(M_{jj}^{-1}(0)\right) + \frac{2\nu^2}{\mu\bar{r}T}\sum_{s,u} M_{js}^{-1}(0)\left(M_{ju}^{-1}(0)\right)^*\left(\delta_{su} + \mathrm{Re}\left(\Sigma\left(\vec{x}_s - \vec{x}_u, 0\right)\right)\right),\end{aligned} \tag{C.18}$$

where Eqs. B.2 and C.3 were used to alter the form of the prefactor in the second term and Eqs. B.21 and B.22 were used to evaluated the $\omega \to 0$ limit. Eq. C.18 is the general expression for the error in the case of juxtacrine signaling and, when only the extrinsic term proportional to $\mathrm{Re}\left(\Sigma\left(\vec{x}_s - \vec{x}_u, 0\right)\right)$ is considered, is utilized in calculating the phase boundaries in Fig. 3 of the main text.

From here, a few properties of M can be used to simplify Eq. C.18 in particular limits of γ or N. First, for $\gamma \ll \nu$, $M(0)$ approximately becomes νI_N, where I_N is the identity matrix of rank N. This makes inverting M trivial and reduces Eq. C.18 to

$$\begin{aligned}\frac{(\delta m)^2}{\bar{m}^2} &= \frac{2}{\nu\bar{m}T} + \frac{2\nu^2}{\mu\bar{r}T}\sum_{s,u}\frac{1}{\nu^2}\delta_{js}\delta_{ju}\left(\delta_{su} + \mathrm{Re}\left(\Sigma\left(\vec{x}_s - \vec{x}_u, 0\right)\right)\right) \\ &= \frac{1}{\nu\bar{m}T} + \frac{2}{\mu\bar{r}T}\left(1 + \mathrm{Re}\left(\Sigma(0,0)\right)\right) \\ &= \frac{1}{2}\frac{1}{\pi a\bar{c}D_c T} + \frac{2}{\mu\bar{r}T} + \frac{1}{\nu\bar{m}T},\end{aligned} \tag{C.19}$$

as seen in Eq. 4 of the main text. Since setting $\gamma \ll \nu$ is equivalent to eliminating any communication between cells and the extrinsic noises from the ligand diffusion and binding and unbinding process are unaffected by the presence of other cells as determined in the previous section, the cell is effectively sensing no effects from the presence of any other cell. Thus, this result must also be valid for a single isolated cell.

Second, for $\gamma \gg \nu$ the cells are effectively communicating at infinite speed. Physically, this implies that every cell in the cluster communicates with every other

cell equally, which mathematically translates to the dictation that M_{jl}^{-1} must be independent of j and l. Let $\vec{X}$ be a column vector with unit entries. By Eq. C.6 it is easy to see that

$$M\vec{X} = (\nu - i\omega)\,\vec{X}. \tag{C.20}$$

Thus, $\vec{X}$ is an eigenvector of M, which in turn implies it must also be an eigenvector of M^{-1} satisfying

$$M^{-1}\vec{X} = (\nu - i\omega)^{-1}\,\vec{X}. \tag{C.21}$$

Since M_{jl}^{-1} must be independent of j and l, the only way Eq. C.21 can be true is if

$$\lim_{\gamma\to\infty} M_{jl}^{-1} = \frac{1}{N\,(\nu - i\omega)}. \tag{C.22}$$

This allows Eq. C.18 to reduce to

$$\begin{aligned}\frac{(\delta m)^2}{\bar{m}^2} &= \frac{2}{\nu\bar{m}TN} + \frac{2\nu^2}{\mu\bar{r}T}\sum_{s,u}\frac{1}{N^2\nu^2}\left(\delta_{su} + \mathrm{Re}\left(\Sigma\left(\vec{x}_s - \vec{x}_u, 0\right)\right)\right) \\ &= \frac{2}{\nu\bar{m}TN} + \frac{2}{\mu\bar{r}TN^2}\left(N + \sum_{s,u}\mathrm{Re}\left(\Sigma\left(\vec{x}_s - \vec{x}_u, 0\right)\right)\right)\end{aligned} \tag{C.23}$$

Once again, when only the extrinsic term proportional to $\mathrm{Re}\left(\Sigma\left(\vec{x}_s - \vec{x}_u, 0\right)\right)$ is considered, Eq. C.23 is utilized in calculating the data depicted in Fig. 2 of the main text.

Finally, Eq. C.18 can be easily represented under no assumptions about γ but for the limiting case of $N = 2$ cells. When the cells are adjacent to each other, M and M^{-1} take the form

$$M = \begin{bmatrix} \nu + \gamma - i\omega & -\gamma \\ -\gamma & \nu + \gamma - i\omega \end{bmatrix} \tag{C.24a}$$

$$M^{-1} = \frac{1}{(\nu - i\omega)\,(\nu - i\omega + 2\gamma)}\begin{bmatrix} \nu + \gamma - i\omega & \gamma \\ \gamma & \nu + \gamma - i\omega \end{bmatrix}. \tag{C.24b}$$

Let $\vec{\ell} = \vec{x}_1 - \vec{x}_2$. With these and Eqs. B.21 and B.22, Eq. C.18 can be calculated to yield

$$\begin{aligned}
\frac{(\delta m)^2}{\bar{m}^2} &= \frac{2}{\bar{m}T}\mathrm{Re}\left(M_{11}^{-1}(0)\right) + \frac{2\nu^2}{\mu\bar{r}T}\sum_{s,u} M_{js}^{-1}(0)\left(M_{lu}^{-1}(0)\right)^*\left(\delta_{su} + \mathrm{Re}\left(\Sigma\left(\vec{x}_s - \vec{x}_u, 0\right)\right)\right) \\
&= \frac{2}{\bar{m}T}\frac{\nu+\gamma}{\nu(\nu+2\gamma)} + \frac{2\nu^2}{\mu\bar{r}T}\left(2\frac{\nu+\gamma}{\nu(\nu+2\gamma)}\frac{\gamma}{\nu(\nu+2\gamma)}\mathrm{Re}\left(\Sigma\left(\vec{\ell},0\right)\right)\right. \\
&\quad \left. + \left(\left(\frac{\nu+\gamma}{\nu(\nu+2\gamma)}\right)^2 + \left(\frac{\gamma}{\nu(\nu+2\gamma)}\right)^2\right)\left(1 + \mathrm{Re}\left(\Sigma(0,0)\right)\right)\right) \\
&= \frac{1}{\pi a\bar{c}D_c T}\frac{\nu^2+3\nu\gamma+3\gamma^2}{2(\nu+2\gamma)^2} + \frac{1}{\mu\bar{r}T}\frac{2\left(\nu^2+2\nu\gamma+2\gamma^2\right)}{(\nu+2\gamma)^2} + \frac{1}{\nu\bar{m}T}\frac{2(\nu+\gamma)}{\nu+2\gamma},
\end{aligned} \tag{C.25}$$

where $\left|\vec{\ell}\right|$ has been set to be exactly $2a$ to reflect the necessity of the cells to be adjacent to each other in order to exchange m molecules. Eq. C.25 can be seen to be easily separable into the three distinct terms which reflect the noise inherited from the ligand diffusion, binding-unbinding process, and m birth-death and exchange processes. Of important note is that under the $\gamma \ll \nu$ limit Eq. C.25 reduces to Eq. B.26 plus the term $\frac{2}{\nu\bar{m}T}$. Conversely, under the $\gamma \gg \nu$ limit (which is equivalent to $\lambda = 2a\sqrt{\frac{\gamma}{\nu}} \gg a$) the second fraction of each term go to $\frac{3}{8}$, 1, and 1 respectively. The first term, which is the extrinsic noise, is reproduced in Eq. 4.20 of the main text.

D. CALCULATIONS FOR AUTOCRINE SIGNALING MODEL

We here assume that the cells produce a messenger molecule with the same production and degradation rate as in the previous section, but instead of being exchanged between neighboring cells they are secreted into the environment and diffuse with a diffusion constant of D_ρ. The purpose of this section is to calculate the statistics of the long-time average of the number of messenger molecules within the volume of a particular cell.

This system can be modeled via

$$\frac{dc}{dt} = D_c \nabla^2 c - \sum_j \delta^3 \left(\vec{x} - \vec{x}_j\right) \frac{dr_j}{dt} + \eta_c \tag{D.1a}$$

$$\frac{dr_j}{dt} = \alpha c \left(\vec{x}_j, t\right) - \mu r_j + \eta_{rj} \tag{D.1b}$$

$$\frac{d\rho}{dt} = D_\rho \nabla^2 \rho - \nu\rho + \sum_j \delta^3 \left(\vec{x} - \vec{x}_j\right) \left(\beta r_j + \eta_{pj}\right) + \eta_d, \tag{D.1c}$$

where $\rho\left(\vec{x}, t\right)$ is the density field of the diffusing messenger molecule and η_{pj} and η_d are the production from the jth cell, and the degradation and diffusive noise terms, respectively, as in the main text. Again, let $\rho\left(\vec{x}, t\right) = \bar{\rho}\left(\vec{x}\right) + \delta\rho\left(\vec{x}, t\right)$, where $\bar{\rho}\left(\vec{x}\right)$ is the mean value of $\rho\left(\vec{x}, t\right)$ as a function of space. Since ρ is being produced at each cell and allowed to diffuse, $\bar{\rho}\left(\vec{x}\right)$ cannot be constant in space and by Eq. D.1c must obey

$$0 = D_\rho \nabla^2 \bar{\rho} - \nu\bar{\rho} + \sum_j \delta^3 \left(\vec{x} - \vec{x}_j\right) \beta \bar{r}_j, \tag{D.2}$$

which is solved by

$$\bar{\rho}\left(\vec{x}\right) = \frac{1}{4\pi D_\rho} \sum_j \frac{\beta \bar{r}_j}{\left|\vec{x} - \vec{x}_j\right|} e^{-\left|\vec{x} - \vec{x}_j\right| \sqrt{\frac{\nu}{D_\rho}}}, \tag{D.3}$$

as in Eq. 8 of the main text. Additionally, Eq. D.1c also dictates

$$\frac{d\delta\rho}{dt} = D_\rho \nabla^2 \delta\rho - \nu\delta\rho + \sum_j \delta^3\left(\vec{x} - \vec{x}_j\right)\left(\beta\delta r_j + \eta_{pj}\right) + \eta_d, \tag{D.4}$$

which can be Fourier transformed into

$$\begin{aligned} -i\omega\tilde{\delta\rho} &= -D_\rho k^2 \tilde{\delta\rho} - \nu\tilde{\delta\rho} + \sum_j e^{i\vec{k}\cdot\left(\vec{x}-\vec{x}_j\right)}\left(\beta\tilde{\delta r}_j + \tilde{\eta}_{pj}\right) + \tilde{\eta}_d \\ \implies \tilde{\delta\rho} &= \frac{\sum_j e^{i\vec{k}\cdot\vec{x}_j}\left(\beta\tilde{\delta r}_j + \tilde{\eta}_{pj}\right) + \tilde{\eta}_d}{\nu + D_\rho k^2 - i\omega}. \end{aligned} \tag{D.5}$$

Since the noise in each r_j is independent of the noise in the production and degradation/diffusion of ρ, and the production and diffusion noises must be independent of each other, the cross spectrum of $\rho\left(\vec{x},t\right)$ can be written as

$$\begin{aligned} \left\langle \tilde{\delta\rho}^*\left(\vec{k}',\omega'\right)\tilde{\delta\rho}\left(\vec{k},\omega\right)\right\rangle &= \left\langle \left(\frac{\sum_l e^{i\vec{k}'\cdot\vec{x}_l}\left(\beta\tilde{\delta r}_l\left(\omega'\right) + \tilde{\eta}_{pl}\left(\omega'\right)\right) + \tilde{\eta}_d\left(\vec{k}',\omega'\right)}{\nu + D_\rho k'^2 - i\omega'}\right)^* \right. \\ &\left. \cdot \left(\frac{\sum_j e^{i\vec{k}\cdot\vec{x}_j}\left(\beta\tilde{\delta r}_j\left(\omega\right) + \tilde{\eta}_{pj}\left(\omega\right)\right) + \tilde{\eta}_d\left(\vec{k},\omega\right)}{\nu + D_\rho k^2 - i\omega}\right)\right\rangle \\ &= \frac{\sum_{j,l} e^{i\left(\vec{k}\cdot\vec{x}_j - \vec{k}'\cdot\vec{x}_l\right)}\left(\beta^2\left\langle\tilde{\delta r}_l^{\,*}\left(\omega'\right)\tilde{\delta r}_j\left(\omega\right)\right\rangle + \left\langle\tilde{\eta}_{pl}^*\left(\omega'\right)\tilde{\eta}_{pj}\left(\omega\right)\right\rangle\right) + \left\langle\tilde{\eta}_d^*\left(\vec{k}',\omega'\right)\tilde{\eta}_d\left(\vec{k},\omega\right)\right\rangle}{\left(\nu + D_\rho k^2 - i\omega\right)\left(\nu + D_\rho k'^2 + i\omega'\right)}. \end{aligned} \tag{D.6}$$

From here the spectra of both η_{pj} and η_d are needed. Since η_d is also a diffusive noise term, it must follow the same formalism used in Eq. A.9. However, unlike c, ρ can degrade, meaning a degradation term must be added to the noise. This yields

$$\left\langle \eta_d\left(\vec{x}',t'\right)\eta_d\left(\vec{x},t\right)\right\rangle = 2D_\rho\delta\left(t-t'\right)\vec{\nabla}_x\cdot\vec{\nabla}_{x'}\left(\bar{\rho}\left(\vec{x}\right)\delta^3\left(\vec{x}-\vec{x}'\right)\right) + \nu\bar{\rho}\left(\vec{x}\right)\delta\left(t-t'\right)\delta^3\left(\vec{x}-\vec{x}'\right), \tag{D.7}$$

as in the mian text. Eq. D.7 can then be Fourier transformed to yield

$$\begin{aligned} \left\langle \tilde{\eta}_d^*\left(\vec{k}',\omega'\right)\tilde{\eta}_d\left(\vec{k},\omega\right)\right\rangle &= \int d^3x d^3x' dt dt' \left\langle \eta_d\left(\vec{x}',t'\right)\eta_d\left(\vec{x},t\right)\right\rangle\left(e^{i\vec{k}\cdot\vec{x}}e^{i\omega t}\right)\left(e^{i\vec{k}'\cdot\vec{x}'}e^{i\omega' t'}\right)^* \\ &= 2D_\rho\int d^3x d^3x' dt dt' e^{i\left(\vec{k}\cdot\vec{x}-\vec{k}'\cdot\vec{x}'\right)}e^{i\left(\omega t-\omega' t'\right)}\delta\left(t-t'\right)\vec{\nabla}_x\cdot\vec{\nabla}_{x'}\left(\bar{\rho}\left(\vec{x}\right)\delta^3\left(\vec{x}-\vec{x}'\right)\right) \\ &\quad + \nu\int d^3x d^3x' dt dt' e^{i\left(\vec{k}\cdot\vec{x}-\vec{k}'\cdot\vec{x}'\right)}e^{i\left(\omega t-\omega' t'\right)}\bar{\rho}\left(\vec{x}\right)\delta\left(t-t'\right)\delta^3\left(\vec{x}-\vec{x}'\right). \end{aligned} \tag{D.8}$$

The δ function makes the t' integrals trivial, which leaves the only time dependent term in the integrands as $e^{it\left(\omega-\omega'\right)}$. Eq. A.11 can then be used to solve the t integral and transform $\delta^3\left(\vec{x}-\vec{x}'\right)$ into an integral form in the first integral. In the second integral, the δ^3 function makes the x' integral trivial. Combining these with Eq. D.3 allows Eq. D.8 to be written as

$$\begin{aligned}\left\langle \tilde{\eta}_d^*\left(\vec{k}',\omega'\right)\tilde{\eta}_d\left(\vec{k},\omega\right)\right\rangle &= \frac{1}{2\pi}\left(2\pi\delta\left(\omega-\omega'\right)\right)\int d^3x d^3x' e^{i\left(\vec{k}\cdot\vec{x}-\vec{k}'\cdot\vec{x}'\right)} \\ &\cdot\vec{\nabla}_x\cdot\vec{\nabla}_{x'}\left(\left(\sum_j \frac{\beta\bar{r}_j}{\left|\vec{x}-\vec{x}_j\right|}e^{-\left|\vec{x}-\vec{x}_j\right|\sqrt{\frac{\nu}{D_\rho}}}\right)\left(\int\frac{d^3\kappa}{\left(2\pi\right)^3}e^{i\vec{\kappa}\cdot\left(\vec{x}-\vec{x}'\right)}\right)\right) \\ &+\frac{\nu}{4\pi D_\rho}\left(2\pi\delta\left(\omega-\omega'\right)\right)\int d^3x e^{i\vec{x}\cdot\left(\vec{k}-\vec{k}'\right)}\sum_j\frac{\beta\bar{r}_j}{\left|\vec{x}-\vec{x}_j\right|}e^{-\left|\vec{x}-\vec{x}_j\right|\sqrt{\frac{\nu}{D_\rho}}}. \end{aligned} \tag{D.9}$$

Focusing on the first integral, moving the κ integral outside the gradient operators before applying them then yields

$$\begin{aligned}\left\langle \tilde{\eta}_d^*\left(\vec{k}',\omega'\right)\tilde{\eta}_d\left(\vec{k},\omega\right)\right\rangle &= \frac{1}{\left(2\pi\right)^4}\left(2\pi\delta\left(\omega-\omega'\right)\right)\int d^3x d^3x' d^3\kappa e^{i\left(\vec{k}\cdot\vec{x}-\vec{k}'\cdot\vec{x}'\right)}\left(-i\vec{\kappa}\right) \\ &\cdot\left(i\vec{\kappa}e^{i\vec{\kappa}\cdot\left(\vec{x}-\vec{x}'\right)}\sum_j\frac{\beta\bar{r}_j}{\left|\vec{x}-\vec{x}_j\right|}e^{-\left|\vec{x}-\vec{x}_j\right|\sqrt{\frac{\nu}{D_\rho}}}+e^{i\vec{\kappa}\cdot\left(\vec{x}-\vec{x}'\right)}\sum_j\vec{\nabla}_x\frac{\beta\bar{r}_j}{\left|\vec{x}-\vec{x}_j\right|}e^{-\left|\vec{x}-\vec{x}_j\right|\sqrt{\frac{\nu}{D_\rho}}}\right) \\ &+\frac{\nu}{4\pi D_\rho}\left(2\pi\delta\left(\omega-\omega'\right)\right)\int d^3x e^{i\vec{x}\cdot\left(\vec{k}-\vec{k}'\right)}\sum_j\frac{\beta\bar{r}_j}{\left|\vec{x}-\vec{x}_j\right|}e^{-\left|\vec{x}-\vec{x}_j\right|\sqrt{\frac{\nu}{D_\rho}}} \\ &=\frac{1}{\left(2\pi\right)^4}\left(2\pi\delta\left(\omega-\omega'\right)\right)\int d^3x d^3x' d^3\kappa e^{i\vec{x}\cdot\left(\vec{k}+\vec{\kappa}\right)}e^{-i\vec{x}'\cdot\left(\vec{k}'+\vec{\kappa}\right)} \\ &\cdot\sum_j\left(\kappa^2\frac{\beta\bar{r}_j}{\left|\vec{x}-\vec{x}_j\right|}e^{-\left|\vec{x}-\vec{x}_j\right|\sqrt{\frac{\nu}{D_\rho}}}-i\vec{\kappa}\cdot\vec{\nabla}_x\frac{\beta\bar{r}_j}{\left|\vec{x}-\vec{x}_j\right|}e^{-\left|\vec{x}-\vec{x}_j\right|\sqrt{\frac{\nu}{D_\rho}}}\right) \\ &+\frac{\nu}{4\pi D_\rho}\left(2\pi\delta\left(\omega-\omega'\right)\right)\int d^3x e^{i\vec{x}\cdot\left(\vec{k}-\vec{k}'\right)}\sum_j\frac{\beta\bar{r}_j}{\left|\vec{x}-\vec{x}_j\right|}e^{-\left|\vec{x}-\vec{x}_j\right|\sqrt{\frac{\nu}{D_\rho}}}. \end{aligned} \tag{D.10}$$

Since x' only appears in the term $e^{-i\vec{x}'\cdot\left(\vec{k}'+\vec{\kappa}\right)}$, Eq. A.11 can again be used to solve the x' integral, which will then make the κ integral trivial due to the resultant δ function. This causes Eq. D.10 to simplify to

$$\begin{aligned}
\left\langle \tilde{\eta}_d^*\left(\vec{k}',\omega'\right)\tilde{\eta}_d\left(\vec{k},\omega\right)\right\rangle &= \frac{1}{2\pi}\left(2\pi\delta\left(\omega-\omega'\right)\right)\int d^3x d^3\kappa e^{i\vec{x}\cdot\left(\vec{k}+\vec{\kappa}\right)}\delta^3\left(\vec{k}'+\vec{\kappa}\right)\\
&\quad\cdot\sum_j\left(\kappa^2\frac{\beta\bar{r}_j}{\left|\vec{x}-\vec{x}_j\right|}e^{-\left|\vec{x}-\vec{x}_j\right|\sqrt{\frac{\nu}{D_\rho}}}-i\vec{\kappa}\cdot\vec{\nabla}_x\frac{\beta\bar{r}_j}{\left|\vec{x}-\vec{x}_j\right|}e^{-\left|\vec{x}-\vec{x}_j\right|\sqrt{\frac{\nu}{D_\rho}}}\right)\\
&\quad+\frac{\nu}{4\pi D_\rho}\left(2\pi\delta\left(\omega-\omega'\right)\right)\int d^3x e^{i\vec{x}\cdot\left(\vec{k}-\vec{k}'\right)}\sum_j\frac{\beta\bar{r}_j}{\left|\vec{x}-\vec{x}_j\right|}e^{-\left|\vec{x}-\vec{x}_j\right|\sqrt{\frac{\nu}{D_\rho}}}\\
&= \frac{1}{2\pi}\left(2\pi\delta\left(\omega-\omega'\right)\right)\int d^3x e^{i\vec{x}\cdot\left(\vec{k}-\vec{k}'\right)}\\
&\quad\cdot\sum_j\beta\bar{r}_j\left(k'^2\frac{1}{\left|\vec{x}-\vec{x}_j\right|}e^{-\left|\vec{x}-\vec{x}_j\right|\sqrt{\frac{\nu}{D_\rho}}}+i\vec{k}'\cdot\vec{\nabla}_x\frac{1}{\left|\vec{x}-\vec{x}_j\right|}e^{-\left|\vec{x}-\vec{x}_j\right|\sqrt{\frac{\nu}{D_\rho}}}\right)\\
&\quad+\frac{\nu}{4\pi D_\rho}\left(2\pi\delta\left(\omega-\omega'\right)\right)\int d^3x e^{i\vec{x}\cdot\left(\vec{k}-\vec{k}'\right)}\sum_j\frac{\beta\bar{r}_j}{\left|\vec{x}-\vec{x}_j\right|}e^{-\left|\vec{x}-\vec{x}_j\right|\sqrt{\frac{\nu}{D_\rho}}}. \qquad \text{(D.11)}
\end{aligned}$$

Let $\vec{v}_j=\vec{x}-\vec{x}_j$ in both integrals. Since the x integral is over all of x-space, this transformation does not change the limits of integration. Additionally, $d^3x=d^3v_j$ and $\vec{\nabla}_x=\vec{\nabla}_{v_j}$ due to x and v_j being related by a simple translation. Utilizing this and moving the summations in Eq. D.11 outside the integrals allows it to be written as

$$\begin{aligned}
\left\langle \tilde{\eta}_d^*\left(\vec{k}',\omega'\right)\tilde{\eta}_d\left(\vec{k},\omega\right)\right\rangle &= \frac{1}{2\pi}\left(2\pi\delta\left(\omega-\omega'\right)\right)\sum_j\beta\bar{r}_j e^{i\vec{x}_j\cdot\left(\vec{k}-\vec{k}'\right)}\int d^3v_j e^{i\vec{v}_j\cdot\left(\vec{k}-\vec{k}'\right)}\\
&\quad\cdot\left(k'^2\frac{1}{v_j}e^{-v_j\sqrt{\frac{\nu}{D_\rho}}}+i\vec{k}'\cdot\vec{\nabla}_{v_j}\frac{1}{v_j}e^{-v_j\sqrt{\frac{\nu}{D_\rho}}}\right)\\
&\quad+\frac{\nu}{4\pi D_\rho}\left(2\pi\delta\left(\omega-\omega'\right)\right)\sum_j\beta\bar{r}_j e^{i\vec{x}_j\cdot\left(\vec{k}-\vec{k}'\right)}\int d^3v_j\frac{1}{v_j}e^{-v_j\sqrt{\frac{\nu}{D_\rho}}}e^{i\vec{v}_j\cdot\left(\vec{k}-\vec{k}'\right)}. \qquad \text{(D.12)}
\end{aligned}$$

Since $\frac{1}{\left|\vec{v}_j\right|}e^{-\left|\vec{v}_j\right|\sqrt{\frac{\nu}{D_\rho}}}$ goes to 0 exponentially as $\left|\vec{v}_j\right|\to\infty$, the second term in the first integral of Eq. D.12 can be integrated by parts with the net result of simply adding

a factor of -1 and moving the gradient to apply to $e^{i\vec{v}_j\cdot\left(\vec{k}-\vec{k}'\right)}$. This causes Eq. D.12 to simplify to

$$\begin{aligned}\left\langle \tilde{\eta}_d^*\left(\vec{k}',\omega'\right)\tilde{\eta}_d\left(\vec{k},\omega\right)\right\rangle &= \frac{1}{2\pi}\left(2\pi\delta\left(\omega-\omega'\right)\right)\sum_j \beta\bar{r}_j e^{i\vec{x}_j\cdot\left(\vec{k}-\vec{k}'\right)} \\ &\cdot\int d^3v_j \frac{1}{v_j}e^{-v_j\sqrt{\frac{\nu}{D_\rho}}}\left(k'^2 e^{i\vec{v}_j\cdot\left(\vec{k}-\vec{k}'\right)} - i\vec{k}'\cdot\vec{\nabla}_{v_j}e^{i\vec{v}_j\cdot\left(\vec{k}-\vec{k}'\right)}\right) \\ &+\frac{\nu}{4\pi D_\rho}\left(2\pi\delta\left(\omega-\omega'\right)\right)\sum_j \beta\bar{r}_j e^{i\vec{x}_j\cdot\left(\vec{k}-\vec{k}'\right)}\int d^3v_j\frac{1}{v_j}e^{-v_j\sqrt{\frac{\nu}{D_\rho}}}e^{i\vec{v}_j\cdot\left(\vec{k}-\vec{k}'\right)} \\ &= \frac{1}{2\pi}\left(2\pi\delta\left(\omega-\omega'\right)\right)\sum_j \beta\bar{r}_j e^{i\vec{x}_j\cdot\left(\vec{k}-\vec{k}'\right)}\int d^3v_j\frac{\vec{k}\cdot\vec{k}'}{v_j}e^{-v_j\sqrt{\frac{\nu}{D_\rho}}}e^{i\vec{v}_j\cdot\left(\vec{k}-\vec{k}'\right)} \\ &+\frac{\nu}{4\pi D_\rho}\left(2\pi\delta\left(\omega-\omega'\right)\right)\sum_j \beta\bar{r}_j e^{i\vec{x}_j\cdot\left(\vec{k}-\vec{k}'\right)}\int d^3v_j\frac{1}{v_j}e^{-v_j\sqrt{\frac{\nu}{D_\rho}}}e^{i\vec{v}_j\cdot\left(\vec{k}-\vec{k}'\right)}. \quad \text{(D.13)}\end{aligned}$$

The integrals in Eq. D.13 can be solved via the known Fourier transformation

$$\int d^3z\frac{1}{z}e^{-zl}e^{i\vec{z}\cdot\vec{\kappa}} = \frac{4\pi}{l^2+\kappa^2}. \quad \text{(D.14)}$$

Letting $\vec{z}=\vec{v}_j$, $l=\sqrt{\frac{\nu}{D_\rho}}$ and $\vec{\kappa}=\vec{k}-\vec{k}'$, substituting Eq. D.14 into Eq. D.13 yields

$$\left\langle \tilde{\eta}_d^*\left(\vec{k}',\omega'\right)\tilde{\eta}_d\left(\vec{k},\omega\right)\right\rangle = \left(2\pi\delta\left(\omega-\omega'\right)\right)\frac{2D_\rho\vec{k}\cdot\vec{k}'+\nu}{\nu+D_\rho\left|\vec{k}-\vec{k}'\right|^2}\sum_j\beta\bar{r}_j e^{i\vec{x}_j\cdot\left(\vec{k}-\vec{k}'\right)}. \quad \text{(D.15)}$$

Returning to η_{pj}, since each cell produces ρ independently of each other cell, the production noises must be independent. Additionally, since the production is a birth only process, its power spectrum must simply be the mean propensity of the production, which in turn yields

$$\left\langle \tilde{\eta}_{pl}^*\left(\omega'\right)\tilde{\eta}_{pj}\left(\omega\right)\right\rangle = \beta\bar{r}_j\delta_{jl}\left(2\pi\delta\left(\omega-\omega'\right)\right), \quad \text{(D.16)}$$

as in the main text. Substituting Eqs. B.18, D.15, and D.16 into Eq. D.6 then yields

$$\left\langle \tilde{\delta\rho}^{*}\left(\vec{k}',\omega'\right)\tilde{\delta\rho}\left(\vec{k},\omega\right)\right\rangle = \frac{2\pi\delta\left(\omega-\omega'\right)}{\left(\nu+D_{\rho}k^{2}-i\omega\right)\left(\nu+D_{\rho}k'^{2}+i\omega'\right)}$$
$$\cdot\left(\sum_{j,l}e^{i\left(\vec{k}\cdot\vec{x}_{j}-\vec{k}'\cdot\vec{x}_{l}\right)}\left(\beta^{2}\frac{2\alpha\bar{c}}{\omega}\mathrm{Im}\left(R_{jl}^{-1}\left(\omega\right)\right)+\beta\bar{r}_{j}\delta_{jl}\right)+\frac{2D_{\rho}\vec{k}\cdot\vec{k}'+\nu}{\nu+D_{\rho}\left|\vec{k}-\vec{k}'\right|^{2}}\sum_{j}\beta\bar{r}_{j}e^{i\vec{x}_{j}\cdot\left(\vec{k}-\vec{k}'\right)}\right)$$
$$=\frac{2\pi\delta\left(\omega-\omega'\right)}{\left(\nu+D_{\rho}k^{2}-i\omega\right)\left(\nu+D_{\rho}k'^{2}+i\omega\right)}\left(\sum_{j,l}\frac{2\alpha\beta^{2}\bar{c}}{\omega}e^{i\left(\vec{k}\cdot\vec{x}_{j}-\vec{k}'\cdot\vec{x}_{l}\right)}\mathrm{Im}\left(R_{jl}^{-1}\left(\omega\right)\right)\right.$$
$$\left.+\left(1+\frac{2D_{\rho}\vec{k}\cdot\vec{k}'+\nu}{\nu+D_{\rho}\left|\vec{k}-\vec{k}'\right|^{2}}\right)\sum_{j}\beta\bar{r}_{j}e^{i\vec{x}_{j}\cdot\left(\vec{k}-\vec{k}'\right)}\right), \tag{D.17}$$

where all instances of ω' outside the δ function have been freely replaced with ω due to the δ function being a global factor.

Now, let $m_j\left(t\right)$ be the number of ρ molecules in the jth cell, which has volume V_j and radius a. $m_j\left(t\right)$ can be calculated from $\rho\left(\vec{x},t\right)$ via

$$m_j\left(t\right)=\int_{V_j}d^3x\rho\left(\vec{x},t\right). \tag{D.18}$$

Once again, let $m_j\left(t\right)=\bar{m}_j+\delta m_j\left(t\right)$, where $\bar{m}_j$ is the mean value of $m_j\left(t\right)$. Since $\bar{\rho}\left(\vec{x}\right)$ is the mean value of $\rho\left(\vec{x},t\right)$, this implies

$$\bar{m}_j=\int_{V_j}d^3x\bar{\rho}\left(\vec{x}\right)\implies\delta m_j\left(t\right)=\int_{V_j}d^3x\delta\rho\left(\vec{x},t\right). \tag{D.19}$$

Fourier transforming the second part of Eq. D.19 then yields

$$\tilde{\delta m}_j\left(\omega\right)=\int_{V_j}d^3x\int\frac{d^3k}{\left(2\pi\right)^3}\tilde{\delta\rho}\left(\vec{k},\omega\right)e^{-i\vec{k}\cdot\vec{x}}. \tag{D.20}$$

With this, the cross spectrum of $m_j\left(t\right)$ can be calculated to be

$$\left\langle \tilde{\delta m}_j^{*}\left(\omega'\right)\tilde{\delta m}_j\left(\omega\right)\right\rangle$$
$$=\left\langle\left(\int_{V_j}d^3x'\int\frac{d^3k'}{\left(2\pi\right)^3}\tilde{\delta\rho}^{*}\left(\vec{k}',\omega'\right)e^{i\vec{k}'\cdot\vec{x}'}\right)\left(\int_{V_j}d^3x\int\frac{d^3k}{\left(2\pi\right)^3}\tilde{\delta\rho}\left(\vec{k},\omega\right)e^{-i\vec{k}\cdot\vec{x}}\right)\right\rangle$$
$$=\frac{1}{\left(2\pi\right)^6}\int_{V_j}d^3xd^3x'\int d^3kd^3k'\left\langle\tilde{\delta\rho}^{*}\left(\vec{k}',\omega'\right)\tilde{\delta\rho}\left(\vec{k},\omega\right)\right\rangle e^{i\left(\vec{k}'\cdot\vec{x}'-\vec{k}\cdot\vec{x}\right)}. \tag{D.21}$$

Again, let $\vec{v}_j = \vec{x} - \vec{x}_j$ and $\vec{v}'_j = \vec{x}' - \vec{x}_j$ and V be the volume of the cell centered at the origin. This, along with Eq. D.17, transforms Eq. D.21 into

$$\begin{aligned}
&\left\langle \tilde{\delta m}_j^* \left(\omega'\right) \tilde{\delta m}_j \left(\omega\right) \right\rangle \\
&\quad = \frac{1}{\left(2\pi\right)^6} \int_V d^3v_j d^3v'_j \int d^3k d^3k' \left\langle \tilde{\delta\rho}^* \left(\vec{k}', \omega'\right) \tilde{\delta\rho} \left(\vec{k}, \omega\right) \right\rangle e^{i\left(\vec{k}'\cdot\vec{v}'_j - \vec{k}\cdot\vec{v}_j\right)} e^{i\vec{x}_j\cdot\left(\vec{k}'-\vec{k}\right)} \\
&\quad = 2\pi\delta\left(\omega-\omega'\right)\left(I_1\left(\omega\right) + I_2\left(\omega\right) + I_3\left(\omega\right) + I_4\left(\omega\right)\right), \qquad \text{(D.22)}
\end{aligned}$$

where

$$\begin{aligned}
I_1\left(\omega\right) &= \frac{1}{\left(2\pi\right)^6} \int_V d^3v_j d^3v'_j \int d^3k d^3k' \frac{1}{\left(\nu + D_\rho k^2 - i\omega\right)\left(\nu + D_\rho k'^2 + i\omega\right)} \\
&\quad \cdot e^{i\left(\vec{k}'\cdot\vec{v}'_j - \vec{k}\cdot\vec{v}_j\right)} e^{i\vec{x}_j\cdot\left(\vec{k}'-\vec{k}\right)} \sum_{s,u} \frac{2\alpha\beta^2\bar{c}}{\omega} e^{i\left(\vec{k}\cdot\vec{x}_s - \vec{k}'\cdot\vec{x}_u\right)} \mathrm{Im}\left(R_{su}^{-1}\left(\omega\right)\right) \qquad \text{(D.23a)} \\
I_2\left(\omega\right) &= \frac{1}{\left(2\pi\right)^6} \int_V d^3v_j d^3v'_j \int d^3k d^3k' \frac{1}{\left(\nu + D_\rho k^2 - i\omega\right)\left(\nu + D_\rho k'^2 + i\omega\right)} \\
&\quad \cdot e^{i\left(\vec{k}'\cdot\vec{v}'_j - \vec{k}\cdot\vec{v}_j\right)} e^{i\vec{x}_j\cdot\left(\vec{k}'-\vec{k}\right)} \sum_s \beta\bar{r}_s e^{i\vec{x}_s\cdot\left(\vec{k}-\vec{k}'\right)} \qquad \text{(D.23b)} \\
I_3\left(\omega\right) &= \frac{1}{\left(2\pi\right)^6} \int_V d^3v_j d^3v'_j \int d^3k d^3k' \frac{1}{\left(\nu + D_\rho k^2 - i\omega\right)\left(\nu + D_\rho k'^2 + i\omega\right)} \\
&\quad \cdot e^{i\left(\vec{k}'\cdot\vec{v}'_j - \vec{k}\cdot\vec{v}_j\right)} e^{i\vec{x}_j\cdot\left(\vec{k}'-\vec{k}\right)} \frac{2D_\rho\vec{k}\cdot\vec{k}'}{\nu + D_\rho\left|\vec{k}-\vec{k}'\right|^2} \sum_s \beta\bar{r}_s e^{i\vec{x}_s\cdot\left(\vec{k}-\vec{k}'\right)}. \qquad \text{(D.23c)} \\
I_4\left(\omega\right) &= \frac{1}{\left(2\pi\right)^6} \int_V d^3v_j d^3v'_j \int d^3k d^3k' \frac{1}{\left(\nu + D_\rho k^2 - i\omega\right)\left(\nu + D_\rho k'^2 + i\omega\right)} \\
&\quad \cdot e^{i\left(\vec{k}'\cdot\vec{v}'_j - \vec{k}\cdot\vec{v}_j\right)} e^{i\vec{x}_j\cdot\left(\vec{k}'-\vec{k}\right)} \frac{\nu}{\nu + D_\rho\left|\vec{k}-\vec{k}'\right|^2} \sum_s \beta\bar{r}_s e^{i\vec{x}_s\cdot\left(\vec{k}-\vec{k}'\right)}. \qquad \text{(D.23d)}
\end{aligned}$$

Beginning with $I_1\left(\omega\right)$, moving the summation outside the integral and collecting terms exponential in $\vec{k}$ and $\vec{k}'$ yields

$$\begin{aligned}
I_1\left(\omega\right) &= \frac{2\alpha\beta^2\bar{c}}{\left(2\pi\right)^6 D_\rho^2 \omega} \sum_{s,u} \mathrm{Im}\left(R_{su}^{-1}\left(\omega\right)\right) \int_V d^3v_j d^3v'_j \int d^3k d^3k' \\
&\quad \cdot \frac{1}{\left(\frac{\nu-i\omega}{D_\rho} + k^2\right)\left(\frac{\nu+i\omega}{D_\rho} + k'^2\right)} e^{i\vec{k}\cdot\left(\vec{x}_s - \vec{x}_j - \vec{v}_j\right)} e^{-i\vec{k}'\cdot\left(\vec{x}_u - \vec{x}_j - \vec{v}'_j\right)}. \qquad \text{(D.24)}
\end{aligned}$$

Inverting Eq. D.14 allows for the k and k' integrals to be easily solved, simplifying $I_1(\omega)$ to

$$\begin{aligned} I_1(\omega) &= \frac{\alpha\beta^2\bar{c}}{2\left(2\pi D_\rho\right)^2\omega}\sum_{s,u}\mathrm{Im}\left(R_{su}^{-1}(\omega)\right)\int_V d^3v_j d^3v_j' \\ &\quad\cdot\left(\frac{1}{\left|\vec{x}_p-\vec{x}_j-\vec{v}_j\right|}e^{-\left|\vec{x}_s-\vec{x}_j-\vec{v}_j\right|\sqrt{\frac{\nu-i\omega}{D_\rho}}}\right)\left(\frac{1}{\left|\vec{x}_u-\vec{x}_j-\vec{v}_j'\right|}e^{-\left|\vec{x}_q-\vec{x}_j-\vec{v}_j'\right|\sqrt{\frac{\nu+i\omega}{D_\rho}}}\right) \\ &= \frac{\alpha\beta^2\bar{c}a^4}{2D_\rho^2\omega}\sum_{s,u}\mathrm{Im}\left(R_{su}^{-1}(\omega)\right)\Lambda\left(\left|\vec{x}_s-\vec{x}_j\right|,a,\lambda(\omega)\right) \\ &\quad\cdot\Lambda\left(\left|\vec{x}_u-\vec{x}_j\right|,a,\lambda(-\omega)\right), \end{aligned} \tag{D.25}$$

where a is the radius of the volume V,

$$\lambda(\omega)\equiv\sqrt{\frac{D_\rho}{\nu-i\omega}}=\sqrt[4]{\frac{D_\rho^2}{4\left(\nu^2+\omega^2\right)}}\left(\sqrt{1+\frac{\nu}{\sqrt{\nu^2+\omega^2}}}+i\,\mathrm{sgn}(\omega)\sqrt{1-\frac{\nu}{\sqrt{\nu^2+\omega^2}}}\right), \tag{D.26}$$

and

$$\Lambda(x,y,z)\equiv\begin{cases}\frac{2z^3}{xy^2}\left(\frac{x}{z}-\left(1+\frac{y}{z}\right)e^{-\frac{y}{z}}\sinh\left(\frac{x}{z}\right)\right) & x<y\\ \frac{2z^3}{xy^2}e^{-\frac{x}{z}}\left(\frac{y}{z}\cosh\left(\frac{y}{z}\right)-\sinh\left(\frac{y}{z}\right)\right) & x>y\end{cases} \tag{D.27}$$

comes from the relation

$$\int_V d^3z\frac{1}{\left|\vec{\kappa}-\vec{z}\right|}e^{-\frac{\left|\vec{\kappa}-\vec{z}\right|}{l}}=2\pi a^2\Lambda(\kappa,a,l), \tag{D.28}$$

which can be shown by writing $\vec{z}$ in spherical coordinates and evaluating.

Moving to $I_2(\omega)$, following the exact same procedure as was done for $I_1(\omega)$ yields

$$\begin{aligned} I_2(\omega) &= \frac{\beta}{(2\pi)^6 D_\rho^2} \sum_s \bar{r}_s \int_V d^3v_j d^3v_j' \int d^3k d^3k' \\ &\quad \cdot \frac{1}{\left(\frac{\nu - i\omega}{D_\rho} + k^2\right)\left(\frac{\nu + i\omega}{D_\rho} + k'^2\right)} e^{i\vec{k}\cdot\left(\vec{x}_s - \vec{x}_j - \vec{v}_j\right)} e^{-i\vec{k}'\cdot\left(\vec{x}_s - \vec{x}_j - \vec{v}_j'\right)} \\ &= \frac{\beta}{\left(4\pi D_\rho\right)^2} \sum_s \bar{r}_s \int_V d^3v_j d^3v_j' \\ &\quad \cdot \left(\frac{1}{\left|\vec{x}_s - \vec{x}_j - \vec{v}_j\right|} e^{-\left|\vec{x}_s - \vec{x}_j - \vec{v}_j\right|\sqrt{\frac{\nu - i\omega}{D_\rho}}}\right)\left(\frac{1}{\left|\vec{x}_s - \vec{x}_j - \vec{v}_j'\right|} e^{-\left|\vec{x}_s - \vec{x}_j - \vec{v}_j'\right|\sqrt{\frac{\nu + i\omega}{D_\rho}}}\right) \\ &= \frac{\beta a^4}{4D_\rho^2} \sum_s \bar{r}_s \left|\Lambda\left(\left|\vec{x}_s - \vec{x}_j\right|, a, \lambda(\omega)\right)\right|^2. \end{aligned} \tag{D.29}$$

Unfortunately, $I_3(\omega)$ cannot be solved by the same procedure as $I_1(\omega)$ and $I_2(\omega)$, but it can be solved. First, utilizing Eq. D.14 again and letting $l = \sqrt{\frac{D_\rho}{\nu}}$ and $\vec{\kappa} = \vec{k} - \vec{k}'$ allows the factor of $\frac{2D_\rho}{\nu + D_\rho\left|\vec{k} - \vec{k}'\right|^2}$ to be transformed into another integral, yielding

$$\begin{aligned} I_3(\omega) &= \frac{1}{(2\pi)^7 D_\rho^2} \int_V d^3v_j d^3v_j' \int d^3k d^3k' d^3z \frac{1}{\left(\frac{\nu - i\omega}{D_\rho} + k^2\right)\left(\frac{\nu + i\omega}{D_\rho} + k'^2\right)} \\ &\quad \cdot e^{i\left(\vec{k}'\cdot\vec{v}_j' - \vec{k}\cdot\vec{v}_j\right)} e^{i\vec{x}_j\cdot\left(\vec{k}' - \vec{k}\right)} \frac{\vec{k}\cdot\vec{k}'}{z} e^{-z\sqrt{\frac{\nu}{D_\rho}}} e^{i\vec{z}\cdot\left(\vec{k} - \vec{k}'\right)} \sum_s \beta \bar{r}_s e^{i\vec{x}_s\cdot\left(\vec{k} - \vec{k}'\right)}. \end{aligned} \tag{D.30}$$

Since v_j and v_j' only appear in a single exponential within the integrand, the factor of $\vec{k}\cdot\vec{k}'$ can be replaced by $\vec{\nabla}_{v_j}\cdot\vec{\nabla}_{v_j'}$ acting on the exponential. The gradient operators can then be moved outside the k, k', and z integrals while the summation is moved outside of all the integrals to produce

$$\begin{aligned} I_3(\omega) &= \frac{\beta}{(2\pi)^7 D_\rho^2} \sum_s \bar{r}_s \int_V d^3v_j d^3v_j' \vec{\nabla}_{v_j}\cdot\vec{\nabla}_{v_j'} \int d^3k d^3k' d^3z \frac{1}{\left(\frac{\nu - i\omega}{D_\rho} + k^2\right)\left(\frac{\nu + i\omega}{D_\rho} + k'^2\right)} \\ &\quad \cdot \frac{1}{z} e^{-z\sqrt{\frac{\nu}{D_\rho}}} e^{i\left(\vec{k}'\cdot\vec{v}_j' - \vec{k}\cdot\vec{v}_j\right)} e^{i\vec{x}_j\cdot\left(\vec{k}' - \vec{k}\right)} e^{i\vec{z}\cdot\left(\vec{k} - \vec{k}'\right)} e^{i\vec{x}_s\cdot\left(\vec{k} - \vec{k}'\right)}. \end{aligned} \tag{D.31}$$

Utilizing the inverse of Eq. D.14 to solve the k and k' integrals then yields

$$I_3(\omega) = \frac{\beta}{4(2\pi)^3 D_\rho^2} \sum_s \bar{r}_s \int_V d^3v_j d^3v_j' \vec{\nabla}_{v_j} \cdot \vec{\nabla}_{v_j'} \int d^3z \frac{1}{z} e^{-z\sqrt{\frac{\nu}{D_\rho}}} \cdot \left(\frac{1}{\left|\vec{z}+\vec{x}_s-\vec{x}_j-\vec{v}_j\right|} e^{-\left|\vec{z}+\vec{x}_s-\vec{x}_j-\vec{v}_j\right|\sqrt{\frac{\nu-i\omega}{D_\rho}}} \right) \left(\frac{1}{\left|\vec{z}+\vec{x}_s-\vec{x}_j-\vec{v}_j'\right|} e^{-\left|\vec{z}+\vec{x}_s-\vec{x}_j-\vec{v}_j'\right|\sqrt{\frac{\nu+i\omega}{D_\rho}}} \right). \tag{D.32}$$

From here the z integral can be moved outside the v_j and v_j' integrals, which can in turn be separated into the product of two independent integrals to produce

$$I_3(\omega) = \frac{\beta}{4(2\pi)^3 D_\rho^2} \sum_s \bar{r}_s \int d^3z \frac{1}{z} e^{-z\sqrt{\frac{\nu}{D_\rho}}} \left(\int_V d^3v_j \vec{\nabla}_{v_j} \frac{1}{\left|\vec{z}+\vec{x}_s-\vec{x}_j-\vec{v}_j\right|} e^{-\left|\vec{z}+\vec{x}_s-\vec{x}_j-\vec{v}_j\right|\sqrt{\frac{\nu-i\omega}{D_\rho}}} \right) \cdot \left(\int_V d^3v_j' \vec{\nabla}_{v_j'} \frac{1}{\left|\vec{z}+\vec{x}_s-\vec{x}_j-\vec{v}_j'\right|} e^{-\left|\vec{z}+\vec{x}_s-\vec{x}_j-\vec{v}_j'\right|\sqrt{\frac{\nu+i\omega}{D_\rho}}} \right). \tag{D.33}$$

Due to the fact that the v_j and v_j' integrands in Eq. D.33 depend only on $\left|\vec{z}+\vec{x}_s-\vec{x}_j-\vec{v}_j\right|$ and $\left|\vec{z}+\vec{x}_s-\vec{x}_j-\vec{v}_j'\right|$ respectively, taking the gradient with respect to v_j and v_j' is identical to taking the gradient with respect to z and multiplying by a factor of -1 in both cases. The extra factors of -1 can be ignored, however, as they will multiply to unity. This allows the gradients to be moved outside of the v_j and v_j' integrals, which in turn allows them to be solved via Eq. D.28 to produce

$$I_3(\omega) = \frac{\beta a^4}{8\pi D_\rho^2} \sum_s \bar{r}_s \int d^3z \frac{1}{z} e^{-z\sqrt{\frac{\nu}{D_\rho}}} \left| \vec{\nabla}_z \Lambda\left(\left|\vec{z}+\vec{x}_s-\vec{x}_j\right|, a, \lambda(\omega) \right) \right|^2. \tag{D.34}$$

Let $\vec{y} = \vec{z}+\vec{x}_s-\vec{x}_j$. Since the z integral is over all of z-space, this transformation does not change the limits of integration. Additionally, $d^3y = d^3z$ and $\vec{\nabla}_y = \vec{\nabla}_z$ since y and z are related by a simple translation. This transformation allows Eq. D.34 to be written as

$$I_3(\omega) = \frac{\beta a^4}{8\pi D_\rho^2} \sum_s \bar{r}_s \int d^3y \frac{1}{\left|\vec{y}+\vec{x}_j-\vec{x}_s\right|} e^{-\left|\vec{y}+\vec{x}_j-\vec{x}_s\right|\sqrt{\frac{\nu}{D_\rho}}} \left| \vec{\nabla}_y \Lambda\left(y, a, \lambda(\omega)\right) \right|^2. \tag{D.35}$$

Let V_y be the spherical volume in y-space centered at the origin with radius a and V_y' be all of y-space excluding V_y. These along with Eq. D.27 allow the integral

in Eq. D.35 to be broken into two separate pieces along the piecewise boundary of $\Lambda\left(y,a,\lambda\left(\omega\right)\right)$ to produce

$$I_3\left(\omega\right)=\frac{\beta a^4}{8\pi D_\rho^2}\sum_s \bar{r}_s\int_{V_y} d^3y\frac{1}{\left|\vec{y}+\vec{x}_j-\vec{x}_s\right|}e^{-\left|\vec{y}+\vec{x}_j-\vec{x}_s\right|\sqrt{\frac{\nu}{D_\rho}}}$$
$$\cdot\left|\vec{\nabla}_y\frac{2}{ya^2}\left(\frac{D_\rho}{\nu-i\omega}\right)^{\frac{3}{2}}\left(y\sqrt{\frac{\nu-i\omega}{D_\rho}}-\left(1+a\sqrt{\frac{\nu-i\omega}{D_\rho}}\right)e^{-a\sqrt{\frac{\nu-i\omega}{D_\rho}}}\sinh\left(y\sqrt{\frac{\nu-i\omega}{D_\rho}}\right)\right)\right|^2$$
$$+\int_{V_y'} d^3y\frac{1}{\left|\vec{y}+\vec{x}_j-\vec{x}_s\right|}e^{-\left|\vec{y}+\vec{x}_j-\vec{x}_s\right|\sqrt{\frac{\nu}{D_\rho}}}$$
$$\cdot\left|\vec{\nabla}_y\frac{2}{ya^2}\left(\frac{D_\rho}{\nu-i\omega}\right)^{\frac{3}{2}}e^{-y\sqrt{\frac{\nu-i\omega}{D_\rho}}}\left(a\sqrt{\frac{\nu-i\omega}{D_\rho}}\cosh\left(a\sqrt{\frac{\nu-i\omega}{D_\rho}}\right)-\sinh\left(a\sqrt{\frac{\nu-i\omega}{D_\rho}}\right)\right)\right|^2. \tag{D.36}$$

Performing the gradient operators then yields

$$I_3\left(\omega\right)=\frac{\beta a^4}{8\pi D_\rho^2}\sum_s \bar{r}_s\int_{V_y} d^3y\frac{1}{\left|\vec{y}+\vec{x}_j-\vec{x}_s\right|}e^{-\frac{\left|\vec{y}+\vec{x}_j-\vec{x}_s\right|}{\lambda(0)}}$$
$$\cdot\left|\frac{\vec{y}}{y}\frac{2\left(\lambda\left(\omega\right)\right)^3}{y^2a^2}\left(1+\frac{a}{\lambda\left(\omega\right)}\right)e^{-\frac{a}{\lambda(\omega)}}\left(\sinh\left(\frac{y}{\lambda\left(\omega\right)}\right)\right.\right.$$
$$\left.\left.-\frac{y}{\lambda\left(\omega\right)}\cosh\left(\frac{y}{\lambda\left(\omega\right)}\right)\right)\right|^2+\int_{V_y'} d^3y\frac{1}{\left|\vec{y}+\vec{x}_j-\vec{x}_s\right|}e^{-\frac{\left|\vec{y}+\vec{x}_j-\vec{x}_s\right|}{\lambda(0)}}$$
$$\cdot\left|\frac{\vec{y}}{y}\frac{2\left(\lambda\left(\omega\right)\right)^3}{y^2a^2}\left(1+\frac{y}{\lambda\left(\omega\right)}\right)e^{-\frac{y}{\lambda(\omega)}}\left(\sinh\left(\frac{a}{\lambda\left(\omega\right)}\right)\right.\right.$$
$$\left.\left.-\frac{a}{\lambda\left(\omega\right)}\cosh\left(\frac{a}{\lambda\left(\omega\right)}\right)\right)\right|^2. \tag{D.37}$$

Once the magnitude squared of each vector is taken, the only term in either integral that depends on the angle of $\vec{y}$ will be $\left|\vec{y}+\vec{x}_j-\vec{x}_s\right|$. Thus, the angular portion of each integral can be performed to yield

$$\begin{aligned} I_3(\omega) = \frac{\beta\left|\lambda(\omega)\right|^6}{D_\rho^2}\sum_s \bar{r}_s \int_0^a dy \frac{\lambda(0)}{y^3\left|\vec{x}_s-\vec{x}_j\right|}\left(e^{-\frac{\left|y-\left|\vec{x}_s-\vec{x}_j\right|\right|}{\lambda(0)}}-e^{-\frac{y+\left|\vec{x}_s-\vec{x}_j\right|}{\lambda(0)}}\right) \\ \cdot\left|\left(1+\frac{a}{\lambda(\omega)}\right)e^{-\frac{a}{\lambda(\omega)}}\left(\sinh\left(\frac{y}{\lambda(\omega)}\right)-\frac{y}{\lambda(\omega)}\cosh\left(\frac{y}{\lambda(\omega)}\right)\right)\right|^2 \\ +\int_a^\infty dy \frac{\lambda(0)}{y^3\left|\vec{x}_s-\vec{x}_j\right|}\left(e^{-\frac{\left|y-\left|\vec{x}_s-\vec{x}_j\right|\right|}{\lambda(0)}}-e^{-\frac{y+\left|\vec{x}_s-\vec{x}_j\right|}{\lambda(0)}}\right) \\ \cdot\left|\left(1+\frac{y}{\lambda(\omega)}\right)e^{-\frac{y}{\lambda(\omega)}}\left(\sinh\left(\frac{a}{\lambda(\omega)}\right)-\frac{a}{\lambda(\omega)}\cosh\left(\frac{a}{\lambda(\omega)}\right)\right)\right|^2. \end{aligned} \tag{D.38}$$

The integrals in Eq. D.38 are well defined and very involved. Nonetheless, they can be performed piece-by-piece with the aid of integral tables or symbolic computational solvers. The result is

$$\begin{aligned} I_3(\omega) = \frac{\beta a^4}{D_\rho^2}\sum_s \bar{r}_s \Bigg(\frac{\left|\left(1+\frac{a}{\lambda(\omega)}\right)e^{-\frac{a}{\lambda(\omega)}}\right|^2}{18}\Upsilon\left(\left|\vec{x}_s-\vec{x}_j\right|,a,\lambda(0),\lambda(\omega)\right) \\ +\left|\left(\frac{\lambda(\omega)}{a}\right)^3\left(\sinh\left(\frac{a}{\lambda(\omega)}\right)-\frac{a}{\lambda(\omega)}\cosh\left(\frac{a}{\lambda(\omega)}\right)\right)\right|^2 \Xi\left(\left|\vec{x}_s-\vec{x}_j\right|,a,\lambda(0),\lambda(\omega)\right)\Bigg), \end{aligned} \tag{D.39}$$

where

$$\Upsilon(x,y,z,w) \equiv \begin{cases} \frac{9\not{2}|w|^6 \sinh\left(\frac{x}{z}\right)}{xy^6} e^{-\frac{y}{z}} \left(2y\mathrm{Re}\left(\frac{1}{w}\right) \sinh\left(2y\mathrm{Re}\left(\frac{1}{w}\right)\right) \right. \\ \quad +2y\mathrm{Im}\left(\frac{1}{w}\right) \sin\left(2y\mathrm{Im}\left(\frac{1}{w}\right)\right) \\ \quad \left. -\left(1-\frac{y}{z}\right)\left(\cosh\left(2y\mathrm{Re}\left(\frac{1}{w}\right)\right) - \cos\left(2y\mathrm{Im}\left(\frac{1}{w}\right)\right)\right)\right) \\ \quad -\frac{9|w|^6}{x^2y^4}\left(\cosh\left(2x\mathrm{Re}\left(\frac{1}{w}\right)\right) - \cos\left(2x\mathrm{Im}\left(\frac{1}{w}\right)\right)\right) \\ \quad -\frac{9|w|^6}{2xy^4z} e^{-\frac{x}{z}} \left(\mathrm{Shi}\left(x\left(\frac{1}{z}+2\mathrm{Re}\left(\frac{1}{w}\right)\right)\right) + \mathrm{Shi}\left(x\left(\frac{1}{z}-2\mathrm{Re}\left(\frac{1}{w}\right)\right)\right) \right. \\ \quad \left. -\mathrm{Shi}\left(x\left(\frac{1}{z}+2i\mathrm{Im}\left(\frac{1}{w}\right)\right)\right) - \mathrm{Shi}\left(x\left(\frac{1}{z}-2i\mathrm{Im}\left(\frac{1}{w}\right)\right)\right)\right) \\ \quad -\frac{9\not{|}w|^6 \sinh\left(\frac{x}{z}\right)}{2xy^4z} \left(\mathrm{Ei}\left(x\left(\frac{1}{z}+2\mathrm{Re}\left(\frac{1}{w}\right)\right)\right) + \mathrm{Ei}\left(x\left(\frac{1}{z}-2\mathrm{Re}\left(\frac{1}{w}\right)\right)\right) \right. \\ \quad -\mathrm{Ei}\left(x\left(\frac{1}{z}+2i\mathrm{Im}\left(\frac{1}{w}\right)\right)\right) - \mathrm{Ei}\left(x\left(\frac{1}{z}-2i\mathrm{Im}\left(\frac{1}{w}\right)\right)\right) \\ \quad -\mathrm{Ei}\left(y\left(\frac{1}{z}+2\mathrm{Re}\left(\frac{1}{w}\right)\right)\right) - \mathrm{Ei}\left(y\left(\frac{1}{z}-2\mathrm{Re}\left(\frac{1}{w}\right)\right)\right) \\ \quad \left. +\mathrm{Ei}\left(y\left(\frac{1}{z}+2i\mathrm{Im}\left(\frac{1}{w}\right)\right)\right) + \mathrm{Ei}\left(y\left(\frac{1}{z}-2i\mathrm{Im}\left(\frac{1}{w}\right)\right)\right)\right) & x<y \\ \frac{9\not{2}|w|^6 \sinh\left(\frac{y}{z}\right)}{xy^6} e^{-\frac{x}{z}} \left(2y\mathrm{Re}\left(\frac{1}{w}\right) \sinh\left(2y\mathrm{Re}\left(\frac{1}{w}\right)\right) \right. \\ \quad \left. +2y\mathrm{Im}\left(\frac{1}{w}\right) \sin\left(2y\mathrm{Im}\left(\frac{1}{w}\right)\right)\right) \\ \quad -\frac{9\not{2}|w|^6\left(\sinh\left(\frac{y}{z}\right)+\frac{y}{z}\cosh\left(\frac{y}{z}\right)\right)}{xy^6} e^{-\frac{x}{z}} \\ \quad \cdot\left(\cosh\left(2y\mathrm{Re}\left(\frac{1}{w}\right)\right) - \cos\left(2y\mathrm{Im}\left(\frac{1}{w}\right)\right)\right) \\ \quad -\frac{9|w|^6}{2xy^4z} e^{-\frac{x}{z}} \left(\mathrm{Shi}\left(y\left(\frac{1}{z}+2\mathrm{Re}\left(\frac{1}{w}\right)\right)\right) + \mathrm{Shi}\left(y\left(\frac{1}{z}-2\mathrm{Re}\left(\frac{1}{w}\right)\right)\right) \right. \\ \quad \left. -\mathrm{Shi}\left(y\left(\frac{1}{z}+2i\mathrm{Im}\left(\frac{1}{w}\right)\right)\right) - \mathrm{Shi}\left(y\left(\frac{1}{z}-2i\mathrm{Im}\left(\frac{1}{w}\right)\right)\right)\right) & x>y, \end{cases} \tag{D.40}$$

$$\Xi(x,y,z,w) \equiv \begin{cases} \frac{z\sinh\left(\frac{x}{z}\right)}{x}\left(\left(1+y\left(2\mathrm{Re}\left(\frac{1}{w}\right)-\frac{1}{z}\right)\right)e^{-y\left(2\mathrm{Re}\left(\frac{1}{w}\right)+\frac{1}{z}\right)}\right. & \\ \left. -\frac{y^2}{z^2}\mathrm{Ei}\left(y\left(2\mathrm{Re}\left(\frac{1}{w}\right)+\frac{1}{z}\right)\right)\right) & x<y \\ \frac{z}{x}e^{-\frac{x}{z}}\left(e^{-2y\mathrm{Re}\left(\frac{1}{w}\right)}\left(\left(1+2y\mathrm{Re}\left(\frac{1}{w}\right)\right)\sinh\left(\frac{y}{z}\right)+\frac{y}{z}\cosh\left(\frac{y}{z}\right)\right)\right. & \\ -\frac{y^2}{2z^2}\left(e^{\frac{2x}{z}}\mathrm{Ei}\left(x\left(2\mathrm{Re}\left(\frac{1}{w}\right)+\frac{1}{z}\right)\right)-\mathrm{Ei}\left(x\left(2\mathrm{Re}\left(\frac{1}{w}\right)-\frac{1}{z}\right)\right)\right. & \\ \left.-\mathrm{Ei}\left(y\left(2\mathrm{Re}\left(\frac{1}{w}\right)+\frac{1}{z}\right)\right)+\mathrm{Ei}\left(y\left(2\mathrm{Re}\left(\frac{1}{w}\right)-\frac{1}{z}\right)\right)\right) & \\ \left.-\frac{y^2}{xz}e^{-x\left(2\mathrm{Re}\left(\frac{1}{w}\right)-\frac{1}{z}\right)}\right) & x>y, \end{cases} \tag{D.41}$$

$$\mathrm{Shi}(x) \equiv \int_0^x dt \frac{\sinh(t)}{t}, \tag{D.42}$$

and

$$\mathrm{Ei}(x) \equiv \int_x^\infty dt \frac{e^{-t}}{t}. \tag{D.43}$$

Lastly, $I_4(\omega)$ must be solved. Similarly utilizing Eq. D.14 allows Eq. D.23d to be transformed into

$$\begin{aligned} I_4(\omega) = \frac{\nu}{2(2\pi)^7 D_\rho^3}\int_V d^3v_j d^3v_j' \int d^3k d^3k' d^3z \frac{1}{\left(\frac{\nu-i\omega}{D_\rho}+k^2\right)\left(\frac{\nu+i\omega}{D_\rho}+k'^2\right)} \\ \cdot e^{i\left(\vec{k}'\cdot\vec{v}_j'-\vec{k}\cdot\vec{v}_j\right)}e^{i\vec{x}_j\cdot\left(\vec{k}'-\vec{k}\right)}\frac{1}{z}e^{-z\sqrt{\frac{\nu}{D_\rho}}}e^{i\vec{z}\cdot\left(\vec{k}-\vec{k}'\right)}\sum_s \beta\bar{r}_s e^{i\vec{x}_s\cdot\left(\vec{k}-\vec{k}'\right)}. \end{aligned} \tag{D.44}$$

Utilizing the inverse of Eq. D.14 to solve the k and k' integrals then yields

$$\begin{aligned} I_4(\omega) = \frac{\beta\nu}{8(2\pi)^3 D_\rho^3}\sum_s \bar{r}_s \int_V d^3v_j d^3v_j' \int d^3z \frac{1}{z}e^{-z\sqrt{\frac{\nu}{D_\rho}}} \\ \cdot\left(\frac{1}{\left|\vec{z}+\vec{x}_s-\vec{x}_j-\vec{v}_j\right|}e^{-\left|\vec{z}+\vec{x}_s-\vec{x}_j-\vec{v}_j\right|\sqrt{\frac{\nu-i\omega}{D_\rho}}}\right)\left(\frac{1}{\left|\vec{z}+\vec{x}_s-\vec{x}_j-\vec{v}_j'\right|}e^{-\left|\vec{z}+\vec{x}_s-\vec{x}_j-\vec{v}_j'\right|\sqrt{\frac{\nu+i\omega}{D_\rho}}}\right). \end{aligned} \tag{D.45}$$

From here the z integral can be moved outside the v_j and v_j' integrals, which can in turn be separated into the product of two independent integrals to produce

$$I_4(\omega) = \frac{\beta\nu}{8(2\pi)^3 D_\rho^3} \sum_s \bar{r}_s \int d^3z \frac{1}{z} e^{-z\sqrt{\frac{\nu}{D_\rho}}} \left(\int_V d^3v_j \frac{1}{\left|\vec{z}+\vec{x}_s-\vec{x}_j-\vec{v}_j\right|} e^{-\left|\vec{z}+\vec{x}_s-\vec{x}_j-\vec{v}_j\right|\sqrt{\frac{\nu-i\omega}{D_\rho}}} \right) \cdot \left(\int_V d^3v_j' \frac{1}{\left|\vec{z}+\vec{x}_s-\vec{x}_j-\vec{v}_j'\right|} e^{-\left|\vec{z}+\vec{x}_s-\vec{x}_j-\vec{v}_j'\right|\sqrt{\frac{\nu+i\omega}{D_\rho}}} \right). \tag{D.46}$$

The v_j and v_j' integrals can then be solved via Eq. D.28 to produce

$$I_4(\omega) = \frac{\beta\nu a^4}{16\pi D_\rho^3} \sum_s \bar{r}_s \int d^3z \frac{1}{z} e^{-z\sqrt{\frac{\nu}{D_\rho}}} \left| \Lambda\left(\left|\vec{z}+\vec{x}_s-\vec{x}_j\right|, a, \lambda(\omega) \right) \right|^2. \tag{D.47}$$

Again, let $\vec{y} = \vec{z}+\vec{x}_s-\vec{x}_j$ as well as V_y be the spherical volume in y-space centered at the origin with radius a and V_y' be all of y-space excluding V_y. These transformations allow the Λ function to be split along its piecewise boundary again and Eq. D.47 to be written as

$$\begin{aligned} I_4(\omega) = \frac{\beta\nu a^4}{16\pi D_\rho^3} \sum_s \bar{r}_s & \int_{V_y} d^3y \frac{1}{\left|\vec{y}+\vec{x}_j-\vec{x}_s\right|} e^{-\left|\vec{y}+\vec{x}_j-\vec{x}_s\right|\sqrt{\frac{\nu}{D_\rho}}} \\ & \cdot \left| \frac{2\left(\lambda(\omega)\right)^3}{ya^2} \left(\frac{y}{\lambda(\omega)} - \left(1+\frac{a}{\lambda(\omega)}\right) e^{-\frac{a}{\lambda(\omega)}} \sinh\left(\frac{y}{\lambda(\omega)}\right) \right) \right|^2 \\ & + \int_{V_y'} d^3y \frac{1}{\left|\vec{y}+\vec{x}_j-\vec{x}_s\right|} e^{-\left|\vec{y}+\vec{x}_j-\vec{x}_s\right|\sqrt{\frac{\nu}{D_\rho}}} \\ & \cdot \left| \frac{2\left(\lambda(\omega)\right)^3}{ya^2} e^{-\frac{y}{\lambda(\omega)}} \left(\frac{a}{\lambda(\omega)} \cosh\left(\frac{a}{\lambda(\omega)}\right) - \sinh\left(\frac{a}{\lambda(\omega)}\right) \right) \right|^2. \end{aligned} \tag{D.48}$$

Once again, the only term in either integral that depends on the angle of $\vec{y}$ will be $\left|\vec{y}+\vec{x}_j-\vec{x}_s\right|$. Thus, the angular portion of each integral can be performed to yield

$$\begin{aligned} I_4(\omega) = \frac{\beta\nu\left|\lambda(\omega)\right|^6}{2D_\rho^3}\sum_s \bar{r}_s \int_0^a dy \frac{\lambda(0)}{y\left|\vec{x}_s-\vec{x}_j\right|}\left(e^{-\frac{\left|y-\left|\vec{x}_s-\vec{x}_j\right|\right|}{\lambda(0)}}-e^{-\frac{y+\left|\vec{x}_s-\vec{x}_j\right|}{\lambda(0)}}\right) \\ \cdot\left|\frac{y}{\lambda(\omega)}-\left(1+\frac{a}{\lambda(\omega)}\right)e^{-\frac{a}{\lambda(\omega)}}\sinh\left(\frac{y}{\lambda(\omega)}\right)\right|^2 \\ +\int_a^\infty dy \frac{\lambda(0)}{y\left|\vec{x}_s-\vec{x}_j\right|}\left(e^{-\frac{\left|y-\left|\vec{x}_s-\vec{x}_j\right|\right|}{\lambda(0)}}-e^{-\frac{y+\left|\vec{x}_s-\vec{x}_j\right|}{\lambda(0)}}\right) \\ \cdot\left|e^{-\frac{y}{\lambda(\omega)}}\left(\frac{a}{\lambda(\omega)}\cosh\left(\frac{a}{\lambda(\omega)}\right)-\sinh\left(\frac{a}{\lambda(\omega)}\right)\right)\right|^2. \end{aligned} \tag{D.49}$$

Relying again on integral tables or computational solvers, these integrals can also be performed and yield

$$I_4(\omega) = \frac{\beta\nu\left|\lambda(\omega)\right|^6}{2D_\rho^3}\sum_s \bar{r}_s\left(\Psi\left(\left|\vec{x}_s-\vec{x}_j\right|,a,\lambda(0),\lambda(\omega)\right)+\Omega\left(\left|\vec{x}_s-\vec{x}_j\right|,a,\lambda(0),\lambda(\omega)\right)\right) \tag{D.50}$$

where

$$
\Psi\left(x,y,z,w\right)=\begin{cases}
\frac{2z^3}{x|w|^2}\left(\frac{x}{z}-\left(1+\frac{y}{z}\right)e^{-\frac{y}{z}}\sinh\left(\frac{x}{z}\right)\right)\\
\quad+\mathrm{Re}\left(\frac{4z^2w}{xw^*}\frac{1+\frac{y}{w}}{w^2-z^2}\left(ze^{-\frac{y}{z}}\sinh\left(\frac{x}{z}\right)+we^{-\frac{y}{w}}\sinh\left(\frac{x}{w}\right)\right)\right)\\
\quad+\frac{z}{2x}\left|\left(1+\frac{y}{w}\right)e^{-\frac{y}{w}}\right|^2\left(e^{-\frac{x}{z}}\left(\mathrm{Shi}\left(x\left(\frac{1}{z}+2\mathrm{Re}\left(\frac{1}{w}\right)\right)\right)\right.\right.\\
\quad+\mathrm{Shi}\left(x\left(\frac{1}{z}-2\mathrm{Re}\left(\frac{1}{w}\right)\right)\right)-\mathrm{Shi}\left(x\left(\frac{1}{z}+2i\mathrm{Im}\left(\frac{1}{w}\right)\right)\right)\\
\quad\left.-\mathrm{Shi}\left(x\left(\frac{1}{z}-2i\mathrm{Im}\left(\frac{1}{w}\right)\right)\right)\right)\\
\quad+\sinh\left(\frac{x}{z}\right)\left(\mathrm{Ei}\left(x\left(\frac{1}{z}+2\mathrm{Re}\left(\frac{1}{w}\right)\right)\right)\right.\\
\quad+\mathrm{Ei}\left(x\left(\frac{1}{z}-2\mathrm{Re}\left(\frac{1}{w}\right)\right)\right)-\mathrm{Ei}\left(x\left(\frac{1}{z}+2i\mathrm{Im}\left(\frac{1}{w}\right)\right)\right)\\
\quad-\mathrm{Ei}\left(x\left(\frac{1}{z}-2i\mathrm{Im}\left(\frac{1}{w}\right)\right)\right)-\mathrm{Ei}\left(y\left(\frac{1}{z}+2\mathrm{Re}\left(\frac{1}{w}\right)\right)\right)\\
\quad-\mathrm{Ei}\left(y\left(\frac{1}{z}-2\mathrm{Re}\left(\frac{1}{w}\right)\right)\right)+\mathrm{Ei}\left(y\left(\frac{1}{z}+2i\mathrm{Im}\left(\frac{1}{w}\right)\right)\right)\\
\quad\left.\left.+\mathrm{Ei}\left(y\left(\frac{1}{z}-2i\mathrm{Im}\left(\frac{1}{w}\right)\right)\right)\right)\right) & x<y\\
\frac{2z^3}{x|w|^2}e^{-\frac{x}{z}}\left(\frac{y}{z}\cosh\left(\frac{y}{z}\right)-\sinh\left(\frac{y}{z}\right)\right)\\
\quad+\mathrm{Re}\left(\frac{4z^2w}{xw^*}\frac{1+\frac{y}{w}}{w^2-z^2}e^{-\frac{x}{z}}\left((w+z)\sinh\left(y\left(\frac{1}{z}-\frac{1}{w}\right)\right)\right.\right.\\
\quad\left.\left.-(w-z)\sinh\left(y\left(\frac{1}{z}+\frac{1}{w}\right)\right)\right)\right)\\
\quad+\frac{z}{2x}\left|\left(1+\frac{y}{w}\right)e^{-\frac{y}{w}}\right|^2e^{-\frac{x}{z}}\left(\mathrm{Shi}\left(a\left(\frac{1}{z}+2\mathrm{Re}\left(\frac{1}{w}\right)\right)\right)\right.\\
\quad+\mathrm{Shi}\left(a\left(\frac{1}{z}-2\mathrm{Re}\left(\frac{1}{w}\right)\right)\right)-\mathrm{Shi}\left(a\left(\frac{1}{z}+2i\mathrm{Im}\left(\frac{1}{w}\right)\right)\right)\\
\quad\left.-\mathrm{Shi}\left(a\left(\frac{1}{z}-2i\mathrm{Im}\left(\frac{1}{w}\right)\right)\right)\right) & x>y,
\end{cases}
\tag{D.51}
$$

and

$$\Omega(x,y,z,w)=\begin{cases}\frac{2z}{x}\sinh\left(\frac{x}{z}\right)\left|\frac{y}{w}\cosh\left(\frac{y}{w}\right)-\sinh\left(\frac{y}{w}\right)\right|^2\mathrm{Ei}\left(y\left(\frac{1}{z}+2\mathrm{Re}\left(\frac{1}{w}\right)\right)\right) & x<y\\ \frac{2z}{x}\sinh\left(\frac{x}{z}\right)\left|\frac{y}{w}\cosh\left(\frac{y}{w}\right)-\sinh\left(\frac{y}{w}\right)\right|^2\mathrm{Ei}\left(x\left(\frac{1}{z}+2\mathrm{Re}\left(\frac{1}{w}\right)\right)\right)\\ \quad+\frac{z}{x}e^{-\frac{x}{z}}\left|\frac{y}{w}\cosh\left(\frac{y}{w}\right)-\sinh\left(\frac{y}{w}\right)\right|^2\left(\mathrm{Ei}\left(y\left(2\mathrm{Re}\left(\frac{1}{w}\right)-\frac{1}{z}\right)\right)\right.\\ \quad-\mathrm{Ei}\left(y\left(2\mathrm{Re}\left(\frac{1}{w}\right)+\frac{1}{z}\right)\right)-\mathrm{Ei}\left(x\left(2\mathrm{Re}\left(\frac{1}{w}\right)-\frac{1}{z}\right)\right)\\ \quad\left.+\mathrm{Ei}\left(x\left(2\mathrm{Re}\left(\frac{1}{w}\right)+\frac{1}{z}\right)\right)\right) & x>y.\end{cases} \tag{D.52}$$

With the power spectrum of $m_j(t)$ solved, the mean $\bar{m}_j$ needs to now be calculated in order to obtain the noise-to-signal ratio. Combining Eqs. D.3 and D.19 yields

$$\bar{m}_j=\int_{V_j}d^3x\frac{1}{4\pi D_\rho}\sum_l\frac{\beta\bar{r}_l}{|\vec{x}-\vec{x}_l|}e^{-|\vec{x}-\vec{x}_l|\sqrt{\frac{\nu}{D_\rho}}}. \tag{D.53}$$

Again, let $\vec{v}_j=\vec{x}-\vec{x}_j$. Utilizing this substitution and Eq. D.28 to solve Eq. D.53 yields

$$\begin{aligned}\bar{m}_j&=\frac{\beta}{4\pi D_\rho}\sum_l\bar{r}_l\int_{V_j}d^3v_j\frac{1}{\left|\vec{v_j}-\left(\vec{x}_l-\vec{x}_j\right)\right|}e^{-\left|\vec{v_j}-\left(\vec{x}_l-\vec{x}_j\right)\right|\sqrt{\frac{\nu}{D_\rho}}}\\&=\frac{\beta a^2}{2D_\rho}\sum_l\bar{r}_l\Lambda\left(\left|\vec{x}_l-\vec{x}_j\right|,a,\lambda(0)\right)\end{aligned} \tag{D.54}$$

Finally, combining Eqs. D.22, D.25, D.29, D.39, D.50, and D.54 yields the time averaged noise-to-signal ratio of $m_j(t)$. To determine the criteria for T in this equation, it is important to note that ω only appears in $\lambda(\omega)$, which directly compares ω to ν in Eq. D.26. However, ν can be taken to 0 without complication, thus leaving ω to be directly compared to $\frac{D_\rho}{a^2}$ as $\lambda(\omega)$ is always found in proportion to a or $\left|\vec{x}_i-\vec{x}_j\right|$, but $\left|\vec{x}_i-\vec{x}_j\right|$ can be taken to ∞ without complication as well. Thus, $\omega\ll\nu$ must be true unless $\nu\ll\frac{D_\rho}{a^2}$, at which point $\omega\ll\frac{D_\rho}{a^2}$ must be true. This in turn implies

$T \gg \tau_4 = \left(\nu + \frac{D_\rho}{a^2}\right)^{-1}$ can be taken as the appropriate criterion for T. Once this is met, the time averaged noise-to-signal ratio of $m_j(t)$ can be calculated to be

$$\frac{(\delta m_j)^2}{\bar{m}_j^2} = \frac{S_m(0)}{\bar{m}_j^2 T} = \frac{1}{\bar{m}_j^2 T}\int \frac{d\omega'}{2\pi}\left\langle \tilde{\delta m}_j^*(\omega')\,\tilde{\delta m}_j(0)\right\rangle$$

$$= \frac{I_1(0)+I_2(0)+I_3(0)+I_4(0)}{\left(\frac{\beta a^2}{2D_\rho}\sum_l \bar{r}_l \Lambda\left(\left|\vec{x}_l-\vec{x}_j\right|,a,\lambda(0)\right)\right)^2 T}$$

$$= \frac{1}{\beta T}\left(\sum_l \bar{r}_l \Lambda\left(\left|\vec{x}_l-\vec{x}_j\right|,a,\lambda(0)\right)\right)^{-2}\left(\sum_s \bar{r}_s\left|\Lambda\left(\left|\vec{x}_s-\vec{x}_j\right|,a,\lambda(0)\right)\right|^2\right.$$

$$+\sum_{s,u} 2\alpha\beta\bar{c}\lim_{\omega\to 0}\left(\frac{1}{\omega}\mathrm{Im}\left(R_{su}^{-1}(\omega)\right)\right)\Lambda\left(\left|\vec{x}_s-\vec{x}_j\right|,a,\lambda(0)\right)\Lambda\left(\left|\vec{x}_u-\vec{x}_j\right|,a,\lambda(0)\right)$$

$$+\sum_s 4\bar{r}_s\left(\frac{\left|\left(1+\frac{a}{\lambda(0)}\right)e^{-\frac{a}{\lambda(0)}}\right|^2}{18}\Upsilon\left(\left|\vec{x}_s-\vec{x}_j\right|,a,\lambda(0),\lambda(0)\right)\right.$$

$$\left.\left.+\left|\left(\frac{\lambda(0)}{a}\right)^3\left(\sinh\left(\frac{a}{\lambda(0)}\right)-\frac{a}{\lambda(0)}\cosh\left(\frac{a}{\lambda(0)}\right)\right)\right|^2\Xi\left(\left|\vec{x}_s-\vec{x}_j\right|,a,\lambda(0),\lambda(0)\right)\right)\right.$$

$$\left.+\sum_s 2\bar{r}_s\left(\frac{\lambda(0)}{a}\right)^4\left(\Psi\left(\left|\vec{x}_s-\vec{x}_j\right|,a,\lambda(0),\lambda(0)\right)+\Omega\left(\left|\vec{x}_s-\vec{x}_j\right|,a,\lambda(0),\lambda(0)\right)\right)\right) \tag{D.55}$$

Eq. D.55 is the general expression for the error in the case of autocrine signaling. Additionally, the data presented in Fig. 3 of the main text is obtained by separating Eq. D.55 into its extrinsic and intrinsic terms and considering only those extrinsic terms caused by the ligand diffusion.

Eq. D.55 can be greatly simplified in form under the limit $\nu \ll \frac{D_\rho}{a^2}$, which by Eq. D.26 implies $\lambda(0) \gg a$. When this limit is taken, the Ψ and Ω functions vanish due

to their original multiplication by ν in Eq. D.23d while the Λ, Υ, and Ξ functions simplify to

$$\lim_{z\to\infty}\Lambda\left(x,y,z\right)\equiv\Lambda_{\infty}\left(\frac{x}{y}\right)=\begin{cases}1-\frac{1}{3}\left(\frac{x}{y}\right)^{2} & \frac{x}{y}<1\\ \frac{2y}{3x} & \frac{x}{y}>1,\end{cases} \tag{D.56a}$$

$$\lim_{z\to\infty}\Upsilon\left(x,y,z,z\right)\equiv\Upsilon_{\infty}\left(\frac{x}{y}\right)=\begin{cases}1-\frac{1}{5}\left(\frac{x}{y}\right)^{4} & \frac{x}{y}<1\\ \frac{4y}{5x} & \frac{x}{y}>1,\end{cases} \tag{D.56b}$$

$$\lim_{z\to\infty}\Xi\left(x,y,z,z\right)\equiv\Xi_{\infty}\left(\frac{x}{y}\right)=\begin{cases}1 & \frac{x}{y}<1\\ \frac{2y}{x}-\left(\frac{y}{x}\right)^{2} & \frac{x}{y}>1,\end{cases} \tag{D.56c}$$

which can be shown by Taylor expanding all the functions in Eqs. D.27, D.40, and D.41 for small $\frac{1}{z}$ and evaluating. Utilizing the same method for the other instances of $\lambda\left(0\right)$ in Eq. D.55 allows it to simplify to

$$\begin{aligned}\lim_{\lambda(0)\to\infty}\frac{(\delta m_j)^2}{\bar{m}_j^2}=\frac{1}{\beta T}&\left(\sum_l \bar{r}_l\Lambda_{\infty}\left(\frac{\left|\vec{x}_l-\vec{x}_j\right|}{a}\right)\right)^{-2}\left(\sum_s \bar{r}_s\left(\Lambda_{\infty}\left(\frac{\left|\vec{x}_s-\vec{x}_j\right|}{a}\right)\right)^{2}\right.\\ &+\sum_{s,u}2\alpha\beta\bar{c}\lim_{\omega\to0}\left(\frac{1}{\omega}\mathrm{Im}\left(R_{su}^{-1}\left(\omega\right)\right)\right)\Lambda_{\infty}\left(\frac{\left|\vec{x}_s-\vec{x}_j\right|}{a}\right)\Lambda_{\infty}\left(\frac{\left|\vec{x}_u-\vec{x}_j\right|}{a}\right)\\ &\left.+\sum_s 4\bar{r}_s\left(\frac{1}{18}\Upsilon_{\infty}\left(\frac{\left|\vec{x}_s-\vec{x}_j\right|}{a}\right)+\frac{1}{9}\Xi_{\infty}\left(\frac{\left|\vec{x}_s-\vec{x}_j\right|}{a}\right)\right)\right)\end{aligned} \tag{D.57}$$

The data presented in Fig. 2 of the main text is similarly obtained by separating Eq. D.57 into its extrinsic and intrinsic terms and considering only those extrinsic terms caused by the ligand diffusion.

For the two cell case Eq. D.55 can be further evaluated. Let $\ell=\left|\vec{x}_1-\vec{x}_2\right|$. Utilizing Eqs. B.21 and B.22 to evaluate R^{-1} and the knowledge that $\bar{r}_1=\bar{r}_2=\bar{r}$ then yields for either cell

$$\frac{(\delta m)^2}{\bar{m}^2} = \frac{1}{\beta T}\left(1+\Lambda_\infty\left(\frac{\ell}{a}\right)\right)^{-2}\left(\frac{1}{\bar{r}}\left(1+\left(\Lambda_\infty\left(\frac{\ell}{a}\right)\right)^2\right)\right.$$
$$+\frac{2\alpha\beta\bar{c}}{\bar{r}^2}\left(\frac{1+\mathrm{Re}\left(\Sigma\left(0,0\right)\right)}{\mu^2}\left(1+\left(\Lambda_\infty\left(\frac{\ell}{a}\right)\right)^2\right)+2\frac{\mathrm{Re}\left(\Sigma\left(l,0\right)\right)}{\mu^2}\Lambda_\infty\left(\frac{\ell}{a}\right)\right)$$
$$\left.+\frac{2}{9\bar{r}}\left(3+\Upsilon_\infty\left(\frac{\ell}{a}\right)+2\Xi_\infty\left(\frac{\ell}{a}\right)\right)\right) \tag{D.58}$$

Utilizing the relation between $\bar{r}$ and $\bar{c}$ in Eq. B.2 as well as the explicit form of $\Sigma\left(\vec{x},0\right)$ in Eqs. B.6 and B.7 (again setting $g=4$) allows Eq. D.58 to be simplified to

$$\frac{(\delta m)^2}{\bar{m}^2} = \frac{1}{\pi a\bar{c}D_cT}\frac{1+\left(\Lambda_\infty\left(\frac{\ell}{a}\right)\right)^2+2\frac{a}{\ell}\Lambda_\infty\left(\frac{\ell}{a}\right)}{2\left(1+\Lambda_\infty\left(\frac{\ell}{a}\right)\right)^2}+\frac{1}{\mu\bar{r}T}\frac{2\left(1+\left(\Lambda_\infty\left(\frac{\ell}{a}\right)\right)^2\right)}{\left(1+\Lambda_\infty\left(\frac{\ell}{a}\right)\right)^2}$$
$$+\frac{1}{\beta\bar{r}T}\frac{\frac{5}{3}+\left(\Lambda_\infty\left(\frac{\ell}{a}\right)\right)^2+\frac{2}{9}\Upsilon_\infty\left(\frac{\ell}{a}\right)+\frac{4}{9}\Xi_\infty\left(\frac{\ell}{a}\right)}{\left(1+\Lambda_\infty\left(\frac{\ell}{a}\right)\right)^2} \tag{D.59}$$

The first term is the extrinsic noise, as in Eq. 4.28 of the main text. Let $\bar{r}$ be large enough such that the second two terms in Eq. D.59 can be neglected. Additionally, assume $\ell > a$. Under these, Eq. D.56a can be used to reduce Eq. D.59 to

$$\frac{(\delta m)^2}{\bar{m}^2} = \frac{1}{\pi a\bar{c}D_cT}\frac{1+\left(\frac{2a}{3\ell}\right)^2+2\frac{a}{\ell}\frac{2a}{3\ell}}{2\left(1+\frac{2a}{3\ell}\right)^2} = \frac{1}{\pi a\bar{c}D_cT}\frac{1+\frac{16a^2}{9\ell^2}}{2\left(1+\frac{2a}{3\ell}\right)^2} \tag{D.60}$$

The coefficient of $\frac{1}{\pi a\bar{c}D_cT}$ in Eq. D.60 achieves its minimum value of $\frac{2}{5}$ at $\ell^* = \frac{8}{3}a$, which is within the bounds of the $\ell > a$ assumption and is also presented in Eq. 4.29 of the main text.

E. CALCULATIONS FOR DIRECT TRANSPORT MODEL

We here assume a system of $N+1$ cells, one source cell and N target cells. The source cell produces morphogen at rate β, and we assume each target cell extends a cytoneme to the source cell capable of transporting the morphogen. To model the dynamics of the morphogen within the cytoneme, we use the model for [60] as it was shown that this model is capable of reproducing experimentally measured accumulation times. The steady state of this model was derived in [60], but for completeness and clarity of notational differences, we rederive the steady state solution here.

Let $u_+^j(x,t)$ and $u_-^j(x,t)$ be the density of forward and backward moving morphogen in the cytoneme leading to the jth target cell respectively and v_+ and v_- be the forward and backward moving velocities respectively. The source cell is capable of depositing morphogen into any cytoneme at a rate γ. The cytoneme can then deposit morphogen into the jth target cell at rate $r_+^j(t) = v_+ u_+^j\left(L_j,t\right)$, where L_j is the length of the jth cytoneme, and back into the source cell at rate $r_-^j(t) = v_- u_-^j(0,t)$. Additionally, backward moving morphogen can become forward moving at rate ζ_- and vice versa at rate ζ_+. Putting all this together with a production rate of β in the source cell and degradation rate ν in each target cell yields the equations

$$\frac{\partial m_0}{\partial t} = \beta - \sum_j \left(\gamma m_0 - r_-^j\right), \tag{E.1}$$

$$\frac{\partial u_+^j}{\partial t} = -v_+ \frac{\partial u_+^j}{\partial x} + \zeta_- u_-^j - \zeta_+ u_+^j + \gamma m_0 \delta(x) - r_+^j \delta\left(x - L_j\right), \tag{E.2}$$

$$\frac{\partial u_-^j}{\partial t} = v_- \frac{\partial u_-^j}{\partial x} - \zeta_- u_-^j + \zeta_+ u_+^j - r_-^j \delta(x), \tag{E.3}$$

$$\frac{\partial m_j}{\partial t} = r_+^j - \nu m_j. \tag{E.4}$$

To solve Eqs. E.1-E.4, let $J^j(x)$ be defined as

$$J^j(x) = v_+ \bar{u}_+^j(x) - v_- \bar{u}_-^j(x). \tag{E.5}$$

Setting the left-hand sides of Eqs. E.2 and E.3 to 0 and summing them then yields

$$0 = -\frac{\partial J^j(x)}{\partial x} + \left(\gamma \bar{m}_0 - \bar{r}_-^j\right)\delta(x) - \bar{r}_+^j \delta\left(x - L_j\right). \tag{E.6}$$

The fact that u_+^j, u_-^j, and J^j should only be defined within the jth cytoneme can be imposed by making each proportional to $H\left(x, L_j\right) = \Theta(x) - \Theta\left(x - L_j\right)$, where $\Theta(x)$ is the Heaviside step function. Given this, let $J^j(x) = K^j(x) H\left(x, L_j\right)$. Substituting this into Eq. E.6 then yields

$$\begin{aligned} 0 &= -H\left(x, L_j\right)\frac{\partial K^j(x)}{\partial x} - K^j(x)\frac{\partial H\left(x, L_j\right)}{\partial x} + \left(\gamma \bar{m}_0 - \bar{r}_-^j\right)\delta(x) - \bar{r}_+^j \delta\left(x - L_j\right) \\ &= -H\left(x, L_j\right)\frac{\partial K^j(x)}{\partial x} + \left(\gamma \bar{m}_0 - \bar{r}_-^j - K^j(x)\right)\delta(x) - \left(\bar{r}_+^j - K^j\left(L_j\right)\right)\delta\left(x - L_j\right). \end{aligned} \tag{E.7}$$

Eq. E.7 can be solved by taking $K^j(x)$ to be constant in space with a value of $\bar{r}_+^j = v_+ \bar{u}_+^j\left(L_j\right)$ and imposing the condition

$$\gamma \bar{m}_0 - \bar{r}_-^j - \bar{r}_+^j = \gamma \bar{m}_0 - v_- w_-^j(0) - v_+ w_+^j\left(L_j\right) = 0. \tag{E.8}$$

Now let $\bar{u}_+^j(x) = w_+^j(x) H\left(x, L_j\right)$ and $\bar{u}_-^j(x) = w_-^j(x) H\left(x, L_j\right)$. Substituting these and $K^j(x) = v_+ \bar{u}_+^j\left(L_j\right) = v_+ w_+^j\left(L_j\right)$ into Eq. E.6 then allows $w_-^j(x)$ to be written as

$$w_-^j(x) = \frac{v_+}{v_-}\left(w_+^j(x) - w_+^j\left(L_j\right)\right). \tag{E.9}$$

Once again setting the left-hand side of Eq. E.2 to 0, it can be rewritten in terms of $w_+^j(x)$ and $w_-^j(x)$. Substituting in Eq. E.9 as well as $\bar{r}_+^j = v_+ w_+\left(L_j\right)$ then yields

$$
\begin{aligned}
0 &= -v_+ w_+^j(x)\frac{\partial H\left(x,L_j\right)}{\partial x} - v_+ H\left(x,L_j\right)\frac{\partial w_+^j(x)}{\partial x} + \zeta_-\frac{v_+}{v_-}\left(w_+^j(x) - w_+\left(L_j\right)\right)H\left(x,L_j\right) - \zeta_+ w_+^j(x \\
&\quad + \gamma\bar{m}_0\delta(x) - v_+ w_+^j\left(L_j\right)\delta\left(x-L_j\right) \\
&= \left(-v_+\frac{\partial w_+^j(x)}{\partial x} + v_+\kappa w_+^j(x) - \zeta_-\frac{v_+}{v_-}w_+\left(L_j\right)\right)H\left(x,L_j\right) + \left(\gamma\bar{m}_0 - v_+ w_+^j(0)\right)\delta(x),
\end{aligned}
\tag{E.10}
$$

where

$$
\kappa = \frac{\zeta_-}{v_-} - \frac{\zeta_+}{v_+}. \tag{E.11}
$$

Once Eq. E.9 is substituted into Eq. E.8, the final two terms in Eq. E.10 are seen to vanish. This also allows the factor of $H\left(x,L_j\right)$ to be ignored if it is assumed the first three terms vanish for all x. Given this, Eq. E.10 can be solved by assuming $w_+^j(x)$ takes the form $C\left(e^{\kappa x}-1\right)+w_+^j(0)$. Substituting this into Eq. E.12 yields

$$
\begin{aligned}
0 &= -v_+\frac{\partial}{\partial x}\left(C\left(e^{\kappa x}-1\right)+w_+^j(0)\right) + v_+\kappa\left(C\left(e^{\kappa x}-1\right)+w_+^j(0)\right) - \zeta_-\frac{v_+}{v_-}\left(C\left(e^{\kappa L_j}-1\right)+w_+^j(0)\right) \\
&= -\frac{\zeta_+ v_- - \zeta_- v_+}{v_-}\left(w_+^j(0) - C\right) - \zeta_-\frac{v_+}{v_-}\left(C\left(e^{\kappa L_j}-1\right)+w_+^j(0)\right) \\
&= -\zeta_+\left(w_+^j(0) - C\left(1-e^{\phi+\kappa L_j}\right)\right),
\end{aligned}
\tag{E.12}
$$

where

$$
\phi = \log\left(\frac{\zeta_- v_+}{\zeta_+ v_-}\right). \tag{E.13}
$$

Solving Eq. E.8 for $w_+^j(0)$ and Eq. E.12 for C then allows $w_+^j(x)$ and $w_-^j(x)$ to be written as

$$
w_+^j(x) = \frac{w_+^j(0)}{1-e^{\phi+\kappa L_j}}\left(e^{\kappa x}-1\right) + w_+^j(0) = \frac{\gamma\bar{m}_0}{v_+}\frac{e^{\kappa x}-e^{\phi+\kappa L_j}}{1-e^{\phi+\kappa L_j}}, \tag{E.14}
$$

$$
w_-^j(x) = \frac{v_+}{v_-}\left(\frac{\gamma\bar{m}_0}{v_+}\frac{e^{\kappa x}-e^{\phi+\kappa L_j}}{1-e^{\phi+\kappa L_j}} - \frac{\gamma\bar{m}_0}{v_+}\frac{e^{\kappa L_j}-e^{\phi+\kappa L_j}}{1-e^{\phi+\kappa L_j}}\right) = \frac{\gamma\bar{m}_0}{v_-}\frac{e^{\kappa x}-e^{\kappa L_j}}{1-e^{\phi+\kappa L_j}}. \tag{E.15}
$$

This in turn forces $\bar{r}_+^j$ and $\bar{r}_-^j$ to take the forms

$$\bar{r}_+^j = v_+ w_+^j \left(L_j\right) = \gamma \bar{m}_0 e^{\kappa L_j} \frac{1 - e^{\phi}}{1 - e^{\phi + \kappa L_j}}, \tag{E.16}$$

$$\bar{r}_-^j = v_- w_-^j \left(0\right) = \gamma \bar{m}_0 \frac{1 - e^{\kappa L_j}}{1 - e^{\phi + \kappa L_j}}. \tag{E.17}$$

With these mean values solved for, $\bar{m}_0$ can now be solved. Setting the left-hand side of Eq. E.1 to 0 and substituting in Eq. E.17 yields

$$0 = \beta - \sum_j \left(\gamma \bar{m}_0 - \gamma \bar{m}_0 \frac{1 - e^{\kappa L_j}}{1 - e^{\phi + \kappa L_j}} \right) = \beta - \bar{m}_0 \sum_j \gamma e^{\kappa L_j} \frac{1 - e^{\phi}}{1 - e^{\phi + \kappa L_j}}, \tag{E.18}$$

which can then be solved to yield

$$\bar{m}_0 = \frac{\beta}{\sum_j \Gamma\left(L_j\right)}, \tag{E.19}$$

where

$$\Gamma\left(L\right) = \gamma e^{\kappa L} \frac{1 - e^{\phi}}{1 - e^{\phi + \kappa L}}. \tag{E.20}$$

Finally, the left-hand side of Eq. E.4 can be set to 0 and Eq. E.16 substituted in to yield

$$0 = \bar{m}_0 \Gamma\left(L_j\right) - \nu \bar{m}_j, \tag{E.21}$$

which when combined with Eq. E.19 can be solved to yield

$$\bar{m}_j = \frac{\beta}{\nu} \frac{\Gamma\left(L_j\right)}{\sum_k \Gamma\left(L_k\right)}. \tag{E.22}$$

Based on the form of Eq. E.21, $\Gamma(L_j)$ can be inferred to be an effective transport rate for morphogen molecules to go from the source cell to the jth target cell. This in turn implies that the fraction of total morphogen molecules that the jth target cell should receive is $\Gamma(L_j)/\sum_k \Gamma(L_k)$, which is precisely what is seen in Eq. E.22 given

that β/ν must be the total number of morphogen molecules within all the target cells. Of important note is that since ϕ and κ must have the same sign, $\Gamma(L)$ as defined in Eq. E.20 cannot be negative.

F. CALCULATIONS FOR SYNTHESIS-DIFFUSION-CLEARANCE MODEL

We here assume there is a single source cell which produces morphogen at rate β, and that the morphogen is subsequently released into the extracellular environment where it freely diffuses at rate D. The morphogen can also spontaneously degrade at rate ν. We will look at diffusion in a multitude of different spaces with different dimensions as well as morphogen sources that span a multitude of different dimensions. In each case, the sources will secrete morphogen molecules into a density field c which must follow

$$\frac{\partial c}{\partial t} = D\nabla^2 c + \eta_D - \nu c - \eta_\nu + \left(\beta + \eta_\beta\right)\delta^{SP-SO}\left(\vec{x}\right), \tag{F.1}$$

where SP is the number of spatial dimensions, SO is the dimensionality of the source, and ∇^2 is taken over all SP dimensions. Each η term is a Langevin noise term that represents Gaussian white noise for the diffusion, degradation, and production processes respectively. Of important note is that $\delta^{SP-SO}\left(\vec{x}\right)$ is a δ function only in the **last** $SP - SO$ dimensions of the space. So, for example, if there was a 1 dimensional source in 3 dimensional space, then $\delta^{3-1}\left(\vec{x}\right)$ would be a δ function in the $\hat{y}$ and $\hat{z}$ directions but not the $\hat{x}$ direction. This means that β and η_β will have units of $T^{-1}L^{-SO}$, where T is time and L is space.

We can now assume c has reached a steady state and separate it into $c = \bar{c} + \delta c$, which in turn allows Eq. F.1 to separate into

$$0 = D\nabla^2 \bar{c} - \nu\bar{c} + \beta\delta^{SP-SO}\left(\vec{x}\right) \tag{F.2}$$

$$\frac{\partial \delta c}{\partial t} = D\nabla^2 \delta c + \eta_D - \nu\delta c - \eta_\nu + \eta_\beta\delta^{SP-SO}\left(\vec{x}\right). \tag{F.3}$$

Fourier transforming Eq. F.2 in space and dividing it by ν then yields

$$0 = -\lambda^2 \left|\vec{k}\right|^2 \tilde{\bar{c}} - \tilde{\bar{c}} + \frac{\beta\lambda^2}{D} (2\pi)^{SO} \delta^{SO}\left(\vec{k}\right) \implies \tilde{\bar{c}} = \frac{\beta\lambda^2}{D} \frac{(2\pi)^{SO} \delta^{SO}\left(\vec{k}\right)}{1 + \lambda^2 \left|\vec{k}\right|^2}, \tag{F.4}$$

where $\lambda = \sqrt{D/\nu}$.

Of similarly important note is that $\delta^{SO}\left(\vec{k}\right)$ is a δ function only in the **first** SO dimensions of k-space. So in the 1 dimensional source, 3 dimensional space example $\delta^{SO}\left(\vec{k}\right)$ would be a δ function in the $\hat{x}$ direction of k-space but not the $\hat{y}$ or $\hat{z}$ directions.

This allows $\bar{\rho}$ to be written as

$$\begin{aligned} \bar{c}\left(\vec{x}\right) &= \int \frac{d^{SP}k}{(2\pi)^{SP}} e^{-i\vec{k}\cdot\vec{x}} \tilde{\bar{c}}\left(\vec{k}\right) = \frac{\beta\lambda^2}{D} \int \frac{d^{SP}k}{(2\pi)^{SP}} e^{-i\vec{k}\cdot\vec{x}} \frac{(2\pi)^{SO} \delta^{SO}\left(\vec{k}\right)}{1 + \lambda^2 \left|\vec{k}\right|^2} \\ &= \frac{\beta\lambda^2}{D} \int \frac{d^{SP-SO}k}{(2\pi)^{SP-SO}} e^{-i\vec{k}\cdot\vec{x}} \frac{1}{1 + \lambda^2 \left|\vec{k}\right|^2} = \frac{\beta\lambda^{2-(SP-SO)}}{D} P_{SP-SO}\left(\frac{|\vec{x}|}{\lambda}\right), \end{aligned} \tag{F.5}$$

where

$$P_N\left(x\right) = \int \frac{d^N u}{(2\pi)^N} e^{-i\vec{u}\cdot\vec{x}} \frac{1}{1 + |\vec{u}|^2}. \tag{F.6}$$

It is important to note that P_N does not integrate over all available dimensions, but only over the last N dimensions of the space. This in turn means that its argument can only depend on the last N dimensions of any input vector. Returning to the 1 dimensional source, 3 dimensional space example, $P_{3-1}\left(|\vec{x}|/\lambda\right)$ should only take the y and z components of $\vec{x}$ into account. The x component is made irrelevant by the translational symmetry of the system along the x-axis.

Moving on to the noise terms, Eq. F.3 can be Fourier transformed in space and time to yield

$$-i\omega\tilde{\delta c} = -D\left|\vec{k}\right|^2 \tilde{\delta c} + \tilde{\eta}_D - \nu\tilde{\delta c} - \tilde{\eta}_\nu + \tilde{\eta}_\beta \implies \tilde{\delta c} = \frac{\tilde{\eta}_D - \tilde{\eta}_\nu + \tilde{\eta}_\beta}{\nu\left(1 + \lambda^2\left|\vec{k}\right|^2 - i\frac{\omega}{\nu}\right)}, \quad \text{(F.7)}$$

where $\eta_\beta\left(\vec{k},\omega\right)$ depends only on the first SO dimensions of k-space. Assuming the η terms are all independent of each other allows the cross spectrum of c to be

$$\left\langle \tilde{\delta c}^{\,*}\left(\vec{k}',\omega'\right)\tilde{\delta c}\left(\vec{k},\omega\right)\right\rangle = \frac{1}{\nu^2\left(1+\lambda^2\left|\vec{k}\right|^2 - i\frac{\omega}{\nu}\right)\left(1+\lambda^2\left|\vec{k}'\right|^2 + i\frac{\omega'}{\nu}\right)}$$
$$\cdot\left(\left\langle\tilde{\eta}_D^*\left(\vec{k}',\omega'\right)\tilde{\eta}_D\left(\vec{k},\omega\right)\right\rangle + \left\langle\tilde{\eta}_\nu^*\left(\vec{k}',\omega'\right)\tilde{\eta}_\nu\left(\vec{k},\omega\right)\right\rangle + \left\langle\tilde{\eta}_\beta^*\left(\vec{k}',\omega'\right)\tilde{\eta}_\beta\left(\vec{k},\omega\right)\right\rangle\right). \quad \text{(F.8)}$$

The cross spectrum of η_D is that of a diffusive term and thus follows the form derived in Eq. A.9.

$$\left\langle\eta_D\left(\vec{x}',t'\right)\eta_D\left(\vec{x},t\right)\right\rangle = 2D\delta\left(t-t'\right)\vec{\nabla}\cdot\vec{\nabla}'\left(\bar{c}\left(\vec{x}\right)\delta^{SP}\left(\vec{x}-\vec{x}'\right)\right). \quad \text{(F.9)}$$

Fourier transforming Eq. F.9 can be easily performed due to the δ functions, integrating the spatial terms by parts, and utilizing Eq. F.4 to yield

$$\begin{aligned}
\left\langle \tilde{\eta}_D^* \left(\vec{k}', \omega'\right) \tilde{\eta}_D \left(\vec{k}, \omega\right) \right\rangle &= \int d^{SP}x d^{SP}x' dt dt' e^{i\vec{k}\cdot\vec{x}} e^{-i\vec{k}'\cdot\vec{x}'} e^{i\omega t} e^{-i\omega' t'} \left\langle \eta_D \left(\vec{x}', t'\right) \eta_D \left(\vec{x}, t\right) \right\rangle \\
&= 2D \int d^{SP}x d^{SP}x' dt dt' e^{i\vec{k}\cdot\vec{x}} e^{-i\vec{k}'\cdot\vec{x}'} e^{i\omega t} e^{-i\omega' t'} \delta\left(t - t'\right) \vec{\nabla}\cdot\vec{\nabla}' \left(\bar{c}\left(\vec{x}\right) \delta^{SP}\left(\vec{x} - \vec{x}'\right)\right) \\
&= 2D \left(2\pi\delta\left(\omega - \omega'\right)\right) \int d^{SP}x d^{SP}x' e^{i\vec{k}\cdot\vec{x}} e^{-i\vec{k}'\cdot\vec{x}'} \vec{\nabla}\cdot\vec{\nabla}' \left(\bar{c}\left(\vec{x}\right) \delta^{SP}\left(\vec{x} - \vec{x}'\right)\right) \\
&= 2D \left(2\pi\delta\left(\omega - \omega'\right)\right) \int d^{SP}x d^{SP}x' \bar{c}\left(\vec{x}\right) \delta^{SP}\left(\vec{x} - \vec{x}'\right) \vec{\nabla}\cdot\vec{\nabla}' \left(e^{i\vec{k}\cdot\vec{x}} e^{-i\vec{k}'\cdot\vec{x}'}\right) \\
&= 2D\vec{k}\cdot\vec{k}' \left(2\pi\delta\left(\omega - \omega'\right)\right) \int d^{SP}x d^{SP}x' \bar{c}\left(\vec{x}\right) \delta^{SP}\left(\vec{x} - \vec{x}'\right) e^{i\vec{k}\cdot\vec{x}} e^{-i\vec{k}'\cdot\vec{x}'} \\
&= 2D\vec{k}\cdot\vec{k}' \left(2\pi\delta\left(\omega - \omega'\right)\right) \int d^{SP}x \bar{c}\left(\vec{x}\right) e^{i\vec{x}\left(\vec{k} - \vec{k}'\right)} \\
&= 2D\vec{k}\cdot\vec{k}' \tilde{\bar{c}}\left(\vec{k} - \vec{k}'\right) \left(2\pi\delta\left(\omega - \omega'\right)\right) \\
&= \frac{2\lambda^2 \vec{k}\cdot\vec{k}'}{1 + \lambda^2 \left|\vec{k} - \vec{k}'\right|^2} \left(\beta \left(2\pi\right)^{SO+1} \delta\left(\omega - \omega'\right) \delta^{SO}\left(\vec{k} - \vec{k}'\right)\right).
\end{aligned} \tag{F.10}$$

Moving on to η_ν, its correlation function must be δ correlated in time and space since it is a purely local reaction and as such, at steady state, must take the form

$$\left\langle \eta_\nu \left(\vec{x}', t'\right) \eta_\nu \left(\vec{x}, t\right) \right\rangle = \nu \bar{c}\left(\vec{x}\right) \delta\left(t - t'\right) \delta^{SP}\left(\vec{x} - \vec{x}'\right). \tag{F.11}$$

Fourier transforming Eq. F.11 is again easily performed due to the δ functions and Eq. F.4. This yields

$$\begin{aligned}
\left\langle \tilde{\eta}_\nu^* \left(\vec{k}', \omega'\right) \tilde{\eta}_\nu \left(\vec{k}, \omega\right) \right\rangle &= \int d^{SP}x d^{SP}x' dt dt' e^{i\vec{k}\cdot\vec{x}} e^{-i\vec{k}'\cdot\vec{x}'} e^{i\omega t} e^{-i\omega' t'} \left\langle \eta_\nu \left(\vec{x}', t'\right) \eta_\nu \left(\vec{x}, t\right) \right\rangle \\
&= \nu \int d^{SP}x d^{SP}x' dt dt' e^{i\vec{k}\cdot\vec{x}} e^{-i\vec{k}'\cdot\vec{x}'} e^{i\omega t} e^{-i\omega' t'} \bar{c}\left(\vec{x}\right) \delta\left(t - t'\right) \delta^{SP}\left(\vec{x} - \vec{x}'\right) \\
&= \nu \left(2\pi\delta\left(\omega - \omega'\right)\right) \int d^{SP}x d^{SP}x' e^{i\vec{k}\cdot\vec{x}} e^{-i\vec{k}'\cdot\vec{x}'} \bar{c}\left(\vec{x}\right) \delta^{SP}\left(\vec{x} - \vec{x}'\right) \\
&= \nu \left(2\pi\delta\left(\omega - \omega'\right)\right) \int d^{SP}x e^{i\vec{x}\cdot\left(\vec{k} - \vec{k}'\right)} \bar{c}\left(\vec{x}\right) \\
&= \nu\tilde{\bar{c}}\left(\vec{k} - \vec{k}'\right) \left(2\pi\delta\left(\omega - \omega'\right)\right) \\
&= \frac{1}{1 + \lambda^2 \left|\vec{k} - \vec{k}'\right|^2} \left(\beta \left(2\pi\right)^{SO+1} \delta\left(\omega - \omega'\right) \delta^{SO}\left(\vec{k} - \vec{k}'\right)\right).
\end{aligned} \tag{F.12}$$

Finally, the cross spectrum of η_β must be δ correlated in ω-space as well as all source dimensions of k-space since it is merely a uniform production term that does not depend on space or time. This yields

$$\left\langle \tilde{\eta}_\beta^* \left(\vec{k}', \omega'\right) \tilde{\eta}_\beta \left(\vec{k}, \omega\right) \right\rangle = \beta \left(2\pi\right)^{SO+1} \delta\left(\omega - \omega'\right) \delta^{SO}\left(\vec{k} - \vec{k}'\right). \tag{F.13}$$

Combining Eqs. F.8, F.10, F.12, and F.13 then yields

$$\begin{aligned}
\left\langle \tilde{\delta c}^{\,*} \left(\vec{k}', \omega'\right) \tilde{\delta c} \left(\vec{k}, \omega\right) \right\rangle &= \frac{\beta \left(2\pi\right)^{SO+1} \delta\left(\omega - \omega'\right) \delta^{SO}\left(\vec{k} - \vec{k}'\right)}{\nu^2 \left(1 + \lambda^2 \left|\vec{k}\right|^2 - i\frac{\omega}{\nu}\right)\left(1 + \lambda^2 \left|\vec{k}'\right|^2 + i\frac{\omega'}{\nu}\right)} \\
&\quad \cdot \left(\frac{2\lambda^2 \vec{k} \cdot \vec{k}'}{1 + \lambda^2 \left|\vec{k} - \vec{k}'\right|^2} + \frac{1}{1 + \lambda^2 \left|\vec{k} - \vec{k}'\right|^2} + 1 \right) \\
&= \frac{\beta \left(2\pi\right)^{SO+1} \delta\left(\omega - \omega'\right) \delta^{SO}\left(\vec{k} - \vec{k}'\right)}{\nu^2 \left(1 + \lambda^2 \left|\vec{k}\right|^2 - i\frac{\omega}{\nu}\right)\left(1 + \lambda^2 \left|\vec{k}'\right|^2 + i\frac{\omega'}{\nu}\right)} \frac{2 + \lambda^2 \left(\left|\vec{k}\right|^2 + \left|\vec{k}'\right|^2\right)}{1 + \lambda^2 \left|\vec{k} - \vec{k}'\right|^2} \\
&= \frac{\tilde{\tilde{c}}\left(\vec{k} - \vec{k}'\right)\left(2\pi\delta\left(\omega - \omega'\right)\right)\left(2 + \lambda^2 \left(\left|\vec{k}\right|^2 + \left|\vec{k}'\right|^2\right)\right)}{\nu \left(1 + \lambda^2 \left|\vec{k}\right|^2 - i\frac{\omega}{\nu}\right)\left(1 + \lambda^2 \left|\vec{k}'\right|^2 + i\frac{\omega'}{\nu}\right)}.
\end{aligned} \tag{F.14}$$

We now define m as

$$m\left(\vec{x}, t\right) = \int_{V(a)} d^{SP} r c\left(\vec{x} + \vec{r}, t\right), \tag{F.15}$$

where $V\left(a\right)$ is a SP-dimensional sphere with radius a. This allows the mean value of m to be written as

$$\begin{aligned}
\bar{m}\left(\vec{x}\right) &= \int_{V(a)} d^{SP} r \bar{c}\left(\vec{x} + \vec{r}\right) = \frac{\beta \lambda^{2-(SP-SO)}}{D} \int_{V(a)} d^{SP} r P_{SP-SO}\left(\frac{\left|\vec{x} + \vec{r}\right|}{\lambda}\right) \\
&= \frac{\beta \lambda^{SO}}{\nu} M_{SP-SO,SP}\left(\frac{\left|\vec{x}\right|}{\lambda}, \frac{a}{\lambda}\right),
\end{aligned} \tag{F.16}$$

where

$$M_{N,N'}(x,y) = \int_{V(y)} d^{N'}u P_N\left(|\vec{x}+\vec{u}|\right). \tag{F.17}$$

Since $P_N\left(|\vec{x}|\right)$ can only depend on the last N dimensions of its input vectors, the same must be true of $M_{N,N'}$. From here we define $S(\vec{x})$ as the 0-frequency limit of the cross spectrum in ω-space of m. This allows it to take the form

$$
\begin{aligned}
S\left(\vec{x}\right) &= \lim_{\omega\to 0}\int \frac{d\omega'}{2\pi}\left\langle \tilde{\delta m}^{\,*}\left(\vec{x},\omega'\right)\tilde{\delta m}\left(\vec{x},\omega\right)\right\rangle \\
&= \lim_{\omega\to 0}\int \frac{d\omega'}{2\pi}\int_{V(a)} d^{SP}r d^{SP}r' \int \frac{d^{SP}k}{\left(2\pi\right)^{SP}}\frac{d^{SP}k'}{\left(2\pi\right)^{SP}} e^{-i\vec{k}\cdot\left(\vec{x}+\vec{r}\right)} e^{i\vec{k}'\cdot\left(\vec{x}+\vec{r}'\right)}\left\langle \tilde{\delta c}^{\,*}\left(\vec{k}',\omega'\right)\tilde{\delta c}\left(\vec{k},\omega\right)\right\rangle \\
&= \frac{1}{\left(2\pi\right)^{2SP}\nu}\int_{V(a)} d^{SP}r d^{SP}r' \int d^{SP}k d^{SP}k' e^{-i\vec{k}\cdot\left(\vec{x}+\vec{r}\right)} e^{i\vec{k}'\cdot\left(\vec{x}+\vec{r}'\right)} \\
&\qquad \cdot \frac{\tilde{\bar{c}}\left(\vec{k}-\vec{k}'\right)\left(2+\lambda^2\left(\left|\vec{k}\right|^2+\left|\vec{k}'\right|^2\right)\right)}{\left(1+\lambda^2\left|\vec{k}\right|^2\right)\left(1+\lambda^2\left|\vec{k}'\right|^2\right)} \\
&= \frac{1}{\left(2\pi\right)^{2SP}\nu}\int_{V(a)} d^{SP}r d^{SP}r' \int d^{SP}k d^{SP}k' d^{SP}z e^{-i\vec{k}\cdot\left(\vec{x}+\vec{r}\right)} e^{i\vec{k}'\cdot\left(\vec{x}+\vec{r}'\right)} e^{i\vec{z}\cdot\left(\vec{k}-\vec{k}'\right)} \\
&\qquad \cdot \bar{c}\left(\vec{z}\right)\frac{2+\lambda^2\left(\left|\vec{k}\right|^2+\left|\vec{k}'\right|^2\right)}{\left(1+\lambda^2\left|\vec{k}\right|^2\right)\left(1+\lambda^2\left|\vec{k}'\right|^2\right)} \\
&= \frac{1}{\left(2\pi\right)^{2SP}\nu}\int_{V(a)} d^{SP}r d^{SP}r' \int d^{SP}k d^{SP}k' d^{SP}z e^{-i\vec{k}\cdot\left(\vec{x}+\vec{r}-\vec{z}\right)} e^{i\vec{k}'\cdot\left(\vec{x}+\vec{r}'-\vec{z}\right)} \\
&\qquad \cdot \bar{c}\left(\vec{z}\right)\left(\frac{1}{1+\lambda^2\left|\vec{k}\right|^2}+\frac{1}{1+\lambda^2\left|\vec{k}'\right|^2}\right) \\
&= \frac{1}{\left(2\pi\right)^{2SP}\nu}\int_{V(a)} d^{SP}r d^{SP}r' \int d^{SP}z\bar{c}\left(\vec{z}\right)\left(\int d^{SP}k e^{-i\vec{k}\cdot\left(\vec{x}+\vec{r}-\vec{z}\right)}\frac{\left(2\pi\right)^{SP}\delta^{SP}\left(\vec{x}+\vec{r}'-\vec{z}\right)}{1+\lambda^2\left|\vec{k}\right|^2}\right. \\
&\qquad \left. + \int d^{SP}k' e^{i\vec{k}'\cdot\left(\vec{x}+\vec{r}'-\vec{z}\right)}\frac{\left(2\pi\right)^{SP}\delta^{SP}\left(\vec{x}+\vec{r}-\vec{z}\right)}{1+\lambda^2\left|\vec{k}'\right|^2}\right)
\end{aligned}
$$

$$
\begin{aligned}
&= \frac{\beta\lambda^{2-(SP-SO)}}{D\nu\lambda^{SP}} \int_{V(a)} d^{SP}r d^{SP}r' \int d^{SP}z P_{SP-SO}\left(\frac{|\vec{z}|}{\lambda}\right) \\
&\quad \cdot \left(\delta^{SP}\left(\vec{x}+\vec{r}'-\vec{z}\right) P_{SP}\left(\frac{|\vec{x}+\vec{r}-\vec{z}|}{\lambda}\right) + \delta^{SP}\left(\vec{x}+\vec{r}-\vec{z}\right) P_{SP}\left(\frac{|\vec{x}+\vec{r}'-\vec{z}|}{\lambda}\right)\right) \\
&= \frac{\beta\lambda^{4-(2SP-SO)}}{D^2} \int_{V(a)} d^{SP}r d^{SP}r' P_{SP}\left(\frac{|\vec{r}-\vec{r}'|}{\lambda}\right)\left(P_{SP-SO}\left(\frac{|\vec{x}+\vec{r}|}{\lambda}\right) + P_{SP-SO}\left(\frac{|\vec{x}+\vec{r}'|}{\lambda}\right)\right) \\
&= \frac{\beta\lambda^{4-(SP-SO)}}{D^2}\left(\int_{V(a)} d^{SP}r M_{SP,SP}\left(\frac{|\vec{r}|}{\lambda},\frac{a}{\lambda}\right) P_{SP-SO}\left(\frac{|\vec{x}+\vec{r}|}{\lambda}\right)\right. \\
&\quad \left. + \int_{V(a)} d^{SP}r' M_{SP,SP}\left(\frac{|\vec{r}'|}{\lambda},\frac{a}{\lambda}\right) P_{SP-SO}\left(\frac{|\vec{x}+\vec{r}'|}{\lambda}\right)\right) \\
&= \frac{2\beta\lambda^{4-(SP-SO)}}{D^2} \int_{V(a)} d^{SP}r M_{SP,SP}\left(\frac{|\vec{r}|}{\lambda},\frac{a}{\lambda}\right) P_{SP-SO}\left(\frac{|\vec{x}+\vec{r}|}{\lambda}\right) \\
&= \frac{2\beta\lambda^{SO}}{\nu^2}\Sigma_{SP-SO,SP}\left(\frac{|\vec{x}|}{\lambda},\frac{a}{\lambda}\right),
\end{aligned} \tag{F.18}
$$

where

$$
\Sigma_{N,N'}(x,y) = \int_{V(y)} d^{N'}u M_{N',N'}(u,y) P_N\left(|\vec{x}+\vec{u}|\right). \tag{F.19}
$$

Wherein once again only the last N dimensions of the input vectors can be taken into account. Combining Eqs. F.16 and F.18 yields the full 0-frequency noise-to-signal ratio of m to be

$$
\frac{\delta m_T^2}{\bar{m}^2} = \frac{S}{\bar{m}^2 T} = \frac{2}{\bar{m}\nu T}\frac{\Sigma_{SP-SO,SP}\left(\frac{|\vec{x}|}{\lambda},\frac{a}{\lambda}\right)}{M_{SP-SO,SP}\left(\frac{|\vec{x}|}{\lambda},\frac{a}{\lambda}\right)} = \frac{2}{\lambda^{SO}\beta T}\frac{\Sigma_{SP-SO,SP}\left(\frac{|\vec{x}|}{\lambda},\frac{a}{\lambda}\right)}{\left(M_{SP-SO,SP}\left(\frac{|\vec{x}|}{\lambda},\frac{a}{\lambda}\right)\right)^2}. \tag{F.20}
$$

With Eq. F.20, once the forms of P_N, $M_{N,N'}$, and $\Sigma_{N,N'}$ are determined for a given SP and SO, the full form of the noise-to-signal ratio can be found. We now calculate these forms for specific choices of SP and SO.

F.1 1D space, 0D source

To begin, we start with the simple scenario in which $SP = 1$ and $SO = 0$. This allows P_1, $M_{1,1}$, and $\Sigma_{1,1}$ to take the forms

$$P_1(x) = \int \frac{du}{2\pi} e^{-iux} \frac{1}{1+u^2} = \frac{1}{2} e^{-|x|} \tag{F.21}$$

$$\begin{aligned} M_{1,1}(x,y) &= \int_{-y}^{y} du P_1\left(|x+u|\right) = \frac{1}{2}\int_{-y}^{y} du e^{-|x+u|} \\ &= \begin{cases} 1 - e^{-y}\cosh(x) & x < y \\ e^{-x}\sinh(y) & x \geq y \end{cases} \end{aligned} \tag{F.22}$$

$$\begin{aligned} \Sigma_{1,1}(x,y) &= \int_{-y}^{y} du M_{1,1}(u,y) P_1\left(|x+u|\right) = \frac{1}{2}\int_{-y}^{y} du \left(1 - e^{-y}\cosh(u)\right) e^{-|x+u|} \\ &= \begin{cases} 1 - \frac{1}{4}e^{-y}\left(\left(5 + 2y - e^{-2y}\right)\cosh(x) - 2x\sinh(x)\right) & x < y \\ \frac{1}{4}e^{-x}\left(4\sinh(y) - e^{-y}\left(2y + \sinh(2y)\right)\right) & x \geq y \end{cases} . \end{aligned} \tag{F.23}$$

Eqs. F.22 and F.23 can then be put into Eq. F.20 along with the assumption $|x| > a$ to obtain

$$\frac{\delta m_T^2}{\bar{m}^2} = \frac{2}{\bar{m}\nu T}\left(1 - e^{-\frac{a}{\lambda}} \frac{\frac{2a}{\lambda} + \sinh\left(\frac{2a}{\lambda}\right)}{4\sinh\left(\frac{a}{\lambda}\right)}\right). \tag{F.24}$$

F.2 2D space, 0D source

For $SP = 2$ and $SO = 0$, P_2, $M_{2,2}$, and $\Sigma_{2,2}$ each take the form

$$P_2(x) = \int \frac{d^2u}{(2\pi)^2} e^{-i\vec{u}\cdot\vec{x}} \frac{1}{1+|\vec{u}|^2} = \frac{1}{2\pi} K_0(x) \tag{F.25}$$

$$M_{2,2}(x,y) = \int_{V(y)} d^2u P_2\left(\left|\vec{x}+\vec{u}\right|\right) = \int_{V(y)} d^2u \int \frac{d^2u'}{(2\pi)^2} e^{-i\vec{u}'\cdot(\vec{x}+\vec{u})} \frac{1}{1+\left|\vec{u}'\right|^2}$$
$$= y\int_0^\infty du' \frac{J_0(xu')\,J_1(yu')}{1+u'^2} \tag{F.26}$$

$$\Sigma_{2,2}(x,y) = \int_{V(y)} d^2u M_{2,2}\left(\left|\vec{u}\right|,y\right) P_2\left(\left|\vec{x}+\vec{u}\right|\right)$$
$$= y\int_{V(y)} d^2u \int_0^\infty du' \int \frac{d^2u''}{(2\pi)^2} \frac{J_0\left(\left|\vec{u}\right|u'\right) J_1(yu')}{1+u'^2} \frac{e^{-i\vec{u}''\cdot(\vec{x}+\vec{u})}}{1+\left|\vec{u}''\right|^2}$$
$$= y^2\int_0^\infty du'du'' \frac{u''J_0(xu'')\,J_1(yu')\left(u'J_0(yu'')\,J_1(yu') - u''J_0(yu')\,J_1(yu'')\right)}{\left(u'^2-u''^2\right)\left(1+u'^2\right)\left(1+u''^2\right)}, \tag{F.27}$$

where $J_n(x)$ and $K_n(x)$ are the Bessel functions of the first kind and modified Bessel functions of the second kind respectively. Unfortunately, the complicated nature of Bessel functions makes the remaining integrals unsolvable analytically. Similar problems arise whenever $SP = 2$ or $SP - SO = 2$.

F.3 3D space, 0D source

For $SP = 3$ and $SO = 0$, P_3, $M_{3,3}$, and $\Sigma_{3,3}$ each take the form

$$P_3(x) = \int \frac{d^3u}{(2\pi)^3} e^{-i\vec{u}\cdot\vec{x}} \frac{1}{1+\left|\vec{u}\right|^2} = \frac{1}{4\pi x} e^{-x} \tag{F.28}$$

$$M_{3,3}(x,y) = \int_{V(y)} d^3u P_3\left(\left|\vec{x}+\vec{u}\right|\right) = \frac{1}{4\pi}\int_{V(y)} d^3u \frac{1}{\left|\vec{x}+\vec{u}\right|} e^{-\left|\vec{x}+\vec{u}\right|}$$
$$= \begin{cases} 1 - \frac{1+y}{x} e^{-y}\sinh(x) & x < y \\ \frac{1}{x} e^{-x}\left(y\cosh(y) - \sinh(y)\right) & x \geq y \end{cases} \tag{F.29}$$

$$\begin{aligned}\Sigma_{3,3}(x,y) &= \int_{V(y)} d^3u M_{3,3}\left(|\vec{u}|, y\right) P_3\left(|\vec{x}+\vec{u}|\right) \\ &= \frac{1}{4\pi}\int_{V(y)} d^3u \left(1 - \frac{1+y}{|\vec{u}|}e^{-y}\sinh\left(|\vec{u}|\right)\right)\frac{1}{|\vec{x}+\vec{u}|}e^{-|\vec{x}+\vec{u}|} \\ &= \begin{cases} 1 - \frac{1}{4x}e^{-y}(1+y)\left(\left(5+2y+e^{-2y}\right)\sinh(x) - 2x\cosh(x)\right) & x < y \\ \frac{1}{4x}e^{-x}\left(4\left(y\cosh(y)-\sinh(y)\right) + e^{-y}(1+y)\left(2y-\sinh(2y)\right)\right) & x \geq y \end{cases}\end{aligned} \tag{F.30}$$

F.4 2D space, 1D source

For $SP = 2$, $SO = 1$, P_1 and $M_{2,2}$ are known from Eqs. F.21 and F.26. This leaves $M_{1,2}$ and $\Sigma_{1,2}$ to take the forms

$$\begin{aligned}M_{1,2}(x,y) &= \int_{V(y)} d^2u P_1\left(|\vec{x}+\vec{u}|\right) = \frac{1}{2}\int_0^y du \int_0^{2\pi} d\theta u e^{-|x_2+u_2|} \\ &= e^{-|x_2|}\int_0^{2\pi} d\theta \frac{1 - e^{-y\sin(\theta)}\left(1+y\sin(\theta)\right)}{2\left(\sin(\theta)\right)^2}\end{aligned} \tag{F.31}$$

$$\begin{aligned}\Sigma_{1,2}(x,y) &= \int_{V(y)} d^2u M_{2,2}\left(|\vec{u}|, y\right) P_1\left(|\vec{x}+\vec{u}|\right) \\ &= \frac{y}{2}\int_0^y du \int_0^{2\pi} d\theta \int_0^{\infty} du' u \frac{J_0(uu')\,J_1(yu')}{1+u'^2} e^{-|x_2+u\sin(\theta)|}\end{aligned} \tag{F.32}$$

Unfortunately, the remaining integrals are unsolvable analytically.

F.5 3D space, 2D source

For $SP = 3$, $SO = 2$, P_1 and $M_{3,3}$ are known from Eqs. F.21 and F.29. This leaves $M_{1,3}$ and $\Sigma_{1,3}$ to take the forms

$$M_{1,3}(x,y) = \int_{V(y)} d^3u P_1\left(|\vec{x}+\vec{u}|\right) = \frac{1}{2}\int_{V(y)} d^3u e^{-|x_3+u_3|}$$
$$= 2\pi \begin{cases} e^{-y}(1+y)\cosh(x) + \frac{y^2-x^2}{2} - 1 & x < y \\ e^{-x}\left(y\cosh(y) - \sinh(y)\right) & x \geq y \end{cases} \tag{F.33}$$

$$\Sigma_{1,3}(x,y) = \int_{V(y)} d^3u M_{3,3}\left(|\vec{u}|, y\right) P_1\left(|\vec{x}+\vec{u}|\right)$$
$$= \frac{1}{2}\int_{V(y)} d^3u \left(1 - \frac{1+y}{|\vec{u}|}e^{-y}\sinh\left(|\vec{u}|\right)\right) e^{-|x_3+u_3|}$$
$$= 2\pi \begin{cases} e^{-y}(1+y)\left(\frac{7+2y+e^{-2y}}{4}\cosh(x) - \frac{x}{2}\sinh(x) - \cosh(y)\right) + \frac{y^2-x^2}{2} - 1 & x < y \\ e^{-x}\left(\frac{4y^2+5y-1}{8}e^{-y} + \frac{1+y}{8}e^{-3y} + \frac{3y}{4}\cosh(y) - \frac{5}{4}\sinh(y)\right) & x \geq y \end{cases} \tag{F.34}$$

G. CALCULATIONS FOR HOPPING MODEL OF DIFFUSION

To obtain a more intuitive understanding of why the SDC model results in the scaling properties seen in the various calculations of $M_{\mathrm{SP-SO,SP}}$ and $\Sigma_{\mathrm{SP-SO,SP}}$, we now look at a simpler version of one dimensional diffusion in which we discretize space into compartments of uniform size. Let molecules still be produced in the 0th compartment at rate β and degrade anywhere in space at rate ν. The process of diffusion can be approximated by letting the molecules hop to neighboring compartments with rate h with equal probability of moving left or right. This allows the dynamics of m_j, the number of molecules in the j compartment for $j \in \mathbb{Z}$, to be written as

$$\frac{\partial m_j}{\partial t} = \beta\delta_{0j} + h\left(m_{j+1} + m_{j-1} - 2m_j\right) - \nu m_j. \tag{G.1}$$

By setting the left-hand side of Eq. G.1 to 0, the resulting system of equations can be easily solved by assuming $\bar{m}_j = A\exp(-2|j|/\lambda)$ and calculating A and λ. Imposing this assumption on Eq. G.1 and taking $j > 0$ yields

$$\begin{aligned} 0 &= h\left(Ae^{-\frac{2(j+1)}{\lambda}} + Ae^{-\frac{2(j-1)}{\lambda}} - 2Ae^{-\frac{2j}{\lambda}}\right) - \nu Ae^{-\frac{2j}{\lambda}} = Ae^{-\frac{2j}{\lambda}}\left(he^{-\frac{2}{\lambda}} + he^{\frac{2}{\lambda}} - 2h - \nu\right) \\ &= Ae^{-\frac{2j}{\lambda}}\left(4h\sinh^2\left(\frac{1}{\lambda}\right) - \nu\right) \\ &\implies \lambda = \operatorname{asinh}^{-1}\left(\sqrt{\frac{\nu}{4h}}\right). \end{aligned} \tag{G.2}$$

With λ solved for, we solve for the proportionality constant by noting that the total number of molecules in the whole system must follow a simple birth-death process with a mean of β/ν. This in turn implies

$$\frac{\beta}{\nu} = \sum_{j=-\infty}^{\infty} Ae^{-\frac{2|j|}{\lambda}} = A\left(2\left(\sum_{j=0}^{\infty} e^{-\frac{2j}{\lambda}}\right) - 1\right) = A\left(\frac{2}{1-e^{-\frac{2}{\lambda}}} - 1\right) = A\left(\frac{e^{\frac{1}{\lambda}}}{\sinh\left(\frac{1}{\lambda}\right)} - 1\right)$$
$$= A\coth\left(\frac{1}{\lambda}\right)$$
$$\implies A = \frac{\beta}{\nu}\tanh\left(\frac{1}{\lambda}\right), \tag{G.3}$$

This in turn gives the average value of m_j to be

$$\bar{m}_j = \frac{\beta}{\nu}\tanh\left(\frac{1}{\lambda}\right)e^{-\frac{2|j|}{\lambda}}. \tag{G.4}$$

Next, we calculate the full distribution of m_j by assuming that at any given moment in time each molecule in the system has probability P_j of being in the jth compartment. This can be combined with the aforementioned fact that N, the total number of molecules in the system, must follow a birth-death process and thus to Poissonianly distributed with mean β/ν. For any given value of N, $P(m_j|N)$ must be a binomial distribution with success probability P_j since each molecule is independent. This allows the marginal distribution $P(m_j)$ to be calculated to be

$$P\left(m_j\right) = \sum_{N=m_j}^{\infty} P\left(N\right)P\left(m_j|N\right) = \sum_{N=m_j}^{\infty} e^{-\frac{\beta}{\nu}}\frac{\left(\frac{\beta}{\nu}\right)^N}{N!}\binom{N}{m_j}P_j^{m_j}\left(1-P_j\right)^{N-m_j}$$
$$= e^{-\frac{\beta}{\nu}}\frac{\left(\frac{\beta}{\nu}P_j\right)^{m_j}}{m_j!}\sum_{N=m_j}^{\infty}\frac{\left(\frac{\beta}{\nu}\left(1-P_j\right)\right)^{N-m_j}}{\left(N-m_j\right)!} = e^{-\frac{\beta}{\nu}}\frac{\left(\frac{\beta}{\nu}P_j\right)^{m_j}}{m_j!}e^{\frac{\beta}{\nu}\left(1-P_j\right)}$$
$$= e^{-\frac{\beta}{\nu}P_j}\frac{\left(\frac{\beta}{\nu}P_j\right)^{m_j}}{m_j!}. \tag{G.5}$$

Thus, m_j is seen to be Poissonianly distributed with mean $\beta P_j/\nu$. Comparing this mean to that derived in Eq. G.4 then implies

$$P_j = \tanh\left(\frac{1}{\lambda}\right)e^{-\frac{2|j|}{\lambda}}. \tag{G.6}$$

We now consider the joint distribution of m_j and m_k for $j \neq k$. Since molecules cannot be in the jth and kth compartment simultaneously, the joint conditional distribution $P(m_j, m_k|N)$ must be trinomially distributed. This allows for the joint distribution to be calculated in a manner similar to Eq. G.5 to produce

$$\begin{aligned}
P\left(m_j, m_k\right) &= \sum_{N=m_j+m_k}^{\infty} P\left(N\right) P\left(m_j, m_k|N\right) \\
&= \sum_{N=m_j+m_k}^{\infty} e^{-\frac{\beta}{\nu}} \frac{\left(\frac{\beta}{\nu}\right)^N}{N!} \binom{N}{m_j, m_k} P_j^{m_j} P_k^{m_k} \left(1 - P_j - P_k\right)^{N-m_j-m_k} \\
&= e^{-\frac{\beta}{\nu}} \frac{\left(\frac{\beta}{\nu} P_j\right)^{m_j}}{m_j!} \frac{\left(\frac{\beta}{\nu} P_k\right)^{m_k}}{m_k!} \sum_{N=m_j+m_k}^{\infty} \frac{\left(\frac{\beta}{\nu}\left(1 - P_j - P_k\right)\right)^{N-m_j-m_k}}{\left(N - m_j - m_k\right)!} \\
&= e^{-\frac{\beta}{\nu}} \frac{\left(\frac{\beta}{\nu} P_j\right)^{m_j}}{m_j!} \frac{\left(\frac{\beta}{\nu} P_k\right)^{m_k}}{m_k!} e^{\frac{\beta}{\nu}\left(1-P_j-P_k\right)} \\
&= \left(e^{-\frac{\beta}{\nu} P_j} \frac{\left(\frac{\beta}{\nu} P_j\right)^{m_j}}{m_j!}\right) \left(e^{-\frac{\beta}{\nu} P_k} \frac{\left(\frac{\beta}{\nu} P_k\right)^{m_k}}{m_k!}\right).
\end{aligned} \tag{G.7}$$

Thus the joint probability distribution of m_j and m_k is seen to be separable into the product of the two marginal distribution, meaning that same-time, instantaneous measurements of m_j an m_k must be uncorrelated.

From here we can begin to calculate the full correlation function for m_j and m_k. We start by defining $\delta m_j(t) = m_j(t) - \bar{m}_j$ and $\delta m_k(t) = m_k(t) - \bar{m}_k$. Since $\bar{m}_j$ is known to set the right-hand side of Eq. G.1 to 0, the dynamics of δm_j can be written as

$$\frac{\partial \delta m_j}{\partial t} = h\left(\delta m_{j+1} + \delta m_{j-1} - 2\delta m_j\right) - \nu \delta m_j, \tag{G.8}$$

with the same being true for δm_k. Additionally, we assume the system is at steady state so that all mean expressions are invariant to time translation. Given this, we can without loss of generality take the correlation function between δm_j and δm_k to have the form

$$C_{j,k}(t) = \left\langle \delta m_k(t)\, \delta m_j(0) \right\rangle, \tag{G.9}$$

where $t > 0$. Applying the dynamic result given in Eq. G.8 then yields

$$\begin{aligned}\frac{\partial C_{j,k}}{\partial t} &= \left\langle \frac{\partial \delta m_k(t)}{\partial t} \delta m_j(0) \right\rangle = \left\langle \Big(h\left(\delta m_{k+1}(t) + \delta m_{k-1}(t) - 2\delta m_k(t)\right) - \nu \delta m_k(t) \Big) \delta m_j(0) \right\rangle \\ &= h\left(C_{j,k+1} + C_{j,k-1}\right) - (2h+\nu) C_{j,k}. \end{aligned} \tag{G.10}$$

The final form of Eq. G.10 can be split into the term $-(2h+\nu)C_{j,k}$ which implies $C_{j,k} \propto \exp(-(2h+\nu)t)$ and the term $h(C_{j,k+1}+C_{j,k-1})$ which is the recursion relation for $I_\ell(2ht)$, the modified Bessel function of the first kind, where ℓ is some function of j and k. This means $C_{j,k}(t)$ can be written as

$$C_{j,k}(t) = A I_{\ell(j,k)}(2ht)\, e^{-(2h+\nu)t}, \tag{G.11}$$

for some proportionality constant A.

To determine the forms of A and $\ell(j,k)$, we can utilize the initial condition that m_j is Poissonianlly distributed and thus has a variance equal to its mean while being completely uncorrelated with m_k when both are measured at the same time. This means $C_{j,k}(0)$ can be written as

$$C_{j,k}(0) = \frac{\beta}{\nu} P_j \delta_{jk}, \tag{G.12}$$

which in turn implies $\ell(j,j) = 0$ as $I_n(0) = \delta_{0n}$ for $n \in \mathbb{Z}$. To satisfy the recursion relation term of Eq. G.10, it must then be the case that $\ell(j, j+n) = n$. Setting $k = j + n$ thus yields $\ell(j,k) = k - j$. Since k and j are integers, $\ell(j,k) = j - k$ is equally valid as $I_n = I_{-n}$ again for $n \in \mathbb{Z}$. Combining these results together yields the final form of $C_{j,k}(t)$ to be

$$C_{j,k}(t) = \frac{\beta}{\nu} P_j I_{k-j}(2ht)\, e^{-(2h+\nu)t}. \tag{G.13}$$

Next, let τ be the autocorrelation time of m_j. This quantity is typically defined by integrating $C_{j,j}(t)/C_{j,j}(0)$ over all time. Using the known properties of modified Bessel functions, this can be solved to yield

$$\tau = \int_0^\infty dt \frac{C_{j,j}\left(t\right)}{C_{j,j}\left(0\right)} = \int_0^\infty dt\, I_0\left(2ht\right) e^{-(2h+\nu)t} = \frac{1}{\sqrt{\nu\left(4h+\nu\right)}}. \tag{G.14}$$

If we now define $M = T/\tau$ where M is the number of effectively independent measurements that can be made in a time T, we see that for $h \gg \nu$, $M \approx 2\sqrt{\nu h}T$. Additionally, from Eq. G.2 we see that in the $h \gg \nu$ regime $\lambda \approx 2\sqrt{h/\nu}$. By equating this λ to the nondimensionalized λ_{SDC}/a from the SDC model we see that $M \approx \lambda\nu T = (\lambda_{\mathrm{SDC}}/a)\nu T$. This is consistent with the fact that for $\lambda_{\mathrm{SDC}} \gg a$ the right-hand side of Eq. F.24 becomes approximately $2/(\bar{m}(\lambda_{\mathrm{SDC}}/a)\nu T) \approx 2/(\bar{m}M)$.

In the $h \ll \nu$ regime we find $M \approx \nu T$. Once again, this consistent with Eq. F.24 when $\lambda_{\mathrm{SDC}} \ll a$ as this causes the right-hand side to become approximately $2/(\bar{m}\nu T) \approx 2/(\bar{m}M)$. Thus, the SDC model is seen to have its noise-to-signal ratio scale as $2/(\bar{m}M)$ in both the large and small h regime.

H. CALCULATIONS FOR INDIVIDUAL-BASED CHEMOTAXIS MODEL

For IC the variance in P_z is

$$\delta P_{zT}^2 = \sum_{i=1}^{N} \delta p_{i,zT}^2 + \sum_{i \neq j} \mathrm{Cov}[p_{i,z}, p_{j,z}] \equiv V_{\mathrm{IC}} + C_{\mathrm{IC}} \ . \tag{H.1}$$

The Fourier-transformed fluctuations in IC cell polarization is given by linearizing and transforming Eq. 7.1 to yield

$$\delta \tilde{p}_{j,z}(\vec{k}, \omega) = \int_V d^3x \int \frac{d^3k}{(2\pi)^3} \cos\theta \delta\tilde{c}(\vec{k}, \omega) e^{-i\vec{k}\cdot(\vec{x}_i + \vec{x})} \ . \tag{H.2}$$

The cross-spectrum for the z-component between two cells is thus given by

$$\begin{aligned} \langle \delta\tilde{p}_{i,z}^*(\omega') \delta\tilde{p}_{j,z}(\omega) \rangle = \int_V d^3x d^3x' \int \frac{d^3k d^3k'}{(2\pi)^6} \cos\theta \cos\theta' \langle \delta\tilde{c}^*(\vec{k}', \omega') \delta\tilde{c}(\vec{k}, \omega) \rangle \\ \cdot e^{-i\vec{k}\cdot(\vec{x}_j + \vec{x})} e^{i\vec{k}'\cdot(\vec{x}_i + \vec{x}')} \ . \end{aligned} \tag{H.3}$$

We can rewrite Eq. H.3 by noting that only the relative locations of cell i and j are relevant for the cross-spectrum. Let $\vec{r}_{ij} = \vec{x}_i - \vec{x}_j$ and $r_{ij} = |\vec{r}_{ij}|$.

$$\begin{aligned} \langle \delta\tilde{p}_{i,z}^*(\omega') \delta\tilde{p}_{j,z}(\omega) \rangle = \int_V d^3x d^3x' \int \frac{d^3k d^3k'}{(2\pi)^6} \cos\theta \cos\theta' \langle \delta\tilde{c}^*(\vec{k}', \omega') \delta\tilde{c}(\vec{k}, \omega) \rangle \\ \cdot e^{-i\vec{k}\cdot\vec{x}} e^{i\vec{k}'\cdot(\vec{r}_{ij} + \vec{x}')} \ . \end{aligned} \tag{H.4}$$

Plugging in Eq. A.17 for $\langle \delta\tilde{c}^*(\vec{k}', \omega') \delta\tilde{c}(\vec{k}, \omega) \rangle$ and writing $\cos\theta$ in terms of spherical harmonic $Y_1^0(\hat{x})$ yields

$$\begin{aligned} \langle \delta\tilde{p}_{i,z}^*(\omega') \delta\tilde{p}_{j,z}(\omega) \rangle &= \int_V d^3x d^3x' \int \frac{d^3k d^3k'}{(2\pi)^6} \frac{4\pi}{3} Y_1^0(\hat{x}) Y_1^0(\hat{x}') \ 2D \\ &\quad \frac{2\pi\delta(\omega - \omega')}{(Dk^2 - i\omega)(Dk'^2 + i\omega')} \int d^3y \vec{k} \cdot \vec{k}' \bar{c}(\vec{y}) e^{i\vec{y}\cdot(\vec{k} - \vec{k}')} e^{-i\vec{k}\cdot\vec{x}} e^{i\vec{k}'\cdot(\vec{r}_{ij} + \vec{x}')} \\ &= \frac{4D}{3(2\pi)^5} 2\pi\delta(\omega - \omega') \int_V d^3x d^3x' \int d^3k d^3k' d^3y \ Y_1^0(\hat{x}) Y_1^0(\hat{x}') \\ &\quad \frac{\bar{c}(\vec{y}) \ \vec{k} \cdot \vec{k}' \ e^{i\vec{y}\cdot(\vec{k} - \vec{k}')}}{(Dk^2 - i\omega)(Dk'^2 + i\omega')} e^{-i\vec{k}\cdot\vec{x}} e^{i\vec{k}'\cdot(\vec{r}_{ij} + \vec{x}')} \ . \end{aligned} \tag{H.5}$$

Plugging the specified mean concentration from Eq. 7.3 into Eq. H.5 allows us to define $S_{ij,z}(0)$ as the 0-frequency limit:

$$\begin{aligned} S_{ij,z}(0) &= \lim_{\omega\to 0}\int \frac{d\omega'}{2\pi}\langle \delta\tilde{p}^*_{i,z}(\omega')\delta\tilde{p}_{j,z}(\omega)\rangle \\ &= \frac{4}{3(2\pi)^5 D}\int_V d^3x d^3x' \int d^3k d^3k' d^3y \; Y_1^0(\hat{x})Y_1^0(\hat{x}')\frac{\vec{k}\cdot\vec{k}'}{k^2k'^2}(c_0+\vec{g}\cdot\vec{y}) \\ &\qquad \cdot e^{i\vec{y}(\vec{k}-\vec{k}')}\; e^{-i\vec{k}\cdot\vec{x}}e^{i\vec{k}'\cdot(\vec{r}_{ij}+\vec{x}')}\;. \end{aligned} \tag{H.6}$$

We can break up Eq. H.6 into two terms: one dependent on the background concentration, the other on the gradient.

$$\begin{aligned} S_{ij,z}(0) = \frac{4}{3(2\pi)^5 D}\int_V d^3x d^3x' \int d^3k d^3k' \; Y_1^0(\hat{x})Y_1^0(\hat{x}')\frac{\vec{k}\cdot\vec{k}'}{k^2k'^2}\; e^{-i\vec{k}\cdot\vec{x}} \\ e^{i\vec{k}'\cdot(\vec{r}_{ij}+\vec{x}')}\left((2\pi)^3\delta^3(\vec{k}-\vec{k}')c_0 + \int d^3y\; \vec{g}\cdot\vec{y}\; e^{i\vec{y}(\vec{k}-\vec{k}')}\right) \end{aligned} \tag{H.7}$$

Let S^1_{ij} represent the background concentration term and S^2_{ij} represent the gradient dependent term in the power spectrum such that $S_{ij,z}(0) = S^1_{ij} + S^2_{ij}$.

$$S^1_{ij} = \frac{4c_0}{3(2\pi)^2 D}\int_V d^3x d^3x' \int d^3k\; Y_1^0(\hat{x})Y_1^0(\hat{x}')\frac{1}{k^2}\; e^{-i\vec{k}\cdot\vec{x}}\; e^{i\vec{k}\cdot(\vec{r}_{ij}+\vec{x}')} \tag{H.8}$$

$$\begin{aligned} S^2_{ij} = \frac{4c_0}{3(2\pi)^5 D}\int_V d^3x d^3x' \int d^3k d^3k' d^3y \; Y_1^0(\hat{x})Y_1^0(\hat{x}')\frac{\vec{k}\cdot\vec{k}'}{k^2k'^2}\;\vec{g}\cdot\vec{y} \\ e^{i\vec{y}(\vec{k}-\vec{k}')}\; e^{-i\vec{k}\cdot\vec{x}}\; e^{i\vec{k}'\cdot(\vec{r}_{ij}+\vec{x}')} \end{aligned} \tag{H.9}$$

The following expansions will prove useful:

$$e^{-i\vec{k}\cdot\vec{r}} = 4\pi\sum_{l,m}(-i)^l j_l(kr)Y_l^m(\hat{k})Y_l^{m*}(\hat{r})\;, \tag{H.10}$$

$$\vec{a}\cdot\vec{b} = \frac{4\pi}{3}ab\sum_{m=-1}^{1} Y_1^m(\hat{a})Y_1^{m*}(\hat{b})\;. \tag{H.11}$$

Starting with Eq. H.8 we expand all the exponential terms, and we use these expansions in order to evaluate the angular integrals in S^1_{ij}.

$$S^1_{ij} = \frac{2^5(2\pi)c_0}{3D}\int_V d^3x d^3x' \int d^3k\ Y_1^{0*}(\hat{x})Y_1^{0*}(\hat{x}')\ \frac{1}{k^2}\left(\sum_{l_1,m_1} i^{-l_1} j_{l_1}(xk)Y_{l_1}^{m_1}(\hat{x})Y_{l_1}^{m_1*}(\hat{k})\right) \cdot \left(\sum_{l_2,m_2} i^{l_2} j_{l_2}(r_{ij}k)Y_{l_2}^{m_2}(\hat{k})Y_{l_2}^{m_2*}(\hat{r}_{ij})\right)\left(\sum_{l_3,m_3} i^{l_3} j_{l_3}(x'k)Y_{l_3}^{m_3}(\hat{k})Y_{l_3}^{m_3*}(\hat{x}')\right) \tag{H.12}$$

The angular integrals over $\hat{x}$ and $\hat{x}'$ eliminate the summations over l_1, m_1 and l_3, m_3.

$$S^1_{ij} = \frac{2^5(2\pi)c_0}{3D}\int_0^a dx dx' \int d^3k\ \frac{1}{k^2}x^2x'^2\ j_1(xk)j_1(x'k)\ Y_1^{0*}(\hat{k})Y_1^0(\hat{k}) \left(\sum_{l_2,m_2} i^{l_2} j_{l_2}(r_{ij}k')Y_{l_2}^{m_2}(\hat{k}')Y_{l_2}^{m_2*}(\hat{r}_{ij})\right), \tag{H.13}$$

and the product of the two spherical harmonics is

$$Y_1^{0*}(\hat{k})Y_1^{0*}(\hat{k}) = \frac{1}{\sqrt{4\pi}}\left(Y_0^0(\hat{k}) + \frac{2\sqrt{5}}{5}Y_2^0(\hat{k})\right)\ . \tag{H.14}$$

Therefore when evaluating the $\hat{k}$ integral in Eq. H.13 only the $l_2 = 0, m_2 = 0$ and $l_2 = 2, m_2 = 0$ terms of the summation will be non-zero.

$$S^1_{ij} = \frac{2^5(2\pi)c_0}{3D\sqrt{4\pi}}\int_0^a dx dx' \int_0^\infty dk\ x^2x'^2\ j_1(xk)j_1(x'k) \left(j_0(r_{ij}k)Y_0^0(\hat{r}_{ij}) - \frac{2\sqrt{5}}{5}j_2(r_{ij}k)Y_2^0(\hat{r}_{ij})\right) \tag{H.15}$$

The integrals over x and x' evaluate to:

$$\int_0^a dx\ x^2 j_1(kx) = \frac{1}{k^3}\left(2 - 2\cos(ak) - ak\sin(ak)\right) \equiv \frac{1}{k^3}h(ak)\ . \tag{H.16}$$

Note that $Y_0^0(\Theta_{ij}, \Phi_{ij}) = \frac{1}{\sqrt{4\pi}}$, and $Y_2^0(\Theta_{ij}, \Phi_{ij}) = \frac{1}{2}\sqrt{\frac{5}{4\pi}}(3\cos^2\Theta_{ij} - 1)$. The angle Θ_{ij} is the angle $\hat{r}_{ij}$ makes relative to the gradient direction $\hat{g}$, $\cos\Theta_{ij} = \hat{r}_{ij}\cdot\hat{g}$. The expression for S^1_{ij} reduces to

$$S^1_{ij} = \frac{2^4c_0}{3D}\int_0^\infty dk\ \frac{h^2(ak)}{k^6}\ \left[j_0(r_{ij}k) - j_2(r_{ij}k)(3\cos^2\Theta_{ij} - 1)\right] \tag{H.17}$$

We can make the integral dimensionless by making the variable substitutions $u \equiv ak$ and $n_{ij} \equiv r_{ij}/a$.

$$S_{ij}^1 = \frac{2^4 c_0 a^5}{3D} \int_0^\infty du \, \frac{h^2(u)}{u^6} \left[j_0\left(n_{ij}u\right) - j_2\left(n_{ij}u\right)\left(3\cos^2\Theta_{ij} - 1\right) \right] \tag{H.18}$$

We can break up Eq. H.18 into two integrals and evaluate them individually based on known properties of spherical Bessel functions. Note that the exact solution to either integral depends parametrically on n_{ij} and that n_{ij} is the number of cells radii separating two cells. If we are evaluating the cross-correlations in one cell then $i = j$ and $n_{ii} = 0$; on the other hand, if $i \neq j$ then $n_{ij} \geq 2$ in order to eliminate the possibility of overlapping cells. In either case the expression simplifies to:

$$S_{ij}^1 = \begin{cases} \frac{4\pi c_0 a^5}{45D} & i = j \\ -\frac{\pi c_0 a^5}{18D} \frac{1}{n_{ij}^3}(3\cos^2\Theta_{ij} - 1) & i \neq j,\ n_{ij} \geq 2 \end{cases} . \tag{H.19}$$

Doing the same set of expansions for S_{ij}^2 in Eq. H.9, and performing the same kind of analysis reveals that the gradient depedendent term is asymmetric under exchange of i and j. Therefore when calculating the cluster polarization variance all the S_{ij}^2 terms will cancel. The variance contributions V and C are

$$V_{\mathrm{IC}} = \sum_{i=1}^{N} \frac{1}{T} S_{ii,z}(0) = \frac{4\pi a^5 c_0}{45DT} N \ , \tag{H.20}$$

$$C_{\mathrm{IC}} = \sum_{i \neq j}^{N} \frac{1}{T} S_{ij,z}(0) = -\frac{\pi a^5 c_0}{18DT} \sum_{i \neq j}^{N} \frac{(3\cos^2\Theta_{ij} - 1)}{n_{ij}^3} \ , \tag{H.21}$$

resulting in the IC collective total variance

$$\delta P_{zT}^2 = \frac{\pi a^5 c_0}{9DT} \left[\frac{4}{5} N - \frac{1}{2} \sum_{i \neq j}^{N} \frac{(3\cos^2\Theta_{ij} - 1)}{n_{ij}^3} \right] . \tag{H.22}$$

Next we will show how Eq. H.22 scales for collectives in one, two and three dimensional configurations.

H.1 One Dimensional Chain

For a one-dimensional chain of IC cells each cell is aligned parallel to the gradient and the angular dependence of $C_{\rm IC}$ (Eq. H.21) vanishes,

$$C_{\rm IC} = -\frac{\pi a^5 c_0}{18DT} \sum_{i\neq j}^{N} \frac{2}{n_{ij}^3} \ . \tag{H.23}$$

We evaluate the sum:

$$\sum_{i\neq j}^{N} \frac{1}{n_{ij}^3} = 2\sum_{i<j}^{N} \frac{1}{n_{ij}^3} = 2\sum_{i=1}^{N-1} \frac{N-i}{(2i)^3} = \frac{1}{4}(NH_{N-1}^{(3)} - H_{N-1}^{(2)}) \ ,$$

with $H_n^{(m)} = \sum_{k=1}^{n} \frac{1}{k^m}$ the generalized harmonic number. This results in a total variance of the form

$$\delta P_{zT}^2 = \frac{\pi a^5 c_c}{9DT} \left[\frac{4}{5}N - \frac{1}{8}\left(NH_{N-1}^{(3)} - H_{N-1}^{(2)} \right) \right] \ . \tag{H.24}$$

For large N, $H_{N-1}^{(i)}$ approaches a constant for $i \geq 2$. Therefore, we see that δP_{zT}^2 scales with N for 1D IC collectives as in Table I of the main text.

H.2 Two Dimensional Sheet

For a two-dimensional sheet of IC cells, pairs of cells can now make a variety of angles with the gradient, and the angular dependence of $C_{\rm IC}$ cannot be easily simplified. In order to find the N scaling for $C_{\rm IC}$ we calculate the sum numerically. Since the covariances rapidly fall-off as $1/n_{ij}^3$, we only track nearest neighbor pairs that are less than 3 cell radii apart. The resulting numerical solution to the sum in $C_{\rm IC}$ is

$$\sum_{i\neq j}^{N} \frac{3\cos^2\Theta_{ij} - 1}{n_{ij}^3} = 2\sum_{i<j}^{N} \frac{3\cos^2\Theta_{ij} - 1}{n_{ij}^3} = \frac{1}{4}(1.70N - 2.67\sqrt{N} + 0.89) \ .$$

Therefore the expression for $C_{\rm IC}$ (Eq. H.21) simplifies to

$$C_{\rm IC} = -\frac{\pi a^5 c_0}{18DT}(0.43N - 0.67\sqrt{N} + 0.22) \ . \tag{H.25}$$

The covariance contribution, $C_{\rm IC}$, to leading order scales linearly with N. The total variance becomes

$$\delta P_{zT}^2 = \frac{\pi a^5 c_c}{9DT}\left(0.59N + 0.33\sqrt{N} - 0.11\right) \ . \tag{H.26}$$

We see that for large N, δP_{zT}^2 scales with N for 2D IC collectives.

H.3 Three Dimensional Cluster

To obtain a scaling for $C_{\rm IC}$ in a three dimensional cluster we assume that cluster is large, such that $a \ll R$ and $N \gg 1$. For a given cell we can calculate its contribution to $C_{\rm IC}$ by considering the covariance contribution it makes with a set of cells a fixed distance away from it. The equidistant cells form a spherical shell with the principal cell in the center. Adapting Eq. H.21 for a cell and its spherical shell of covariance pairs yields:

$$C_{\rm cell} = -\frac{\pi a^5 c_0}{18DT}\frac{1}{n_{\rm shell}^3}\sum_{i_{\rm shell}} 3\cos^2\Theta_i - 1 \ , \tag{H.27}$$

with $n_{\rm shell}$ the radius of the shell in terms of cell radii. Going to continuum we can calculate the contribution from the cell and all its pairs

$$\begin{aligned} C_{\rm cell} &= -\frac{\pi a^5 c_0}{18DTn_{\rm shell}^3}\int_0^{2\pi} d\phi \int_0^{\pi} d\theta \ \sin\theta(3\cos^2\theta - 1) \\ &= -\frac{\pi^2 a^5 c_0}{9DTn_{\rm shell}^3}\int_0^{\pi} d\theta \ (3\cos^2\sin\theta - \sin\theta) = 0 \ . \end{aligned} \tag{H.28}$$

In the last step, we see that the integral vanishes. Thus, the contribution from a single cell and its shell of pairs sum to zero. Repeating this argument for all cells in the cluster results in the total $C_{\rm IC} = 0$. Therefore for 3D clusters there is no covariance contribution to the total variance, and $\delta P_{zT}^2 = V_{\rm IC} \sim N$.

I. CALCULATIONS FOR EMERGENT CHEMOTAXIS MODEL

For EC the variance in P_z is

$$\delta P_{zT}^2 = \sum_{i=1}^{N} \delta p_{i,zT}^2 + \sum_{i \neq j} \mathrm{Cov}[p_{i,z}, p_{j,z}] \equiv V_{\mathrm{EC}} + C_{\mathrm{EC}} \ . \tag{I.1}$$

The Fourier-transformed fluctuations in EC edge cell polarization is given by linearizing and transforming Eq. 7.12 to yield

$$\delta \tilde{p}_{i,z}(\vec{k}, \omega) = \cos\Theta_i \int_V d^3x \int \frac{d^3k}{(2\pi)^3} \delta\tilde{c}(\vec{k}, \omega) e^{-i\vec{k}\cdot(\vec{x_i}+\vec{x})} \ , \tag{I.2}$$

with Θ_i the angle cell i makes with the gradient. The cross-spectrum for the z-component between two cells is thus given by

$$\langle \delta\tilde{p}_i^*(\vec{k}', \omega') \delta\tilde{p}_j(\vec{k}, \omega) \rangle = \cos\Theta_i \cos\Theta_j \int_V d^3x d^3x' \int \frac{d^3k d^3k'}{(2\pi)^6} \langle \delta\tilde{c}^*(\vec{k}', \omega') \delta\tilde{c}(\vec{k}, \omega) \rangle \cdot e^{-i\vec{k}\cdot(\vec{x}_j+\vec{x})} e^{i\vec{k}\cdot(\vec{x}_i+\vec{x}')} \tag{I.3}$$

Following the same procedure as in the case of IC, we get an expression for S_{ij}^1 for EC:

$$S_{ij}^1 = \begin{cases} \frac{16\pi c_0 a^5}{15D} \cos^2\Theta_i & i = j \\ \frac{8\pi c_0 a^5}{9D} \frac{1}{n_{ij}} \cos\Theta_i \cos\Theta_j & i \neq j, \ n_{ij} \geq 2 \end{cases} \ . \tag{I.4}$$

Since again $S_{ij}^2 = 0$ by symmetry, the variance for any configuration of EC cells is

$$V_{\mathrm{EC}} = \frac{16\pi a^5 c_0}{15DT} \sum_{i=1}^{N_{\mathrm{edge}}} \cos^2\Theta_i \ , \tag{I.5}$$

$$C_{\mathrm{EC}} = \frac{8\pi a^5 c_0}{9DT} \sum_{i \neq j} \frac{\cos\Theta_i \cos\Theta_j}{n_{ij}} \ . \tag{I.6}$$

The resulting total variance is

$$\delta P_{zT}^2 = \frac{8\pi a^5 c_0}{3DT} \left[\frac{2}{5} \sum_{i=1}^{N_{\mathrm{edge}}} \cos^2\Theta_i + \frac{1}{3} \sum_{i \neq j} \frac{\cos\Theta_i \cos\Theta_j}{n_{ij}} \right] \ . \tag{I.7}$$

I.1 One Dimensional Chain

For a one-dimensional chain of cells only the two cells on the opposing ends are polarized. The cell variance contribution to the total variance therefore does not change with increasing cluster size,

$$V_{\rm EC} = \frac{16\pi a^5 c_0}{15DT} \sum_{i=1}^{N_{\rm edge}} \cos^2\Theta_i = \frac{32\pi a^5 c_0}{15DT} \ . \tag{I.8}$$

Therefore $V_{\rm EC} \sim N^0$ for 1D collectives. For $C_{\rm EC}$ the distance between the two edge cells increases by two cell radii for each cell added to the chain:

$$C_{\rm EC} = \frac{8\pi a^5 c_0}{9DT} \sum_{i\neq j} \frac{\cos\Theta_i \cos\Theta_j}{n_{ij}} = -\frac{8\pi a^5 c_0}{9DT} \frac{1}{2(N-1)} \ . \tag{I.9}$$

So $C_{\rm EC} \sim N^{-1}$ for 1D collectives. To leading order in N the total collective variance depends only on $V_{\rm EC}$:

$$\delta P_{zT}^2 = \frac{32\pi a^5 c_0}{15DT} \ , \tag{I.10}$$

and so δP_{zT}^2 does not depend on collective size for 1D EC.

I.2 Two Dimensional Sheet

In order to evaluate the variance for a two-dimensional disc of cells we will approximate the sums as integrals over the circumference of the disc as we did in evaluating the mean polarization. Assuming that $a \ll R$ Eq. I.5 can be written as an integral

$$V_{\rm EC} = \frac{16\pi a^5 c_0}{15DT} \frac{R}{2a} \int_0^{2\pi} d\theta \ \cos^2\theta \ . \tag{I.11}$$

Using the relation $N = (R/a)^2$ yields

$$V_{\rm EC} = \frac{8\pi^2 a^5 c_0}{15DT} \sqrt{N} \ . \tag{I.12}$$

Hence for 2D EC, the variance contribution $V_{\rm EC}$ scales as $\sqrt{N}$. In order to determine how $C_{\rm EC}$ scales with N we approximate the sums over i and j as a double integral, again assuming that $a \ll R$.

$$C_{\rm EC} = \frac{16\pi a^5 c_0}{9DT} \left(\frac{R}{2a^2}\right) \int_{\Delta/2}^{2\pi-\Delta/2} d\theta_1 \int_{\theta_1+\Delta/2}^{2\pi} d\theta_2 \ \frac{\cos\theta_1 \cos\theta_2}{n(\theta_1,\theta_2)} \tag{I.13}$$

Here $\Delta = 2a/R$ is the anguler separation between two edge cells, and

$$n(\theta_1, \theta_2) = \frac{2R}{a} \sin\left(\frac{1}{2}(\theta_2 - \theta_1)\right) \tag{I.14}$$

is the number of cell radii separating two edge cells. Using this expression for $n(\theta_1, \theta_2)$ we evaluate the integral over θ_2:

$$\begin{aligned}\left(\frac{R}{2a^2}\right) \int_{\Delta/2}^{2\pi-\Delta/2} d\theta_1 \int_{\theta_1+\Delta/2}^{2\pi} d\theta_2 \; \frac{\cos\theta_1 \cos\theta_2}{n(\theta_1, \theta_2)} \\ = \frac{R}{8a} \int_{\Delta/2}^{2\pi-\Delta/2} d\theta_1 \cos\theta_1 \Big[-4\left(\cos(\theta_1/2) + \cos(\theta_1 + \Delta/2)\right) \\ -2\cos\theta_1 \log\left(\tan(\Delta/4)\tan(\theta_1/4)\right)\Big] \; . \end{aligned} \tag{I.15}$$

Breaking up the integral into four separate terms we find:

$$\int_{\Delta/2}^{2\pi-\Delta/2} d\theta_1 \cos\theta_1 \cos(\theta_1/2) = 0 \; , \tag{I.16}$$

$$\int_{\Delta/2}^{2\pi-\Delta/2} d\theta_1 \cos\theta_1 \cos(\theta_1 + \Delta/2) = -\frac{1}{2}\cos(\Delta/2)(\Delta + \sin\Delta - 2\pi) \; , \tag{I.17}$$

$$\int_{\Delta/2}^{2\pi-\Delta/2} d\theta_1 \cos\theta_1 \log\left(\tan(\Delta/4)\right) = -\frac{1}{2}(\Delta + \sin\Delta - 2\pi)\tan(\Delta/4) \; , \tag{I.18}$$

$$\int_{\Delta/2}^{2\pi-\Delta/2} d\theta_1 \cos\theta_1 \log\left(\tan(\theta_1/4)\right) = 0 \; . \tag{I.19}$$

The first and last integrals are equal to zero since the integrands are odd functions over the range $[0, 2\pi]$. With these results, the whole expression simplifies to

$$C_{\rm EC} = \frac{16\pi a^5 c_0}{9DT} \frac{1}{4} \sqrt{N} \left(\frac{1}{2}\log N + \log 2 - 2\right)\left(\pi - \frac{2}{\sqrt{N}}\right) \tag{I.20}$$

Keeping only the leading order terms in N yields

$$C_{\rm EC} = \frac{2\pi^2 a^5 c_0}{9DT} \sqrt{N} \log N \; . \tag{I.21}$$

The resulting total variance is

$$\delta P_{zT}^2 = \frac{8\pi^2 a^5 c_0}{3DT} \sqrt{N} \left[\frac{1}{5} + \frac{1}{12}\log N\right] \; , \tag{I.22}$$

which to to leading order scales as $\sqrt{N}\log N$.

I.3 Three Dimensional Cluster

For the three-dimensional cluster, numerical methods must be used in order to find the scaling properties of the variance. We numerically evaluate the total variance (Eq. I.7) on a cubic lattice and obtain the following results.

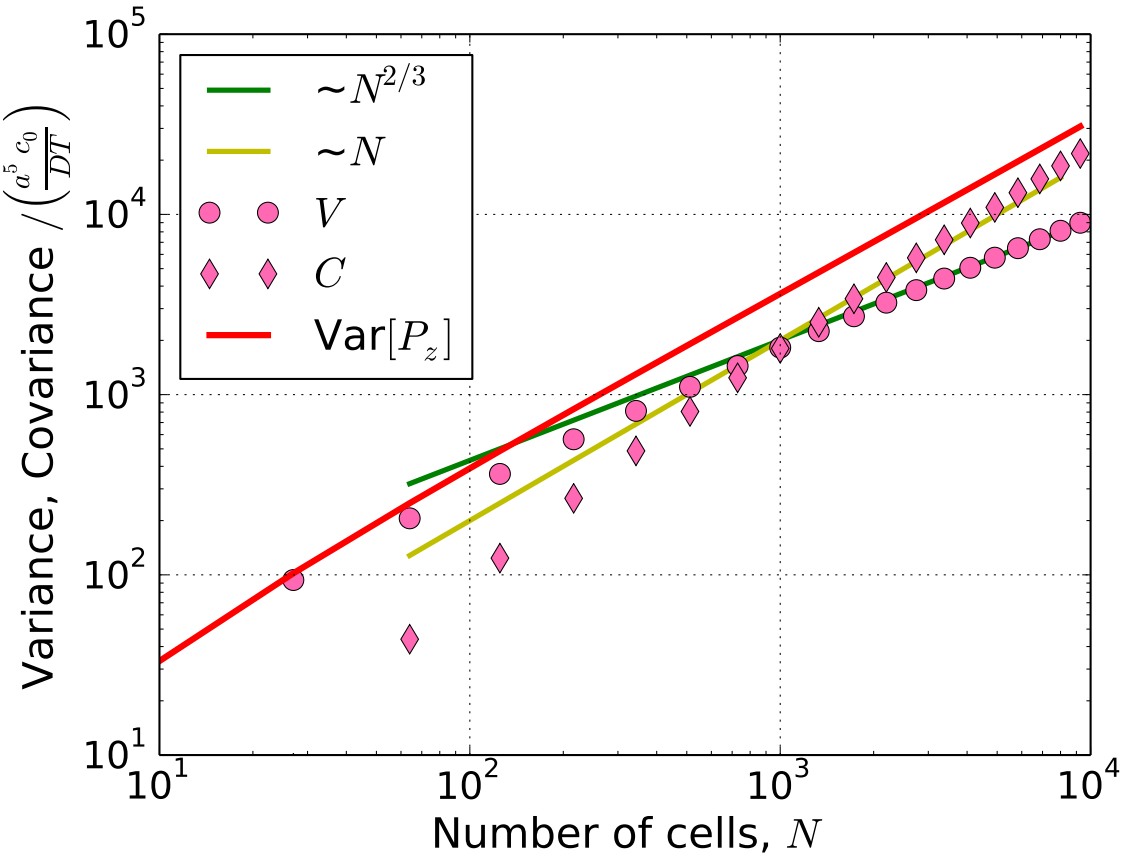

Figure I.1. δP_{zT}^2 for a 3D cluster of EC cells. Cluster variance shown in red. Pink circles are the single cell variance contributions V, and pink diamonds are the cell-cell covariance contributions C.

The numerical results [Fig. I.1] show that $V \sim N^{2/3}$ since the number of edge cells also scales as $N^{2/3}$. We also find that $C \sim N$; the covariance contribution to the total cluster polarization grows linearly with N. For large clusters the N scaling

dominates the behavior of δP_{zT}^2. Therefore, in 3D the leading order scaling for the variance is $\delta P_{zT}^2 \sim N$.

REFERENCES

[1] Howard C Berg and Edward M Purcell. Physics of chemoreception. *Biophysical journal*, 20(2):193, 1977.

[2] William Bialek and Sima Setayeshgar. Physical limits to biochemical signaling. *Proceedings of the National Academy of Sciences of the United States of America*, 102(29):10040–10045, 2005.

[3] David Ellison, Andrew Mugler, Matthew D Brennan, Sung Hoon Lee, Robert J Huebner, Eliah R Shamir, Laura A Woo, Joseph Kim, Patrick Amar, Ilya Nemenman, Andrew J Ewald, and Andre Levchenko. Cell–cell communication enhances the capacity of cell ensembles to sense shallow gradients during morphogenesis. *Proceedings of the National Academy of Sciences*, 13(6):E679–E688, 2016.

[4] Kazunari Kaizu, Wiet de Ronde, Joris Paijmans, Koichi Takahashi, Filipe Tostevin, and Pieter Rein ten Wolde. The berg-purcell limit revisited. *Biophysical journal*, 106(4):976–985, 2014.

[5] Alex H Lang, Charles K Fisher, Thierry Mora, and Pankaj Mehta. Thermodynamics of statistical inference by cells. *Physical review letters*, 113(14):148103, 2014.

[6] Thierry Mora. Physical limit to concentration sensing amid spurious ligands. *Physical review letters*, 115(3):038102, 2015.

[7] Brendan A Bicknell, Peter Dayan, and Geoffrey J Goodhill. The limits of chemosensation vary across dimensions. *Nature communications*, 6, 2015.

[8] Robert G Endres and Ned S Wingreen. Maximum likelihood and the single receptor. *Physical review letters*, 103(15):158101, 2009.

[9] Masahiro Ueda and Tatsuo Shibata. Stochastic signal processing and transduction in chemotactic response of eukaryotic cells. *Biophysical journal*, 93(1):11–20, 2007.

[10] Robert G Endres and Ned S Wingreen. Accuracy of direct gradient sensing by single cells. *Proceedings of the National Academy of Sciences*, 105(41):15749–15754, 2008.

[11] Bo Hu, Wen Chen, Wouter-Jan Rappel, and Herbert Levine. Physical limits on cellular sensing of spatial gradients. *Physical review letters*, 105(4):048104, 2010.

[12] Thomas Gregor, David W Tank, Eric F Wieschaus, and William Bialek. Probing the limits to positional information. *Cell*, 130(1):153–164, 2007.

[13] Shuizi Rachel Yu, Markus Burkhardt, Matthias Nowak, Jonas Ries, Zdeněk Petrášek, Steffen Scholpp, Petra Schwille, and Michael Brand. Fgf8 morphogen gradient forms by a source-sink mechanism with freely diffusing molecules. *Nature*, 461(7263):533, 2009.

[14] Marcus Bischoff, Ana-Citlali Gradilla, Irene Seijo, Germán Andrés, Carmen Rodríguez-Navas, Laura González-Méndez, and Isabel Guerrero. Cytonemes are required for the establishment of a normal hedgehog morphogen gradient in drosophila epithelia. *Nature cell biology*, 15(11):1269, 2013.

[15] Thorsten Erdmann, Martin Howard, and Pieter Rein Ten Wolde. Role of spatial averaging in the precision of gene expression patterns. *Physical review letters*, 103(25):258101, 2009.

[16] Andrew Mugler, Andre Levchenko, and Ilya Nemenman. Limits to the precision of gradient sensing with spatial communication and temporal integration. *Proceedings of the National Academy of Sciences*, 13(6):E689–E695, 2016.

[17] PM Kulesa and SE Fraser. Neural crest cell dynamics revealed by time-lapse video microscopy of whole embryo chick explant cultures. *Developmental biology*, 204(2):327–344, 1998.

[18] Anna Haeger, Katarina Wolf, Mirjam M Zegers, and Peter Friedl. Collective cell migration: guidance principles and hierarchies. *Trends in cell biology*, 25(9):556–566, 2015.

[19] Gema Malet-Engra, Weimiao Yu, Amanda Oldani, Javier Rey-Barroso, Nir S Gov, Giorgio Scita, and Loïc Dupré. Collective cell motility promotes chemotactic prowess and resistance to chemorepulsion. *Current Biology*, 25(2):242–250, 2015.

[20] Mathias Felix Leber and Thomas Efferth. Molecular principles of cancer invasion and metastasis (review). *International journal of oncology*, 34(4):881–895, 2009.

[21] Cedric Gaggioli, Steven Hooper, Cristina Hidalgo-Carcedo, Robert Grosse, John F Marshall, Kevin Harrington, and Erik Sahai. Fibroblast-led collective invasion of carcinoma cells with differing roles for rhogtpases in leading and following cells. *Nature cell biology*, 9(12):1392–1400, 2007.

[22] Crispin W Gardiner et al. *Handbook of stochastic methods*, volume 3. Springer Berlin, 1985.

[23] Sean Fancher and Andrew Mugler. Fundamental limits to collective concentration sensing in cell populations. *Physical review letters*, 118(7):078101, 2017.

[24] Bruce Alberts, Alexander Johnson, Julian Lewis, Martin Raff, Keith Roberts, and Peter Walter. *Molecular Biology of the Cell, 4th Ed.* Garland Science, 2002.

[25] Amar B Singh and Raymond C Harris. Autocrine, paracrine and juxtacrine signaling by egfr ligands. *Cellular signalling*, 17(10):1183–1193, 2005.

[26] Hyun Youk and Wendell A Lim. Secreting and sensing the same molecule allows cells to achieve versatile social behaviors. *Science*, 343(6171):1242782, 2014.

[27] Mathieu Coppey, Alexander M Berezhkovskii, Stuart C Sealfon, and Stanislav Y Shvartsman. Time and length scales of autocrine signals in three dimensions. *Biophysical journal*, 93(6):1917–1922, 2007.

[28] William J Rosoff, Jeffrey S Urbach, Mark A Esrick, Ryan G McAllister, Linda J Richards, and Geoffrey J Goodhill. A new chemotaxis assay shows the extreme sensitivity of axons to molecular gradients. *Nature neuroscience*, 7(6):678–682, 2004.

[29] Shawn C Little, Mikhail Tikhonov, and Thomas Gregor. Precise developmental gene expression arises from globally stochastic transcriptional activity. *Cell*, 154(4):789–800, 2013.

[30] Alexander M Berezhkovskii and Attila Szabo. Effect of ligand diffusion on occupancy fluctuations of cell-surface receptors. *The Journal of chemical physics*, 139(12):09B610_1, 2013.

[31] Kai Wang, Wouter-Jan Rappel, Rex Kerr, and Herbert Levine. Quantifying noise levels of intercellular signals. *Physical Review E*, 75(6):061905, 2007.

[32] Daniel T Gillespie. The chemical langevin equation. *The Journal of Chemical Physics*, 113(1):297–306, 2000.

[33] Howard C Berg. *Random walks in biology*. Princeton University Press, 1993.

[34] Daniel Grünbaum. Schooling as a strategy for taxis in a noisy environment. *Evolutionary Ecology*, 12(5):503–522, 1998.

[35] Adi Shklarsh, Gil Ariel, Elad Schneidman, and Eshel Ben-Jacob. Smart swarms of bacteria-inspired agents with performance adaptable interactions. *PLoS Comput Biol*, 7(9):e1002177, 2011.

[36] Wai-Leung Ng and Bonnie L Bassler. Bacterial quorum-sensing network architectures. *Annual review of genetics*, 43:197, 2009.

[37] Burkhard A Hense, Christina Kuttler, Johannes Müller, Michael Rothballer, Anton Hartmann, and Jan-Ulrich Kreft. Does efficiency sensing unify diffusion and quorum sensing? *Nature Reviews Microbiology*, 5(3):230–239, 2007.

[38] Philip S Stewart. Diffusion in biofilms. *Journal of bacteriology*, 185(5):1485–1491, 2003.

[39] Antonio Trovato, Flavio Seno, Marina Zanardo, Sara Alberghini, Alessandra Tondello, and Andrea Squartini. Quorum vs. diffusion sensing: a quantitative analysis of the relevance of absorbing or reflecting boundaries. *FEMS microbiology letters*, 352(2):198–203, 2014.

[40] Amy L Schaefer, Brian L Hanzelka, Matthew R Parsek, and E Peter Greenberg. Detection, purification, and structural elucidation of the acylhomoserine lactone inducer of vibrio fischeri luminescence and other related molecules. *Methods in enzymology*, 305:288–301, 2000.

[41] James Q Boedicker, Meghan E Vincent, and Rustem F Ismagilov. Microfluidic confinement of single cells of bacteria in small volumes initiates high-density behavior of quorum sensing and growth and reveals its variability. *Angewandte Chemie International Edition*, 48(32):5908–5911, 2009.

[42] Daniel A Goodenough and David L Paul. Gap junctions. *Cold Spring Harbor Perspectives in Biology*, 1(1):a002576, 2009.

[43] Claudia Elfgang, Reiner Eckert, Hella Lichtenberg-Fraté, Anette Butterweck, Otto Traub, Roger A Klein, Dieter F Hülser, and Klaus Willecke. Specific permeability and selective formation of gap junction channels in connexin-transfected hela cells. *The Journal of Cell Biology*, 129(3):805–817, 1995.

[44] Pengfei Lu, Andrew J Ewald, Gail R Martin, and Zena Werb. Genetic mosaic analysis reveals fgf receptor 2 function in terminal end buds during mammary gland branching morphogenesis. *Developmental biology*, 321(1):77–87, 2008.

[45] Nataly Kravchenko-Balasha, Jun Wang, Francoise Remacle, RD Levine, and James R Heath. Glioblastoma cellular architectures are predicted through the characterization of two-cell interactions. *Proceedings of the National Academy of Sciences*, 111(17):6521–6526, 2014.

[46] Geoffrey J Goodhill. Diffusion in axon guidance. *European Journal of Neuroscience*, 9(7):1414–1421, 1997.

[47] T Miura and R Tanaka. In vitro vasculogenesis models revisited-measurement of vegf diffusion in matrigel. *Mathematical Modelling of Natural Phenomena*, 4(04):118–130, 2009.

[48] Angela Marino and Nicola Giotta. Cinacalcet, fetuin-a and interleukin-6. *Nephrology Dialysis Transplantation*, 2007.

[49] Phillip Yen, Stacey D Finley, Marianne O Engel-Stefanini, and Aleksander S Popel. A two-compartment model of vegf distribution in the mouse. *PloS one*, 6(11):e27514, 2011.

[50] Sean Fancher and Andrew Mugler. Diffusion vs. direct transport in the precision of morphogen readout. *arXiv preprint arXiv:1806.08318*, 2018.

[51] Julien O Dubuis, Gašper Tkačik, Eric F Wieschaus, Thomas Gregor, and William Bialek. Positional information, in bits. *Proceedings of the National Academy of Sciences*, 110(41):16301–16308, 2013.

[52] Bahram Houchmandzadeh, Eric Wieschaus, and Stanislas Leibler. Establishment of developmental precision and proportions in the early drosophila embryo. *Nature*, 415(6873):798, 2002.

[53] Aitana Morton De Lachapelle and Sven Bergmann. Precision and scaling in morphogen gradient read-out. *Molecular systems biology*, 6(1):351, 2010.

[54] Takuya Akiyama and Matthew C Gibson. Morphogen transport: theoretical and experimental controversies. *Wiley Interdisciplinary Reviews: Developmental Biology*, 4(2):99–112, 2015.

[55] Alfred Gierer and Hans Meinhardt. A theory of biological pattern formation. *Kybernetik*, 12(1):30–39, 1972.

[56] Arthur D Lander, Qing Nie, and Frederic YM Wan. Do morphogen gradients arise by diffusion? *Developmental cell*, 2(6):785–796, 2002.

[57] Patrick Müller, Katherine W Rogers, R Yu Shuizi, Michael Brand, and Alexander F Schier. Morphogen transport. *Development*, 140(8):1621–1638, 2013.

[58] Katherine W Rogers and Alexander F Schier. Morphogen gradients: from generation to interpretation. *Annual review of cell and developmental biology*, 27:377–407, 2011.

[59] Scott G Wilcockson, Catherine Sutcliffe, and Hilary L Ashe. Control of signaling molecule range during developmental patterning. *Cellular and Molecular Life Sciences*, 74(11):1937–1956, 2017.

[60] Paul C Bressloff and Hyunjoong Kim. Bidirectional transport model of morphogen gradient formation via cytonemes. *Physical biology*, 2018.

[61] Thomas B Kornberg and Sougata Roy. Cytonemes as specialized signaling filopodia. *Development*, 141(4):729–736, 2014.

[62] Wolfgang Driever and Christiane Nüsslein-Volhard. The bicoid protein determines position in the drosophila embryo in a concentration-dependent manner. *Cell*, 54(1):95–104, 1988.

[63] Alexander M Berezhkovskii, Christine Sample, and Stanislav Y Shvartsman. Formation of morphogen gradients: Local accumulation time. *Physical Review E*, 83(5):051906, 2011.

[64] Hai Huang and Thomas B Kornberg. Myoblast cytonemes mediate wg signaling from the wing imaginal disc and delta-notch signaling to the air sac primordium. *Elife*, 4:e06114, 2015.

[65] Eliana Stanganello and Steffen Scholpp. Role of cytonemes in wnt transport. *J Cell Sci*, 129(4):665–672, 2016.

[66] Stanislav Y Shvartsman and Ruth E Baker. Mathematical models of morphogen gradients and their effects on gene expression. *Wiley Interdisciplinary Reviews: Developmental Biology*, 1(5):715–730, 2012.

[67] Hamid Teimouri and Anatoly B Kolomeisky. New model for understanding mechanisms of biological signaling: Direct transport via cytonemes. *The journal of physical chemistry letters*, 7(1):180–185, 2015.

[68] Hamid Teimouri and Anatoly B Kolomeisky. Mechanisms of the formation of biological signaling profiles. *Journal of Physics A: Mathematical and Theoretical*, 49(48):483001, 2016.

[69] Filipe Tostevin, Pieter Rein Ten Wolde, and Martin Howard. Fundamental limits to position determination by concentration gradients. *PLoS computational biology*, 3(4):e78, 2007.

[70] Oliver Grimm, Mathieu Coppey, and Eric Wieschaus. Modelling the bicoid gradient. *Development*, 137(14):2253–2264, 2010.

[71] Thomas Gregor, Eric F Wieschaus, Alistair P McGregor, William Bialek, and David W Tank. Stability and nuclear dynamics of the bicoid morphogen gradient. *Cell*, 130(1):141–152, 2007.

[72] Anna Kicheva, Periklis Pantazis, Tobias Bollenbach, Yannis Kalaidzidis, Thomas Bittig, Frank Jülicher, and Marcos Gonzalez-Gaitan. Kinetics of morphogen gradient formation. *Science*, 315(5811):521–525, 2007.

[73] Jitendra S Kanodia, Richa Rikhy, Yoosik Kim, Viktor K Lund, Robert DeLotto, Jennifer Lippincott-Schwartz, and Stanislav Y Shvartsman. Dynamics of the dorsal morphogen gradient. *Proceedings of the National Academy of Sciences*, 106(51):21707–21712, 2009.

[74] Thomas B Kornberg. Cytonemes and the dispersion of morphogens. *Wiley Interdisciplinary Reviews: Developmental Biology*, 3(6):445–463, 2014.

[75] Timothy A Sanders, Esther Llagostera, and Maria Barna. Specialized filopodia direct long-range transport of shh during vertebrate tissue patterning. *Nature*, 497(7451):628, 2013.

[76] Julien Varennes, Sean Fancher, Bumsoo Han, and Andrew Mugler. Emergent versus individual-based multicellular chemotaxis. *Physical review letters*, 119(18):188101, 2017.

[77] Anna Kicheva, Tobias Bollenbach, Ortrud Wartlick, Frank Jülicher, and Marcos Gonzalez-Gaitan. Investigating the principles of morphogen gradient formation: from tissues to cells. *Current opinion in genetics & development*, 22(6):527–532, 2012.

[78] Sophia N Carrell, Michael D O'Connell, Thomas Jacobsen, Amy E Pomeroy, Stephanie M Hayes, and Gregory T Reeves. A facilitated diffusion mechanism establishes the drosophila dorsal gradient. *Development*, 144(23):4450–4461, 2017.

[79] Louisa M Liberman, Gregory T Reeves, and Angelike Stathopoulos. Quantitative imaging of the dorsal nuclear gradient reveals limitations to threshold-dependent patterning in drosophila. *Proceedings of the National Academy of Sciences*, 106(52):22317–22322, 2009.

[80] Ortrud Wartlick, Peer Mumcu, Anna Kicheva, Thomas Bittig, Carole Seum, Frank Jülicher, and Marcos Gonzalez-Gaitan. Dynamics of dpp signaling and proliferation control. *Science*, 331(6021):1154–1159, 2011.

[81] Katherine W Rogers and Patrick Müller. Nodal and bmp dispersal during early zebrafish development. *Developmental biology*, 2018.

[82] Patrick Müller, Katherine W Rogers, Ben M Jordan, Joon S Lee, Drew Robson, Sharad Ramanathan, and Alexander F Schier. Differential diffusivity of nodal and lefty underlies a reaction-diffusion patterning system. *Science*, 336(6082):721–724, 2012.

[83] Charles B Kimmel, William W Ballard, Seth R Kimmel, Bonnie Ullmann, and Thomas F Schilling. Stages of embryonic development of the zebrafish. *Developmental dynamics*, 203(3):253–310, 1995.

[84] T Smith, S Fancher, A Levchenko, I Nemenman, and A Mugler. Role of spatial averaging in multicellular gradient sensing. *Physical biology*, 13(3):035004, 2016.

[85] Matthew David Onsum, Kit Wong, Paul Herzmark, Henry R Bourne, and Adam Paul Arkin. Morphology matters in immune cell chemotaxis: membrane asymmetry affects amplification. *Physical biology*, 3(3):190, 2006.

[86] Loling Song, Sharvari M Nadkarni, Hendrik U Bödeker, Carsten Beta, Albert Bae, Carl Franck, Wouter-Jan Rappel, William F Loomis, and Eberhard Bodenschatz. Dictyostelium discoideum chemotaxis: threshold for directed motion. *European journal of cell biology*, 85(9):981–989, 2006.

[87] Mark D Sternlicht, Hosein Kouros-Mehr, Pengfei Lu, and Zena Werb. Hormonal and local control of mammary branching morphogenesis. *Differentiation*, 74(7):365–381, 2006.

[88] Ambra Bianco, Minna Poukkula, Adam Cliffe, Juliette Mathieu, Carlos M Luque, Tudor A Fulga, and Pernille Rørth. Two distinct modes of guidance signalling during collective migration of border cells. *Nature*, 448(7151):362–365, 2007.

[89] Peter Friedl and Darren Gilmour. Collective cell migration in morphogenesis, regeneration and cancer. *Nature reviews Molecular cell biology*, 10(7):445–457, 2009.

[90] Madhav Mani, Sidhartha Goyal, Kenneth D Irvine, and Boris I Shraiman. Collective polarization model for gradient sensing via dachsous-fat intercellular signaling. *Proceedings of the National Academy of Sciences*, 110(51):20420–20425, 2013.

[91] Erika Donà, Joseph D Barry, Guillaume Valentin, Charlotte Quirin, Anton Khmelinskii, Andreas Kunze, Sevi Durdu, Lionel R Newton, Ana Fernandez-Minan, Wolfgang Huber, et al. Directional tissue migration through a self-generated chemokine gradient. *Nature*, 503(7475):285–289, 2013.

[92] Shirin M Pocha and Denise J Montell. Cellular and molecular mechanisms of single and collective cell migrations in drosophila: themes and variations. *Annual review of genetics*, 48:295–318, 2014.

[93] Robert J Huebner and Andrew J Ewald. Cellular foundations of mammary tubulogenesis. In *Seminars in cell & developmental biology*, volume 31, pages 124–131. Elsevier, 2014.

[94] Geoffrey J Goodhill and Jeffrey S Urbach. Theoretical analysis of gradient detection by growth cones. *Journal of neurobiology*, 41(2):230–241, 1999.

[95] Andre Levchenko and Pablo A Iglesias. Models of eukaryotic gradient sensing: application to chemotaxis of amoebae and neutrophils. *Biophysical journal*, 82(1):50–63, 2002.

[96] Robert G Endres and Ned S Wingreen. Accuracy of direct gradient sensing by cell-surface receptors. *Progress in biophysics and molecular biology*, 100(1):33–39, 2009.

[97] Alexandra Jilkine and Leah Edelstein-Keshet. A comparison of mathematical models for polarization of single eukaryotic cells in response to guided cues. *PLoS Comput Biol*, 7(4):e1001121, 2011.

[98] Andrew J Ewald, Audrey Brenot, Myhanh Duong, Bianca S Chan, and Zena Werb. Collective epithelial migration and cell rearrangements drive mammary branching morphogenesis. *Developmental cell*, 14(4):570–581, 2008.

[99] Arthur D Lander. Pattern, growth, and control. *Cell*, 144(6):955–969, 2011.

[100] Thomas R Sokolowski and Gašper Tkačik. Optimizing information flow in small genetic networks. iv. spatial coupling. *Physical Review E*, 91(6):062710, 2015.

[101] Brian A Camley, Juliane Zimmermann, Herbert Levine, and Wouter-Jan Rappel. Emergent collective chemotaxis without single-cell gradient sensing. *Physical review letters*, 116(9):098101, 2016.

[102] Kristen F Swaney, Chuan-Hsiang Huang, and Peter N Devreotes. Eukaryotic chemotaxis: a network of signaling pathways controls motility, directional sensing, and polarity. *Annual review of biophysics*, 39:265, 2010.

[103] Eric Theveneau, Lorena Marchant, Sei Kuriyama, Mazhar Gull, Barbara Moepps, Maddy Parsons, and Roberto Mayor. Collective chemotaxis requires contact-dependent cell polarity. *Developmental cell*, 19(1):39–53, 2010.

[104] Danfeng Cai, Wei Dai, Mohit Prasad, Junjie Luo, Nir S Gov, and Denise J Montell. Modeling and analysis of collective cell migration in an in vivo three-dimensional environment. *Proceedings of the National Academy of Sciences*, 113(15):E2134–E2141, 2016.

[105] Denise J Montell. Morphogenetic cell movements: diversity from modular mechanical properties. *Science*, 322(5907):1502–1505, 2008.

[106] Beum Jun Kim, Pimkhuan Hannanta-Anan, Michelle Chau, Yoon Soo Kim, Melody A Swartz, and Mingming Wu. Cooperative roles of sdf-1α and egf gradients on tumor cell migration revealed by a robust 3d microfluidic model. *PloS one*, 8(7):e68422, 2013.

[107] Peter Friedl, Joseph Locker, Erik Sahai, and Jeffrey E Segall. Classifying collective cancer cell invasion. *Nature Cell Biology*, 14(8):777–783, 2012.

[108] Thomas S Deisboeck and Iain D Couzin. Collective behavior in cancer cell populations. *Bioessays*, 31(2):190–197, 2009.

[109] Andrew M Simons. Many wrongs: the advantage of group navigation. *Trends in ecology & evolution*, 19(9):453–455, 2004.

[110] Julien Varennes, Bumsoo Han, and Andrew Mugler. Collective chemotaxis through noisy multicellular gradient sensing. *Biophysical Journal*, 111(3):640, 2016.

[111] Kevin J Cheung, Edward Gabrielson, Zena Werb, and Andrew J Ewald. Collective invasion in breast cancer requires a conserved basal epithelial program. *Cell*, 155(7):1639–1651, 2013.

[112] Nabeel Bardeesy and Ronald A DePinho. Pancreatic cancer biology and genetics. *Nature Reviews Cancer*, 2(12):897–909, 2002.

[113] Roberto Mayor and Carlos Carmona-Fontaine. Keeping in touch with contact inhibition of locomotion. *Trends in cell biology*, 20(6):319–328, 2010.

[114] Kosuke Takeda, Danying Shao, Micha Adler, Pascale G Charest, William F Loomis, Herbert Levine, Alex Groisman, Wouter-Jan Rappel, and Richard A Firtel. Incoherent feedforward control governs adaptation of activated ras in a eukaryotic chemotaxis pathway. *Science signaling*, 5(205):ra2, 2012.

[115] Peter JM Van Haastert and Marten Postma. Biased random walk by stochastic fluctuations of chemoattractant-receptor interactions at the lower limit of detection. *Biophysical journal*, 93(5):1787–1796, 2007.